UNIVERSITY OF STRATHCLYDE
DEPARTMENT OF PHYSICS

Investigation of laser-solid interaction physics with tightly focused, ultra-intense laser pulses

by

Timothy P. Frazer

in partial fulfilment of the requirements for the degree of Doctor of Philosophy in Physics

2021

Copyright Declaration

Signed:

Date:

Abstract

This thesis reports on experimental investigations of laser-solid interactions for intensities at the frontier of what is possible using current laser technology. Peak laser intensities of up to 5×10^{21} Wcm^{-2} were achieved through the focusing of picosecond laser pulses to near-wavelength sized focal spots with a novel, elliptical focusing plasma mirror. The influence of these high intensities and small focal spot sizes on proton acceleration in the relativistic transparency regime and on the temperature scaling and dynamics of fast electrons is explored. These two aspects of laser-solid interactions are of critical importance to the realisation of many envisioned applications, in addition to providing insight into the fundamental underpinning physics. The work reported here is structured into two main sections.

The first study reports on an investigation of the influence of ultra-high intensity and near-wavelength sized focal spot, achieved through the use of F/1 focusing plasma optics, on proton acceleration from ultra-thin foil targets, for which the highest proton energies to date are achieved. In this regime, acceleration occurs via a transparency-enhanced, TNSA-RPA hybrid mechanism. When comparing the spectral properties of protons accelerated using F/1 focusing to a F/3 focusing geometry, significant reductions in both maximum proton energy and laser-to-proton energy conversion efficiency were observed, despite the higher nominal laser intensity. Furthermore, the measured holeboring velocity was also found to be reduced for F/1 focusing, when compared with the F/3 case. These findings are explained in terms of transparency-induced self-focusing, which occurs very strongly in the F/3 case, but to a negligible extent for F/1 focusing, and is shown by 2D particle-in-cell simulations. This results in an enhancement

in the peak intensity achieved by the F/3 following the onset of transparency, boosting the intensity beyond the nominal peak intensity of the F/1 focusing geometry. This increased intensity subsequently results in enhanced proton energies, with both the peak intensity and proton energy maximised for an optimal focal spot size ($\phi_L = 5$ μm) and target thickness ($\ell = 100$ nm). Limited enhancement occurs for F/1 focusing to close to the laser wavelength or when the target remains opaque for the duration of the interaction, as self-focusing cannot take place. This result will help guide the design of future experiments, by showing that optimal proton energies in the transparency regime are obtained for more conventional focusing conditions, significantly reducing the technical challenges and financial expense involved.

The second study presents findings related to the scaling of fast electron temperature within thin foil targets, and the effect of this on electron refluxing and proton acceleration via the TNSA mechanism. Using measurements of copper K_α photons from 25 μm thick copper targets and protons accelerated via the TNSA mechanism from 6 μm thick aluminium targets, the fast electron temperature scaling with intensity was determined. This was found to scale more slowly with increasing intensity than would be expected from existing models, resulting in reduced electron temperatures. Analytical modelling shows that this slower scaling is likely due to the inhibition of electron heating as a result of the relativistic skin-depth, which becomes on the order of ~ 10 nm for intensities $> 10^{21}$ Wcm^{-2}. The decreasing skin-depth alone is however not suffice to fully explain the slowing of the temperature scaling. Modifications to the plasma density within the skin-depth, based on relativistic effects or radiation pressure induced compression are discussed, supported by analytical modelling and 2D particle-in-cell simulations, are shown to produce better agreement with the results measured experimentally. The electron temperatures measured are also shown to result in significantly increased electron refluxing within the target, whilst the effect of the slower scaling with intensity is shown to adversely affect the scaling of maximum proton energies generated via the TNSA mechanism. This result highlights that, when moving to higher intensities, the gains in electron temperature may not be as significant

as previously predicted, which has a significant impact on the generation of high energy particles and ionising radiation.

Acknowledgements

The completion of this thesis, the work presented within, and the numerous other experiments and projects of which I have been a part, would not have been possible without the help and support of a number of people. First and foremost, thanks must go to my supervisor, Prof. Paul McKenna, whose wisdom, extensive experience and knowledge have been invaluable throughout my Ph.D. His patient and insightful approach is something that I wish to emulate in my own work, and his drive to always take the next step forward, both in terms of scientific research for the group and personal career development is inspiring.

Besides my supervisor, there are a number of other key figures, who have contributed in many ways to my Ph.D. First of all, Dr. Ross Gray, for passing on some of his extensive knowledge on all aspects of physics, and science in general. Without his day-to-day input and advice, much of the work in this thesis would not have reached completion. His encouragement to think critically about your own work and recognise potential weaknesses undoubtedly improved the overall quality of my research. I would also like to thank Dr. Martin King for his contributions to my work. Without his insight and computational skill, much of this work, and in particular that presented in Chapter 4, would not have been possible. Dr Robbie Wilson is also deserving of a great deal of appreciation. I have learnt most of what I know regarding the practical side of experimental physics from Robbie. His friendship from day one and down-to-earth nature played a key part in me settling into the research group and more generally life in Scotland. Additional thanks must go to Drs. Ross Gray and Robbie Wilson for reviewing drafts of my thesis, which has been enhanced substantially by their input and suggestions.

Thanks must also be directed to the late Prof. David Neely. Despite only knowing him for a few years, he proved himself time-and-again to be a kind and helpful individual, always willing to offer a solution to any problem in the lab, ask the most pertinent questions and push work forward with unparalleled drive and enthusiasm. His loss is a terrible blow to the field of laser-plasma physics worldwide, and I know experiments at the CLF won't be the same in his absence.

I additionally thank my numerous colleagues, both past and present; Nick, Jonathan, Adam, Sam, Remi, Chris, Alana, Egle, Antonio, Ewan D., Ewan B. and Jack. Each has contributed in some way towards my Ph.D., whether that be help on an experiment or something as simple as a chat over a coffee in the office. Special thanks however must be directed towards Dr. Matthew Duff, who over the several years we shared an office became a good friend. His enthusiasm for all things physics was infectious, and we had many an interesting discussion in the office, on both physics and music. His patience in dealing with my MATLAB queries is to be applauded, and his advice and suggestions would often be the spark that would inspire forward progress in my research when I'd seemingly hit a dead end or didn't know how to proceed.

Finally, I must thank my mum and dad for their unending support and encouragement. Whilst they never attempted to steer my career path, they have supported me every step along the way, including my decision to move to Scotland to pursue my Ph.D. From a very young age, they encouraged me to ask questions and to be curious about the world around me, which certainly contributed to my eventual fascination with physics. Their perseverance with my incessant questioning and desire to read through that encyclopedia on dinosaurs, warships or aircraft for what probably seemed like the hundredth time as a child certainly paid off, as without it, I most certainly wouldn't have made it this far.

Role of Author

The results presented in this thesis are the work of the author over several experimental campaigns, performed as part of a team of researchers led by Prof. P. McKenna. The author had a primary role in the planning, execution, data analysis, numerical simulations and interpretation of results.

Chapter 4: The author played no role in the planning or execution of the experimental campaign, as it was undertaken prior to the start of the author's Ph.D. studentship. Digitisation of the proton dosimetry film was carried out by the author. Analysis of the proton spectra from the dosimetry stacks was undertaken by the author using a code developed by Dr David Carroll, with modifications made by the author. Analysis of the backscatter spectra to obtain the holeboring velocity was performed by the author. PIC simulations were carried out by Dr Martin King, and analysed by Dr Martin King, with input from the author.

Chapter 5: The author was involved in the planning and execution of the experimental campaign (as DTAO) reported in this chapter. The focusing plasma optics used in the experiment were tested by the author. The experiment was set up by Drs. Robbie Wilson, Nicholas Butler, Ross Gray and the author. The K_α diagnostic was designed and set up by Drs. Jonathan Jarrett and Robbie Wilson. Analysis of the K_α data was performed by the author, and the analytical model used was developed by the author, benchmarked against a previous model developed by Dr. Mark Quinn. Analysis of proton maximum energy data was performed by the author and Dr. Robbie Wilson. PIC simulations were performed by Dr Martin King and analysed by Dr. King and the author.

Publications

Publications directly resulting from the work presented in this thesis

1. **Enhanced laser intensity and ion acceleration due to self-focusing in relativistically transparent ultrathin targets**

   T. P. Frazer, R. Wilson, M. King, N. M. H. Butler, D. C. Carroll, M. J. Duff, A. Higginson, J. Jarrett, Z. E. Davidson, C. Armstrong, H. Liu, D. Neely, R. J. Gray and P. McKenna. *Phys. Rev. Research* **2**, 042015(R), 2020.

Additional publications resulting from this PhD work

1. **Spectrally peaked proton beams shock accelerated from an optically shaped overdense gas jet by a near-infrared laser**

   G. S. Hicks, O. C. Ettlinger, M. Borghesi, D. C. Carroll, R. J. Clarke, E. J. Ditter, **T. P. Frazer**, R. J. Gray, A. McIlvenny, P. McKenna, C. A. J. Palmer, L. Willingale and Z. Najmudin. *arXiv*:2104.13977v1, 2021.

2. **Influence of spatial-intensity contrast in ultra-intense laser-plasma interactions**

   R. Wilson, M. King, N. M. H. Butler, D. C. Carroll, **T. P. Frazer**, M. J. Duff, A. Higginson, R. J. Dance, J. Jarrett, Z. E. Davidson, C. D. Armstrong, H. Liu, S. J. Hawkes, R. J. Clarke, D. Neely, R. J. Gray and P. McKenna. *Scientific Reports*, Accepted/In press, 5 Jan 2022.

Contents

List of Figures

List of Tables

Chapter 1

Introduction

The subject matter of this thesis is the investigation of the interaction of an ultra-intense laser pulse with solid density matter. Advances in laser technology since the first practical demonstration in 1960 [1] have led to the capability for relativistically intense laser pulses ($I_L > 10^{18}$ Wcm^{-2} for a wavelength of ~ 1 μm) to be routinely generated in the laboratory. The generation of laser pulses with sufficiently high energy to achieve such intensities, with short pulse durations (femtoseconds to picoseconds), first became possible due to the advent of the chirped pulse amplification (CPA) technique [2]. The interaction of relativistic laser pulses with thin foil targets have been extensively investigated, as a driver for energetic ions [3, 4], bright x-rays [5, 6], and high harmonics [7, 8]. Furthermore, laser-plasma interactions can provide a means of generating in the laboratory conditions analogous to those found in astrophysical environments [9, 10]. Aside from the investigation of these processes from a fundamental physics point of view, exploitation of laser-plasma interactions is envisioned to potentially yield a range of applications of societal benefit, such as proton oncology [11], 3D x-ray imaging [12] or inertial confinement fusion schemes [13]. It is apparent that laser-plasma interactions open the door to a wide range of applications, which has resulted in extensive research being undertaken in this area worldwide over the past few decades.

In this thesis, one application of primary interest is the potential for laser-solid interactions to complement, or in certain circumstances replace, conventional

radio frequency (RF) accelerator technology. Conventional accelerators based on RF cavities are subject to significant limitations, preventing this technology from being available for widespread use within university, medical or industrial settings by increasing the cost and footprint. This ultimately limits the societal impact of this technology and slows the advancement of our understanding of fundamental physics.

The primary limitation of conventional accelerator technology is the footprint (or put more simply, size) and the associated cost. Due to the breakdown voltage of the accelerating structures with RF accelerators, the accelerating fields are limited to ~ 100 MV m^{-1} [14]. This results in the requirement of large accelerator facilities, limiting the placement of these facilities to national laboratories, whilst incurring significant financial costs, both in the construction and operation phases. The Large Hadron Collider (LHC) provides the most stark example of this. In order to accelerate protons to TeV energies, a synchrotron accelerator of circumference 27 km was constructed in a multi-billion pound, multi-national project. Perhaps a more everyday example would be proton sources for hadron therapy purposes. Facilities using linear or synchrotron accelerators for this purpose are currently coming online, but at a cost on the order of hundreds of millions of pounds each. The cost, combined with the footprint, prevents this technology from being made widely available at local hospitals or most research organisations. In contrast, as plasma is an ionised state of matter, the accelerating fields are not limited by electrical breakdown, enabling fields of several TV m^{-1} to be achieved. Combined with the increasing availability of ultra-intense, table-top laser systems, this opens up the potential of a new regime of compact laser-driven particle accelerators, reducing both the footprint and cost of high energy particle and radiation sources.

Conventional RF accelerators typically operate with one of two end goals in mind, either generating a beam of energetic particles (e.g. the LHC at CERN), or using those particles to produce bright sources of radiation (e.g. the Diamond light source at RAL). Laser-plasma interactions provide the capability of multi-modal operation, i.e. several sources of ionising radiation may be produced

simultaneously. It is not uncommon for one interaction to generate accelerated ions and electrons, bright x-rays and neutrons. This enables greater flexibility of use, as the desired product may be selected without requiring significant modification to the experimental setup. Moreover, by splitting the laser driver into two or more beams, multiple types of radiation, in synchronised pulses, can be produced, opening up new opportunities for pump-probe investigation or mixed-modality irradiation. This may open up applications of industrial interest, such as using accelerated protons to induce lattice melting within a target material, followed by probing the damage with laser-generated x-rays for example [15]. Of course, if only one form of ionising radiation is required, the other forms will need to be separated, which will present a significant challenge given the variety of radiation produced. Furthermore, the generation mechanisms are currently unstable, and, particularly in the case of ion acceleration, yield sub-optimal energy spectra, both in terms of the spectral shape, and the maximum energies generated. Optimisation and stabilisation of laser-solid interactions for use as a compact particle accelerator remains the focus of substantial research efforts worldwide [3, 4].

In addition to providing a more compact and cost-effect approach to particle acceleration, with multi-modal operational capabilities, the ion beams generated by laser-solid interactions have a number of unique properties which make them well-suited for a range of applications. Ion bunches produced from laser-solid interactions have a bunch duration on the order of the driving laser pulse duration, typically a few picoseconds, although the temporal structure increases with propagation distance from the target in the case of ion beams with a broadband energy spectrum. This remains however several orders of magnitude shorter than may be obtained using conventional accelerators, which are typically limited to a minimum of several hundreds of picoseconds [16]. Additionally, ion beams accelerated from laser-solid interactions are highly laminar (i.e. ion trajectories do not frequently cross), and have a low beam emittance. Beam emittance values of $< 4 \times 10^{-4}$ π.mm.mrad have been observed [17], making laser-driven ions sources ideal for ultra-fast pump-probe experiments. Both the short bunch duration and

low emittance are aided by the presence of a co-propagating electron population, which prevents space-charge induced spreading of the ion beam. Some of the applications envisioned for laser-driven ion sources will be briefly discussed in the following section.

1.1 Applications

1.1.1 Inertial confinement fusion

Employing intense laser pulses as a means of inducing nuclear fusion reactions was first proposed in the 1960's [18] and theoretically explored in a 1972 work by Nuckolls *et al.* [19]. The use of lasers for energy production via nuclear fusion is referred to as inertial fusion energy (IFE), with the most common scheme, inertial confinement fusion (ICF), involving the compression and heating of a deuterium-tritium (D-T) fuel capsule to a sufficient density and temperature that fusion reactions are initiated and the burn wave propagates throughout the entire fuel. Compression is driven by laser irradiation of the outer layer of the target, which is ablated (in the direct drive approach [20]). The expansion of this coronal plasma outwards induces the compression of the fuel, due to conservation of momentum. This process requires highly uniform compression, due to the nanosecond durations over which the interaction will take place. Over such timescales, hydrodynamic instabilities can grow [21], seeded by asymmetries in the laser confinement or the target density profile for example, which will impede the coupling of energy from the laser driver into the fuel.

An alternative to this approach, addressing certain limiting aspects of ICF, and potentially enabling higher energy gain, was first proposed in 1994 in Tabak *et al.* [13]. This mechanism, referred to as fast ignition, involves the compression of the fuel target, similar to conventional ICF but to lower densities. A secondary high intensity pulse then irradiates the target, producing energetic particles to deliver energy into the compressed fuel and induce ignition. These particles are typically fast electrons, but proton fast ignition schemes have also been proposed

[22]. The fast ignition scheme reduces the degree of target compression needed from the nanosecond pulses and therefore the input energy required to achieve fusion, thus improving the potential energy gain. In addition, the sensitivity to hydrodynamic instabilities is reduced, as the degree of symmetry required in the compression is relaxed. Proton fast ignition, with the protons sourced from a laser-solid interaction, has fundamental advantages over its electron counterpart. Due to the localised energy deposition profile of ions within the fuel target, spatial control of the energy deposition is possible for spectrally controlled ions, with the maximum possible energy used to achieve ignition instead of being wasted by heating the surrounding plasma. Furthermore, protons are less susceptible to transport instabilities than electrons, and so can more efficiently couple laser energy into the reaction.

Fast ignition, using either electrons or protons, has however not yet come to fruition, due to a number of important limitations. If we consider the more common case of electron fast ignition schemes, there are significant challenges associated with the generation of a suitable fast electron population, and transporting these electrons to the fuel. Inherent beam divergence and transport instabilities reduce the energy density of the fast electron beam [23, 24]. More fundamentally, generating a sufficiently hot electron population remains a challenge, necessitating further study into the heating of electrons within solid targets.

1.1.2 Hadron therapy

Treatment of cancerous tumours, via a radiotherapy approach, conventionally involves the use of x-rays to irradiate the tumour from multiple angles to maximise the dose deposited in the tumour, whilst minimising the collateral damage to surrounding healthy tissue. It is however inevitable that some damage to surrounding tissue will occur, which is particularly problematic in areas of the body which are highly sensitive to radiation, for example the brain or spinal cord. This collateral damage arises due to the energy deposition profile of x-rays in matter, which follows Beer's law. In short, the largest dose of x-rays is delivered at the surface of the target/patient, decaying exponentially with increasing depth. This

not only subjects healthy tissue, both in front of and behind the tumour, to radiation exposure, but also reduces the effectiveness of the cancer treatment, as a majority of the x-ray dose is wasted on the healthy tissue. This issue may be resolved through the use of protons or heavier ion species, referred to as hadron therapy.

Hadron therapy, most commonly using protons, is a significant improvement over conventional x-ray radiotherapy due to the difference in how ions deposit energy within matter. Ions deposit energy in a characteristic Bragg peak (see Chapter 3.5.1 for proton stopping in iron). The ion will propagate through the patient, depositing minimal energy until just prior to stopping, at which point all the remaining energy will be deposited, with the initial energy of the ion determining the depth to which it will penetrate. This enables precise targeting of the tumour, while simultaneously minimising collateral damage to healthy tissue before or after the tumour. This concept was first proposed in a 1946 article, in which it was proposed that conventional RF accelerators could generate proton beams for therapeutic purposes [25]. Widespread adoption of this technique has however been slow, in spite of the clear advantages, with only $\sim$ 40 facilities worldwide. This is primarily due to the limitations of RF accelerator technology discussed earlier, namely the footprint and associated costs.

To date, the proton energies required to treat deep-seated tumours (200-250 MeV) is only achievable through conventional RF accelerators. The maximum energy of protons accelerated via laser-driven schemes is however steadily increasing, with a current maximum of $\sim$ 100 MeV [26]. Furthermore, the unique properties of laser-driven proton beams have the potential to bring additional benefits. Multi-modal treatment schemes may also be feasible due to the simultaneous generation of protons, heavier ions, electrons and x-rays from laser-plasma interactions, enabling tailoring of the delivered radiation to each individual clinical case. The short ion bunch durations and high flux also increase the radiobiological effectiveness of hadron therapy. A number of early-stage experiments have explored the biological effect of laser accelerated ions on cellular material [27]. Dose rates exceeding $\sim 10^9$ Gy s^{-1} in a single exposure have been reported, with a

relative biological effectiveness (RBE) of 1.4±0.2, which represents an substantial increase over conventional, X-ray based radiobiological approaches.

Whilst laser-driven proton energies have been steadily increasing, the current record of $\sim$ 100 MeV remains approximately half of the energy required to treat the most deep-seated tumours. Furthermore, clinical use of laser-driven protons will require substantial improvements to the beam parameters currently achievable, such as spectral control and beam focusability, in order to ensure accurate deposition of energy into the tumour, whilst minimising damage to surrounding, healthy tissue. As such, significant research effort is still required if laser-driven protons are to be widely employed as a realistic therapeutic option.

1.2 Thesis outline

In order to fully exploit the potential of laser-driven plasma accelerators, it is imperative that we can not only generate protons suitable for the above applications, but also understand the underpinning physics. Furthermore, in order for any applications to be widely accepted, significant control of these processes must be demonstrated. Achieving such control poses a major challenge due to the highly non-linear nature of laser-plasma interactions, resulting in high sensitivity to small variations in initial conditions. This is compounded by the inherent variability in the performance of current laser systems. The work presented in this thesis goes some way towards achieving a better understanding of the fundamental physics underpinning laser-solid interactions, and uncovers new means by which these interactions may be controlled and optimised.

One route to the control and optimisation of laser-solid interactions is through the drive pulse parameters, and in particular the pulse intensity. Increasing the intensity is predicted to result in higher energy electrons and protons [3, 28], and so would seem to be an important step in the campaign to see the above applications realised. Increasing the pulse intensity is however not without its challenges. Doing so through an increase in energy is very expensive, both technically and financially. Instead, the commonly adopted approach has been to

employ short pulse laser systems and tight focusing geometries. The question therefore arises, does the increased intensity and tighter focusing conditions result in the expected changes in source properties, or does new physics come in to play? The investigation reported in this thesis attempts to go some way towards answering this question, by examining two aspects of laser-solid interactions of relevance to the aforementioned applications, namely the scaling of proton energies in the relativistic self-induced transparency regime and the scaling of fast electron temperature.

This thesis reports on the experimental investigation of the physics underpinning laser-solid interactions, in the ultra-high intensity regime, through the use of near-wavelength sized focal spots. In particular, proton acceleration via a transparency-enhanced, hybrid mechanism and electron heating in micron thick metal targets are examined. The remainder of this thesis is structured as follows;

- **Chapter 2:** The physics underpinning laser-solid interactions is reviewed, which provide an essential foundation for the following chapters.
- **Chapter 3:** The key experimental and numerical techniques employed in the investigations reported in thesis, including details of laser systems, diagnostic techniques and simulation tools, are described.
- **Chapter 4:** This chapter presents experimental and numerical studies on the influence of laser focal spot size, including spots sizes approaching the laser wavelength, on proton acceleration via a transparency-enhanced, hybrid acceleration mechanism.
- **Chapter 5:** Experimental, analytical and numerical investigation of electron heating in laser-solid interactions, for laser intensities of up to $\sim 5\times10^{21}$ Wcm^{-2}, is reported in this chapter.
- **Chapter 6:** Finally, the results and interpretations presented in chapters 4 and 5 are summarised, with the impact for the wider field of laser-solid interactions highlighted. Potential future avenues of research are also discussed.

Chapter 2

Underpinning physics of intense laser interactions with dense plasma

2.1 Introduction

Before presenting the main investigations in this thesis, it is important to review the fundamental physics of the interaction between an intense laser pulse and a dense plasma. In this chapter, we begin by discussing the physics of electromagnetic radiation, defining key properties such as intensity and polarisation, which is vital for understanding the laser pulses that are foundational to the work presented in this thesis. We will then proceed to examine how a single electron will act when subjected to such electromagnetic radiation, as this is the most fundamental interaction involved in laser-matter studies. At this point, the concept of plasma as a state of matter will be introduced, before reviewing some of the basics of laser interactions with such plasma, namely laser-induced expansion and laser propagation. Once the basic physics has been reviewed, more complex topics such as laser energy absorption and fast electron generation within dense plasmas will be explored. Finally, by bringing all of the aforementioned physics together, the mechanisms by which laser interactions with dense plasma may result in the acceleration of ions to multi-MeV energies will be discussed,

relevant to the investigations presented in both results chapters. This chapter is intended merely as a review of the physics most relevant to the work presented later in this thesis and is by no means exhaustive. Further details on the concepts presented in this chapter, and other aspects of laser-plasma interactions, may be found in the plethora of pre-existing literature, including (but not limited to) the textbooks by Kruer [29] and Gibbon [30].

2.2 Electromagnetic radiation

Before attempting to understand how laser light interacts with a single electron, let alone a dense plasma, we must first begin by understanding the laws of classical electrodynamics and how these apply to electromagnetic (EM) radiation of the form seen in intense laser pulses. In order to do so, we begin with Maxwell's equations, which describe the generation of electric and magnetic fields and how they relate, and the Lorentz equation of motion for a charged particle in an EM field. Maxwell's equations are written as follows

$$\nabla \cdot \mathbf{E} = \frac{\rho}{\epsilon_0} \tag{2.1}$$

$$\nabla \cdot \mathbf{B} = 0 \tag{2.2}$$

$$\nabla \times \mathbf{E} = -\frac{\partial \mathbf{B}}{\partial t} \tag{2.3}$$

$$\nabla \times \mathbf{B} = \mu_0 \mathbf{J} + \mu_0 \epsilon_0 \frac{\partial \mathbf{E}}{\partial t} \tag{2.4}$$

where $\mathbf{E}$ is the electric field, $\mathbf{B}$ is the magnetic field and $\mathbf{J}$ is the current density. Bold font represents a vectorial quantity throughout this chapter. Eqn. 2.1 describes how an electric field is generated from some source of charge density, ρ, where ϵ_0 is the electric permittivity of free space. Eqn. 2.2 represents the conservation of magnetic flux. The relation between a spatially varying electric field and a temporally varying magnetic field is described in Eqn. 2.3. Finally, Eqn. 2.4 shows how an electric current generates a magnetic field, where μ_0 is the magnetic permeability of free space.

The force acting on a charged particle under the influence of an electromagnetic field, $\mathbf{F}_L$, is described by the Lorentz equation

$$\mathbf{F}_L = q\left(\mathbf{E} + \mathbf{v} \times \mathbf{B}\right) \tag{2.5}$$

where q and $\mathbf{v}$ are the particle charge and velocity respectively. In the case of a plane wave, with oscillating electric and magnetic field components, the $\mathbf{v} \times \mathbf{B}$ term in Eqn. 2.5 can be neglected where $v \ll c$, as the magnetic field is significantly weaker than the electric field, such that the electron oscillates purely in the electric field direction. As $v \to c$ however, the magnetic field component becomes significant, inducing a drift motion in addition to the oscillatory term, as described in more detail in section 2.3.

The version of Maxwell's equations presented above describes the generalised behaviour of electric and magnetic fields. In terms of describing EM radiation specifically, it is useful to reformulate these in the form of a wave equation, the solutions to which represent EM waves propagating with a characteristic speed, $c = (\mu_0 \epsilon_0)^{-1/2}$, which is the speed of light in vacuum. This is achieved by taking the curl of Eqn. 2.3 as follows

$$\nabla \times (\nabla \times \mathbf{E}) = -\frac{\partial}{\partial t}(\nabla \times \mathbf{B}) \tag{2.6}$$

$$\nabla (\nabla \cdot \mathbf{E}) - \nabla^2 \mathbf{E} = -\frac{\partial}{\partial t}(\nabla \times \mathbf{B}) \tag{2.7}$$

For propagation of the EM wave in vacuum, it is assumed that no charge or current density is present. Substitution of Eqns. 2.1 and 2.4 into the above yields the final form of the wave equation

$$\nabla^2 \mathbf{E} = \frac{1}{c^2}\frac{\partial^2 \mathbf{E}}{\partial t^2} \tag{2.8}$$

One solution to this wave equation is a plane wave, by which we mean a monochromatic wave with an infinite wavefront, whose amplitude is described by some

sinusoidally varying function. The solution for a plane wave in 3D is given by

$$\mathbf{E}(\mathbf{r}, t) = \mathbf{E}_0 \cos(\mathbf{k} \cdot \mathbf{r} - \omega t - \phi) \tag{2.9}$$

where $\mathbf{r}$ is the position vector, $\mathbf{E}_0$ is the amplitude of the wave, and $\mathbf{k}$ is the wave vector with magnitude $|\mathbf{k}| = 2\pi/\lambda$, where λ is the wavelength. The angular frequency of the wave is given by ω and ϕ describes any phase shift of the wave. The plane wave solution can also be expressed in a polar representation as follows

$$\mathbf{E}(\mathbf{r}, t) = \tilde{\mathbf{E}}_0 \exp[i(\mathbf{k} \cdot \mathbf{r} - \omega t)] \tag{2.10}$$

In this case, $\tilde{\mathbf{E}}_0$ is the complex amplitude, which constitutes both the amplitude, $\mathbf{E}_0$, and the phase angle, ϕ, of the wavefunction. An expression of an identical form exists for the $\mathbf{B}$ field. This plane wave solution enables determination of the relative magnitude and spatial orientation of the electric and magnetic fields. By substituting these plane wave solutions into Maxwell's equations, we find the following relations

$$i\mathbf{k} \cdot \mathbf{E} = 0 \quad \text{and} \quad i\mathbf{k} \cdot \mathbf{B} = 0 \tag{2.11}$$

$$i\mathbf{k} \times \mathbf{B} = \frac{-i\omega}{c^2}\mathbf{E} \quad \Rightarrow \quad |\mathbf{B}| = \frac{|\mathbf{E}|}{c} \tag{2.12}$$

From Eqn. 2.11, we see that the electric and magnetic fields are mutually orthogonal, and that both oscillate perpendicular (transversely) to the propagation direction of the wave. The relation set out in Eqn. 2.12 shows that the magnitude of the electric field is greater than that of the magnetic field by a factor of c. It is for this reason, within the context of laser-matter interactions, that the magnetic field induced drift motion of an electron subjected to a laser field may be neglected unless the electron velcoity within the laser pulse is sufficiently high.

It is also useful to examine at this point how such an EM wave will propagate in vacuum. The 3D plane wave solution given in Eqn. 2.10 may be substituted into the wave equation, Eqn. 2.8, to yield the dispersion relation for vacuum, given as follows

$$\omega = ck \tag{2.13}$$

As this is a linear relation between the angular frequency and wave vector of the EM wave, the phase and group velocities (v_ϕ and v_g) are equal, and take the value of c

$$\frac{\omega}{k} = \frac{\mathrm{d}\omega}{\mathrm{d}k} = c \tag{2.14}$$

where $v_\phi = \omega/k$ and $v_g = \mathrm{d}\omega/\mathrm{d}k$. This is, by definition, the case for EM wave propagation in vacuum, but this is not always true for other propagation media, as will be discussed later in section 2.4.4, when the propagation of a laser field within a plasma will be considered.

2.2.1 Polarisation of an EM wave

A key property of light, which has a significant impact on the interaction of intense laser light with a plasma, as will be explored later, is the optical polarisation. The polarisation is a crucial factor when considering laser energy absorption to the plasma (see section 2.5), and thus by extension, plays a key role in the generation of fast electrons and the subsequent acceleration of ions.

The polarisation of an EM wave describes the oscillation orientation of the electric field, of course assuming that the oscillations are confined to a single, well defined plane. Unpolarised light consists of a superposition of randomly oriented electric field oscillations, with the resultant electric field vector changing rapidly as the pulse propagates. If we assume an EM wave propagating along the z-axis, i.e. the wave vector k is aligned with the z-axis, then the electric field oscillations must only have components in the x-y plane, defined as the polarisation plane. At any given point along the propagation axis, the total electric field can be decomposed into two orthogonal components, as follows

$$\mathbf{E}\left(\mathbf{r}, t\right) = E_{0,x} \cos\left(\phi + \phi_x\right) \hat{\mathbf{x}} + E_{0,y} \cos\left(\phi + \phi_y\right) \hat{\mathbf{y}} \tag{2.15}$$

where the phase is given by $\phi = \mathbf{k} \cdot \mathbf{r} - \omega t$, the phase difference between the x and y components of the electric field is given by $\phi_x - \phi_y$, and the amplitude of the two components are given by $E_{0,x}$ and $E_{0,y}$. These field amplitudes may be

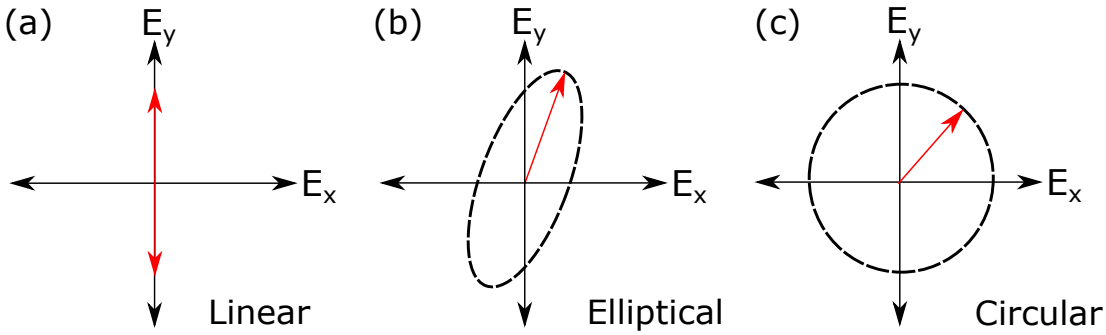

Figure 2.1: Illustration of the polarisation ellipse for three polarisation states; (a) linear, (b) elliptical and (c) circular.

related by the following trigonometric identity [31]

$$\sin^2(\phi_x - \phi_y) = \left(\frac{E_x}{E_{0,x}}\right)^2 + \left(\frac{E_y}{E_{0,y}}\right)^2 - 2\left(\frac{E_x}{E_{0,x}}\right)\left(\frac{E_y}{E_{0,y}}\right)\cos(\phi_x - \phi_y) \quad (2.16)$$

where $E_x = E_{0,x}\cos(\phi + \phi_x)$, and E_y is similarly defined.

The polarised EM wave is described by two parameters, the relative magnitudes of the two orthogonal electric field components, and their relative phase. It can be seen from Eqn. 2.16 that the total electric field vector forms a so-called 'polarisation' ellipse in the polarisation plane. As with any ellipse, the polarisation may then be quantified by the ratio of the semi-major and semi-minor axes, and the angle between the semi-major axis and one axis of the polarisation ellipse. In the general case, the semi-major and semi-minor axes will be rotated through some angle θ, relative to the axes which define the polarisation plane. It is therefore useful to define a rotated coordinate system in x' and y', and to express the electric fields in terms of these coordinates, as follows

$$E_x = E'_x\cos\theta - E'_y\sin\theta \quad (2.17)$$

$$E_y = E'_x\sin\theta + E'_y\cos\theta \quad (2.18)$$

The rotation angle can be defined in terms of the ratio of the electric field components such that $\alpha = E_{0,x}/E_{0,y}$. From this definition of α, the rotation angle may be expressed as $\tan 2\theta = \cos(\phi_x - \phi_y)\tan 2\alpha$.

Now that the polarisation ellipse has been defined, any polarisation state

may be visualised using the ellipse. In general, such EM waves are referred to as elliptically polarised, however two special cases exist which are of great importance, and which are frequently referenced throughout this thesis. The first special case is linear polarisation, in which the quantity $(\phi_x - \phi_y) = 0$ or $n\pi$, where n is some integer. In this case, the electric field vector oscillates along the semi-major or semi-minor axis of the ellipse, and thus we have the condition that $\theta = \alpha$. The interactions explored in the upcoming results chapters all involve linearly polarised laser pulses. The second special case is where the two electric field components are equal in magnitude, with a relative phase given by $(\phi_x - \phi_y) = n\pi/2$. In this case, the total electric field vector generates a circle in the polarisation plane. The general case of some elliptical polarisation, along with these two special cases, is illustrated in Fig. 2.1.

2.2.2 Intensity of an EM wave

The intensity of a laser pulse is a cornerstone of much of the experimental, numerical and analytical investigation presented in this thesis. As such, it is imperative that we define what this means, and how it is related to the more fundamental properties of an EM wave. To begin, we must define the Poynting vector, $\mathbf{S}$, given by

$$\mathbf{S}(\mathbf{r}, t) = \frac{\mathbf{E} \times \mathbf{B}}{\mu_0} \tag{2.19}$$

The Poynting vector describes the instantaneous intensity in terms of the electric and magnetic field strengths at that point in time and space. In a typical laser pulse, these field strengths vary sinusoidally over a laser period, and so the laser intensity is more usually defined in terms of the average Poynting vector over a singular laser period. The magnitude of the Poynting vector may be determined in a useful way for the plane wave solution by substituting Eqn. 2.10 and its B-field equivalent into Eqn. 2.19, yielding

$$|\mathbf{S}(\mathbf{r}, t)| = \frac{|\mathbf{E}_0|^2}{\mu_0 c} \cos^2(\mathbf{k} \cdot \mathbf{r} - \omega t - \phi) \tag{2.20}$$

The intensity of a linearly polarised laser pulse, I_L, is then found by averaging this over one laser period, where $\langle \cos^2(x) \rangle = 1/2$, such that

$$I_L = \langle |\mathbf{S}| \rangle = \frac{\epsilon_0 c E_0^2}{2} \tag{2.21}$$

In addition to defining the laser intensity, it is also common to define the strength of the electric field in terms of the normalised vector potential, a_0, given as

$$a_0 = \frac{e \langle E \rangle}{m_e c \omega} \tag{2.22}$$

where $\langle E \rangle$ is the cycle-averaged electric field. When averaging over a full laser cycle, in the linear polarised case, a_0 is reduced by a factor of 2 relative to a circularly polarised laser pulse, as unlike a linearly polarised pulse, the field in the circular case does not oscillate in magnitude, but only rotates around the propagation axis. The above expression for a_0 is useful from a theoretical standpoint, but experimentally it is normally easier to determine the laser intensity as opposed to the electric field strength. As such, a useful expression for a_0, in terms of the laser irradiance ($I_L \lambda_L^2$), is given as follows

$$a_0 = 0.84 \left(I_L \lambda_L^2 \left[10^{18} \text{ Wcm}^{-2} \mu\text{m}^2 \right] \right)^{1/2} \tag{2.23}$$

Aside from being a useful means of defining what may be considered a relativistically intense laser pulse, the laser a_0 may also be related to the relativistic γ-factor of electrons oscillating in the laser field, where γ is defined in terms of the cycle-averaged electron oscillation velocity, $\langle v_{osc} \rangle$, as follows

$$\gamma = \left(1 - \frac{\langle v_{osc} \rangle^2}{c^2} \right)^{-1/2} \tag{2.24}$$

When expressed in terms of a_0, we find the following expression for the electron γ-factor

$$\gamma = \left(1 + a_0^2 \right)^{1/2} \tag{2.25}$$

This equation provides a useful means of relating a parameter of the EM field,

i.e. a_0, directly to the motion of an electron in that field.

2.3 Single electron motion in an EM field

2.3.1 Single electron motion in an infinite, homogeneous field

Before describing the collective motion of an ensemble of electrons subjected to a laser pulse, it is useful to begin by considering the simplified case of single electron motion in an infinite plane wave. Ion motion in such a wave can be largely neglected due to their higher mass compared with that of an electron. As mentioned previously, the dynamics of a free electron in an EM field are described by the Lorentz equation 2.5. For simplicity, we shall consider only the temporally varying aspect of the electric field, such that $|\mathbf{E}| = E_0 \sin(\omega t)$. If we first consider purely the motion due to the electric field component, as this dominates in the non-relativistic regime due to the relation given in Eqn. 2.12, we can use the Lorentz force, given by Eqn. 2.5, to see that

$$m_e \frac{d\mathbf{v}}{dt} = -eE_0 \sin(\omega t) \tag{2.26}$$

and so an electron will oscillate in the electric field with a velocity of magnitude

$$v_{osc} = \frac{eE_0}{m_e \omega} \cos(\omega t) \tag{2.27}$$

Therefore, an electron initially at rest will oscillate perpendicular to the direction of propagation, orientated along the polarisation axis, and with a frequency equal to that of the driving EM field. The maximum quiver velocity achieved by the electron is given by $v_{max} = eE_0/m_e\omega$. It is apparent that the maximum quiver velocity of an electron in an EM field may be related to the normalised vector potential a_0 via $a_0 \sim v_{max}/c$. This expression is only true in the case of non-relativistic electron motion, where contributions from the $\mathbf{v} \times \mathbf{B}$ component of the Lorentz force may be neglected. It does however clearly show a useful condition,

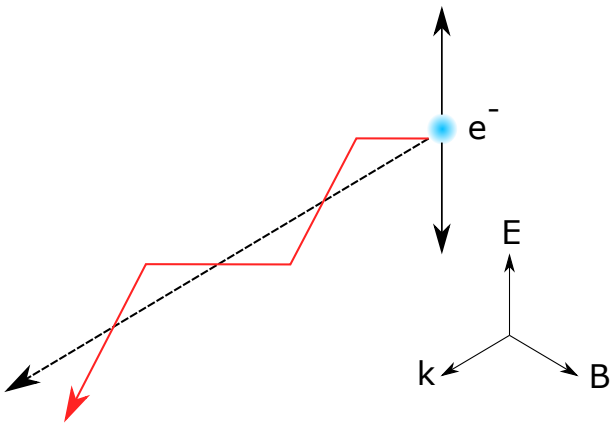

Figure 2.2: Diagram illustrating the 'zig zag' motion of an electron along the axis of laser propagation in the laboratory frame, for a laser pulse of $a_0 \gg 1$.

in that the electron quiver velocity approaches c for $a_0 \sim 1$.

If a stronger field is employed, such that the electron motion is relativistic (i.e. $v_{osc} \sim c$, or $E_e \sim m_e c^2$ in terms of kinetic energy), as is the case for the laser pulses employed in this thesis, the contribution of the magnetic field term can no longer be ignored. As the electron velocity is confined to the polarisation axis of the electric field, and the magnetic field acts orthogonal to this, the cross-product of the two will result in a longitudinal motion in the direction of propagation of the EM field. As a result, in addition to the previously defined transverse quiver velocity, we have a longitudinal velocity, of magnitude

$$v_{long} = \frac{e^2 E_0^2}{4 m_e^2 c \omega^2} \cos\left(2\omega t\right) \tag{2.28}$$

For convenience, the quiver and longitudinal velocities may be expressed in terms of the normalised vector potential (see Eqn. 2.22), as follows

$$v_{osc} = a_0 c \cos(\omega t) \tag{2.29}$$

$$v_{long} = \frac{a_0^2 c}{4} \cos(2\omega t) \tag{2.30}$$

From Eqn. 2.30, it is apparent that the longitudinal component of the velocity oscillates at twice the frequency of the driving field, unlike the transverse oscillation. There exists also a drift component of the longitudinal velocity, i.e. a velocity which is non-oscillatory. This velocity may be described by the following

equation [32]

$$v_{drift} = \frac{a_0^2}{a_0^2 + 4} c \tag{2.31}$$

The combined transverse and longitudinal components of the velocity result in a 'zig zag' motion of the electron in the laboratory frame of reference, and a characteristic 'figure of eight' motion in the electron rest frame. The motion of an electron in a relativistically intense laser field, in the laboratory frame, is illustrated in Fig. 2.2. This is the case for linear polarisation, if the plane wave is instead circularly polarised, the electron traces a circular path in the rest frame, as there is no longer an oscillating EM field to drive the $\mathbf{v} \times \mathbf{B}$ component of the Lorentz force.

2.3.2 Single electron motion in an inhomogeneous field

For a realistic laser pulse, such as those employed in this thesis, the fields are inhomogeneous, with typically a Gaussian spatial and temporal intensity profile, and a centrally peaked intensity distribution. As such, discussion of the influence of such inhomogeneities on electron dynamics is required.

For a spatially homogeneous field, the electron will return to its initial position after one full laser cycle, and thus gains no net energy from the laser pulse [14]. In the case of a Gaussian pulse however, electrons initially located at the centre of the pulse will experience stronger electric and magnetic fields than those at a larger radial distance, and thus by extension, a stronger Lorentz force. We can thus define the ponderomotive force as the gradient of the cycle-averaged oscillation potential of an electron in such an inhomogeneous laser field [30]. The electrons accelerated by this potential will carry energy away from the pulse into the surrounding plasma as they are expelled from the region of locally higher intensity. The cycle averaged ponderomotive force on a single, non-relativistic electron, $\mathbf{F}_p$, may be derived from the Lorentz equation (Eqn. 2.5), and is expressed in terms of the spatial gradient in the electric field as follows

$$\mathbf{F}_p = -\frac{e^2}{2m_e\omega^2} \left\langle \nabla \mathbf{E}^2 \right\rangle \tag{2.32}$$

This equation demonstrates that the ponderomotive force acts independently of the sign of the particle charge. It is, however, inversely proportional to the mass of the particle, and thus, for the laser intensities considered in this thesis (up to 10^{22} Wcm^{-2}), has a negligible influence on the motion of ions. It is also notable that the above equation (Eqn. 2.32) does not account for the influence of the magnetic field on the electron motion, and so is restricted to the non-relativistic regime. The ponderomotive force for a relativistically intense laser pulse (i.e. $v_{osc} \sim c$) is described in detail in Refs. [33, 34], and is given by

$$\mathbf{F}_p = -m_e c^2 \nabla \langle \gamma \rangle \tag{2.33}$$

where $\langle \gamma \rangle$ is the cycle-averaged γ factor of the electrons.

It is also useful to define the potential associated with the ponderomotive force, referred to as the ponderomotive potential, Φ_{p}, which is given by

$$\Phi_{\mathrm{p}} = m_e c^2 \left(\langle \gamma \rangle - 1 \right) \tag{2.34}$$

The amplitude of the electron oscillation resulting in this energy gain, y_0, increases with the intensity of the driving EM field, given by [35]

$$y_0 = \frac{a_0 \lambda_L}{2\pi} \tag{2.35}$$

For intensities of $> 10^{20}$ Wcm^{-2}, this amplitude becomes of the order of microns. Throughout this thesis, pulses of this intensity and higher are employed, focused to a spot size of the same order of magnitude as this oscillation amplitude. It is therefore possible, should the appropriate conditions be met, that electrons escape the focal spot and are transversely scattered before attaining the full ponderomotive potential, resulting in reduced electron energies. This concept is explored further in Chapter 5 and in Dover *et al.* [35].

Due to the influence of the magnetic field on a relativistic electron, its motion will consist of both transverse and longitudinal components. This will result in the ejection of the electron at some angle, θ_s, with respect to the central axis of

the EM field, as described in Moore *et al.* [36]. The scattering angle may be calculated by considering the angle subtended by the transverse ($p_\perp = \Phi_\mathrm{p}/c$), and longitudinal ($p_\parallel = p_\perp/2m_e c$) momenta of the electron, as follows

$$\tan\theta_s = \frac{p_\perp}{p_\parallel} = \left(\frac{2}{\langle\gamma\rangle - 1}\right)^{1/2} \tag{2.36}$$

From this equation, it is clear that as the field strength is increased, and thus by extension the γ-factor of the electron, the scattering angle is reduced, resulting in the electron being scattered closer to the axis of propagation.

2.4 Fundamentals of laser-plasma interactions

In the previous sections, the physics underpinning high intensity laser pulses and their interaction with a single electron has been reviewed. We are now able to proceed to explore the fundamental physics of laser-plasma interactions. The unique dynamics of particles within a plasma result in a variety of non-linear and often counter-intuitive effects, influencing both the plasma itself, and the interacting laser pulse.

2.4.1 Definition of a plasma

A plasma is produced through the ionisation of a material (solid foils in this thesis), producing a 'soup' of positively charged ions and free, negatively charged electrons. However, this is non-commutative, i.e. whilst all plasmas are composed of ionised material, not all ionised material can be considered a plasma. In general, a plasma is classified subject to three conditions being met. These are:

1. $L \gg \lambda_D$

   One key feature of a plasma is that it is quasi-neutral, i.e. when considered globally, the plasma is electrically neutral. If a test charge is placed within the plasma, the electrons will rapidly re-arrange themselves, thus changing the electrostatic potential, to effectively shield the remaining plasma from

the potential of the newly introduced charge. Due to their increased mass, the ions within the plasma are unable to respond quickly to this changing electrostatic potential, and so remain stationary over the timescales on which the electrons screen the charge. The shielding by the electrons is not impervious however, with the magnitude of the potential decaying exponentially over a characteristic distance, given by the Debye length

$$\lambda_D = \sqrt{\frac{\epsilon_0 k_B T_e}{e^2 n_e}} \tag{2.37}$$

where $k_B T_e$ is the electron temperature in joules (see section 2.6.1) and n_e is the electron density. This process is therefore often referred to as Debye shielding. As the electron temperature is increased, the magnitude of the thermal oscillations of the electrons increases, resulting in less effective screening of the test charge, and thus the potential is observed over a greater distance. A larger electron density however will result in enhanced screening, as more electrons are available to shield the plasma from the test charge. Therefore, whilst some local region of the plasma may be positively or negatively charged, the influence of this is not seen throughout the plasma as a whole due to the screening, thus maintaining quasi-neutrality. If the spatial extent of the plasma, L, is less than the Debye length however, the electrons are unable to effectively screen local charge inhomogeneities and quasi-neutrality is broken.

2. $N_D \gg 1$

   This condition is closely related to the previous, as it pertains to the ability of the plasma to screen any local charge imbalances. In order for Debye shielding to be effective, there must be a sufficient number of electrons to shield the test charge. These electrons must exist within a defined Debye sphere, i.e. a sphere of radius λ_D. The number of particles within such a sphere, N_D, is given by

$$N_D = \frac{4}{3} n_e \pi \lambda_D^3 \tag{2.38}$$

If the number of electrons within this sphere is greater than one, then Debye shielding may take place. One consequence of this condition is that a plasma exhibits collective behaviour, as a large number of electrons act in unison, each influencing the other, to screen the test charge, and the potential of the test charge is in turn felt by a large number of electrons.

3. $\omega_{p,e} > \nu_e$

The third condition for defining a plasma is related to the collective effects mentioned in the previous point. In the case of a gas, for example, particle dynamics are dominated by short range, binary collisions. In a plasma however, particle behaviour is dominated by long range, Coulomb interactions, which can influence many charged particles simultaneously. This long range, collective behaviour results in the formation of electron plasma waves, which must dominate over collisional processes when considering the electron dynamics in order for the ionised material to be considered a plasma. The frequency of these plasma waves is described by the plasma frequency, $\omega_{p,e}$, where

$$\omega_{p,e} = \left(\frac{n_e e^2}{\gamma m_e \epsilon_0} \right)^{1/2} \tag{2.39}$$

where γ is the relativistic Lorentz factor, as previously defined. It is worth noting a similar form is adopted for ion plasma waves, although at much lower frequency due to the increase in mass. In order for this collective plasma oscillation behaviour to dominate, the electron plasma frequency must be greater than the collision frequency, ω_c, given by

$$\nu_e = \frac{n_e e^4}{16\pi\epsilon_0^2 m_e^2 v^3} \tag{2.40}$$

where v is the electron velocity. This equation holds true for small-angle Coulomb collisions with ions, but not collisions with neutral particles. It is apparent that collisions are reduced for lower electron density and for faster electrons.

When considering the impact of collisions on the plasma dynamics investi-

gated in this thesis, we must first define two populations of electrons which exist within the target (these will be discussed further in section 2.6). The first population is made up of the electrons forming the bulk of the target, and those contributing to the return current (see section 2.6). This is a high density population of low energy electrons, and as such will be highly collisional. The second population consists of the fast electrons, which have been accelerated to high kinetic energies by the drive laser pulse. This population is considered to be collisionless, as the mean free path of these fast electrons is greater than the spatial extent of the plasma. However, this does not mean that collisions never occur. Firstly, the mean free path is, by nature, an average, and so some electrons will undergo collisions after a propagation distance of less than the mean free path. Furthermore, refluxing (or recirculation) of the electrons (see section 2.6.2) will result in the propagation distance within the plasma being greater than the mean free path for some fraction of the total electron population. Electron-ion collisions, either from the bulk population or from a refluxing fast population are key for the generation of x-rays used to diagnose key plasma parameters explored in this thesis.

2.4.2 Laser-induced ionisation

The subject of this thesis is the study of laser interactions with dense plasma, yet experimentally, we place a solid target foil at the focal position of the laser pulse. Clearly, this solid target is converted into a dense plasma due to the incident laser light. This is a result of laser-induced ionisation, whereby the atoms of target are stripped (either completely or partially) of their electrons, leaving behind positively charged ions and a number of free electrons. In order for the solid target to be ionised to form a plasma, sufficient energy must be deposited by the laser to overcome the binding energy of the electrons within the atoms. This binding energy increases as one moves from the outer to innermost atomic orbitals. The energy required to eject an electron from a particular energy state within an atom, and free it completely from the electrostatic influence of the ion,

is known as the ionisation potential, I_p.

In order to relate this ionisation to a parameter of the incident laser pulse, namely the intensity, it is insightful to consider the simple case of the hydrogen atom. If we consider the semi-classical Bohr model of the atom, which is a good approximation in the case of atomic hydrogen, the mean radius of the orbit of the electron around the nucleus, when in the ground energy state, is given by the Bohr radius, a_B, as follows

$$a_B = \frac{4\pi\epsilon_0\hbar^2}{m_e e^2} \tag{2.41}$$

where $\hbar = h/2\pi$ is the reduced Planck constant. Calculation of the Bohr radius yields a value of $a_B = 0.053$ nm, which may be substituted into Coulomb's law to determine the magnitude of the electric field binding the electron to the nucleus, assuming both the nucleus and the electron act as point charges. This binding field, E_a, is given by

$$E_a = \frac{e}{4\pi\epsilon_0 a_B^2} \tag{2.42}$$

which yields a value for the binding field in atomic hydrogen of $E_a \sim 9 \times 10^{11}$ Vm^{-1}. This can then be converted to be in terms of laser intensity via

$$I_a = \frac{\eta c \epsilon_0}{2} E_a^2 \tag{2.43}$$

where η is the refractive index of the propagation medium. In the case of propagation in vacuum, i.e. $\eta = 1$, this gives an intensity of $I_a \sim 3.5 \times 10^{16}$ Wcm^{-2}. Any laser field of this intensity or higher will therefore strip the electron from the hydrogen atom. However, ionisation is observed for intensities of several orders of magnitude lower than this, indicating the existence of other ionisation mechanisms which can reduce this limit. These mechanisms will now be described and the conditions for which they are dominant discussed.

Multiphoton ionisation

As discussed, an electron will be ejected from an atom if an incident source of photons delivers an energy exceeding the ionisation potential. The simplest

mechanism by which this can take place is single photon ionisation, illustrated in Fig. 2.3 (a). This mechanism places a threshold on energy (and thus wavelength) of the incident photon, below which (above in the case of wavelength) electrons cannot be ionised, regardless of the incident laser intensity. The energy of the ejected electron in this case is given by $E_e = \hbar\omega - I_p$. For a hydrogen atom, with $I_p = 13.6$ eV, only light of wavelength lower than 91 nm, which falls in the extreme ultra-violet (XUV) region of the spectrum, can ionise the ground state with the absorption of a single photon. The laser system employed in this thesis however, produces photons in the mid infra-red (IR) region of the spectrum, with a wavelength of $\lambda_L \sim 1$ μm and a corresponding photon energy of $\hbar\omega \sim 1.2$ eV.

There is however a mechanism by which multiple photons, of energy less than I_p, may result in the ionisation of an electron, referred to as multi-photon ionisation (MPI) [37], as shown in Fig. 2.3 (b). An atom may absorb a photon which does not have a resonant transition to an excited state, by excitation to a virtual state, which exists for a short time, Δt, determined by the uncertainty principle, given by

$$\Delta t = \frac{\hbar}{\Delta E} = \frac{\lambda_L}{2\pi c} \tag{2.44}$$

After this time period, the electron will decay to the ground state and the photon will be re-emitted. However, if during this time a second photon is absorbed, the electron may be further excited to another, higher energy, virtual or real state. This process may continue until the electron is sufficiently energetic to be liberated into the continuum. The ionisation rate, W_N, is proportional to the photon flux, and thus the laser intensity, and is given by

$$W_N = \sigma_N \left(\frac{I_L}{\hbar\omega}\right)^N \tag{2.45}$$

where σ_N is the multi-photon absorption cross-section. This absorption mechanism becomes feasible for light intensities of $I_L > 10^{12}$ Wcm^{-2}, and was first experimentally observed a few years after the invention of the first laser [38, 39]. It is important to note that for higher intensities, where the electric field strength is comparable to the atomic potential, this process breaks down due to the sig-

nificant perturbation caused to the atomic potential, leading to other routes to ionisation which will be discussed below.

An electron may absorb additional photons, beyond that required for ionisation, in a process referred to as above-threshold ionisation (ATI). In this case, the energy of the free electron is given by $E_e = (N + s)\hbar\omega - I_p$, where N is the number of photons with collective energy I_p and s is the number of additional photons absorbed. ATI can be observed to have taken place experimentally by a characteristic peaked electron spectrum, with the peaks separated by $\hbar\omega$ [40].

Tunnelling ionisation

When considering the MPI scheme, it is assumed that the intensity is sufficiently low that the atomic potential remains unperturbed by the incident laser pulse. However, as the electric field of the laser increases in strength, it modifies the atomic potential, as illustrated in Fig. 2.3 (b). Mathematically, the Coulomb potential, $V(x)$, under the influence of an external field, E_{Ext}, takes the following form

$$V(x) = -\frac{Ze^2}{4\pi\epsilon_0 x} + eE_{\text{Ext}}x \tag{2.46}$$

where Z is the atomic number. The second term on the right hand side represents the external electric field of the incident laser pulse, which acts to suppress the Coulomb potential of the atom. Bound electrons may then quantum mechanically tunnel through this reduced potential barrier. The process of tunnelling ionisation enables the laser-induced ionisation of electrons which would classically remain bound within the parent atom. Tunnelling ionisation is illustrated in Fig. 2.3 (c).

The Keldysh parameter

We have thus far defined two ionisation schemes, MPI and tunnelling ionisation, which each provide a mechanism by which an atom may be ionised for incident laser conditions (i.e. intensity and wavelength) which would be forbidden by a classical, single photon ionisation approach. In the calculation of theoretical

tunnelling rates, however, it is assumed that the applied electric field is quasi-static, i.e. it remains constant for the duration of the tunnelling process. The time for which the laser is said to be quasi-static is defined as a short interval near the peak of a laser cycle, corresponding to $T/4\pi = 1/2\omega$, which equates to $\sim 8\%$ of a complete laser period. In this time period, the field changes between a maximum value of E_0 and a minimum of $0.97E_0$. In order to determine which of the mechanisms dominate, and under what conditions, it is helpful to define the Keldysh parameter [41], γ_K, given by

$$\gamma_K = \frac{\Delta t}{1/2\omega} \tag{2.47}$$

where Δt is the tunnelling time. This fraction is the ratio of the tunnelling time to the time for which the laser filed is quasi-static. If the electron can traverse the barrier before the external field reduces, thus increasing the barrier (i.e. $\gamma_K < 1$), tunnelling ionisation will dominate. If this is not possible, i.e. $\gamma_K > 1$, then MPI will dominate. When $\gamma_K \sim 1$, both mechanisms will equally contribute.

The Keldysh parameter may be re-cast in terms of the ratio between the ionisation potential of the bound electron, I_p, and its ponderomotive potential, Φ_p (see section 2.3.2)

$$\gamma_K = \left(\frac{I_p}{2\Phi_\mathrm{p}}\right)^{1/2} \tag{2.48}$$

This form of the equation enables easy comparison between the energy typically gained by an electron from the laser pulse via the ponderomotive force and the energy required to ionise that electron from its parent atom. For a ground state hydrogen atom ($I_p = 13.6$ eV), the transition between MPI and tunnelling ionisation (i.e. $\gamma_K \sim 1$) occurs for laser intensities of $\sim 10^{14}$ Wcm^{-2}, for a laser of central wavelength of $\lambda_L = 1$ μm. This threshold shows that, for the pulse parameters considered in this thesis, MPI processes will only occur for lower intensity light temporally preceding the main pulse (see section 3.2), and all ionisation causes by the main pulse will result from suppression of the atomic potential.

Over the barrier ionisation

An extension to the case of tunnelling ionisation, where the incident laser field is stronger still, is the case of over the barrier ionisation (OBI). In this instance, the external laser field is sufficiently strong so as to completely suppress the atomic potential, as illustrated in Fig. 2.3, to the point that it is lower than the ionisation potential of the bound electron. From Eqn. 2.46, setting $k = ze^2/4\pi\epsilon_0$ for convenience, it can be shown that the maximum potential of the barrier, V_{max}, is given by

$$V_{max} = -2\left(keE_{\text{Ext}}\right)^{1/2} \tag{2.49}$$

at a distance, x_{max}, from the atomic nucleus of

$$x_{max} = \left(\frac{k}{eE_{\text{Ext}}}\right)^{1/2} \tag{2.50}$$

The condition required for OBI is that the binding energy of the electron is greater than the maximum barrier potential (i.e. $|I_p| > |V_{max}|$). Therefore, the minimum electric field strength required for OBI, E_{OBI}, is given by

$$E_{OBI} = \frac{I_p^2}{4ke} \tag{2.51}$$

This electric field strength corresponds to an intensity of

$$I_{OBI} = \frac{\epsilon_0^3\pi^2 c}{2e^6}\frac{I_p^4}{Z^2} = 4\times10^9\frac{I_p^4\,[\text{eV}]}{Z^2} \quad \left[\text{Wcm}^{-2}\right] \tag{2.52}$$

Therefore, all atoms are ionised for intensities greater than I_{OBI}. Once again using atomic hydrogen as an example, ionisation of the electron in the ground state will require an intensity of $I_{OBI} = 1.4\times10^{14}$ Wcm^{-2}. The process of OBI is illustrated in Fig. 2.3 (d).

Collisional ionisation

The final ionisation mechanism reviewed here is not specifically a laser-induced process, but is nonetheless an important mechanism when considering laser-

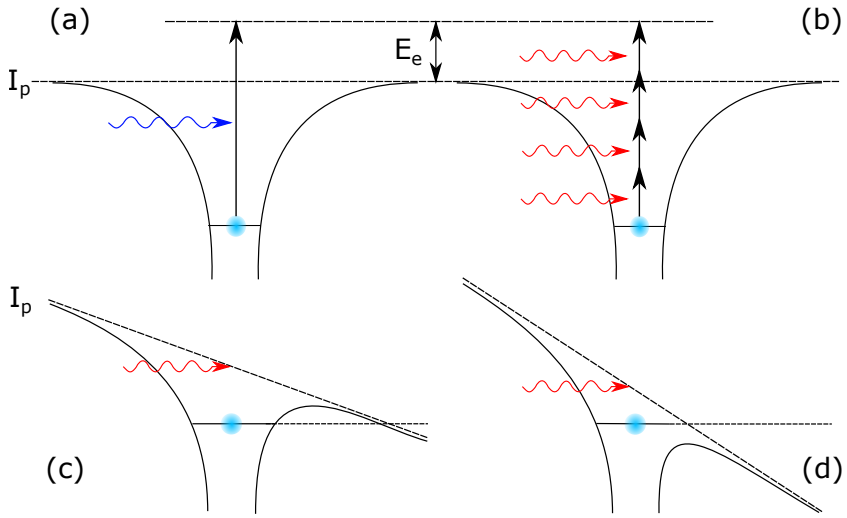

Figure 2.3: Illustration of four ionisation processes, relevant to laser-solid interactions: (a) single photon ionisation, (b) multi-photon ionisation, (c) tunnelling ionisation and (d) over the barrier ionisation. The blue circles represent an initially bound electron and the waves represent incident photons, with the colour loosely illustrating the energy/wavelength of the photon.

plasma interactions. In this process, a bound electron is ionised through a binary collision with a free electron. Such free electrons may be generated as a result of (even partial) ionisation due to the directly laser-induced ionisation processes discussed previously. In the collision of a free electron with a bound electron, energy will be transferred to the bound electron, which may be in excess of the ionisation potential. As previously stated, the collision frequency is given by Eqn. 2.40, and the frequency of collisional ionisation, (ν_{CI}) may be expressed as [42, 43]

$$\nu_{CI} \sim n_e v_e 4\pi a_b^2 \left(\frac{I_H^2}{I_p k_B T_e}\right) \ln\left(\frac{k_B T_e}{I_p}\right) \tag{2.53}$$

where $I_H = 13.6$ eV is the ionisation potential of hydrogen, I_p is the ionisation potential of the ionised species, v_e is the electron velocity and $k_B T_e$ is the electron temperature. It is clear that the collisional ionisation frequency does not depend directly on any laser parameters, and so ionisation via collisional mechanisms is not limited to the irradiance time of the incident laser pulse. Collisional ionisation is a crucial aspect of the process resulting in the emission of K_α photons (see chapter 3.5.3), which forms the cornerstone of Chapter 5.

2.4.3 Laser-induced plasma expansion

In the previous section, the mechanisms by which an intense laser pulse may generate a plasma have been discussed. It is now important that we examine the dynamics of this plasma once it has been formed at the front surface of the target. The front surface plasma dynamics have a key influence on numerous aspects of laser-plasma interactions discussed later, such as laser energy absorption into the plasma electrons.

The dynamics of the interaction of a laser pulse with a solid density plasma is dependent on a number of laser parameters, including the energy, pulse duration, focal spot size and quality, and the temporal intensity contrast. The temporal intensity contrast quantifies, in very simple terms, the intensity of the laser light at a given point in time prior to the main pulse, and will be discussed in more detail in the next chapter (section 3.1.1). The light arriving before the main pulse, whilst significantly less intense, is still sufficient to ionise the target ($I_L = 10^{10} - 10^{15}$ Wcm^{-2}), producing what is known as a 'pre-plasma'. Due to thermal pressure, this preformed plasma will expand, with the expansion front travelling with a velocity approximately equal to the local sound speed, c_s, given by

$$c_s = \left(\frac{Z k_B \left(T_e + 3T_i \right)}{m_i} \right)^{1/2} \tag{2.54}$$

where T_i is the ion temperature, m_i is the ion mass and the rest of the parameters take their usual meaning. The thermal expansion of the plasma results in the formation of a density 'ramp', with the density decreasing with increasing distance from the initial position of the target surface. This spatial electron density profile, $n_e(z)$, is typically represented mathematically in the form of an exponentially decaying function [29]

$$n_e(z) = n_0 \exp\left(-\frac{z}{L_s} \right) \tag{2.55}$$

where z is the distance along the laser propagation axis, n_0 is the initial target electron density and L_s is the density scale length, i.e. the distance at which the density falls to $1/e$ of n_0. The density scale length is used as the primary means of

quantifying the spatial extent of the pre-plasma, and has a significant influence on the interaction, for example by altering the coupling of laser energy to the target electrons [44, 45, 46] or by altering the incident laser pulse via processes such as self-focusing [44, 47] (see section 2.4.4). A simple estimate of this scale length may be made using the following equation

$$L_s = c_s \tau_L \tag{2.56}$$

Alternatively, a more rigorous estimation of the scale length may be made by employing hydrodynamic simulations for realistic initial laser and plasma conditions, and by fitting Eqn. 2.55 to the modelled density profile.

In order to conserve momentum, the rapid thermal expansion of the pre-plasma results in a counter-propagating shock wave, launched into the target foil. The propagation velocity of this shock wave may be calculated from

$$v_s = \frac{c_s}{2}\left[(1+x)^{1/2}+1\right] \tag{2.57}$$

where x is given by

$$x = \left(\frac{4\alpha}{\rho_0 c_s^2}\right) P \tag{2.58}$$

The external pressure applied to the target is given by P and is proportional to the incident laser intensity, and α is an empirical constant related to the target material. If we assume a typical intensity of $I \sim 10^{12}$ Wcm^{-2} for light preceding the pulse, the shock velocity will be of the order of μm per ns. When the shock wave reaches the rear surface of the target, the surface will be decompressed and distorted, which will have a significant influence on the properties of the accelerated protons, therefore imposing a limiting condition for the target thickness used for a given laser temporal intensity contrast. This is of particular importance for ultra-thin targets, where the time taken for the shock wave to traverse the target is very short, thus requiring a very high contrast laser pulse.

2.4.4 Laser propagation in plasmas

Thus far, we have seen how a laser pulse may form an expanding plasma on the front surface of a solid foil target. But the question remains of how the laser pulse will interact with this plasma once it has been formed. We will begin by considered the propagation of EM radiation within a plasma, which differs in several key aspects from the simple case of laser propagation in vacuum considered at the beginning of this chapter.

As in section 2.2, it is useful to begin with a wave equation for an EM propagating in a plasma. Unlike the previously discussed wave equation in vacuum however, the current density can no longer be assumed to be zero due to the presence of charged particles within the plasma. Assuming quasi-neutrality (i.e. $\rho = 0$), the wave equation becomes

$$\nabla^2 \mathbf{E} - \frac{1}{c^2}\frac{\partial^2 \mathbf{E}}{\partial t^2} - \mu_0 \frac{\partial \mathbf{J}}{\partial t} = 0 \tag{2.59}$$

By setting $\nabla = ik$ and $\partial/\partial t = -i\omega$, and using $\mathbf{J} = -n_e e \mathbf{v}$, the dispersion relation of an EM wave in a plasma may be determined

$$\omega^2 = \omega_{p,e}^2 + k^2 c^2 \tag{2.60}$$

From this dispersion relation, it is apparent that the plasma, through the electron plasma frequency, impacts the propagation of an EM wave, and thus will influence the propagation of a laser pulse. An expression for the phase velocity of the laser pulse may be derived using this dispersion relation, given by

$$v_\phi = \frac{\omega}{k} = \frac{c}{\sqrt{1 - \frac{\omega_{p,e}^2}{\omega^2}}} \tag{2.61}$$

Initially, this equation may appear to violate the tenets of relativity, in that for $\omega > \omega_{p,e}$, the phase velocity is greater than c. However this is not the case, as information is carried by an EM wave at the group velocity, which due to the influence of the plasma, is no longer equal to the phase velocity as in the vacuum

case. Differentiation of the plasma dispersion relation, Eqn. 2.60, yields a group velocity of

$$v_g = \frac{\mathrm{d}\omega}{\mathrm{d}k} = c\sqrt{1 - \frac{\omega_{p,e}^2}{\omega^2}} \tag{2.62}$$

From this equation, it is clear that the group velocity remains less than c for the condition of $\omega > \omega_{p,e}$, thus preserving the laws of relativity.

If the dispersion relation (Eqn. 2.60) is rearranged in terms of the wave vector k

$$k = \frac{\sqrt{\omega^2 - \omega_{p,e}^2}}{c} \tag{2.63}$$

two distinct regimes become clear. In the first regime, when $\omega > \omega_{p,e}$, the resulting value of k is real. Therefore, the laser will propagate through the plasma, i.e. the plasma is transparent to the laser pulse. In the second regime, where $\omega < \omega_{p,e}$, the resulting value of k is imaginary. The plasma is therefore opaque to the laser pulse, as the plasma electrons can oscillate with a sufficiently high frequency to react to the incident EM field, which will thus be reflected from the plasma. A transition frequency therefore exists, at which a transparent plasma becomes opaque, or vice versa, given by $\omega = \omega_{p,e}$. This condition is commonly re-expressed in terms of the plasma density, defining the critical density n_c, determined by substituting the laser frequency for the plasma frequency in Eqn. 2.39, yielding

$$n_c = \frac{m_e \epsilon_0 \omega^2}{e^2} \sim 1.1 \times 10^{21} \lambda_{\mu\mathrm{m}}^{-2} \quad \left[\mathrm{cm}^{-3}\right] \tag{2.64}$$

where $\lambda_{\mu\mathrm{m}}$ is the laser wavelength in microns. The 2D plane at which the electron density is equal to the critical density is often referred to as the critical surface. A plasma with an electron density less than n_c is known as underdense, while conversely, a plasma of density greater than n_c is referred to as overdense.

The pulse will not be completely reflected at this surface however, as the electric field will penetrate the plasma, evanescently decaying over a characteristic distance known as the skin-depth, ℓ_s. The skin-depth is defined as the distance over which the electric field will decay to $1/e$ of it's amplitude at the critical

surface, and in the non-relativistic case, is given by

$$\ell_s = \frac{c}{\sqrt{\omega_{p,e}^2 - \omega^2}} \tag{2.65}$$

This can be simplified to the form of $\ell_s = c/\omega_{p,e}$ for the case where the plasma density is significantly higher than the critical density. In the relativistic case, as per Haines *et al.* [48], the skin-depth takes the form

$$\ell_s \approx \frac{c}{\omega_{p,e}} \left(\frac{\omega}{\omega_{p,e}} \right)^{2/3} a_0^{1/3} \tag{2.66}$$

The ability of the laser light to penetrate beyond the critical surface in this manner is essential to laser energy absorption by the plasma electrons, as will be discussed in section 2.5.

The statement that the laser is reflected at the critical density of the plasma is only true when the angle of incidence is $\theta_i = 0°$. It is therefore necessary that we find an expression for the density at which the laser is reflected, as a function of θ_i. In order to achieve this, we must first define the refractive index of the plasma. The refractive index of a medium may be related to the phase velocity of the laser via $\eta = c/v_\phi$, and so, using Eqn. 2.61, we find that

$$\eta = \sqrt{1 - \frac{\omega_{p,e}^2}{\omega^2}} = \sqrt{1 - \frac{n_e}{n_c}} \tag{2.67}$$

It is apparent that as the plasma density changes, so too does the refractive index. If the laser pulse is obliquely incident, it will refract away from the normal axis as it propagates into the density ramp at the target front surface. This will ultimately result in the pulse turning within the density ramp. By employing Snell's law, the density at which the laser will be reflected, n_f, may be determined, for the general case of some non-zero angle of incidence, given by

$$n_f = n_c \cos^2 \theta_i \tag{2.68}$$

Therefore, the density of reflection is only the critical density for normal incidence,

with laser pulses incident at greater angles being reflected at an electron density of $n_f < n_c$.

Relativistically self-induced transparency

When considering relativistically intense laser pulses ($I_L > 10^{18}$ Wcm^{-2} for $\lambda_L = 1$ μm), we begin to observe the influence of relativistic effects on laser propagation in a plasma. As the laser intensity increases, so too does the value of a_0, which in turn results in an increase in the Lorentz factor of the plasma electrons via Eqn. 2.25, assuming linear polarisation. This increasing Lorentz factor modifies the relativistic mass of the electrons oscillating in the laser field, such that $m'_e = \gamma m_e$. This relativistic mass increase in turn influences the critical density of the plasma, given in the non-relativistic case by Eqn. 2.64. The relativistic critical density, n'_c, is therefore related to the non-relativistic case by $n'_c = \gamma n_c$. It is apparent that as the laser pulse becomes increasingly intense, the critical density will also increase, thus enabling the laser pulse to propagate further into the plasma than would be possible without the influence of relativistic effects, known as relativistically-induced transparency (RIT).

From the above condition, it is clear that transparency takes place for an initially opaque target when the electron density meets the condition $n_e < n'_c$. There are two mechanisms by which this may occur: 1) an increase in n'_c due to an increasing electron Lorentz factor or 2) a decrease in n_e resulting from thermal expansion of the target or ponderomotive expulsion of plasma electrons from the focal spot region. For the laser and target conditions investigated experimentally in this thesis, transparency occurs due to a combination of these effects, as laser intensities are not sufficiently high to result in purely relativistically-induced transparency. For example, if we take the case of a laser pulse of central wavelength $\lambda_L = 1$ μm, incident on a solid density aluminium target, the intensity required for transparency through purely relativistic effects would be $I_L \sim 8\times10^{23}$ Wcm^{-2}, several orders of magnitude higher than the intensities employed in this thesis. To reflect this, the process of transparency, as occurring in the investigations presented in thesis, is referred to as relativistically self-induced transparency

(RSIT).

Self-focusing of a laser pulse in plasma

In section 2.4.4, it was discussed how the refractive index can be shown to depend on both the critical density and the plasma electron density (see Eqn. 2.67). It is therefore apparent that variation in either of these densities will result in a changing refractive index, which will in turn influence the propagation of the laser pulse through a plasma. One key way in which this takes place is through self-focusing of the laser pulse. In this process, the spatial-intensity profile of the plasma refractive index is altered such that the refractive index is largest along the central axis of the laser pulse, and decreases with increasing radial distance from this axis. In this way, the plasma acts as a positive lens, focusing the laser pulse as it propagates through the plasma.

Firstly, we consider the case of relativistic self-focusing. As seen in the previous section, for a relativistically intense laser pulse, the critical density becomes $n_c' = \gamma n_c$ and so the plasma refractive index is now given by $\eta = \sqrt{1 - n_e/n_c'}$. We thus have a refractive index which is dependent on the laser a_0, via the Lorentz factor γ, with higher intensities resulting in a higher refractive index for a fixed laser wavelength. Due to the spatial intensity profile of the laser pulse, the Lorentz factor, and thus by extension the refractive index, is highest along the central axis of propagation, decreasing with increasing radial distance, resulting in a focusing of the laser pulse. Physically, this is due to the outer 'wings' of the pulse travelling with a greater velocity than the centre, inducing a concave curvature of the wavefront.

The other primary mechanism which causes focusing of the laser pulse, is known as ponderomotive self-focusing. As discussed in section 2.3.2, the ponderomotive force is an intensity dependent force, acting to expel electrons from regions of high laser intensity. The result of this expulsion is that the electron density is reduced in regions of high laser intensity. From Eqn. 2.67, it is clear that such a decrease in electron density will result in an increased refractive index. As the ponderomotive force depends on the laser intensity, the spatial intensity

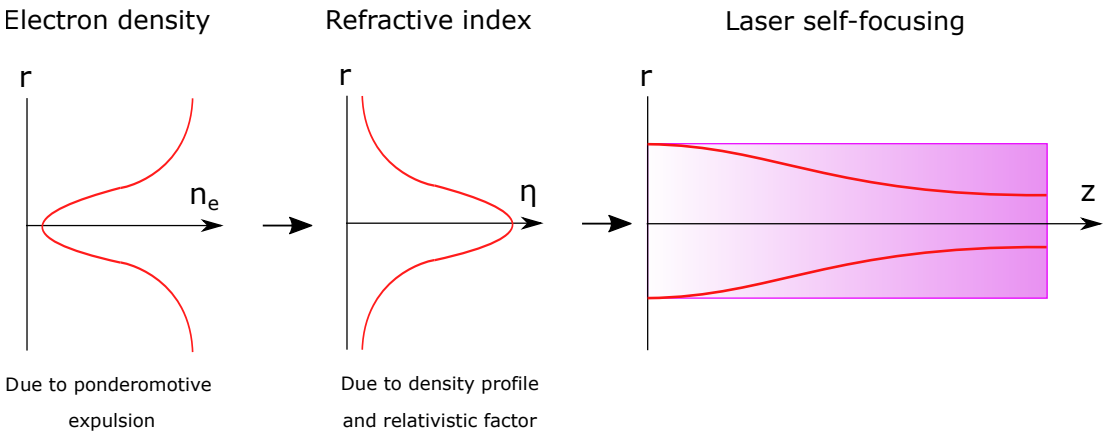

Figure 2.4: Illustration of a spatial electron density profile for an incident laser pulse with a Gaussian spatial-intensity profile. This results in a spatially varying refractive index, causing the laser pulse to self-focus within the plasma.

profile of the laser pulse drives a radially varying refractive index, similar to the relativistic case.

In reality, self-focusing is likely to occur due to a combination of these factors, with the spatial intensity profile of the laser pulse driving a radially varying refractive index through both ponderomotive expulsion of electrons and a relativistic increase in critical density. In order for plasma self-focusing to take place however, a threshold of incident laser power must be exceeded, known as the relativistic critical power, P_{cr}, given by [49]

$$P_{cr} = \frac{m_e^2 c^5 \omega^2}{e^2 \omega_{p,e}^2} \sim 17 \left(\frac{\omega}{\omega_{p,e}} \right)^2 \quad [\text{GW}] \tag{2.69}$$

If we consider the example case of a laser pulse with central wavelength $\lambda_L = 1$ μm and an intensity of $I_L = 10^{20}$ Wcm^{-2}, propagating through an underdense plasma of initially uniform density $\sim 0.1 n_c$, we find a relativistic critical power of $P_{cr} \sim 1.15$ TW. This is two to three orders of magnitude less than the peak power of the Vulcan laser, employed in this thesis, and so the possibility of self-focusing in underdense plasma, either formed at the target front surface due to pre-expansion, or by the effects of RSIT in ultra-thin foil targets, must be considered. The process of laser self-focusing is illustrated in Fig. 2.4, showing how spatial variations in electron density map onto the refractive index, ultimately resulting in a focusing of the laser pulse as it propagates through the plasma.

2.5 Laser energy absorption in dense plasmas

Now that the fundamentals of the interaction of a relativistic laser pulse with a plasma have been established, it is crucial to discuss the mechanisms by which energy is coupled from the laser to the plasma. For the case of a single electron oscillating in an infinite plane wave in vacuum, the electron will have no net gain in energy, as the energy will be transferred back to the laser during the second half of a pulse cycle. This is referred to as the Lawson-Woodward theorem [50, 51]. When a realistic laser pulse is considered however, with spatial intensity gradients, net energy may be gained by the electron as the laser is unable to recover the full energy imparted to the electron. This is the case for ponderomotive heating, discussed in section 2.3.2. In the interaction of high intensity laser pulse with a dense plasma, a number of additional mechanisms are introduced, in which the nature of the plasma enables a net energy gain to occur.

The mechanisms of laser energy absorption may be divided into two groups; collisional and collisionless. In general, collisional absorption schemes involve the heating of an electron by the laser pulse, with the electron subsequently undergoing a binary collision with an ion, referred to as inverse bremsstrahlung. As a result of this collision, energy cannot be returned to the laser. As discussed in section 2.4.1, this process is dependent on the mean free path of the electrons and on the collision frequency (see Eqn. 2.40), which is in turn dependent on the electron density and velocity, along with the atomic number of the ion species. Collisional absorption therefore dominates for high electron densities and low laser intensities (up to $\sim 10^{15}$ Wcm^{-2}), and where the spatial extent of the plasma is greater than the mean free path of the electrons. Collisional absorption schemes will thus play an important role in the heating of the pre-plasma initially formed by the lower intensity laser light preceding the main pulse.

For the interaction of the main pulse however (peak intensity $> 10^{20}$ Wcm^{-2}), the plasma may be considered to be collisionless, with laser energy absorption proceeding primarily via a number of collisionless mechanisms. In the general case, these mechanisms rely on the large amplitude of the electron motion induced

by such an intense laser field. Electrons are injected into the plasma, beyond the critical surface, and so into a region beyond the influence of the laser pulse. Three mechanisms by which this may occur, which are of relevance to the work presented in this thesis, will now be discussed.

2.5.1 Resonance absorption

In the case where a non-relativistic laser pulse ($a_0 \ll 1$) is obliquely incident ($\theta_i > 0°$) on a long scale-length plasma ($L_s \gg \lambda_L$), the dominant absorption mechanism is resonance absorption. In this scheme, laser energy is coupled to the plasma electrons via the resonant excitation of electron plasma waves at the critical surface, as illustrated in Fig. 2.5. In order to achieve this, the electric field must drive electron oscillations into the plasma, i.e. parallel to target normal. This condition necessitates a linearly polarised laser, with the polarisation axis in the plane of the interaction. Furthermore, oblique incidence is required in order for the laser pulse to turn as it propagates up the density gradient (see section 2.4.4), thus enabling the electric field to oscillate parallel to target normal. The oscillating electric field results in the formation of electron plasma waves within the plasma, which grow in amplitude over time, until wave breaking occurs. These plasma waves are resonantly excited at the critical surface due to the condition $\omega = \omega_{p,e}$. The average temperature of the electron population measured experimentally, resulting from heating via this mechanism, has been found to scale as $k_B T_e \propto (I_L \lambda_L^2)^{1/3}$ [52].

As the turning of the laser pulse within the pre-plasma is dependent on the angle of incidence (Eqn. 2.68), so too is the efficiency of resonance absorption. The response of this absorption to the incidence angle of the laser pulse is described by the Denisov function [53], $\Phi(\xi)$, which is given, to a good approximation, by

$$\Phi(\xi) \sim 2.3\xi \exp\left(-\frac{2}{3}\xi^3\right) \tag{2.70}$$

where

$$\xi = (kL_s)^{1/3} \sin\theta_i \tag{2.71}$$

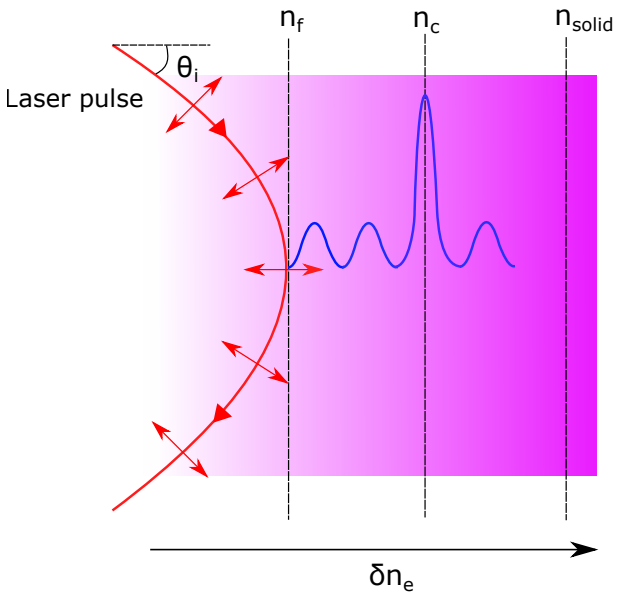

Figure 2.5: Illustration of the concept of resonance absorption, in which an obliquely incident laser pulse driving electron plasma waves in an expanding plasma. The plasma wave is resonantly excited at the critical density surface, resulting in a larger amplitude oscillation.

The fractional absorption of laser energy via this mechanism is given by

$$f_a = \frac{1}{2}\Phi^2(\xi) \tag{2.72}$$

From Eqn. 2.68, it is clear that as θ_i is increased (i.e. a glancing angle), the density to which the laser pulse may penetrate is decreased. If θ_i is too small, the fraction of the laser field penetrating to the critical surface is greatly reduced. There is, therefore, an optimal incidence angle, for which absorption is maximised, dependent on the scale-length of the pre-plasma. Such an optimum was reported in Freidberg *et al.* [54], with $\theta_i \sim 23°$ yielding maximum absorption for a scale-length of $L_s = 10\lambda_L/2\pi$. The model outlined here is shown to agree well with experimental findings for intensities of $10^{12} < I_L < 10^{17}$ Wcm^{-2}. Above this intensity however, the model breaks down due to the onset of relativistic effects, resulting in other absorption mechanisms dominating.

2.5.2 Vacuum heating

Vacuum heating, also referred to as Brunel heating or 'not-so-resonant' absorption [55], involves the injection of electrons into a steep density gradient plasma

($L_s \ll \lambda_L$) by a p-polarised laser pulse, incident at some oblique angle. Under these conditions, the spatial extent of the pre-plasma is less than the amplitude of the electron transverse oscillation in the laser electric field. Therefore, during the first half of the laser cycle, electrons will be pulled out of the plasma and into vacuum, before being re-injected into the plasma as the electric field changes direction in the second half of the cycle. The amplitude of the electron oscillation will carry it beyond the critical surface, thus escaping the influence of the laser field. The net gain in energy by the electron is on the order of the ponderomotive potential (Eqn. 2.34), as the electrons are injected into the plasma at approximately the quiver velocity (see Eqn. 2.27). Due to the steep density gradient, plasma oscillations are not supported, and energy absorption proceeds via the injection of electron bunches at a frequency equal to the driving laser frequency. The fractional energy absorption for a non-relativistic laser pulse is greatest for an incidence angle of $\theta_i = 90°$, as the polarisation of the laser is always directed into the plasma, although practically this incidence geometry is of limited feasibility. In the relativistic case of relevance in this thesis, i.e. $a_0 > 1$, the fractional absorption is given by

$$f_a = \frac{4\pi\alpha'}{(\pi + \alpha')^2} \tag{2.73}$$

where $\alpha' = \sin^2\theta_i / \cos\theta_i$. In this relativistic case, the maximum fractional absorption is found for an incidence angle of $\theta_i \sim 73°$, and the electron temperature is theoretically predicted to scale with $I_L\lambda_L^2$. Vacuum heating is illustrated in Fig. 2.6, shown by mechanism (i).

2.5.3 Relativistic j×B heating

In the case of a relativistically intense laser pulse, where the $\mathbf{v} \times \mathbf{B}$ component of the Lorentz force becomes comparable in magnitude to the electric field component, electron motion is driven at a frequency of 2ω along the laser propagation axis (see section 2.3.1). Due to the magnitude of the peak laser intensities employed in this thesis ($> 10^{20}$ Wcm^{-2}), this mechanism is the dominant source of heating in the interaction of the main pulse with the plasma. This can expressed

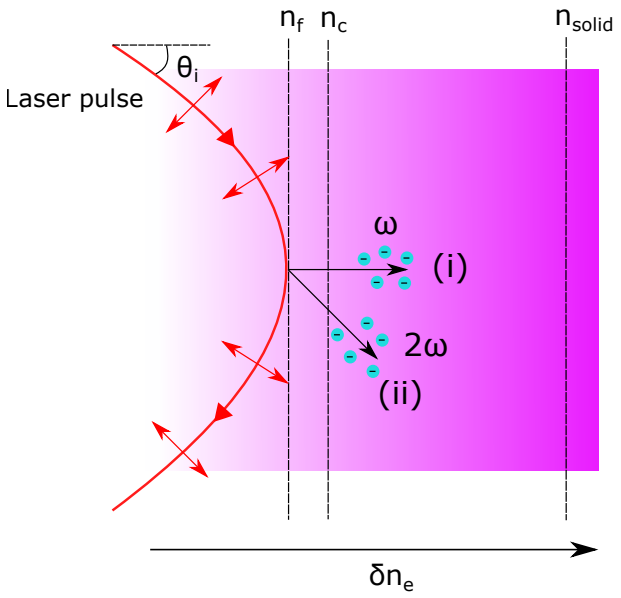

Figure 2.6: Illustration of the vacuum (i) and $\mathbf{j}\times\mathbf{B}$ (ii) heating mechanisms. For a steep density gradient and p-polarised laser light, electron bunches are injected into the target beyond the critical surface. In (i), this injection is normal to the density gradient, and occurs at the laser frequency (ω). For (ii), the injection is along the laser propagation axis, and occurs at a frequency of twice the laser frequency (2ω).

by the addition of a temporally oscillating component to the ponderomotive force [56], which is now given by

$$\mathbf{F}_p = -\frac{e^2}{4m_e\omega^2}\nabla\left\langle E^2\right\rangle\left(1-\frac{1-\varepsilon}{1+\varepsilon}\cos 2\omega t\right)\hat{\mathbf{z}} \tag{2.74}$$

where $\hat{\mathbf{z}}$ is the propagation direction of the laser pulse and ε is the ellipticity of the laser polarisation. It is apparent that the first term is simply the conventional ponderomotive force, as discussed in section 2.3.2, which will act to expel electrons from regions of high laser intensity. The second, temporally oscillating term, describes the acceleration of electron bunches in the direction of laser propagation, with a frequency of 2ω. These electron bunches will propagate beyond the critical surface, and thus beyond the influence of the laser, coupling laser energy into the target plasma.

Furthermore, it is clear that this second term is strongly dependent on the laser polarisation. For circular polarisation ($\varepsilon = 1$), the temporally oscillating component of the ponderomotive force collapses to zero, effectively switching off electron heating via this mechanism. This suppression of electron heating is

beneficial for processes which rely on laser pressure, as opposed to heating, such as the radiation pressure acceleration scheme of ion acceleration [57], as will be discussed in greater detail in section 2.7.2.

2.6 Laser-generated fast electrons

The absorption of laser energy via the mechanisms outlined in the previous section results in the generation of a population of energetic electrons, often referred to as the 'hot' or 'fast' electron population. These electrons often have relativistic energies i.e. the kinetic energy is greater than the rest-mass energy ($E_f > m_e c^2$) and are primarily sourced from the laser focal spot region before propagating through the target. The spectral and propagation characteristics of these fast electrons are of fundamental importance to the acceleration of ions and the generation of x-rays, and so it is necessary to review these in order to gain a deeper understanding of laser-solid interactions.

2.6.1 Fast electron spectrum and temperature

The energy gained by the population of fast electrons from the laser pulse cannot be described by a single value, with differences in, for example, the initial position of an electron relative to the laser focal spot, resulting in varying energies across the population. As such, a statistical distribution is used to describe the spectral properties of the fast electron population. In the non-relativistic case, this distribution, $f(E_0)$, has been shown to take the form of a Maxwellian distribution [58], described by the function

$$f(E_0) = 2\left(\frac{E_0}{\pi\left(k_B T_e\right)^3}\right)^{1/2} \exp\left(-\frac{E_0}{k_B T_e}\right) \tag{2.75}$$

where E_0 is the electron kinetic energy and $k_B T_e$ is the temperature of the spectrum. This distribution function may be multiplied by the total number of electrons to convert from yielding a probability into a number of electrons with a given energy. This is however an idealised case, with absorption via multiple

mechanisms and in different regions of plasma resulting in a departure from a simple, single temperature, Maxwellian distribution. Furthermore, for relativistic electron energies, the spectrum may be modified, such that it may be described by a Maxwell-Jüttner distribution [59], as follows

$$f(\gamma) = \frac{\gamma^2 \beta}{\theta K_2 (1/\theta)} \exp\left(-\frac{\gamma}{\theta}\right) \tag{2.76}$$

where $\beta = v/c$, $\theta = k_B T_e / m_e c^2$, and K_2 is the modified Bessel function of the second kind.

A useful parameter used to quantify the mean kinetic energy of a fast electron distribution is the temperature $k_B T_e$. The scaling of this parameter with laser intensity (or more appropriately, with laser irradiance) has been subject to extensive investigation, discussed in more detail in Chapter 5.2, but a brief introduction to the concept, along with some limited discussion of some common scaling laws, will be included here. Several scalings have been proposed, which differ in the predicted rate of scaling, but all agree that the fast electron temperature increases with increasing laser irradiance. For laser-solid interactions in the relativistic regime, heating is primarily driven by the full form of the ponderomotive force, given in Eqn. 2.74. The scaling of electron temperatures, heated via this mechanism, is commonly referred to as the 'ponderomotive' or 'Wilks scaling' [28], and is given by

$$k_B T_e = m_e c^2 \left[\left(1 + \frac{a_0^2}{2} \right)^{1/2} - 1 \right] \tag{2.77}$$

for linear polarised laser pulses. This is an analytically derived expression for the scaling of electron temperatures for the interaction of a relativistic laser pulse with a solid density target at normal incidence. This scaling essentially describes the perfect scenario, where the electrons are able to gain the full ponderomotive potential, and so acts as a useful baseline for comparison with other scaling models.

A number of alternative scaling models have been proposed [35, 48, 60], ob-

tained through experimental and/or analytical investigation, by varying the laser or target conditions, each of which provide a good description of the experimental data for their specific parameters, again discussed further in Chapter 5.2. For now, it is suffice to say that the characterisation of fast electron temperature has proven to be a complex subject, primarily due to the trapping of the majority of the fast electron population within the target by the sheath fields formed at the surfaces. Therefore, measurements of electron temperature are usually based on indirect methods, such as x-ray emission from the target [60, 61], or through measurement of the escaping electron population i.e. electrons not trapped within the target [47]. Results from the investigation of the scaling of electron temperature for laser intensities $> 10^{21}$ Wcm^{-2}, determined from measurements of copper K_α x-ray emission, are presented in Chapter 5.

2.6.2 Fast electron transport

The fast electrons, generated with the spectral properties discussed in the previous section, are driven into the target in the form of a beam, with a current reaching the order of mega-amperes (MA) [23]. Such a current will induce a large (on the order of mega-gauss), self-generated magnetic field, which will inhibit the propagation of the electron beam [62]. The current limit, above which propagation will be completely inhibited, is referred to as the Alfvén limit and may be estimated as follows [63]

$$I_A \sim \frac{4\pi\epsilon_0 m_e c^3}{e}\beta\gamma = 17000\beta\gamma \ \ [A] \tag{2.78}$$

If we take the case of a beam of 1 MeV electrons, the current limit is found to be 47.5 kA, assuming a beam of infinite width. This is several orders of magnitude lower than the MA current of fast electrons which has been shown experimentally to propagate through the target [23]. Therefore, additional physics must be at play, enabling the fast electron current to violate the Alfvén current limit.

The Alfvén limit may be surpassed if the net current inside the target is considered, as opposed to merely the fast electron current. As the fast electrons

enter the target, with a current $\mathbf{j}_f$, a charge-separation field is induced, drawing a spatially-localised current from the bulk target in the opposing direction to $\mathbf{j}_f$, and of similar magnitude [23]. This secondary current is known as the return current, $\mathbf{j}_r$, and has a significantly reduced temperature compared to the fast electron current (10s of eV, assuming similar temperature to bulk target from which they are drawn [23]), but consists of a larger number of electrons, thus balancing the current. This current is drawn from the rear of the target by space charge effects as the front surface becomes positively charged by the injection of laser heated electrons into the bulk target. The net current within the target therefore falls beneath the Alfvén current limit, enabling the fast electron current to propagate unhindered by suppressing the formation of self-generated magnetic fields. Beyond reducing the net current below I_A, a condition known as current neutrality is induced, such that the fast and return currents almost completely cancel each other out, such that

$$\mathbf{j}_f + \mathbf{j}_r \sim 0 \tag{2.79}$$

Perfect current neutrality is however not achieved, with the uncompensated currents resulting in the formation of magnetic fields, albeit with a significantly reduced magnitude. These fields are still sufficiently strong however to influence the transport dynamics of the fast electron beam. These magnetic fields arise from spatial variations in the electric field which draws the return current, and in the resistivity of the background plasma. The electric field may be described by Ohm's law, such that $\mathbf{E} = -\eta \mathbf{j}_f$, where η is the resistivity of the plasma, and the temporal dynamics of the magnetic field may be related to this via Faraday's law as follows

$$\frac{\partial \mathbf{B}}{\partial t} = -\nabla \times \mathbf{E} = \nabla \times (\eta \mathbf{j}_f) \tag{2.80}$$

and therefore

$$\frac{\partial \mathbf{B}}{\partial t} = \eta \left(\nabla \times \mathbf{j}_f\right) + \nabla \eta \times \mathbf{j}_f \tag{2.81}$$

It is apparent from Eqn. 2.81 that two distinct sources of magnetic field exist

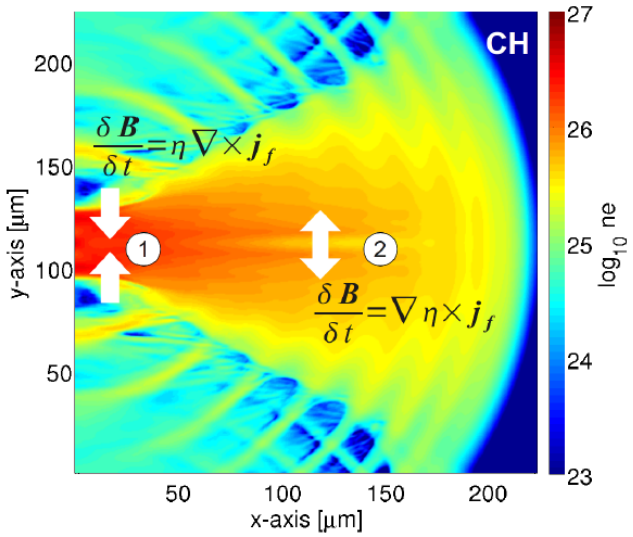

Figure 2.7: Simulation of fast electron transport within a CH target. The effects of the pinching (1) and hollowing (2) components of the magnetic field are shown. Reprinted from [65].

within the target. The first, corresponding to the first term on the RHS of Eqn. 2.81, results from spatial gradients in the current density across the fast electron beam. The current density decreases with increasing radial distance from the central axis of the beam, resulting in a magnetic field which acts to pinch the electrons, reducing the beam divergence. Such magnetic fields may also be generated due to localised current density modulations within the beam. This generates a feedback loop, whereby the magnetic field acts to increase the current density of the already higher current density regions, resulting in filamentation through Weibel instabilities [24, 64] and, ultimately, break-up of the beam.

The second term in Eqn. 2.81 describes the evolution of magnetic fields due to resistivity gradients within the plasma. If the plasma is composed of a uniform material, such resistivity gradients may form due to temperature variations. As the return current, which is collisional, is spatially overlapped with the fast electron current, and as the current density is highest on-axis, heating will be maximised on-axis. As the temperature influences the resistivity, this will result in a resistivity gradient, resulting in the generation of magnetic fields. The resulting magnetic fields will act to either expand or pinch the beam, depending on the gradient of the resistivity [23].

The combined effect of these two terms results in a highly complex, dynamic evolution of the self-generated magnetic field structures within the target, illustrated in Fig. 2.7. This, in turn, leads to the transport dynamics of the fast electron beam evolving significantly over the duration of the beam. Exploitation of these dynamics has been explored as a means of enhancing and tailoring the transport of fast electrons, through careful choice of target structure [66] or target material [67].

One key parameter relating to the fast electron beam, which has yet to be discussed, is the inherent divergence. The fast electron beam is not collimated, but instead diverges with some angle as it propagates through the target. A number of factors contribute to the divergence of the fast electron beam, including the injection angle, and the relative strengths of the competing magnetic force terms, which act to pinch or expand the beam. Experimental studies have shown that the half-angle divergence is likely to be of the order of 25° for intensities of 10^{20} Wcm^{-2} [68], however accurate measurement of this angle remains a significant challenge as most of the diagnostics employed to measure this angle are time integrated [69].

2.7 Laser-driven ion acceleration

The interaction of a relativistically intense laser pulse with a solid density target can be used as a means of accelerating ions to multi-MeV energies. Ions accelerated using laser-driven sources have the potential to compliment conventional accelerator technology, or replace it altogether for certain applications. Over the last two decades, laser-driven ion acceleration has been subject to extensive investigation, due to the increasing availability of laser systems capable of delivering short pulses (fs-ps regime) and peak intensities of $> 10^{18}$ Wcm^{-2}. Over this time, a number of mechanisms by which ions may be accelerated have been proposed, with several having been demonstrated experimentally.

Differentiation between the mechanisms, and thus determination of which will dominate, is dependent on a number of laser and target parameters, including, but

not limited to, the laser peak intensity and the thickness of the target. In certain cases, multiple mechanisms may occur over the course of a single interaction, as the laser and target parameters dynamically change, resulting in multi-mechanism (or hybrid) ion acceleration schemes [26, 70]. Whilst the various mechanisms differ in many important ways, there are similarities between them, primarily that the acceleration proceeds via space-charge fields set up due to the laser-driven electron motion. The charge separation fields generated can be of the order of several TV m^{-1}, two orders of magnitude higher than the fields achievable using conventional accelerators. The result of these fields has been the acceleration of protons to experimentally measured energies of ~ 100 MeV [26].

In the following sections, the primary ion acceleration mechanisms of relevance to the work presented in this thesis will be reviewed, making use of the underpinning physics discussed in the previous sections.

2.7.1 Target normal sheath acceleration

Around the turn of the century, laser-driven ion acceleration via the mechanism which would later become known as target normal sheath acceleration (TNSA) was reported in Snavely *et al.* [71], Hatchett *et al.* [72] and Clark *et al.* [73]. The underpinning physics of this mechanism was later detailed in a study reported in Wilks *et al.* [74], and is illustrated in Fig. 2.8. In this mechanism, an intense laser pulse irradiates a solid density target foil. These foils are typically many microns thick, ensuring that the target remains opaque to the laser pulse for the full duration of the interaction. The front surface of the target is rapidly ionised by the lower intensity light preceding the main pulse (see Chapter 3.2), forming an expanding plasma. The main pulse interacts with this plasma, heating the plasma electrons via the processes outlined in section 2.5. These electrons, sourced in the laser focal spot region, propagate through the target in a diverging cone geometry, resulting in a so-called 'lateral spreading' of the electron beam. The lateral spreading of the fast electrons significantly impacts the transport dynamics.

On reaching the rear of the target, propagation of the electron beam becomes

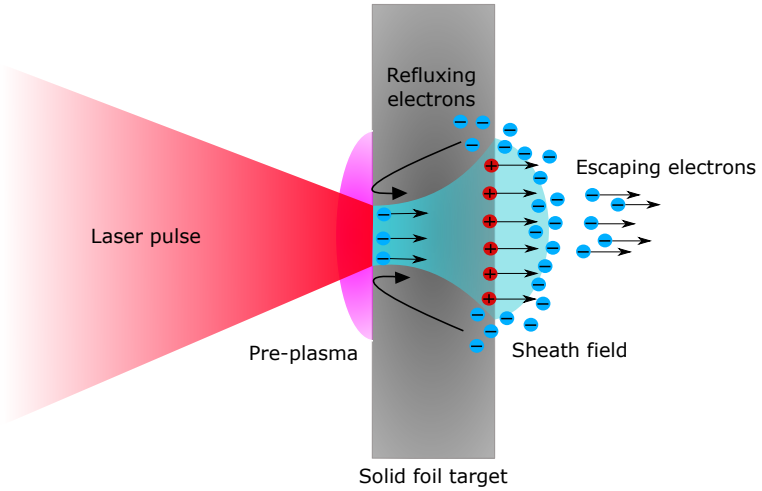

Figure 2.8: Diagram depicting the key aspects of the TNSA mechanism. A laser pulse is incident on the front surface of the target, forming a plasma and generating fast electrons, which propagate through the target. On reaching the rear surface, some electrons escape, with the remainder forming a strong sheath field, which acts to generate and accelerate ions from the target rear surface.

prohibited at the vacuum boundary, as no return current can be drawn. Electrons therefore accumulate at the rear surface, although a fraction will be sufficiently energetic to escape, resulting in a positive charging of the target. This results in the generation of a strong (of the order of TV m^{-1}) electrostatic sheath field, which acts to reflect the fast electrons still being generated by the laser back into the target. The reflected electrons recirculate (or reflux) within the target, due to the formation of a similar sheath field at the target front surface [75]. On returning to the front surface of the target, the electrons may gain additional energy from the laser pulse, further extending the refluxing process [76] and altering the energy spectrum of the electron population. Electron refluxing significantly impacts proton acceleration via the TNSA mechanism, by increasing the 'lifetime' of the accelerating sheath field [77].

Due to the lateral spreading of the fast electrons as they propagate through the target, the sheath field will form at the rear surface with a transverse spatial extent [17, 78, 79]. This is dependent on the injection and transport dynamics of the fast electrons, primarily the source size and divergence angle. The sheath area, S_{sheath}, may be estimated as follows

$$S_{sheath} = \pi \left(w_0 + L \cdot \tan \theta_{Div} \right)^2 \tag{2.82}$$

where w_0 is the radius of the laser focal spot, L is the target thickness and θ_{Div} is the divergence half-angle of the fast electron beam. The longitudinal extent of the sheath field is given by the Debye length of the sheath electron population, λ_s, given by

$$\lambda_s = \sqrt{\frac{\epsilon_0 k_B T_e}{e^2 n_{sheath}}} \tag{2.83}$$

where n_{sheath} is the electron density of the sheath electrons. In order to estimate the electron density, it is first necessary to calculate the number of fast electrons generated in the interaction. This is given by

$$N_e = \frac{\eta_{\ell \to e} E_L}{k_B T_e} \tag{2.84}$$

where $\eta_{\ell \to e}$ is the laser-to-electron conversion efficiency. The number of fast electrons generated in a laser-solid interactions is usually on the order of 10^{12} to 10^{13}. Using this, the sheath electron density may be estimated as

$$n_{sheath} = \frac{N_e}{c \tau_L S_{sheath}} \tag{2.85}$$

Using this expression for the sheath electron density, the Debye length of the sheath is typically found to be of the order of microns for electron temperatures in the MeV range. A sheath field of this size, formed on the rear surface of the target, will result in the formation of a strong accelerating electric field of strength E_s, estimated as follows

$$E_s = \frac{k_B T_e}{e \lambda_s} \tag{2.86}$$

This will result in a field strength of ~ 3 TV m^{-1}, for an electron temperature of 1 MeV and a sheath electron density of $\sim 10^{21}$ cm^{-3}. As the electrons which are reflected back into the target are continuously replenished, the electric field at the target rear may be considered quasi-static over the duration of the interaction. This electric field strength at the target rear is sufficient to ionise atoms, primarily those constituting the hydrocarbon contaminant layer present on the surface [43]. Over the longitudinal extent of the sheath field, these ions are accelerated to

several tens of MeV energies, due to the transfer of energy from the electrons to the ions via the charge separation fields [71, 72, 73].

It is clear that the acceleration of protons via the TNSA mechanism is highly dependent on a large number of factors, including the front surface dynamics and the fast electron transport. Direct, simultaneous measurement of the relevant parameters experimentally is impossible, and so a range of analytical and numerical models have been developed to provide an improved quantitative understanding of the underpinning physics of the acceleration mechanism [80, 81, 82]. One of the most widely employed is the plasma fluid model outlined in Mora [80], which is a 1D plasma expansion model, describing its expansion into vacuum. The temporal evolution of the accelerating electric field may be calculated from this model, enabling the maximum energy gain of the ions to be determined. The analytical approach set out in Mora enables estimation of the maximum ion energy and energy spectrum, over a wide range of experimental conditions [83]. The maximum proton energy, ϵ_p, predicted by the model is given by

$$\epsilon_p = 2q_i k_B T_e \left\{ \ln \left[\tau + \left(\tau^2 + 1 \right)^{1/2} \right] \right\}^2 \tag{2.87}$$

where q_i is the ion charge and τ is the acceleration time, given by $\tau = 0.55\omega_{p,i}\tau_L$ [83]. The ion plasma frequency is given by $\omega_{p,i} = \left[n_i \left(q_i e \right)^2 / \epsilon_0 m_i \right]^{1/2}$, where $n_i = n_e/q_i$ is the plasma ion density. One important point to note is that isothermal plasma expansion may only be assumed for the duration of fast electron generation by the laser pulse. Due to the finite temporal intensity profile of the pulse, an upper limit is placed on the maximum ion energies achievable, obtained using an acceleration time, t_{acc}. Simulations, for laser intensities of $> 3 \times 10^{19}$ Wcm^{-2}, have shown this time to be $t_{acc} \sim 1.3\tau_L$ for picosecond laser systems [83]. It is apparent from Eqn. 2.87 that the maximum proton energy is strongly dependent on the fast electron temperature. Conventional, the ponderomotive scaling of electron temperature has been used [28], giving rise to maximum proton energies that are predicted to scale with $\left(I_L \lambda_L^2 \right)^{1/2}$. We re-examine this scaling in Chapter 5, and show that for intensities beyond $\sim 5 \times 10^{20}$ Wcm^{-2}, this is no

longer true, and alternative fast electron temperature scalings must be explored.

The Mora model is a useful tool for estimating the maximum achievable ion energies, but experimental and analytical studies have shown that a TNSA ion beam consists of a broad spectrum of ion energies. The spectrum is typically described by a Maxwellian distribution, exhibiting a decreasing number of ions with increasing energy, up to a sharp cut-off energy, dependent on the fast electron temperature, and thus by extension the laser irradiance. The temperature of the ion energy spectrum may be calculated by fitting to the following distribution

$$N_i(\varepsilon) = N_0 \exp\left(-\frac{\varepsilon}{k_B T_i}\right) \tag{2.88}$$

where N_0 is a fitting parameter and ε is the ion energy. It is however, not uncommon for the best fit to a given spectrum to be described by a multi-temperature fit, with the temperature varying dependent on the energy range sampled. The broad energy distribution results from the temporally and spatially evolving sheath fields at the target rear, which in turn influence the acceleration of the ion population.

2.7.2 Radiation pressure acceleration

A second ion acceleration mechanism, which shows promise for generating high energy, quasi-monoenergetic ion beams, is radiation pressure acceleration (RPA). This mechanism relies on the exploitation of the momentum carried by a photon, which is transferred to a target as the photon is reflected. As a result of this, EM waves will exert a pressure upon reflection from a surface, of magnitude [84]

$$P_{rad} = (1 + R - T)\frac{I_L}{c} = (2R + A)\frac{I_L}{c} \tag{2.89}$$

where R is the reflectivity coefficient, T is the transmission coefficient and A is the absorption coefficient. Conservation of energy imposes the condition that $R + T + A = 1$. For the peak laser intensities explored in this thesis ($\sim 10^{21}$ Wcm^{-2}), this pressure can exceed 100 Gbar, often significantly larger than the

opposing thermal pressure of the expanding plasma.

If we specifically consider the interaction of an intense laser pulse with an overdense target, plasma electrons will be directly accelerated by the pulse when the radiation pressure exceeds the thermal pressure. As a result, a strong charge separation field will be formed, due to the displacement of the plasma electrons, acting to accelerate ions. Unlike TNSA, where the ions are sourced from the target rear surface, the RPA mechanism results in the acceleration of front surface and bulk ions. Furthermore, RPA does not rely on heating of the plasma electrons as is the case for TNSA, with excessive heating acting to de-optimise ion acceleration by reducing the drive efficiency of the pulse, and by inducing expansion of the target, which is particularly problematic for the light sail approach discussed in section 2.7.2. One potential benefit of using a radiation pressure-based approach to ion acceleration is the more rapid predicted scaling of ion energies with intensity when compared with TNSA. For example, at intensities of 10^{23} Wcm^{-2}, soon to be available at a number of laser facilities internationally [85], it has been theoretically proposed that RPA will become dominant for linearly polarised laser pulses, and may yield proton energies of up to 1 GeV [86, 87]. Intensities of such magnitude are not completely necessary however. Intensities on the order of 10^{20} Wcm^{-2} are sufficient for RPA to make a significant contribution to the acceleration of energetic ions, for the correct laser conditions, namely the use of normally incident, circularly polarised pulses [57, 88]. This acts to inhibit heating of the plasma electrons via the $\mathbf{j} \times \mathbf{B}$ mechanism, and in so doing, reduce the effectiveness of sheath-dependent acceleration mechanisms, enabling RPA to have a greater influence on the acceleration of ions.

It is useful to consider the case of a circularly polarised laser pulse (thus assuming negligible electron heating) interacting with a target, the front surface of which may be considered as a reflector, travelling with a velocity equal to $v = \beta c$. The surface reflectivity of the target, $R(\omega')$, is a function of the laser frequency in a moving frame, defined such that the target surface is at rest. The radiation pressure in the laboratory and rest frames is equal, due to the pressure

being an invariant quantity, and is expressed as follows

$$P_{rad} = P'_{rad} = \frac{2I_L}{c} R(\omega') \frac{1-\beta}{1+\beta} \tag{2.90}$$

The relationship between the incoming (ω') and reflected (ω) frequencies is described by the relativistic Doppler shift

$$\omega' = \omega \sqrt{\frac{1-\beta}{1+\beta}} \tag{2.91}$$

Exploitation of the relativistic Doppler shift enables for the recession velocity of the plasma critical surface to be determined, by measuring the spectral shift in the reflected laser light.

Ion acceleration via RPA schemes may be split into two general interaction regimes; Hole-boring (HB) and Light-sail (LS). In the holeboring regime, the laser pressure effectively bores a hole into a relatively thick (micron scale), overdense target. This results in a deformation of the target front surface and a steepening of the density profile at this surface. The resulting electron displacement drives the acceleration of ions, sourced at the front surface of the target. In the light-sail regime however, the pulse accelerates the entire target, within the volume subtended by the laser focal spot, due to the ultra-thin nature of the target foils (nanometre scale). Each of these cases will be discussed in greater depth in the following sections.

Hole-boring regime

The effect of the radiation pressure, to drive the critical surface into the target and deform the target front surface, was identified from early PIC simulations of intense laser-solid interactions [28, 89]. In this regime, plasma electrons are driven into the target, in the direction of laser propagation, forming a compressed, high density layer. The ions, which are significantly heavier, remain largely unperturbed, resulting in the formation of a strong electrostatic field between the two separated particle populations. The temporal evolution of this process is

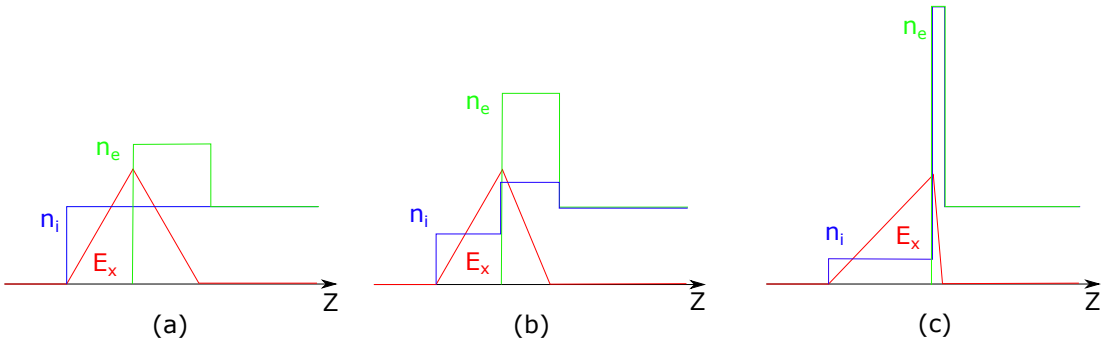

Figure 2.9: Illustration of the holeboring process, with time increasing from (a)-(c). The electron population of the target is shown in green, with the ions in blue and the electrostatic field shown in red.

depicted in Fig. 2.9. The recession velocity of the critical surface, referred to as the holeboring velocity, v_{hb}, was first derived in the study presented in Wilks *et al.* [28], given by

$$\frac{v_{hb}}{c} = \sqrt{\frac{n_c}{n_e}\frac{I_L\lambda_L^2}{2.74\times10^{18}}\frac{Z}{A}\frac{m_e}{m_p}} \tag{2.92}$$

where Z is the ionisation state and A is the ion mass number. It is clear that the holeboring velocity is dependent on the plasma density and laser intensity, enabling these parameters to be indirectly accessed through measurement of this velocity. In the relativistic regime, and for a circularly polarised pulse, a modification to this equation is necessary, as otherwise, unphysical hobeboring velocities of $v_{hb} > c$ may be predicted. This modification is set out in Robinson *et al.* [90], with the reformulated holeboring velocity taking the following form

$$\frac{v_{hb}}{c} = \frac{\sqrt{\vartheta}}{1+\sqrt{\vartheta}} \tag{2.93}$$

where

$$\vartheta = a_0\sqrt{\frac{Z}{A}\frac{m_e}{m_p\cdot n_e/n_c}} = \frac{I_L}{n_i m_i c^3} \tag{2.94}$$

It is clear that, in addition to the instantaneous laser intensity, the holeboring velocity is dependent on the ion composition of the target and the ion density. The choice of target material is therefore a key consideration when attempting to enhance or inhibit holeboring, for given laser parameters.

Holeboring of the laser pulse through the target proceeds until the interaction

with the laser pulse has ceased, or until the holeboring front reaches the rear surface of the target. Another means by which holeboring may be halted, is if the target undergoes transparency, either through thermal expansion (thus decreasing the density), relativistic effects or through the combined RSIT process. The maximum energy of ions accelerated via the HB-RPA mechanism is predicted to scale with the laser irradiance, $\epsilon_i \propto I_L \lambda_L^2$, more quickly than the scaling predicted for ions accelerated via the TNSA mechanism, which scales approximately as $\epsilon_i \propto \sqrt{I_L \lambda_L^2}$ [3]. Furthermore, unlike the TNSA mechanism, which yields a broad ion energy spectrum, HB-RPA is predicted to result in the acceleration of a quasi-monoenergetic population of ions (i.e. an energy spectrum with a localised peak at a given ion energy).

One final consideration is the influence of target surface deformation, driven by the holeboring process. For a laser pulse with a Gaussian spatial intensity profile, radiation pressure will result in a concave critical surface within the focal spot region. This can significantly impact the front surface dynamics of the interaction, particularly in the case of a high intensity, small focal spot laser pulse. One example of the induced behaviour, of particular relevance to the RPA process, is the energy absorption from the laser into the plasma. For a normally incident laser pulse, front surface deformation results in the electric field no longer oscillating parallel with the surface, with a component of the field now directed into the plasma. This enables processes such as resonance absorption to occur for interaction geometries for which it should be suppressed without the influence of holeboring [91]. This will in turn result in increased electron heating, which is counter-productive for the acceleration of ions via the HB-RPA mechanism.

Light-sail regime

If the target employed in the interaction is very thin (tens of nanometre scale), the ion front will reach the rear surface of the target very quickly, unlike in the holeboring regime. Under these conditions, the full target volume within the focal spot region may be accelerated, forming a high density slab of plasma, co-propagating with the laser pulse. This is clearly shown in simulation results

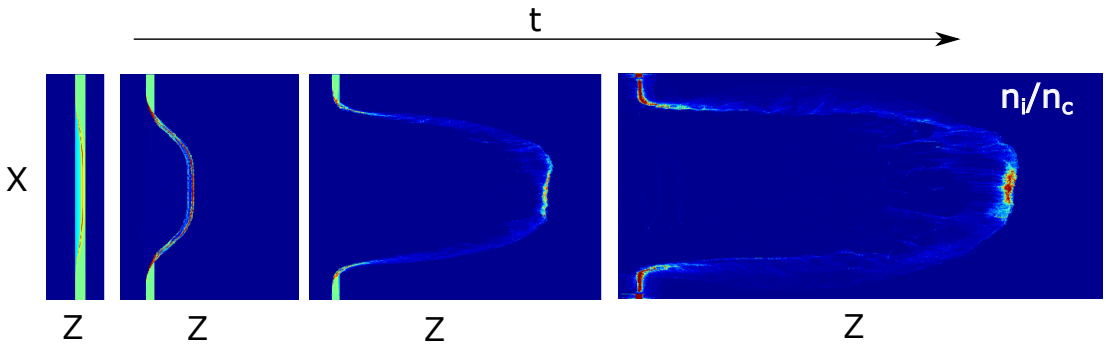

Figure 2.10: Spatial profiles of ion density, with time increasing from left to right. It is clear that the whole volume of the target is accelerated, within the central region subtended by the laser focal spot. Reprinted with edits from Qiao *et al.* [92].

presented in Qiao *et al.* [92], for a circularly polarised laser pulse of intensity 10^{22} Wcm^{-2}, shown for illustrative purposes in Fig. 2.10. This mechanism was proposed theoretically in Esirkepov *et al.* [86], in which electrons are expelled from the target front surface due to their acceleration by $\mathbf{j} \times \mathbf{B}$ heating over the course of a single laser cycle. The accelerating potential is maintained as the radiation pressure continues to drive the electrons at the critical surface for the duration of the interaction, enabling the ions to reach relativistic velocities. The target, in this scenario, behaves effectively as a relativistically propagating plasma mirror, where the reflected light is red-shifted by the relativistic Doppler effect, thus resulting in energy transfer to the plasma slab [4].

The velocity with which the target propagates when accelerated by the radiation pressure, may be calculated by considering the conservation of momentum between the laser pulse and the target. If a flat top spatial intensity profile is assumed for the incident laser pulse, the light-sail velocity, v_{LS}, may be expressed as follows [93]

$$v_{LS} = \frac{(2R + A)\,\tau_{acc}}{n_i m_i L} \frac{I_L}{c} \tag{2.95}$$

where L is the target thickness and $\tau_{acc} \sim \tau_L$ is the acceleration time [3]. It is clear that, in addition to the laser intensity, the ion mass to charge ratio also determines the ion velocity, and so protons will travel with higher velocities than heavier ions [94]. It is also apparent that the maximum ion kinetic energy achieved from LS-RPA scales as $\epsilon_i \propto I_L^2$, quicker than the scalings predicted by either TNSA or HB-RPA. Through the use of circularly polarised laser pulses, signatures of

LS-RPA have been observed experimentally in the interaction of ultra-thin foil targets with picosecond duration pulses, showing quasi-monoenergetic features within the measured ion energy spectra [95].

As the light-sail mechanism relies of the acceleration of the entire bulk target by the laser pulse, any process which disrupts this process will limit the efficiency and maximum ion energies achievable. One such process is the onset of Raleigh-Taylor instabilities [96]. These occur at the boundary between two fluids of differing densities. In this case, the laser pulse acts like the less dense fluid, with the plasma behaving as the 'heavy' fluid. This instability will result in modulations to the plasma surface, which will grow over time. Due to the very low thickness of the target used in light-sail (a few tens of nanometres at most, usually < 10 nm), these modulations quickly destroy the target, inhibiting further acceleration by the laser pulse and modulating the spatial profile of the accelerated ion beam [97].

2.7.3 Relativistic transparency-enhanced acceleration

As discussed in section 2.4.4, if the target is sufficiently thin, then the target may undergo RSIT, through the combined effects of target decompression and the relativistic mass increase of the plasma electrons. This acts to suppress ion acceleration via the RPA mechanism, of either form, as both RPA regimes require an opaque target, with P_{rad} decreasing with increasing transmission (see Eqn. 2.89). On transmission through the target, the laser pulse will however act to volumetrically accelerate the target electrons [98, 99], resulting in an enhancement of the accelerating sheath fields, and therefore an increase in ion energies. The exact mechanism by which energy is transferred to the sheath-accelerated ions remains the subject of investigation, but we will discuss two prominent theories here.

Simulation studies have shown that streaming instabilities in transparent targets may result in energy exchange between the electrons and ions [100, 101], which is invoked in the acceleration scheme referred to as the break-out afterburner (BOA) scheme [102]. In particular, the relativistic two-stream Buneman

instability is attributed to the energy transfer in this regime [102]. Initially, BOA proceeds via the same process as TNSA, i.e. the formation of a sheath field at the target rear resulting from the transport of fast electrons through the target. As the target undergoes transparency, the interaction of the relativistic electron beam and the slower moving ions supports the growth of the two-stream instability, which is resonant with the ion population, thus acting to couple energy from the electrons to the ions.

In order to estimate the ion energies achievable through the BOA mechanism, the analytical model developed in Yan *et al.* [103] may be used. The acceleration of ions due to the influence of transparency induced effects occurs in the BOA mechanism from the time of relativistic transparency, t_1, until the time of classical transparency, t_2. If the assumption that target expansion proceeds along the laser propagation axis in 1D prior to the onset of transparency, the time t_1 may be calculated by balancing the ponderomotive force with the force due to the charge separation fields, yielding the following

$$t_1 = \left(\frac{12}{\pi^2}\right)^{1/4} \left(\frac{n_e \tau_L L}{n_c a_0 C_s}\right)^{1/2} \tag{2.96}$$

where

$$C_s = \left(\frac{Q m_e c^2 a_0}{m_i}\right)^{1/2} \tag{2.97}$$

where Q_i is the charge of the primary ion species. At the time t_2, acceleration via BOA ceases, as all of the plasma electrons have been heated by the laser, resulting in strong expansion. By employing a 3D isospheric expansion model [103], t_2 may be calculated as

$$t_2 = \Delta t + t_1 = \frac{n_e L \left(\gamma^{1/3} - 1\right)}{n_c \gamma C_s \sin\left(\pi t_1 / 2\tau_L\right)} + t_1 \tag{2.98}$$

The energy obtained by the ions via this acceleration process is dependent on the electron energy, ϵ_e, given by

$$\epsilon_e \sim \frac{m_e c^2}{t_1 - t_2} \int_{t_1}^{t_2} \left(\sqrt{a_0^2 + 1} - 1\right) \mathrm{dt} \tag{2.99}$$

This is the time-averaged electron energy due to the ponderomotive force, as limitations to the energy gain of the electrons due to, for example, the plasma skin-depth [48], do not apply here due to the transparency of the target. It is worth noting that, in the case where tight-focusing of the laser pulse is employed, focal spot size limitations to the heating of these electrons, as discussed for thicker, opaque targets in Dover *et al.* [35], may result in lower electron energies, even once the target has undergone transparency. The response of the ions to the electrostatic field of these electrons results in maximum ion energies of

$$\epsilon_i \sim (1+2\alpha)\, Q\epsilon_e \left\{ \left[1+\omega_{p,e}\,(t_2-t_1)\right]^{1/(2\alpha+1)} - 1 \right\} \tag{2.100}$$

where α is the coherence parameter, describing how efficiently the ions couple to the electrons, and is estimated to take a value of $\alpha \sim 3$, as seen in Yan *et al.* [103].

Experimental studies undertaken using picosecond duration laser pulses show an enhancement in the maximum proton energies for targets having undergone transparency [26]. Further numerical investigation of this unveiled a novel, transparency enhanced TNSA-RPA hybrid acceleration scheme, with an optimum occurring for targets undergoing transparency near the peak of the pulse ($\sim$ 100 nm thick CH foils for the laser intensities employed). At early times in the interaction, when the intensity is relatively low, ion acceleration proceeds via the TNSA mechanism, with a sheath field formed at the target rear surface. As the intensity increases, approaching the peak of the pulse, radiation pressure begins to become more dominant, inducing an electric field component that accelerates protons and heavier ions from the target front surface. A dual-peaked, longitudinal, electro-static field structure is formed [26, 104], comprising the sheath and radiation pressure generated fields. Protons accelerated from the target front surface by the radiation pressure induced field catch up to those accelerated by the sheath field, forming a single proton bunch, trapped between the dual peaks of the field [26, 105].

At a point during the interaction, the target will undergo RSIT, due to the

electron density along the laser propagation axis falling below the relativistically-corrected critical density. Increased volumetric heating of the plasma electrons by the transmitted fraction of the laser pulse enhances both field components, resulting in a strong, double peaked field accelerating the trapped proton bunch. This process continues until late times, when the field structure decays, resulting in a broadening of the proton bunch. Following the onset of RSIT, a localised fraction of the proton population, close to the laser propagation axis, gains additional energy. This is driven by the formation of a super-thermal jet of electrons, directly accelerated by the transmitted fraction of the laser pulse [26, 106]. This jet is collimated by a self-generated, azimuthal magnetic field, and extends through the TNSA ion front. Due to the high electron density of the jet, a transverse electrostatic field is formed, which attracts protons towards the laser axis, which is where the dual-peaked field is strongest due to the enhanced volumetric heating and influence of the jet itself. Acceleration of protons via this mechanism has yielded record laser-driven proton energies of $\sim$ 100 MeV [26], and so further investigation of the optimisation and control of this mechanism is imperative.

2.8 Summary

In summary, the interaction of a high intensity laser pulse with a solid density target, resulting in the generation of high energy electron and ion beams, is a complex process, sensitive to an array of laser and target parameters. These parameters do not act individually however, instead combining to produce effects which are often, as yet, not fully understood. That being said, continual progress is being made towards understanding the underpinning physics of these interactions more fully, and in doing so, moving towards the ultimate goal of harnessing laser-solid interactions for wide ranging envisioned applications of societal benefit.

Chapter 3

Methodology: Lasers, Diagnostics and Simulations

In the previous chapter, the fundamental physics of the interaction of a high intensity, short pulse laser and a dense plasma was explored. It is however equally important that the practicalities of studying these interactions are discussed, including how such intense laser pulses are produced, the diagnostics employed to characterise the interaction and the numerical codes used to help model and interpret the experimental measurements. In this chapter, the experimental and numerical techniques employed in this thesis are set out and described in detail.

3.1 Properties of a short pulse, high intensity laser

When considering the interaction of a high power laser pulse with dense plasma, there are a number of laser and target parameters that are of crucial importance to the resulting dynamics. This section will focus on three key laser properties relevant to the results presented later. In this section, we will explore the temporal intensity contrast and the laser focal spot, which can significantly impact the plasma dynamics. Both of these cases can be summarised by asking to what extent does a realistic laser pulse vary from the assumed Gaussian spatial and temporal profiles. Finally, the laser wavefront will be discussed, including how

this may be measured and characterised.

3.1.1 Laser pulse temporal intensity contrast

As was the case in Chapter 2, the laser pulse is often assumed to take the form of a Gaussian profile in time, with the full width at half maximum (FWHM) being defined as the pulse duration, or pulse length. In reality, the laser pulse has features on much longer timescales than the main pulse, that can be sufficiently intense to impact the laser-plasma dynamics and so play an important role when investigating laser-solid interactions. The laser light surrounding the main pulse is of lower intensity and is referred to as the pulse pedestal. If this pedestal is sufficiently intense, or is incident on the target for a long period of time before the arrival of the main pulse, significant target pre-expansion can result, which can drastically impact the interaction physics. The most common means of defining the intensity of this pedestal is via the temporal intensity contrast ratio, which is the ratio of the intensity of the peak of the main pulse to the pedestal intensity at a given point in time relative to the main pulse. This is typically quoted at a few tens of picoseconds before the main pulse and at a few nanoseconds before the pulse, as these timescales are of relevance for the heating and hydrodynamic expansion of the target respectively. A sketch illustrating the components of a typical laser pulse, including their temporal location relative to the main pulse and their contrast level, compared with the idealised case is shown in Fig 3.1.

The primary source of this pulse pedestal is amplified spontaneous emission (ASE). This occurs due to the spontaneous emission of photons within the gain medium of the amplifiers from atomic decays resulting from excitation induced by the flash lamps / pump laser. As this emission is not induced by a photon from the seed pulse (i.e. stimulated emission), the emission is incoherent with the seed pulse and is emitted in a random direction. A significant number of these photons will be emitted into a solid angle Ω, such that they will propagate along the beam path to subsequent stages of the laser chain, thus remaining trapped in the laser system and being amplified in successive amplifiers, as illustrated in Fig. 3.2. Pockels cells, in combination with a polariser set to a fixed orientation,

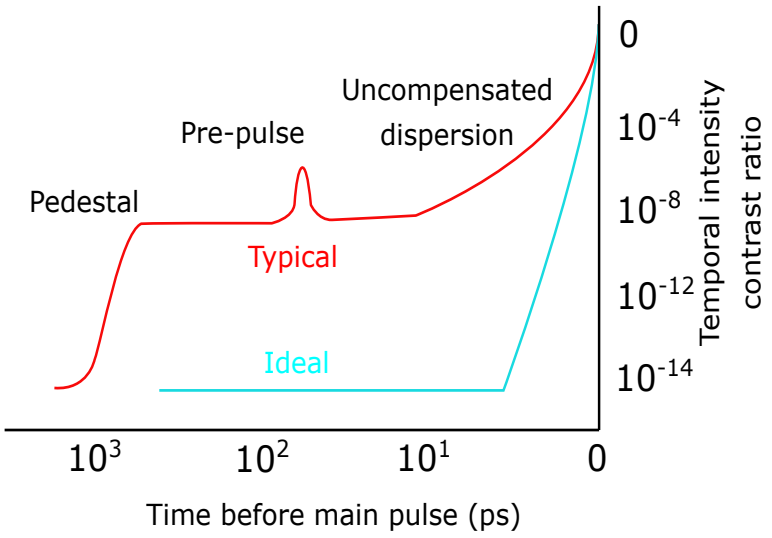

Figure 3.1: Illustration comparing the ideal laser temporal intensity contrast (in blue) to a more realistic pulse profile (in red), featuring a pulse pedestal formed due to ASE and an example pre-pulse on the rising edge. The x-axis is the time before the main pulse and the y-axis is the ratio of the peak intensity to the intensity at a given point in time relative to the main pulse.

are frequently used as a means of gating the pulse, but are only capable of gating on the nanosecond timescale due to the limit imposed by the electronic triggers, which is still a long time ahead of the main pulse. If left unmitigated, a pedestal on such a timescale could result in significant target pre-expansion, which can have a major impact on the resulting interaction physics, for example the TNSA acceleration of protons [45] or the energy coupling to fast electrons [44].

Furthermore, a laser pulse may exhibit significant uncompensated dispersion, often referred to as the rising edge of the pulse as it occurs temporally close to the main pulse (tens of ps). During the process of chirped pulse amplification, dispersion is introduced to the pulse in order to stretch it temporally, as described in section 3.2.1. Inherent imperfections in the manufacture and alignment of the compressor gratings (used to induce dispersion in CPA based laser systems), or the introduction of secondary sources of dispersion due to pulse propagation through optics in the laser chain for example [107], may result in sub-optimal re-compression of the pulse in certain regions. This can result in parts of the stretched laser pulse not being fully recompressed after amplification, resulting a temporal broadening of the main pulse.

Additionally, 'pre-pulses' can exist preceding the main pulse, with peaks ex-

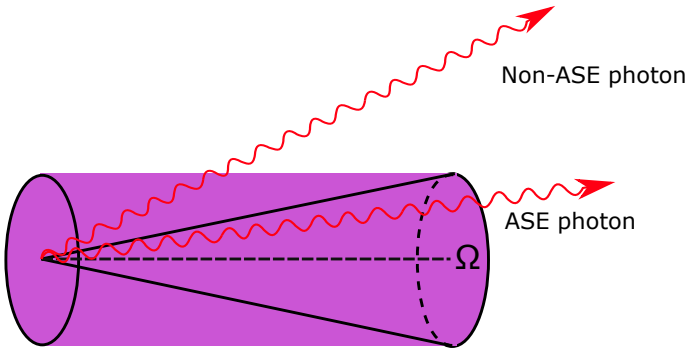

Figure 3.2: Simple illustration of ASE emission in a rod amplifier. Photons emitted into solid angle Ω, as shown, will be amplified and trapped in the laser system.

tending above the level of the ASE pedestal. These pre-pulses result from internal reflections from optics in the laser chain and may extend tens to hundreds of picoseconds prior to the main pulse. These internal reflections are often due to reflections off the back surfaces of optics, and can thus often be remedied by introducing a wedge to the optics, thus deflecting the reflections from the path of the main pulse. Alternatively, applying an anti-reflection (AR) coating to the rear surface of the optic will reduce reflections by approximately two orders of magnitude.

Temporal intensity contrast is often a difficult problem to solve in high intensity laser systems, and achieving good temporal contrast is often crucial in experimental investigations, particularly those involving ultra-thin targets, as used in Chapter 4. In modern systems, optical parametric amplification schemes are often used in the earlier stages of amplification as a means of reducing the ASE, as described in section 3.2.3, although this is not without its own drawbacks when considering contrast. Frequency doubling of the pulse may also be employed as essentially an intensity gating technique. As the process of second harmonic generation is intensity dependent, the pulse intensity through the crystal can be tuned (e.g. through varying the focus) such that only the main pulse is converted, with the lower intensity pedestal remaining unconverted. Dielectric mirrors, coated to reflect second harmonic light and transmit the fundamental frequency, may then be used to dump the unconverted ASE and pulse pedestal. Cross-polarised wave generators (XPW) have recently become increasingly used as a further means of improving temporal intensity contrast, particularly in fem-

tosecond pulse laser systems. This technique consists of a non-linear crystal (BaF_2 for example) placed between two polarisers with opposite orientations. As the laser pulse propagates through the non-linear crystal, its polarisation is rotated by 90°. This process depends on the cube of the input laser intensity, thus rotating the polarisation of the main pulse whilst retaining the initial polarisation of the ASE and pedestal. The second polariser will then filter out the unconverted light, resulting in improved temporal intensity contrast. In this way, an XPW behaves similarly to a Pockels cell, but where the laser itself acts as the 'switch', thus enabling significantly faster response times. Another commonly used technique, employed in all experiments contributing to this thesis, is the use of plasma mirrors, which similarly act as an effective temporal intensity filter, the principle of which is explored in more detail in section 3.4.

3.1.2 Focal spot size and encircled energy

In laser-plasma experiments, the focal spot (i.e. the spatial-intensity profile of the laser pulse at focus) is a key parameter which not only influences the peak laser intensity, but can also have a significant impact on the interaction physics, independent of the intensity-driven effects. It is therefore vital that the size and quality of this focal spot is characterised, in addition to its susceptibility to change when subjected to wavefront aberrations such as astigmatism or wavefront curvature. As such, the focal spot is optimised prior to every laser shot using a combination of off-axis parabola (OAP) alignment and wavefront correction using an adaptive optic (AO), and the resulting focal spot is imaged, allowing for measurement of the focal spot size and encircled energy. As it is often difficult and impractical to measure the focal spot under high power conditions [108], this measurement, combined with a measure of the on-shot wavefront profile, is the best characterisation of the spatial-intensity profile currently broadly available.

To characterise the focal spot, two key parameters will be used; firstly the size (ϕ_L) and secondly the encircled energy (E_E) within an area of diameter ϕ_L. In addition to these parameters of the focal spot, it is also useful to define the Rayleigh range (z_R) of the focusing laser pulse. Each of these parameters will

now be explored individually.

Firstly, the focal spot size is defined based on the spatial-intensity distribution of light in the laser focal spot. Most laser systems employ a circular beam shape pre-focusing, with circular optics and apertures used throughout the laser chain. This results in a near-field beam profile defined by Fraunhofer diffraction (i.e. far from focus) and a far-field spatial profile described by an Airy disk (i.e. at/near focus). The central spot of the Airy disk profile is well described using a Gaussian distribution. It is thus possible to define the size of the focal spot in two ways, with one method preferable over the other depending on the situation. The diameter of the Gaussian profile, defined at the FWHM (ϕ_L), is the first method, and is used as the definition of focal spot size throughout this thesis. Secondly however, the spot waist (w_0) may be defined, characterising the radius at which the intensity has fallen to $1/e^2$ of the peak value. Both definitions of spot size are illustrated in Fig. 3.3 (a). If the laser pulse has been focused to the theoretical best condition, this spot can be referred to as being diffraction limited, with a diameter $2w_0$ defined by

$$2w_0 = 1.3\frac{\lambda_L f}{D} \tag{3.1}$$

where f is the focal length of the focusing optic and D is the diameter of the collimated beam. It is often convenient to define the ratio f/D as the F-number ($F/\#$), which is a parameter frequently used to describe the minimum focal spot size achievable using a certain focusing optic for a particular laser wavelength. The F-number describes how quickly a pulse focuses, with a lower number denoting a quicker focusing. This can be seen from the ratio defining F-number, $F/\# = f/D$, which shows that, for a fixed beam diameter, a smaller F-number results in a shorter focal length. A lower F-number will also result in a smaller focal spot. In this thesis, two F-numbers are commonly used experimentally, F/3.1 and F/1. These correspond to focal spot sizes of approximately $\phi_L = 4$ μm and $\phi_L = 1.5$ μm respectively, for a laser wavelength of ~ 1 μm.

The second parameter of importance to the focal spot characterisation is the encircled energy, which is used frequently throughout this thesis as a means of quantifying the quality and energy content of the focal spot, which ultimately

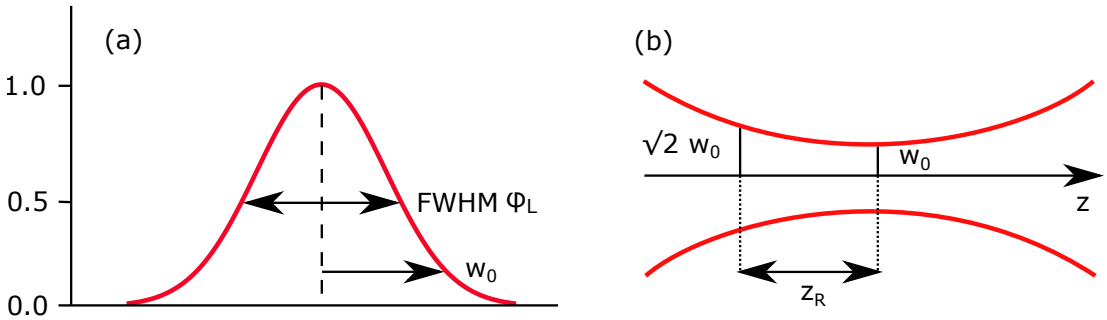

Figure 3.3: (a) Illustration of the definition of focal spot size for a Gaussian spot intensity profile, showing FWHM and mode waist measurements. (b) Focusing spatial profile of a Gaussian beam, outlining the mode waist w_0, determined by the diffraction limit, and defining the Rayleigh range z_R.

has an impact on the estimation of the on-target peak laser intensity. The E_E is essentially a measure of the energy contained within the central region of the spot. The size of the central region, as defined in this thesis, is based on the FWHM spot size, as discussed above. For realistic focal spots, values of fractional encircled energy f_{EE} in the range of $20-40\%$ are typical, with a higher encircled energy corresponding to a higher quality focal spot. A reduction in spot encircled energy may result from poor optimisation of, or damage to, the focusing optic or aberrations in the pulse wavefront resulting from thermal effects for example.

The final parameter of relevance to the characterisation of the focal spot is the Rayleigh range z_R, which is more so a property of the focusing beam than the focal spot itself, but has an important impact on the resulting focal spot and the effectiveness of placing a target foil in the precise focal plane of the incident laser pulse. The Rayleigh range may be mathematically expressed as follows

$$z_R = \frac{2\pi w_0}{\lambda_L} \tag{3.2}$$

where w_0 and λ_L have the same meaning as before. Physically, the Rayleigh range describes the longitudinal distance along the propagation axis (z) from the spot waist to where the waist has increased by a factor $\sqrt{2}$ for a Gaussian beam (i.e. a reduction in peak intensity of a factor 2), as shown in Fig. 3.3 (b). This spatial condition is equivalent to the point in the focusing beam where the intensity is reduced by a factor 2 compared to the peak intensity. The Rayleigh

range essentially places a spatial limit on the combination of target placement and focal spot longitudinal defocus. If, as a result of either or both of these, the target is irradiated at a position more than a Rayleigh range from the optimal focus position, the intensity will be significantly reduced. It is for this reason that measurement of the defocus aberration on every shot is of crucial importance.

3.1.3 Wavefront characterisation and optimisation

Characterisation and optimisation of the laser wavefront is essential to the successful deployment of any tight-focusing scheme, including the focusing plasma mirror (see section 3.4.2). This is especially important to discuss here as such focusing schemes are employed in both results chapters presented in this thesis.

Wavefront aberrations can be produced throughout the laser chain, and represent a deviation from the ideal case of a perfectly planar wavefront profile. The sources of these aberrations may be divided into two categories, steady state sources and dynamic sources. Steady state sources of wavefront aberrations may consist of surface imperfections or subtle misalignments of the optics in the laser chain, i.e. constant sources of wavefront aberrations. Conversely, dynamic sources include processes such as thermal lensing effects as the amplifiers heat or cool and non-linear optical effects resulting from higher order refractive index terms, such as the Pockels or Kerr effects, as the pulse propagates through the optics of the laser system. The most common aberrations include astigmatism, coma, tilt and defocus, although other, higher order aberrations are also possible. The extent to which a measured wavefront deviates from the ideal planar profile is characterised by the Zernike polynomials [109]. Each individual polynomial describes a particular form of aberration, for example astigmatism or defocus, and the sum of the polynomials can be used to represent highly complex wavefront geometries.

For the results presented in this thesis, the aberration of particular interest is the defocus aberration, which is essentially an unwanted curvature of the wavefront acting to alter the divergence of the collimated beam. The defocus aberration often results from a combination of steady state and dynamic aberrations, making it difficult to pre-compensate and has a significant impact when

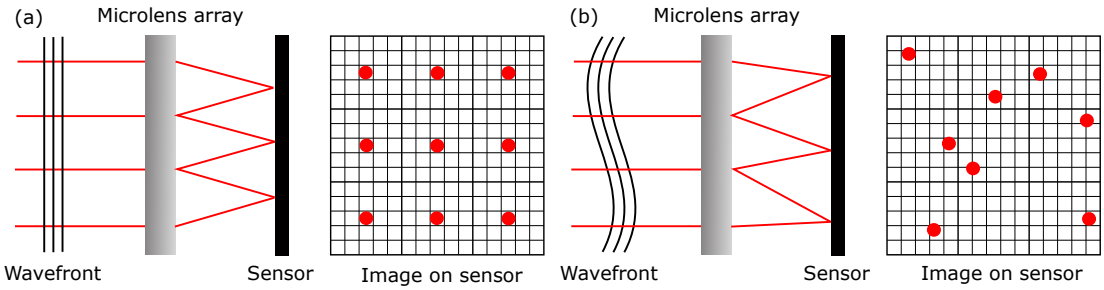

Figure 3.4: Schematic illustrating the principle of operation of a Shack-Hartmann wavefront sensor. (a) Incident planar wavefront, with dots formed at the centre of the grid squares. (b) Incident curved/aberrated wavefront, with dots displaced from the centre of the grid squares, or missing entirely.

focusing the beam, as it will result in a longitudinal displacement in the focal point along the laser propagation axis, for example a concave wavefront would result in the pulse focusing earlier than anticipated and vice-versa. This longitudinal offset from the nominal focal position , $\Delta\delta$, may be calculated using the following equation [110]

$$\Delta\delta = \frac{Z_F \cdot 4\lambda_L}{N_A^2} \tag{3.3}$$

where Z_F is the Zernike coefficient and N_A is the numerical aperture of the focusing optic. Quantifying this offset enables the calculation of the peak on-target intensity to be suitably corrected, as the target is placed at the nominal focal position, assuming the Zernike coefficient for the defocus of the wavefront is known.

In order to measure the Zernike coefficient experimentally, therefore allowing the spatial offset of the focal point to be determined, a Shack-Hartmann wavefront sensor is employed. This wavefront diagnostic is often employed in an adaptive optic (AO) setup, to first measure the wavefront before relaying this information to a deformable mirror in order to perform suitable corrections. A Shack-Hartmann sensor consists of a CCD or CMOS camera, with an array of micro-lenses of equal focal length placed in front of the chip. This effectively divides the incident beam into sub-beams, with each being focused onto the chip, as illustrated in Fig. 3.4. If the incident beam has a perfectly uniform, planar wavefront, the sub-beams will come to focus on the optical axis of each lens, generating a grid of equally spaced focal spots. An aberrated wavefront will how-

ever result in the focal spots being offset from the optical axis, resulting in a distorted grid, with some of the constituent focal spots displaced or missing from their nominal positions. The image captured of this focal spot grid can be used to reconstruct the wavefront profile of the incident beam, enabling the Zernike coefficients to be determined, through comparison with a reference flat wavefront.

3.2 High Power Laser Technology

The study of ultra-intense light-matter interactions necessitates the use of high power, high intensity laser pulses. In this section, the general concepts and techniques used in the production of high intensity laser pulses will be reviewed, essentially providing a foundation prior to the discussion in section 3.3 of the specific details of the Vulcan Petawatt laser used for the experimental work presented in this thesis.

3.2.1 Chirped Pulse Amplification

Investigation of laser-plasma interactions in the relativistic regime ($> 10^{18}$ Wcm^{-2}) only became possible several decades after the first practical demonstration of the laser [1]. Generation of laser pulses with such intensities was prohibited by the high fluence required, and indeed from effects driven by the high intensity itself. The high fluence of such pulses exceeds the damage threshold of the solid-state optics within the laser system, and in particular the laser amplifiers, which are highly susceptible to damage as the laser pulse propagates through them. Furthermore, even without the fluence effects, the peak intensities are sufficiently high to drive non-linear optical effects. Self-focusing of the beam, self-phase modulation and beam filamentation driven by the optical Kerr effect can lead to the formation of 'hot spots' in the beam. These not only degrade the wavefront quality of the beam by altering the perfectly flat ideal wavefront, but can also lead to the damage threshold of optics in the laser chain being exceeded, even where the pulse energy is comparatively low. The optical Kerr effect is most frequently quantified via the refractive index, including its intensity dependent

component as follows

$$\eta = \eta_0 + \eta_2(I_L) \tag{3.4}$$

In this equation, η_0 is the conventional refractive index and η_2 is the intensity dependent term, which increases in importance as the intensity is increased. It is often useful to quantify the degree to which non-linear optical effects need to be considered in the laser propagation. To this end, a mathematical description of the phase change of the pulse as it propagates over a distance L through some optical material can be defined as

$$\phi = \frac{2\pi}{\lambda_L} \int_0^L \eta(z) dz \tag{3.5}$$

$$\phi = \frac{2\pi}{\lambda_L} \int_0^L \eta_0(z) dz + \frac{2\pi}{\lambda_L} \int_0^L \eta_2 I_L(z) dz \tag{3.6}$$

The second, intensity dependent term in Eqn. 3.6 is defined as the 'B-integral', quantifying the non-linear optical effects. In order to avoid the issues of energy fluence and laser intensity, these parameters must be reduced for the duration of the amplification and beam transport process. One way of achieving this is to spatially expand the beam, however this approach is often infeasible due to the size and monetary cost of the optics required. The other method is to expand the beam temporally, and it was by introducing a method for achieving this that ultra-intense laser-plasma interactions became practical experimentally.

The ability to generate peak intensities of $> 10^{18}$ Wcm^{-2}, and thus open up the field of relativistic laser-plasma interactions for the first time, came in 1985 with the development of Chirped Pulse Amplification (CPA) [2], a technique for which the Nobel Prize in physics was awarded in 2018. In this scheme, the laser pulse is kept at a low intensity, below the threshold for the onset of non-linear optical effects, by stretching it in time before the amplification process. Once the pulse has been amplified, it can then be recompressed before being focused onto the target. The pulse is stretched by introducing a spectral chirp, achieved through the use of a diffraction grating (or in some cases a prism may also be used), named the 'Stretcher'. The stretcher induces a positive group

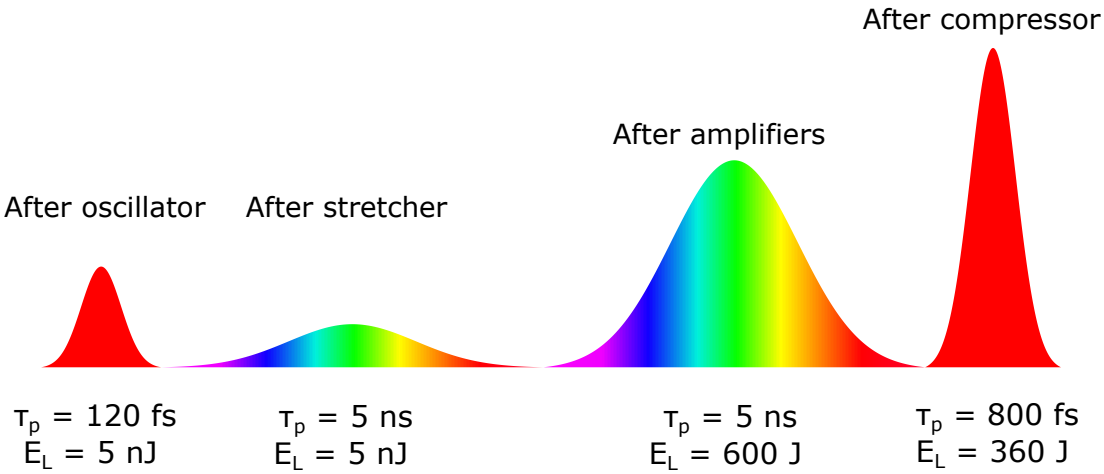

Figure 3.5: Illustration of the evolution of a laser pulse throughout the CPA process, progressing from left to right. The seed pulse from the oscillator is temporally stretched by inducing a spectral chirp, whereupon it can be amplified to higher energies without causing damage to the amplifiers or solid-state optics. The pulse is the recompressed by removing the chirp, before being directed into the target chamber. Typical pulse parameters at each stage of the process for the Vulcan Petawatt laser are also shown.

delay dispersion (GDD) by altering the path length travelled by each wavelength within the bandwidth of the pulse. An increase in pulse duration of the order of $10^3 - 10^5$ can be achieved, increasing a femtosecond/picosecond seed pulse to a duration on the order of nanoseconds. Once the pulse has been amplified (using the methods outlined in section 3.2.2), it may then be recompressed by using a second diffraction grating, named the 'Compressor', inducing an equal GDD of opposite sign to the stretcher. Ideally, the original pulse shape and duration will be recovered, but now with significantly higher energy content as a result of the amplification process. An illustration of this process is shown in Fig. 3.5. Gain narrowing [111], resulting in a reduction in bandwidth of the laser pulse during amplification, will however result in the final pulse having a slightly longer pulse duration than the seed due to preferential amplification of the photons of wavelength close to the central wavelength of the gain medium.

3.2.2 Regenerative and multi-pass amplifiers

In section 3.2.1, the concept of the laser seed pulse being stretched prior to amplification before being recompressed, was introduced. No thought however was given to how the pulse might be amplified once it has been stretched to a suit-

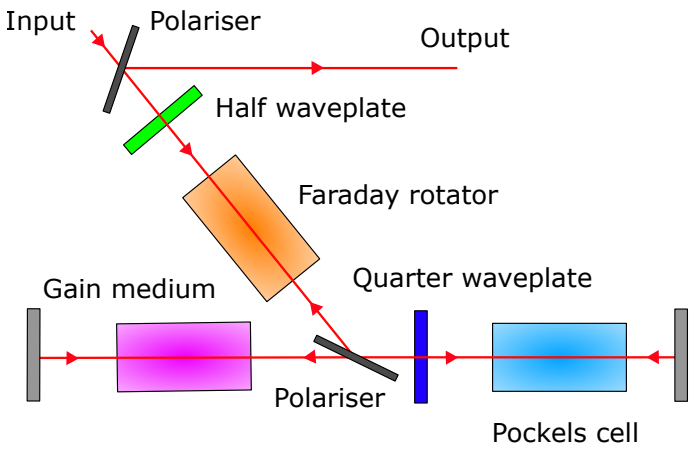

Figure 3.6: Simple schematic showing the optical setup of a regenerative amplification scheme. The pulse makes several passes of the gain medium before being released. The pulse is trapped in the gain medium section by a polarisation gating mechanism, with the pulse polarisation controlled by a Pockels cell and quarter waveplate combination.

ably long pulse duration. In this section, the main amplification schemes within the CPA technique will be explored to address this. The two primary schemes discussed will be regenerative and multi-pass amplification. Often, a multi-stage approach to amplification is adopted, and as such both methods outlined here may be used in the same laser system.

In a regenerative amplification scheme, often used in the pre-amplification stage of a CPA laser system, the injection, trapping and ejection of the laser pulse is controlled by a polarisation gating technique, as illustrated in Fig. 3.6. Initially, the laser pulse is injected through a polariser, half-wave plate and a Faraday rotator. The half-wave plate is set at an angle of 45° to the input polarisation and will rotate the polarisation angle by 90°. The Faraday rotator will then further rotate the polarisation by a controllable amount, dependent on the material properties such as the length and Verdet constant, and on the strength of the externally applied magnetic field. Following the Faraday rotator, the pulse encounters a second polariser, set to selectively reflect or transmit the pulse based on the polarisation state. Initially, the pulse is reflected, entering a Pockels cell, which will behave as a quarter-wave plate when the correct voltage is applied (known as the 'quarter-wave' voltage). The pulse will therefore leave the Pockels cell with circular polarisation, the rotation direction of which is reversed on reflection from the cavity mirror. The pulse then makes a second pass of

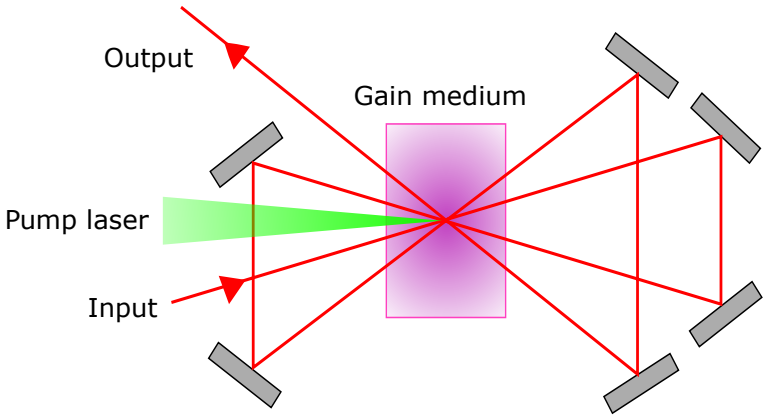

Figure 3.7: Basic schematic of a typical multi-pass amplifier setup as frequently used in high power laser systems. A geometric arrangement of mirrors is used to pass the pulse through the gain medium several times before extracting it.

the Pockels cell, resulting in a linear polarisation state at 90° to that which left the Faraday rotator. The pulse will now be transmitted by the polariser, allowing access to the gain medium. The pulse will make a double-pass of the gain medium each time it is allowed to transmit through the polariser, with this round-trip undergoing a number of repetitions. In order to switch the pulse out of the cavity, the voltage of the Pockels cell is set to zero, thus inducing no polarisation rotation. When the pulse now encounters the polariser, it is no longer transmitted, but is now reflected back through the entry optics and is able to leave the system. Due to the required transmission of the laser pulse through a number of optics, regenerative amplification schemes are not suitable for amplification to high laser energies. As a result, regenerative amplifiers are most commonly found early in the amplifier chain of high power laser systems.

In the multi-pass amplification scheme, the laser is guided using a geometrically based system of mirrors such that it makes multiple passes through the optically pumped gain medium, as shown in Fig. 3.7. As the energy gain from a single pass of the gain medium is limited, using a multi-pass approach can enable much higher pulse energies than any single pass system. The exit mechanism of the amplifier is rather simple when compared with the exit in a regenerative amplifier scheme. After the final pass of the gain medium, instead of being reflected back into the medium by an additional mirror, the pulse is allowed to escape the amplifier and proceed to the next step of the amplification process, or

to be transported to the compressor. As the optics employed in this system are primarily reflective, the energy gain can be maximised (higher than achievable with a regenerative amplifier) as the lack of pulse propagation within the optics reduces the risk of non-linear optical effects resulting from high B-integral. As such, in multi-stage amplification processes, the multi-pass scheme is often the final amplification stage before recompression, when the pulse energy is highest.

3.2.3 Optical Parametric Amplification

The amplification methods discussed in section 3.2.2 are primarily used in CPA systems due to the potential high energy gain. These schemes however are not without their drawbacks. Any amplification process involving the optical pumping of a gain medium is subject to the generation of ASE, which severely impacts the final temporal intensity contrast of the laser pulse, as discussed in section 3.1.1. Optical parametric amplification (OPA) is often used in modern laser systems during the pre-amplification stage as a means of amplifying the pulse without generating ASE, and thus improve the contrast of the final laser pulse.

In this amplification scheme, the seed pulse of frequency ω_s is propagated through a crystalline material which exhibits a $\chi^{(2)}$ non-linearity, the most common example of which, at least in high power laser systems, is β-barium borate (BBO). The $\chi^{(2)}$ non-linearity enables parametric frequency conversion within the crystal, while the natural birefringent properties of BBO ensures phase-matching by compensating for the wavelength dependence of the refractive index. A second, higher energy, pump pulse of shorter wavelength ω_p is phase-matched to the seed as it is propagated through the crystal. The phase-matching of the two pulses enables photons from the pump pulse to be converted to have the same frequency as the seed pulse, thus acting to amplify the seed. A third source of 'idler' photons, of frequency ω_i, is generated as a by-product of this conversion process, such that $\omega_p = \omega_s + \omega_i$, as illustrated in Fig. 3.8.

The main advantage of this approach for high power laser systems for use in laser-plasma experiments, is the temporal intensity contrast improvement, as already mentioned. Parametric conversion cannot take place without the presence

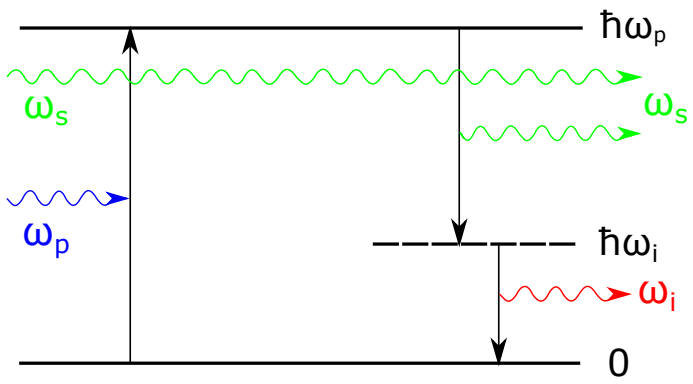

Figure 3.8: Atomic energy level diagram illustrating the process of OPA. The seed pulse and a pump pulse, of differing frequency, are incident on a non-linear crystal. The state excited by the pump pulse undergoes a stimulated decay when exposed to the seed pulse, resulting in amplification. A third frequency, forming the idler pulse, is generated as a by-product of this interaction, as shown.

of both the seed and pump pulses, thus removing the possibility for spontaneous emission. The contrast harming effects are not completely removed however, as a pump photon may 'split' into the two components outlined above within the non-linear crystal in a process referred to as amplified optical parametric fluorescence (AOPF). This process however is limited to the duration of the pump pulse, not to the excitation time of the gain medium as in ASE, and so is considerably closer in time to the main pulse. Another advantage of using OPA, particularly given the extensive use of tight-focusing geometries in this thesis, which are highly sensitive to wavefront aberrations, is the thermal behaviour of the system. The energy transfer between the pump and seed pulses is highly efficient, and as such results in a substantial reduction in the heating of the crystal. This in turn suppresses thermal lensing effects, which can be significant in other amplification schemes. This reduces the likelihood of optic damage caused by temperature induced focusing of the beam, and also minimises potential aberrations affecting the quality of the final focal spot. Minimising sources of wavefront aberrations, in particular wavefront curvature, is imperative when employing tight-focusing geometries due to the shortened Rayleigh range, as discussed in section 3.1.2.

3.3 Vulcan Petawatt Laser

The laser technology discussed in section 3.2 is employed in many high power laser systems around the world, each capable of delivering relativistically intense laser pulses with intensities exceeding 10^{18} Wcm^{-2}, with current peak intensities achievable of $> 10^{22}$ Wcm^{-2} [112]. These systems are however by no means identical, differing in pulse energy, pulse duration, focal spot size and quality, temporal intensity contrast, repetition rate and many more variables which make each laser system unique. It is therefore important the we consider here the specifics of the Vulcan Petawatt laser, as used in both results chapters 4 and 5.

The Vulcan laser is located at the Central Laser Facility (CLF), Rutherford Appleton Laboratory, UK, and is a CPA system capable of producing pulsed powers in the Petawatt regime (10^{15} W). The laser can deliver pulses via eight beamlines into two experimental target areas, Target Area West (TAW) and Target Area Petawatt (TAP). The full layout of the Vulcan laser facility, including laser areas, target areas and control rooms, is shown in Fig. 3.9. As only experiments performed in TAP are presented in this thesis, it is the laser and pulse parameters relating to the picosecond TAP beamline which will be explored here.

The laser pulse is originally seeded from a mode-locked Ti:Sapphire oscillator, with a frequency doubled, continuous wave (CW) Nd:YAG pump. This outputs a train of pulses of duration 120 fs FWHM each, a central wavelength of 1053 nm (bandwidth ±15 nm) and energy of 5 nJ. The wavelength has been shifted to 1053 nm to match later amplification stages. One of these pulses is selected and gated out to seed the amplification system. The pre-amplification stage is based on the OPA scheme outlined in section 3.2.3, employing a BBO non-linear crystal with a frequency doubled, Q-switched Nd:YAG laser providing a pump pulse of energy 1 J and pulse duration of 15 ns FWHM. An approximately flat-top intensity profile for the pump pulse is achieved by using a Pockels cell to select a 3 ns portion from the centre of the pulse.

Prior to any further amplification, the pulse duration is stretched from 120 fs to 4.8 ns using an Offner Triplet diffraction grating system [114]. This system

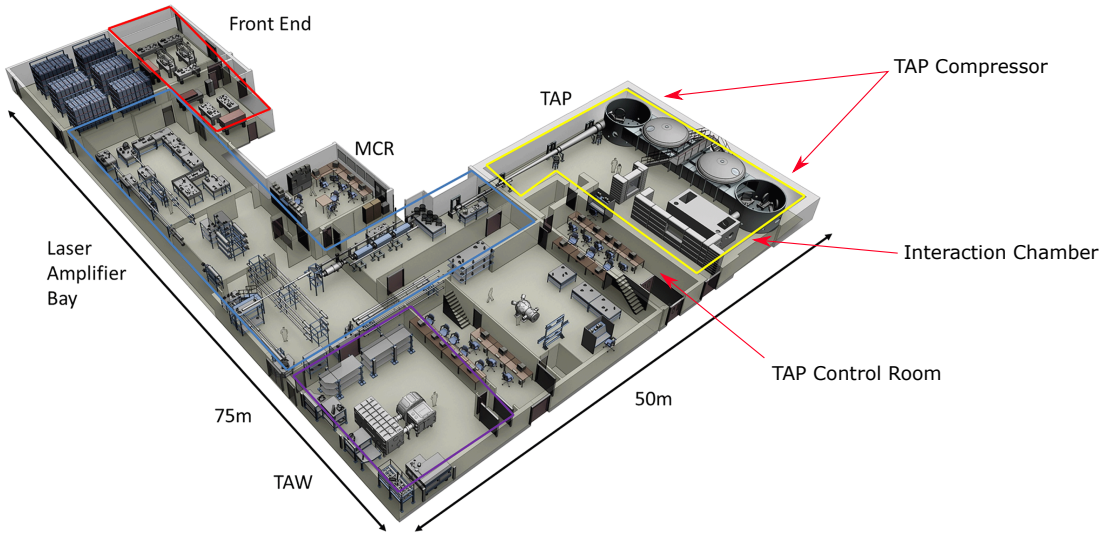

Figure 3.9: Layout of the Vulcan laser facility, including the laser front end and amplifier bay, both target areas, West and Petawatt, and the associated control rooms. Reprinted with edits from [113].

consists of two holographic diffraction gratings and concentric mirrors of a concave and convex geometry, applying a linear chirp across the bandwidth. This system also minimises spectral aberrations, enabling more efficient recompression following the amplification process. The amplifiers used have a gain medium of neodymium doped glass, which are optically pumped using white light flash lamps. Initially, the gain crystals are of the form of 9 mm diameter rod amplifiers, with both the amplifier and laser pulse diameter increasing as the pulse propagates down the laser chain. This maintains the pulse fluence below the damage threshold as it undergoes amplification. The final gain crystals are 208 mm diameter disk amplifiers. The pulse energy achievable using purely the rod amplifiers is approximately 85 J, increasing to approximately 600 J when using the larger disk amplifiers. The pulse is then recompressed from 4.8 ns to the final nominal pulse duration of 500 fs FWHM using a compressor consisting of two 940 mm diameter diffraction gratings.

Earlier in the laser chain, prior to the pulse being expanded and amplified, the beam is spatially filtered to remove high spatial frequency components. This acts to improve the spatial profile of the pulse, which is beneficial for improving the final focal spot size and quality when the pulse is focused onto the target. A second spatial filter is located after amplification, prior to compression, and

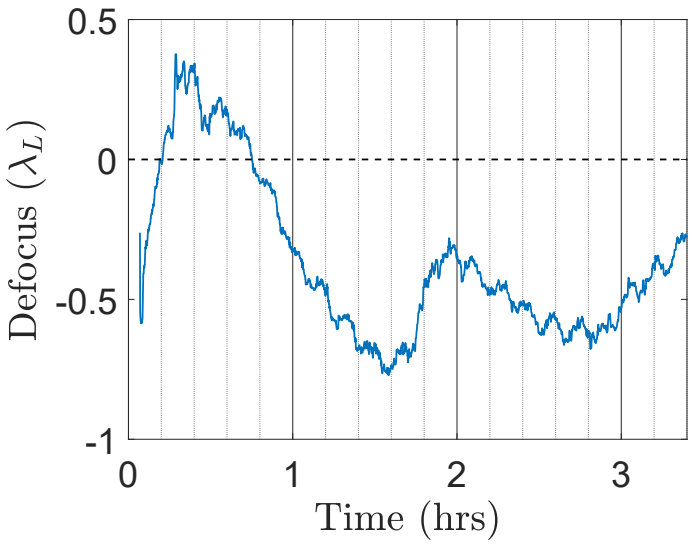

Figure 3.10: Defocus aberration, expressed in terms of the laser wavelength, as a function of time following the delivery of a full power pulse from the Vulcan petawatt laser, shown in blue.

further improves the spatial quality of the beam. To further improve compression and focusing, an adaptive optic (AO) is employed, working in conjunction with a Shack-Hartmann wavefront sensor (as described in section 3.1.2). Measurements of the wavefront distortion from the Shack-Hartmann are fed into the AO system, allowing for aberrations such as astigmatism or lensing effects to be corrected. This correction is achieved using a deformable mirror manipulated by 64 piezo-electric actuators. By correcting for wavefront distortions and thus forming the desired flat wavefront in the collimated beam, the final focus of the laser pulse is greatly improved, resulting in higher peak intensities on target. Furthermore, correcting wavefront curvature resulting from lensing effects (for example thermal lensing) is essential to the successful employment of tight focusing optics, due to the short Rayleigh range (see sections 3.1.2 and 3.4.2). Given that the employment of tight focusing schemes is one of the main themes of this thesis, the effect of the AO on the final focal spot is invaluable. This is especially true in the case of the elliptical plasma mirror setups employed in this thesis, where ensuring a precise spatial overlap of the OAP focal position with the first focus of the ellipse is essential to achieving intensity enhancement, as discussed further in section 3.4.2.

The combination of Shack-Hartmann sensor and deformable mirror is effective

for correcting steady state aberrations, as these will not change between the time of running the wavefront optimisation and the laser pulse being delivered onto the target. Dynamic wavefront aberrations are significantly harder to compensate for, as these can vary significantly between the time of wavefront optimisation and the pulse delivery onto the target. As part of the work presented in this thesis, it was discovered this is an issue present on the Vulcan laser and likely many other high energy systems, due to thermal lensing effects resulting from the amplification of the laser pulses to high energies. Following the delivery of a full power laser pulse, the defocus coefficient was found to increase by $\sim 1\lambda_L$ over a relatively short period of $\sim$ 15 minutes due to heating of the amplifiers, before a longer thermal recovery took place, returning the defocus to its initial value after a period of $\sim$ 1 hour. A trace of the defocus following delivery of a full power laser pulse is shown in Fig. 3.10. Following this time however, the defocus coefficient was found to periodically oscillate, resulting in a large rate of change in the defocus coefficient, making pre-compensation of the wavefront prior to the delivery of a subsequent laser pulse a significant challenge. Further investigation of this oscillatory behaviour showed that this took place even when the laser had not been used, and thus was related to the ambient temperature of the laser laboratory. The oscillatory nature of the variation was linked to the 'on/off' cycle of the air conditioning units, which resulted in a ~ 2°C temperature fluctuation, with a period of $\sim$ 30 minutes, matching the sinusoidal function of the laser defocus. This highlights the extreme sensitivity of the laser wavefront to even small thermal variations. A number of additional 'test shots' show that the restoration of the laser wavefront following each full power pulse was similar each time, and that after a period of $\sim$ 1.5 hours, an approximately steady thermal state had been achieved. In order to best pre-compensate for the dynamic sources driving the on-shot defocus aberrations, the restoration curves were used to predict the necessary AO corrections, which were performed within a fixed time prior to the delivery of a full power laser pulse onto the target. Through this process of better understanding the primary source of dynamic aberrations, and the resulting procedural implementations, improved control of the laser wavefront

Laser parameters	Values
Pre-compressor energy	600 J
Energy on target	250 J
Focal spot size (Using F/3.1 OAP)	4.5 μm (FWHM)
Pulse duration	1 ps (FWHM)
Central wavelength	1.053 μm
Polarisation	Horizontal
Peak intensity	$\sim 7 \times 10^{20}$ Wcm^{-2}

Table 3.1: Summary table of typical Vulcan petawatt laser parameters, as used in the experimental campaigns reported in this thesis.

curvature was achieved. This issue is of particular importance for the work using ellipsoidal, focusing plasma mirrors reported later in this thesis. Mitigating the effects of this issue via the improved process of AO correction enabled near-optimal performance of the FPMs to be achieved.

Prior to the pulse entering the target chamber, a leak is taken from a turning mirror within the compressor, and is used to measure a number of crucial pulse parameters. The pulse energy pre-compression is measured using a calibrated calorimeter and the pulse duration is characterised using a second-order, single-shot autocorrelator [115]. Once the pulse has been re-compressed and its properties measured, it is directed into the target chamber, where it is focused onto target using a 620 mm diameter off-axis parabola (OAP), with a f-number of $f/3.1$. When correctly optimised, this focusing scheme yields a spot at best focus of size $\phi_L \approx 4$ μm FWHM and fractional encircled energy $f_{EE} \sim$ 30-40%. The compressor does result in a loss of energy, due to lower than unity reflectivity, with the measured energy throughput being approximately 60%. A summary of relevant pulse parameters is presented in Table 3.1. The temporal intensity contrast ratio (see section 3.1.1) has been measured to be approximately 10^{-8} at a period of around 1 ns before the main pulse. For peak intensities of $> 10^{20}$ Wcm^{-2}, this would result in intensities of $\sim 10^{12}$ Wcm^{-2} being incident on the target prior to the main pulse. Such intensities are sufficient to induce pre-ionisation, resulting in target deformation and extensive pre-plasma formation long before the arrival of the main pulse. This is particularly important when employing ultra-thin targets, as employed in Chapter 4 (tens to hundreds of nm thickness),

as this pre-ionisation can drive heating and a shock-wave which will destroy the target. As such, in all experimental setups employed in this thesis, plasma mirrors were used as an optical tool to enhance the temporal intensity contrast by two orders of magnitude (described in section 3.4).

3.4 Plasma Mirrors

Enhancement of the temporal intensity contrast of the laser pulse is of vital importance. Due to the high peak intensities available on current laser systems (typically $10^{20} - 10^{21}$ Wcm^{-2}), pulse pedestal intensities in the range of 10^{12} to 10^{13} Wcm^{-2} are to be expected several hundreds of picoseconds, or potentially nanoseconds, before the peak of the pulse. As such, it is imperative that the contrast is improved. One method for achieving this is the use of plasma mirrors, positioned in the focusing beam [116, 117]. On the Vulcan laser system, a single plasma mirror setup is typical, especially when employing ultra-thin, nm scale targets where minimal pre-plasma formation is required, and is employed in all experimental campaigns featured in this thesis, although it is not uncommon to run a multiple plasma mirror setup on other laser systems. Each additional plasma mirror will further enhance the temporal intensity contrast of the laser pulse, holding off target ionisation until later in the rising edge of the pulse, but at the cost of increasing energy losses, thus requiring these two parameters to be carefully balanced when designing an experiment.

3.4.1 Principles of operation

The key aspect of a plasma mirror is employing a material which is optically transparent when irradiated by low intensity light and which has an optical quality surface. The quality of an optical surface is usually quantified through comparison of the magnitude of surface imperfections and irregularities to the laser wavelength. The plasma mirrors employed are manufactured with a surface flatness of $\lambda_L/8$, thus preventing aberrations from degrading the optical performance of the system, i.e. the reflected wavefront is identical to the incident wavefront.

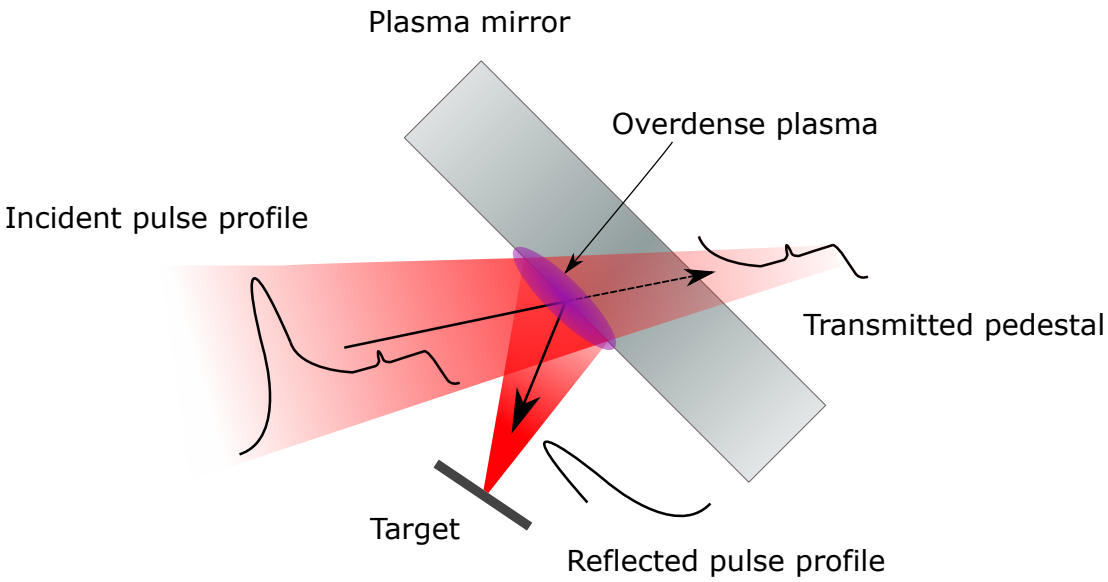

Figure 3.11: Schematic of the basic principle of operation of a plasma mirror, in this case the planar geometry is shown. The pulse pedestal and pre-pulses are transmitted through the un-ionised glass slab. The peak however is sufficiently intense to form an overdense plasma layer, thus reflecting the remaining pulse onto the target with an improved temporal intensity contrast.

To achieve this, a plasma mirror is usually precision machined to form a planar, dielectric glass block. The glass is transparent to the laser wavelength, and is often coated in an anti-reflection (AR) coating, of reflectivity 0.25% [118]. The planar geometry is important, as alterations to this geometry can be used to induce tighter focusing of the pulse, as described in section 3.4.2. In order to differentiate between the focusing and planar designs, plasma mirrors of the planar geometry will be referred to by 'PPM'.

The principle of operation of a PPM, as illustrated in Fig. 3.11, is relatively simple, yet very effective for improving laser temporal intensity contrast. The PPM is placed in the path of a focusing laser pulse. The positioning of the PPM in the focusing beam must be such that the light forming the pulse pedestal is below the ionisation threshold of the PPM, and will thus be transmitted with minimal reflection. Additionally, the position of the PPM must be tuned to ensure maximum reflectivity in the plasma regime, defined by the intensity of the incident laser pulse as it irradiates the PPM [119]. This transmission may be enhanced by angling the PPM relative to the incident pulse at the Brewster angle for the specific refractive index of the PPM material, giving maximum

transmission. At some point in the laser temporal intensity profile, the intensity will become sufficient to ionise the PPM. An overdense layer of plasma will form rapidly on the surface, thus reflecting a large fraction of the subsequent laser light from the critical density surface. As such, the PPM acts as an intensity gate, switching from highly transparent to highly reflective on sub-picosecond timescales ($<$ 500 fs [119]). This acts to temporally clean the pulse, as the transmitted fraction, comprising of unwanted pedestal light, is directed away from the target. Furthermore, the wavefront quality is preserved throughout this process as, due to fast switch on time, there is insufficient time for surface instabilities or significant plasma expansion to occur (for pulse durations of $<$ 3.5 ps) [108].

There are a few important conditions which must be considered before deploying a PPM setup. Firstly, the energy content of the reflected beam is reduced by typically $\sim 20-30\%$ when compared to the beam prior to the PPM. This reduction in energy arises primarily from a combination of the transmitted light prior to the formation of the overdense plasma and the plasma physics of the beam-plasma mirror interaction itself. A fraction of the laser energy will be absorbed into the plasma electrons, with the size of this fraction depending on laser parameters such as polarisation and angle of incidence, with the plasma optic also exhibiting a varying cold (i.e. non-plasma) reflectivity depending on the polarisation state. Furthermore, the absorption of laser energy into a plasma is intensity dependent, with optimal specular reflectivity occurring for intensities of $10^{15}-10^{16}$ Wcm^{-2} [108, 119]. Peak intensities of greater than 10^{16} Wcm^{-2} result in a decreased, and highly erratic, reflectivity. This results from the plasma mirror switching on earlier, enabling a greater degree of plasma expansion before the arrival of the peak of the pulse. This expansion, combined with the resulting growth of surface filamentation, results in an increase in diffuse scatter from the plasma surface and thus a corresponding decrease in the specular reflectivity [108]. Furthermore, plasma processes such as resonance absorption for example [30], begin to become increasingly dominant at these intensities, which further reduce the specular reflectivity by increasing the absorption into the plasma.

The second consideration, which has yet to be discussed in detail, is the wavefront quality of the reflected beam, which should ideally exhibit no degradation on reflection. In order to achieve this, the surface of the overdense plasma must be as close as possible to the surface of the un-ionised glass, thus being essentially optically flat [119]. This condition is met when the ionisation of the PPM, and thus formation of the overdense plasma, occurs soon before the peak of the pulse (within a few picoseconds). This condition can be expressed using the approximate condition that; $c_s \Delta t < \lambda_L$; where c_s is the ion sound speed and Δt is the time of plasma formation before the peak of the main pulse. If this condition is met, high specular reflectivity will be achieved, otherwise the reflected light will be more diffuse in nature. This inequality, in physical terms, places a limit on the extent of plasma deformation on the arrival of the main pulse, requiring it to be less than the wavelength of the incident laser pulse. For the laser wavelength of Vulcan (~ 1 μm), as used in this thesis, and assuming a sound speed of $c_s = 3 \times 10^5$ ms^{-1}, the limiting time is ~ 3.5 ps prior to the arrival of the peak of the pulse. After this time, the optical quality of the plasma surface is significantly degraded and any subsequent light will be scattered diffusely. Destruction of the optical surface in such a fashion will result in a significantly reduced energy throughput and a degradation of the wavefront quality, ultimately resulting in a poorer quality focal spot formed on the target. This result was verified experimentally in the studies presented in Scott *et al.* [108].

Assuming the above conditions for intensity and plasma formation time are met, PPMs are a common feature of any experiment requiring high temporal intensity contrast. Both the effects of ASE and pre-pulses may be suppressed [120, 121]. As such, many studies into the dynamics surrounding the use of plasma mirrors have been undertaken [108, 122, 123], which have independently verified the contrast enhancements possible. In addition to the above, there have been several studies into further functions of plasma mirrors. One such application is the alteration of the focusing geometry of the laser beam, enabling the generation of near-wavelength scale focal spots. This particular plasma mirror sub-group is a key tool employed in this thesis and is explored in greater detail in the following

section, 3.4.2.

3.4.2 Focusing Plasma Mirrors

As the wavefront of a laser pulse reflected off a PPM is essentially the same as that reflected off a planar, solid-state mirror, the question is raised if plasma optics of different geometries can be used to achieve goals other than just reflection with improved contrast. Given that the plasma is formed in a thin layer on the surface of the glass slab, curvature of the surface could be used to induce focusing, just as in conventional optics. By choosing an appropriate surface curvature, tighter focusing can be achieved relative to the incident focusing beam (in this thesis, the incident beam has a F/3.1 focusing geometry), enabling a relatively low cost means of increasing laser intensities on current laser systems without significant alteration of the existing beamline, whilst simultaneously improving the temporal intensity contrast.

It has been shown in proof-of-principle experiments that an ellipsoidal geometry, henceforth referred to as a focusing plasma mirror (FPM), with two foci located such that the path length between the optic surface and one is greater than the surface to the other, can achieve significant reduction in focal spot size and thus a large gain in intensity [124, 125]. An example of this design is shown in Fig. 3.12. The input focal spot from the F/3.1 OAP is spatially overlapped with the focal position f_1, with the light diverging from this point onto the surface of the FPM. The target is positioned at the output focus position f_2, with a focal spot demagnification of approximately $\times 3$ ($m = 1/3$ as given by Eqn. 3.7). This results in a near diffraction limited focal spot of size ~ 1.5 μm FWHM and an approximately F/1 focusing geometry. Such a reduction in focal spot size can result in an intensity enhancement of up to $\times 9$, which represents a substantial increase even when considering the finite reflectivity of the plasma mirror, especially given the relatively low cost of the plasma optics. Furthermore, it can be seen clearly from Fig. 3.12 that the ellipsoidal geometry satisfies the need for off-axis focusing, ensuring the target does not block the incoming beam.

Now that the basic principles of a FPM has been introduced, it is appropriate

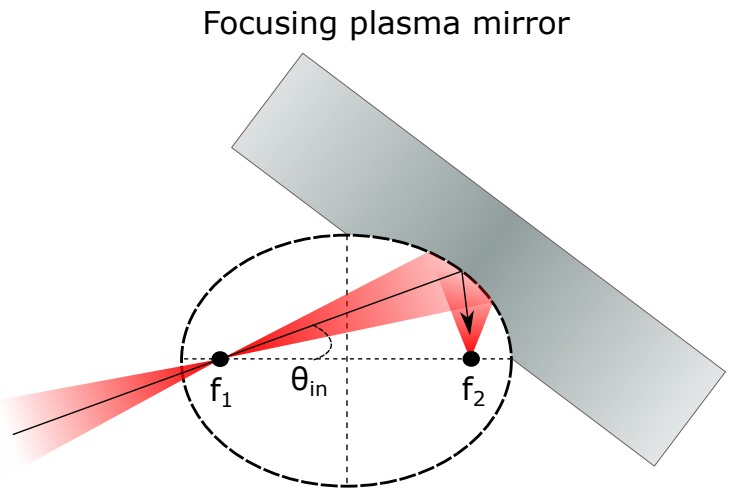

Figure 3.12: Schematic of the principle of operation of a focusing plasma mirror. The incident F/3.1 pulse is focused to the f_1 focal position. From here, the beam expands onto the surface of the FPM before being refocused to the focal position f_2 whilst also achieving an enhancement in temporal intensity contrast.

to explore the specific details of the FPM design used in this thesis, which has been developed and characterised in detail [126, 127, 128]. As mentioned previously, an ellipsoidal geometry was chosen, with two foci located on the major axis, equidistant from the centre of the ellipse, as illustrated in Fig. 3.12. The specific geometry of the ellipse defines the size of the focal spot demagnification achievable at the position f_2, depending on the eccentricity of the ellipse e and the angle of incidence of the beam θ_{in} as follows

$$m = \frac{(1+e^2) - 2e \cdot \cos\theta_{in}}{(1-e^2)} \tag{3.7}$$

This equation is an expanded form of the conventional magnification equation used throughout optics; $m = v/u$; where v is the image distance and u is the object distance. In the specific case of the ellipse, v is the distance from f_1 to the optic surface and u is the distance from the optic surface to f_2. In the design employed throughout this thesis, the distance v is $\times 3$ larger than u, thus resulting in the $\times 3$ demagnification of the laser focal spot at f_2 relative to the input focal spot at f_1.

In order to achieve intensity enhancements close to the theoretical maximum (i.e. $\times 9$ increase in intensity for a $\times 3$ reduction in focal spot size), the alignment

of the FPM must be precisely optimised. The FPM is highly sensitive to the spatial overlap of the incident focal spot with f_1, with even small offsets resulting in a reduction in the encircled energy and a deterioration of the focal spot quality. Unlike a conventional OAP however, variations in tip/tilt of the FPM, whilst changing the pointing of the output beam, have a minimal effect on the focal spot quality. The requirements for intensity enhancement can be reduced down to three parameters: focal spot size (ϕ_{in} and ϕ_{out}), focal spot encircled energy (E_{in} and E_{out}) and the reflectivity of the FPM itself in the plasma regime (Γ_p). These parameters can be combined mathematically to give an intensity enhancement factor, given by the following

$$I_{enh} = \left(\frac{\phi_{in}}{\phi_{out}}\right)^2 \cdot \Gamma_p \cdot \left(\frac{E_{out}}{E_{in}}\right) \tag{3.8}$$

If this factor is greater than one, then intensity has been gained relative to the conventional F/3.1 focusing. Conversely, if this factor is less than one, poor optic alignment has destroyed the focal spot or poor reflectivity has significantly reduced the energy content of the focal spot, resulting in a lowered on-target peak intensity. Successful employment of a FPM therefore clearly depends on achieving a well optimised alignment, corresponding to an accurate overlap of the input F/3.1 focal spot with the f_1 focus of the ellipse.

Misalignment may come from two sources. Firstly, the placement of the FPM may be poor. This however is not a particularly common issue as this will be noticed when the focal spot is imaged and the positioning can be corrected prior to the shot. The second, and significantly more likely source is natural variations in the focal position of the laser on shot. Effects such as spatial jitter or thermal lensing may alter the transverse (Δx and Δy) and longitudinal (Δz) position of the incident focal spot relative to the f_1 focus of the ellipse. Testing of FPM optics [126, 127, 128] show that misalignments of > 10 μm in either transverse direction (Δx or Δy) will result in a degradation of the focal spot quality such that no intensity enhancement is achieved. Furthermore, when a misalignment occurs in both transverse directions simultaneously (Δxy), it is almost impossible to

achieve intensity enhancement. Similarly, longitudinal misalignments of $\Delta z > 30$ μm will result in intensity degradation, assuming a fixed target position, due to the falloff in focal spot quality and encircled energy. It is important to note that misalignments less than these thresholds, whilst resulting in some intensity enhancement, will fall well short of the maximum possible intensity. It is for this reason that the measurement and control of the laser defocus aberration is crucial for the application of this technique.

3.5 Diagnosing laser-solid interactions

Due to the inherent complexity of the underpinning physics of laser-solid interactions, a wide range of techniques are commonly employed in the experimental investigation of these interactions, depending on which particular aspects of the interaction are being probed. This includes, but is not limited to, diagnostics designed to characterise the spatial and spectral properties of the emitted particles and radiation, the spatial and spectral properties of the transmitted and reflected laser and self-generated light, and a range of pump-probe techniques. Each diagnostic gives insight into a particular aspect of the interaction, and so it is necessary to employ a wide range of diagnostics, potentially over several experimental campaigns, in order to gain insight into the fundamental physics of high intensity, laser-plasma interactions. In this section, the experimental diagnostics and techniques employed in the investigations carried out in this thesis are reviewed.

3.5.1 Proton spectroscopy using stacked Radiochromic film

A primary diagnostic used in this thesis to measure the spatial and spectral properties of the protons accelerated during a laser-solid interaction is stacked Radiochromic film (RCF). Unlike photons or electrons, which deposit their energy in an exponentially decaying fashion within matter, protons and other ions deposit a significant fraction of their energy at a specific depth within the material, referred to as the Bragg peak. The energy deposited in the material before or

after this peak is small in comparison (afterwards, the energy deposited quickly falls to zero). This peak in energy loss results from the energy dependence of the interaction cross-section, which increases as the proton loses energy within the material, thus increasing the probability of a subsequent interaction. Higher energy protons will penetrate further into the material before being stopped. An example of these Bragg peaks, for the stopping of protons in iron, is shown in Figure 3.13 (a), calculated using SRIM (Stopping and Range of Ions in Matter) [129] ion stopping data, which uses a Monte Carlo approach to generate stopping range tables for a wide variety of materials and incident ion species, averaged over a large number of ions. This data enables the stopping of ions within a given material to be mapped and the characteristic Bragg peaks to be identified.

A stack of RCF, consisting of many individual layers of RCF, each of known thickness and material composition, interspersed with layers of filter materials (e.g. iron, copper, Mylar or aluminium as used in this thesis) can therefore be used to exploit this behaviour, as each layer corresponds to a narrow range of Bragg peaks. As higher energy protons will penetrate further into the stack, measuring the dose at each layer yields an energy spectrum of the accelerated proton population. In addition to the filter materials situated throughout the stack, a thin (13 μm thick) layer of aluminium is typically added to the front of the stack. This layer serves two purposes: Firstly it protects the front layers from laser damage and optical exposure should the laser be transmitted through the target (as typically happens in interactions where the target undergoes RSIT) and secondly, this layer is thick enough to stop heavier ion species such as carbon ions to ensure that the measured ion signal is purely from the proton population [130].

The RCF itself is a form of proton sensitive dosimetry film, composed of layers of plastic and a radiation sensitive, organic, active layer, which discolours when irradiated by ionising radiation. This discolouration alters the optical density (OD) of the RCF proportionally to the incident dose of radiation, where a higher OD corresponds to a greater deposited dose. The OD is expressed mathemati-

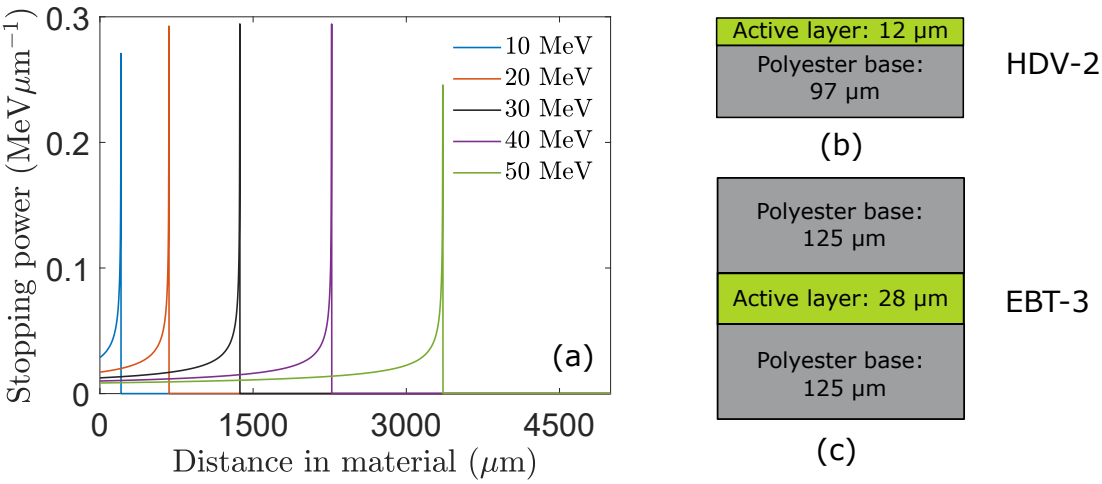

Figure 3.13: (a) Stopping power of protons in MeVμm^{-1} with initial energies of $10 - 50$ MeV in iron, a common material used as a filter in RCF stacks, as calculated using SRIM [129]. The plot takes the form of the characteristic Bragg peaks, with the maximum stopping power occurring deeper into the material as the initial energy is increased. (b) Layer composition of HDV-2 film, used at the front of RCF stacks due to its lower sensitivity to incident ionising radiation. (c) Layer/material composition of EBT-3 film, typically used at the rear of the RCF stack, due to the higher sensitivity to ionising radiation resulting from the thicker active layer.

cally as follows

$$OD = -\log_{10}\left(\frac{I}{I_{max}}\right) \tag{3.9}$$

where I is the signal intensity at a given point and I_{max} is the saturated intensity of the film at that point. In order to capture the spectral data of the entire population of accelerated protons, several different forms of RCF may be used throughout the stack. In this thesis, two types of RCF were used, HDV-2 and EBT3 (both manufactured by Vertec). The layer structure of each is shown in Figure 3.13 (b) and (c) respectively. HDV-2 is used at the front of the RCF stack, where the dose deposited by the protons is higher due to the shape of the typical energy spectrum (i.e. higher number of protons with lower energies), whilst EBT3 is used at the back. EBT3 is more sensitive to lower doses of radiation due to its composition, having a thicker active layer than HDV-2. Due to the transverse dimensions of the RCF (typically several cm), and the distance the stack is placed from the target rear (typically 3-5 cm), the distribution of the dose across the film gives spatial information about the proton beam, in addition to the measurement of the energy spectra.

In order to convert the measured proton signal into a more useful, digital

form, the RCF is scanned using a Nikon CoolScan3000 high resolution, optical scanner. The spatial resolution of the scanner is > 600 pixels/inch. The scanner itself consists of an array of light-emitting diodes (LEDs), with operational wavelengths of 474 nm, 532 nm and 643 nm, with the light transmitted through the scanned RCF before being detected by a 16-bit colour CCD. Scanning using three wavelengths enables the optical response to differing proton doses to be tuned, for example the 643 nm channel is highly sensitive to changes in optical density for low proton doses but plateaus for doses exceeding a few hundred Gray. In contrast, the 474 nm channel exhibits a flat response for low deposited doses, but the region with high sensitivity to proton dose extends to tens of thousands of Grays. The optical density measured for each pixel may then be converted to proton dose via a calibration undertaken using a known, well-characterised proton source. This calibration was performed for all types of RCF used in this thesis using protons accelerated using a cyclotron accelerator located at the University of Birmingham.

Once the process of digitising the RCF and subsequently extracting the proton dose has been undertaken, the energy spectrum can be determined by quantifying the proton numbers detected on each layer of the RCF, N_p, and the energy of the Bragg peak which corresponds to the depth of that layer within the stack, E_B. The total energy, E_T, deposited in a layer of thickness d_ℓ and density ρ_ℓ, may be calculated using the following equation

$$E_T = d_\ell \rho_\ell \sum_{n=1}^{N} (D_n A_n) \tag{3.10}$$

where D is the measured proton dose and A is the area of a given pixel n. The number of protons may then be calculated using the following

$$N_p = \frac{E_T}{E_B dE} \tag{3.11}$$

where dE is the 'width' in energy terms of the RCF layer.

Determination of the proton energy spectrum enables the measurement of

additional parameters of the accelerated proton population, which are of use in characterising laser-solid interactions. One such parameter, as explored in Chapter 4, is the laser-to-proton conversion energy efficiency. Once the energy spectrum of the protons is known, the laser-to-proton energy conversion efficiency, $\eta_{\ell \to p^+}$, may be calculated using the following

$$\eta_{\ell \to p^+} = \frac{\sum_{E=0}^{E_{max}} N_E E_p}{E_L} \tag{3.12}$$

where E_{max} is the maximum measured proton energy, N_E is the number of protons with energy E_p and E_L is the laser energy. This therefore gives a fractional measure of the laser energy converted in the accelerated proton population.

3.5.2 Backscatter spectrometry

Another key diagnostic of laser-solid interactions, used in Chapter 4, is the measurement of the backscattered light, i.e. the light reflected off the target back along the laser axis. In particular in this thesis, the measured spectrum of this light is used as a means of diagnosing the recession velocity of the plasma critical surface, referred to as the holeboring velocity. The light reflected off the target along the laser incidence axis is captured and re-collimated by the focusing OAP before propagating backwards through the laser chain. In this thesis, leakage light through the final turning mirror (due to it not being 100% reflective), prior to the OAP, is collected and directed onto a PTFE scattering screen, chosen due to its high reflectivity and lambertian characteristics. An illustration of this setup is shown in Fig. 3.14. A sample of the scattered light is collected by an optical fibre, and is passed into a spectrometer, in this case an Avantes AvaSpec spectrometer is used. The wavelength range of this spectrometer is 200-1160 nm, enabling measurement of the laser frequency and harmonics up to and including the fifth order (although the higher orders are typically too dim to detect). The holeboring velocity is typically determined from the generated second harmonic light, which falls well within the optimal range of this spectrometer. Wavelength calibration of this spectrometer was performed using a HgAr light source, cho-

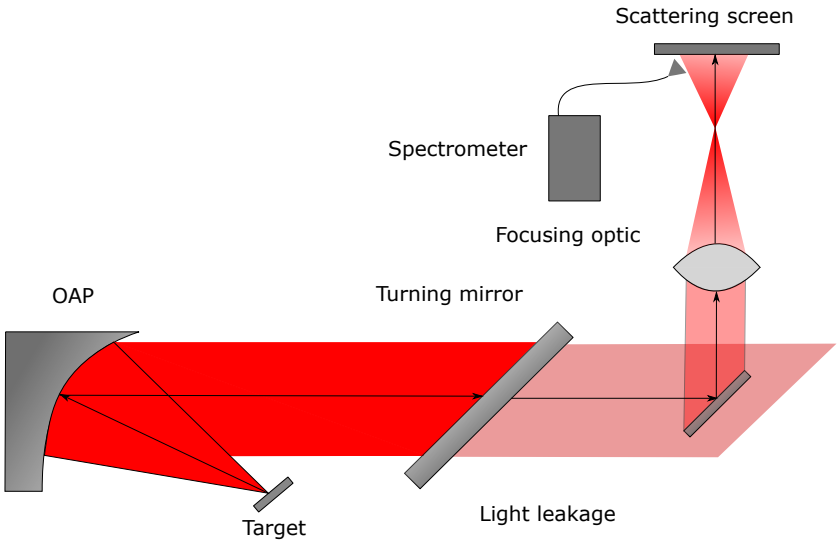

Figure 3.14: Simple illustration of a typical setup used to measure backscattered laser light in the Petawatt target area of the Vulcan laser. A subsample of the leak through the final turning mirror is directed onto a scattering screen, with the spectrum of the scattered light measured using a spectrometer.

sen due to its large number of characteristic emission lines within the pertinent wavelength range.

The measured spectrum of the backscattered light may be used to calculate the holeboring velocity via the Doppler effect. If the holeboring velocity were to be zero, i.e. the plasma critical surface is not moving at all, the second harmonic light would be measured to have a wavelength of $\lambda_{2\omega} = 527$ nm for the Vulcan laser ($\lambda_L = 1054$ nm). In reality, the critical surface is receding with some velocity, and so all reflected light, including the second harmonic, will be red-shifted. This holeboring velocity will vary over the course of the interaction as the laser intensity and plasma density dynamically change [28, 90], and so a range of red-shifts will be observed depending on the time of reflection/emission. By measuring the maximum red-shifted wavelength detected, whilst remaining above the background signal level, the peak holeboring velocity, v_{hb}, may be determined using the following equation

$$\frac{v_{hb}}{c} = \frac{\lambda - \lambda_{2\omega}}{\lambda_{2\omega}} \tag{3.13}$$

where λ is the maximum measured red-shifted wavelength.

3.5.3 K_α imaging

One tool employed in the characterisation of laser-solid interactions for measuring parameters of the fast electron population within the target foil, such as electron divergence [68] and refluxing [131, 132], is the K_α imager. The diagnostic collects and images the x-ray emission resulting from collisions between the atoms within the target bulk and the fast electron current. Many transitions may occur during the interaction and thus yield a spectrum of x-ray energies, in addition to the x-rays emitted due to Bremsstrahlung radiation, but this diagnostic specifically images those resulting from the K_α transition. This particular atomic transition occurs when an electron bound in the K-shell of an atom is ejected by collision with a fast electron. This empty state may then be filled by an electron decaying from the L-shell, resulting in the emission of a photon with a characteristic energy (E_{K_α} = 8.048 keV for copper). A simple schematic of this process is shown in Fig. 3.15. The fraction of decays proceeding via this radiative process is given by the fluorescence yield ω_K. The probability of such a collision taking place, where a fast electron ionises a K-shell electron, is given by the K-shell ionisation cross-section σ_K. This cross-section is dependent on the energy of the incoming electron and is maximised at a few times the ionisation potential (8.979 keV for copper) of the material. For high electron energies, $E_f > m_e c^2$, relativistic effects cause this cross-section to rise once again due to Lorentz contraction of the electron's field. Due to the large number of electrons moving through the target (see Chapter 2.6), a large number of K_α photons will be emitted, with the random emission direction resulting in a spherical 4π solid angle spread.

The K_α imager itself collects the photons emitted into a small portion of the total solid angle emission and images these onto a detector. For the measurements reported in this thesis, the detector used was x-ray sensitive BAS-TR IP, as described below, although x-ray sensitive CCD cameras, x-ray films or scintillating materials may also be used. The image plate has shielding material placed in front of it such that K_α photons may pass through, but other sources of radiation are blocked or significantly attenuated. Additionally, a 1 T magnet

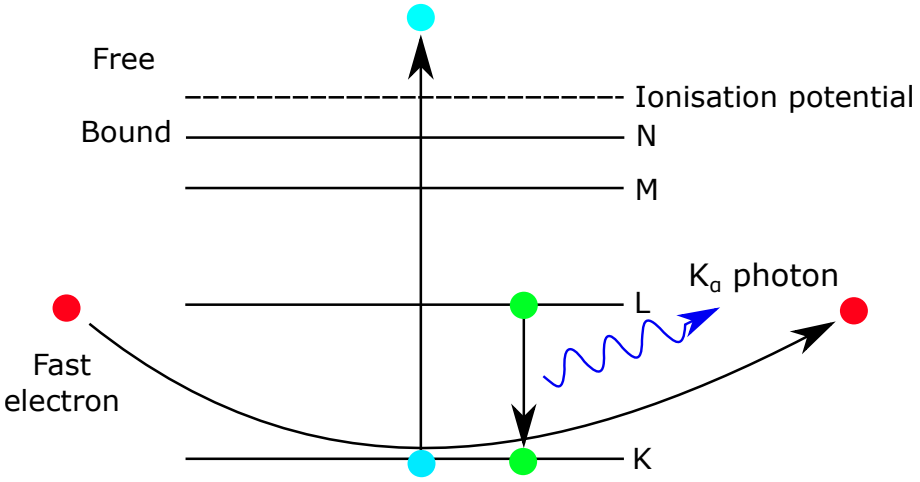

Figure 3.15: Atomic energy level diagram showing the process of K_α photon emission. A fast electron ejects a K-shell electron from the atom / ion. An electron from the L-shell radiatively decays to the K-shell, releasing a K_α photon of characteristic wavelength and thus energy.

was placed in front of the detector to sweep away any charged particles which may otherwise contaminate the measured signal. The strength of the measured signal gives information on the number of x-ray photons generated [133], which can in turn be related to the properties of the fast electron population within the target. Furthermore, the spatial distribution of the emission region gives information of the size of the fast electron beam, and allows information regarding the electron beam divergence to be built up over a number of shots. A spherically bent, quartz Bragg crystal was used to collect the photons, reflecting and imaging the photons onto the IP detector. The angle of incidence of the photons onto the crystal is of great importance as this determines the energy of the photons collected. In order to satisfy the Bragg condition for the crystal, K_α photons of energy E_{K_α} and corresponding wavelength $\lambda_{K_\alpha} = hc/E_{K_\alpha}$ will have a Bragg angle of $\theta_{Bragg} = \sin^{-1}(n\lambda_{K_\alpha}/2d)$, where d is the crystal spacing. The focal length f is determined based on the radius of curvature of the crystal (R) and the Bragg angle (θ_{Bragg}) by $f = R/2\sin\theta_{Bragg}$. An illustration of the general form of a typical K_α detecting setup is shown in Fig. 3.16.

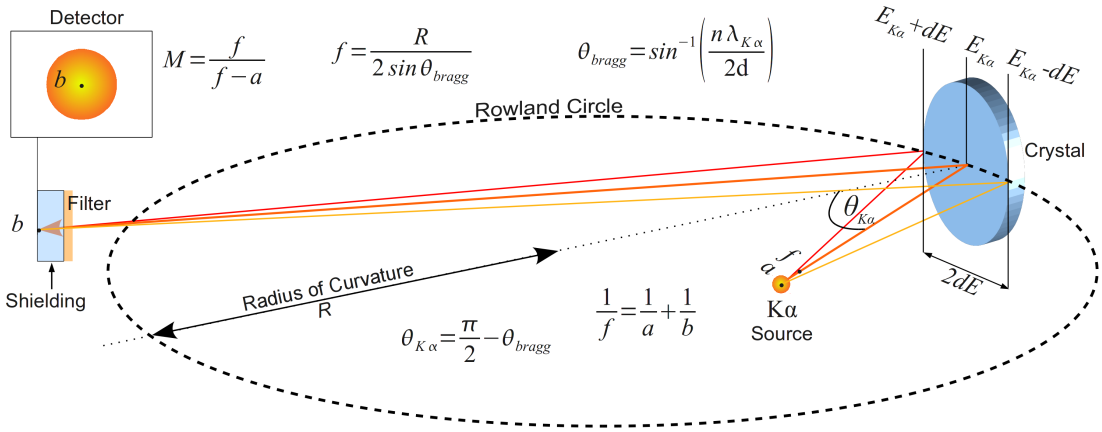

Figure 3.16: Schematic of a typical K_α imaging diagnostic. The K_α photons emitted into a small solid angle are collected by a spherically bent Bragg crystal. This radiation is reflected and imaged onto the detector, in this case image plate, with some magnification M, as determined by the specific geometry of the system used. Reprinted from [65].

3.5.4 Image Plate

Image plate (IP) is the detector used in Chapter 5 as the primary means of detecting the emission of X-rays from the target, as part of the copper K_α imaging diagnostic described in the previous section. IP consists of multiple layers; namely a luminescent phosphor layer (with a composition of $BaF(Br_{0.85}I_{0.15}):Eu^{2+}$) and a supporting steel layer (some forms also have a protective Mylar layer over the phosphor layer, but not the type used in this thesis). The layer structure of the IP used (Fujifilm BAS-TR) is shown in Fig. 3.17 (a).

The underpinning physics of IP is based on atomic transitions induced by the interaction of the incident radiation (in this case X-rays) with the Eu^{2+} ions in the phosphor layer. Assuming sufficient energy, the incident X-rays ionise the Eu^{2+} ions to produce Eu^{3+} through the ejection of a photoelectron. This electron is excited into the conduction band and trapped in a metastable state with a lifetime of several hours, which results from defects in the crystal structure induced by the Eu doping of the material. The information on the image plate is digitised using a laser scanner by utilising the process of photostimulated emission. In this procedure, the IP is scanned by a focused laser with a wavelength of 632 nm. The focal spot size of this laser is typically around 25 μm, setting the theoretical limit on the spatial resolution of the scanner, although the actual resolution is

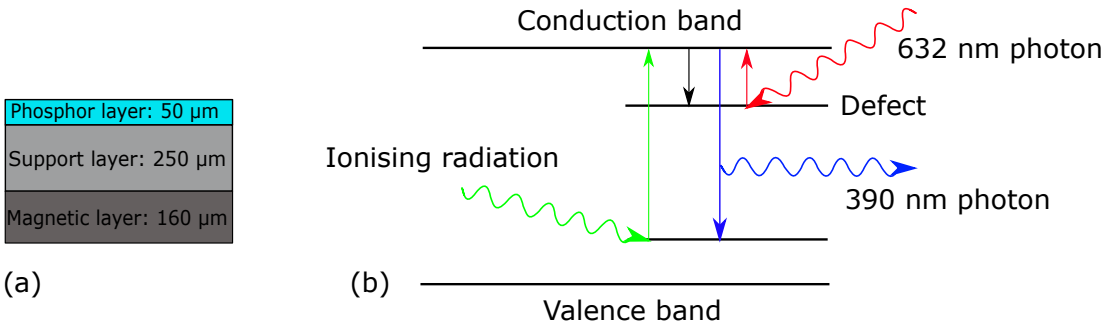

Figure 3.17: (a) Layer composition of BAS-TR image plate, as employed in this thesis. (b) Atomic energy level diagram of the processes occurring during the exposure of the image plate to the ionising radiation source, and subsequently during the scanning process.

typically larger than this due to bloom effects. These photons cause the electrons to decay from their metastable state and recombine with their 'parent' ions. This decay process results in the emission of a 390 nm wavelength photon, which is in turn detected by a photomultiplier tube (PMT) and amplified. This process is illustrated in Fig. 3.17 (b).

The digital image formed from the photostimulated luminescence (PSL) is in the form of a 16-bit grey scale image. It is therefore necessary to convert this signal back into a physical PSL value. This conversion is performed using the formula

$$\mathrm{PSL} = \left(\frac{R}{100}\right)^2 \left(\frac{4000}{S}\right) 10^{L[G/(2^B-1)-1/2]} \tag{3.14}$$

In this equation, R is the scanner resolution, S is the sensitivity setting, L is the latitude, G is the greyscale value of the raw image and B is the dynamic range. The number of photons detected is a more useful unit for comparison with analytical and numerical data and so a further conversion must be made to extract the number of x-ray photons incident on the IP. The response of various types of IP to radiation has been extensively studied, for a wide range of incident photon energies and fluxes. In one such study, line emission from a variety of atomic sources were used, producing a calibration curve of PSL per photon as a function of photon energy [133]. As one of the atomic sources employed was a copper K-shell transition, an accurate conversion for the determination of the yield of copper K_α photons may be made, as used in Chapter 5.

3.6 Particle-in-Cell simulations

In order to fully understand the physics of laser-plasma interactions and to accurately explain the experimental observations, ideally a complete and self-consistent description of the plasma dynamics would be produced. This however is simply impossible, owing to the large number of particles involved (typically around $10^{27}\mathrm{m}^{-3}$ for a solid density target), and the collective behaviour resulting from the electromagnetic fields generated by the moving charged particles. As such, a kinetic description of the plasma is often employed, where a distribution function $f_s(\mathbf{r}, \mathbf{p}, t)$ describes the probability of finding the particles within a discrete region of the position-velocity phase space at a given point in time. The evolution of this distribution, where the contribution of collisions can be ignored (i.e. when the plasma frequency is much greater than the collision frequency), is given by the Vlasov equation [134], as follows

$$\frac{\partial f_s}{\partial t} + \mathbf{v} \cdot \nabla f_s + \frac{q}{m} (\mathbf{E} + \mathbf{v} \times \mathbf{B}) \cdot \frac{\partial f_s}{\partial \mathbf{p}} = 0 \tag{3.15}$$

Solving this distribution remains computationally intensive due to the high dimensionality (three position and three velocity components), and for typical simulation setups, where a large portion of the area is vacuum or low density plasma, much of the available computational resource is unnecessarily spent on these areas.

Particle-in-cell (PIC) codes provide a solution to this issue by converting the distribution function into finite elements referred to as macro-particles [135]. A single macro-particle acts as an ensemble of many real particles, the motion of which is dictated by the Lorentz force. The properties of the macro-particle (charge-to-mass ratio for example) are defined to be the same as the constituent particles, thus ensuring the behaviour when subjected to external fields is well approximated. Due to the inherent lack of collisions resulting from the use of the Vlasov equation without a collision function in PIC, macro-particles are collisionless and can therefore occupy the same space without perturbation. The motion

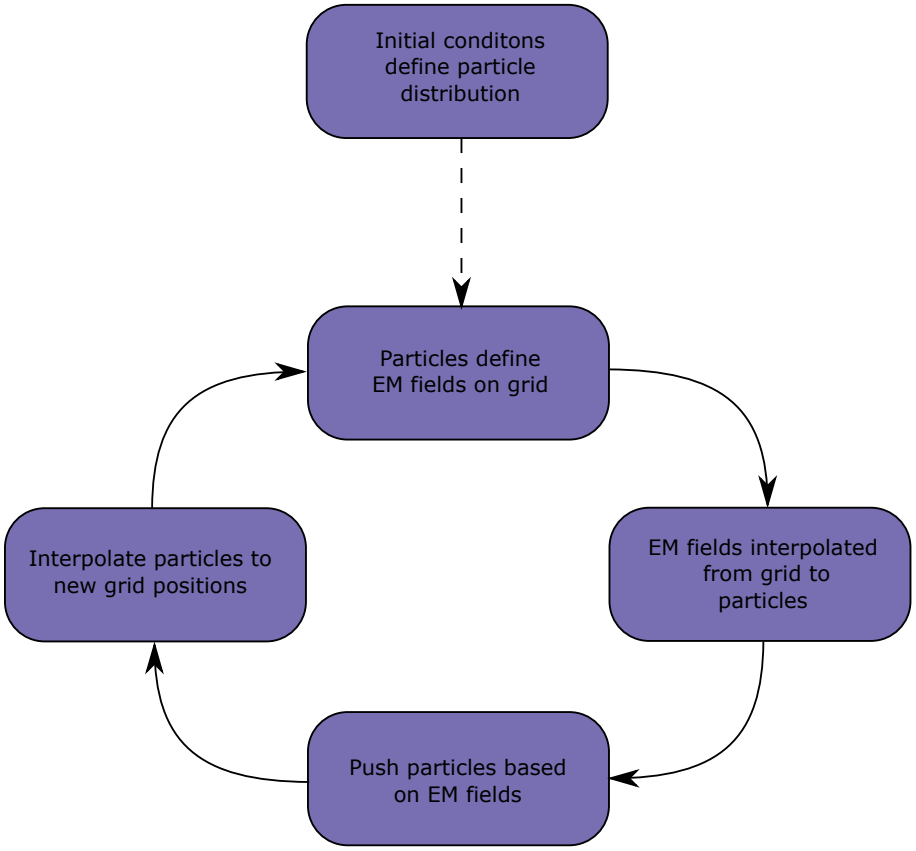

Figure 3.18: Illustration of the steps of the PIC simulation approach. Initially, the particle distribution is determined from the defined initial condition, shown at the top, which is then fed into the loop, where the particles and fields are calculated alternately and interpolated onto a grid.

of the macro-particles and the associated electromagnetic fields are described with the following equations

$$\frac{d\mathbf{r}}{dt} = \mathbf{p} \tag{3.16}$$

$$\frac{d\mathbf{u}}{dt} = \frac{q}{m}\left(\mathbf{E} + \mathbf{v} \times \mathbf{B}\right) \tag{3.17}$$

$$\frac{\partial \mathbf{B}}{\partial t} = -\nabla \times \mathbf{E} \tag{3.18}$$

$$\frac{\partial \mathbf{E}}{\partial t} = c^2 \nabla \times \mathbf{B} - \frac{\mathbf{j}}{\epsilon_0} \tag{3.19}$$

where $\mathbf{u} = \gamma \mathbf{v}$ and $\mathbf{j}$ is the current density. Provided that the condition $\nabla \cdot \mathbf{B} = 0$ is met at the initiation of the simulation, it will remain satisfied throughout and so is not included in the above set of equations. Similarly, charge will be conserved provided that Gauss' law is satisfied [136].

The electric and magnetic fields are defined on a Yee staggered grid [137]. In order to determine the evolution of the electric and magnetic fields, and thus the evolving particle trajectories, a cyclic process called the Finite Difference Time Domain (FDTD) is used [136, 137]. In the PIC code EPOCH [136], which is used in this thesis, the fields are calculated on both half-integer and integer time-steps, in a modified version of the leap-frog method. First, the electric and magnetic fields are advanced from n to $n + 1/2$ using the current density known at n as follows

$$\frac{\mathbf{E}^{n+1/2} - \mathbf{E}^{n}}{\Delta t/2} = c^2 \nabla \times \mathbf{B}^{n} - \frac{\mathbf{j}^{n}}{\epsilon_0} \tag{3.20}$$

$$\frac{\mathbf{B}^{n+1/2} - \mathbf{B}^{n}}{\Delta t/2} = -\nabla \times \mathbf{E}^{n+1/2} \tag{3.21}$$

where Δt is the time-step size defined by the Courant-Friedrichs-Lewy (CFL) condition. These fields are inserted into the equations of motion, pushing the particles to a new position, enabling the current density to be updated to $\mathbf{j}^{n+1}$. Using this new current density value, the fields are updated to the integer $n + 1$, using

$$\frac{\mathbf{B}^{n+1} - \mathbf{B}^{n+1/2}}{\Delta t/2} = -\nabla \times \mathbf{E}^{n+1/2} \tag{3.22}$$

$$\frac{\mathbf{E}^{n+1} - \mathbf{E}^{n+1/2}}{\Delta t/2} = c^2 \nabla \times \mathbf{B}^{n+1} - \frac{\mathbf{j}^{n+1}}{\epsilon_0} \tag{3.23}$$

The resulting particle positions are interpolated onto a grid, with the particle weight defining the fraction of a macro-particle located at a given grid position. The flux of macro-particles determines the current density, allowing the process to repeat iteratively, as illustrated in Fig. 3.18. This FDTD method enables all fields to be defined simultaneously, on the same time-step, whilst also obtaining the half-integer values required for the particle pusher.

PIC simulations are a powerful tool for investigating laser-plasma interactions, however there are a number of potential pit falls which must be avoided and limitations which must be considered. A selection of the most commonly encountered of these will be discussed here. Firstly, the issue of spatial resolution must be discussed. If the spatial resolution of the simulation is insufficient to re-

solve the Debye length (see chapter 2.4.1), numerical heating will occur [135, 138]. This is an artificial heating of the plasma until the Debye length can be resolved, resulting from the electric fields being aliased over multiple adjacent cells. In addition to spatial resolution, it is vital that the simulation has sufficient temporal resolution to resolve the highest frequencies in the system. In laser-plasma interactions, the plasma frequency of the electrons $\omega_{p,e}$ is of utmost importance to the plasma dynamics, and as such it is imperative to ensure that the condition $\Delta t \leq \omega_{p,e}^{-1}$ is met at all times. In simulations of interactions involving strong magnetic fields, one must also ensure that the cyclotron frequency ω_c is resolved, such that $\Delta t \leq \omega_c$. Finally, numerical noise may be introduced by using too few macro-particles per cell. There is no concrete condition for how many particles per cell are necessary, but this can be determined by convergence testing the code (i.e. adding additional particles until a chosen output remains fixed).

PIC simulations are also not without their limitations, even if the above conditions are carefully considered. Due to restrictions on available computational resources, it is often impossible to simultaneously meet the above conditions for spatial and temporal resolution while also simulating a laser-solid interaction fully in 3D. As a result, it is often necessary to simulate the interaction using a lower number of spatial dimensions, for example 2D. Doing so can often have a significant impact on the simulated interaction physics, affecting aspects such as plasma expansion and laser intensity scaling with focal spot size. Another limitation results from the definition of the incident laser pulse, which typically will take the form of a perfect Gaussian (or whichever alternative laser mode is desired). This ignores the often significant effects of ASE and pre-pulses on the interaction, with the effect of such required to be added manually. This results in much 'cleaner' simulated interactions than those observed in experimental studies, which can often lead to differences in the observed interaction physics, for example plasma expansion.

Assuming the above pitfalls are avoided and limitations carefully considered, PIC simulations provide a powerful tool for understanding the often complex dynamics of laser-plasma interactions. PIC approaches are becoming increasingly

common as a means of bridging the gap between theory and experiment, being used by both experimentalists and theoreticians as a means to relate the often complex mathematics of the theory to the experimental observations, which are often limited by the diagnostic technology available. PIC simulations have also become a cornerstone in the explanation and understanding of the experimental data. Often, it is only possible to measure time-averaged behaviour, thus losing crucial information regarding the temporal evolution of the system. Other processes can only be observed indirectly via secondary measurements of the resulting products. PIC simulations can provide insight in both cases, by enabling the interaction to be studied in a time resolved manner, and by enabling any aspect of the interaction to be interrogated, unlimited by the technology available experimentally. Finally, PIC simulations allow for large parameter spaces to be explored with relative speed and ease when compared with an experimental investigation. This is often beneficial in the lead up to an experimental campaign, where a guide on which areas of the parameter space are of greatest interest is often crucial, especially when using low repetition rate laser systems, such as the Vulcan Petawatt laser.

Chapter 4

Laser self-focusing in relativistically transparent, ultra-thin targets

4.1 Introduction

In order to achieve the proton energies and laser-to-proton conversion efficiencies required for societal applications, for example proton oncology [11, 139], various mechanisms for the acceleration of protons have been investigated, using foil targets with thicknesses ranging from tens of microns down to tens of nanometres. Recent measurements of protons accelerated using a transparency-enhanced, hybrid acceleration scheme, have demonstrated that proton energies of up to ~ 100 MeV are achievable [26]. Further improvements in terms of maximum proton energy, along with stability and reproducibility, are still required however, before this scheme is viable for practical applications. To this end, we further explore this transparency-enhanced regime, pushing the nominal peak intensity beyond 10^{21} Wcm^{-2} through the use of near wavelength sized focal spots. The acceleration mechanisms which contribute to this transparency-enhanced hybrid regime are discussed in detail in chapter 2.7, but will be briefly reviewed here for convenience.

The first, and most widely studied mechanism for the acceleration of high

energy ions is the TNSA scheme [74]. In this mechanism, a strong electrostatic field, of the order of TV m^{-1} in strength, is formed at the rear surface of the target, sourced by the current of fast electrons generated by the laser at the front surface. The proton energies achievable through the TNSA scheme are predicted to scale favourably with increasing laser intensity [80], due to the increase in fast electron temperature [28, 48]. Proton energies in excess of 85 MeV have been reported by exploiting this mechanism [140].

Another mechanism, RPA, has also been explored, where the radiation pressure exerted by the incident laser pulse can be exploited to accelerate ions from the front side of the target [57, 86]. RPA benefits from the suppression of electron heating, achieved by 'switching off' $\mathbf{j}\times\mathbf{B}$ heating (see Chapter 2.5.3) through the use of circular polarised laser pulses [57, 88], with proton energies predicted to scale favourably with increasing laser intensity (more quickly than TNSA). The RPA scheme has shown promise for producing high energy protons [141] and peaked, quasi-monoenergetic proton energy spectra [95]. Theoretical and numerical studies of a hybrid mechanism involving RPA and shielded Coulomb repulsion (SCR) have also shown the possibility of efficiently generating energetic protons for moderate power laser systems (hundreds of TW), using circular polarised pulses [142]. If circular polarisation is not used however, and instead some linearly polarised state is employed, a dual-peaked acceleration field can be formed due to the interplay of the fields generated by the RPA mechanism at the front surface and the TNSA mechanism at the rear [104]. Such a dual-peaked field structure was predicted to create a TNSA-RPA hybrid ion acceleration scheme [105], and this scheme is inferred in the results reported in Higginson *et al.* [26].

Ion acceleration from ultra-thin foil targets, being irradiated with higher intensity pulses ($I_L > 10^{20}$ Wcm^{-2}) must also consider the effects of the onset of RSIT during the interaction [143], i.e. where the target transitions from being opaque to the incident laser pulse to transparent as a result of a combination of relativistic effects and target expansion (see Chapter 2.4.4). As a result of this phenomenon, a fraction of the laser pulse will be transmitted through the target, with the size of this fraction depending on how early/late the onset of

transparency occurs [70]. It has been shown that the transparency time may be diagnosed by spectral analysis of the transmitted light [144]. The transmission of laser light through the target will strongly effect both the laser pulse itself and the accelerated proton population, through the induced electron dynamics. Short, high contrast pulses will form a relativistic plasma aperture as the target undergoes RSIT, resulting in the formation of a diffraction pattern in the transmitted laser light [145], and the generation of higher order modes when the combination of transmitted and generated light is carefully tuned [146]. The modulation of the electrostatic acceleration field resulting from the diffraction of the laser pulse acts to perturb the spatial distribution of the accelerated proton beam [147]. Furthermore, the onset of transparency results in a transition from surface to volumetric heating [99], which has been shown to enhance the energy of TNSA-generated ions [98]. In addition to the volumetric absorption, a linear polarised laser pulse with a pulse duration of hundreds of femtoseconds or a picosecond will form a plasma jet at the rear of the target after the onset of transparency [106]. This dense jet of highly energetic electrons will locally boost the energy of the accelerated protons [148]. In some cases, namely the BOA acceleration scheme [100], streaming instabilities are also observed numerically following the onset of transparency, and are cited as a means of energy transfer between the heated electron population and the ions [102, 149]. The combined effects of transparency also act to enhance the aforementioned TNSA-RPA hybrid acceleration scheme, where the onset of transparency interrupts the RPA phase of the acceleration, but results in increased proton energies due to the effects of the volumetric heating and plasma jet formation. Such an enhancement was presented in Higginson *et al.* [26], and was found to result in high laser-to-proton conversion efficiencies and maximum proton energies of up to ~ 100 MeV.

Given that the transparency enhanced, TNSA-RPA hybrid acceleration scheme has been shown to result in high maximum proton energies and laser-to-proton conversion efficiencies [26], further exploration of this mechanism to expand our understanding of the underpinning physics is of great importance. As mentioned previously (and in Chapter 2.7), proton energies achieved using both of the con-

stituent acceleration mechanisms are predicted to scale favourably with increasing laser intensity. Furthermore, next-generation, multi-petawatt laser facilities are coming online [85], yielding focused intensities of up to 10^{23} Wcm^{-2}. At such intensities, solid-density foils will be quickly rendered transparent to the incident laser pulse. It is therefore likely that future studies of ion acceleration, focusing on achieving high proton energies, will rely heavily on the physics of RSIT, and as such, achieving an understanding of the transparency enhanced, hybrid mechanism at higher intensities is vital. Achieving focused intensities of 10^{23} Wcm^{-2} is beyond the scope of current laser technology when employing a picosecond pulse, high energy laser system such as Vulcan (see chapter 3.3), as is required for the hybrid acceleration scheme. It is however possible to boost the focused intensity of the Vulcan laser through the employment of a tight focusing scheme, enabling peak on-target intensities of up to 5×10^{21} Wcm^{-2} to be obtained. This is achieved through the use of ellipsoidal, focusing plasma mirrors [126, 127], as discussed in detail in chapter 3.4.2.

This chapter reports on an experimental and numerical investigation of proton acceleration from ultra-thin foils irradiated by ultra-high intensity laser pulses (up to $I_L = 5 \times 10^{21}$ Wcm^{-2}), focused to a near-wavelength sized focal spot. Ref. [150] directly results from the work presented in this chapter.

4.2 Review of relevant literature

Proton acceleration via the mechanisms of TNSA, RPA and transparency enhanced schemes have been subject to extensive experimental investigation. Only a small fraction of this research has been performed using tight-focusing schemes (below F/3) however, with these primarily directed towards the understanding of the TNSA mechanism. Furthermore, much of the research undertaken has been performed for peak laser intensities of $\ll 10^{21}$ Wcm^{-2}. In this chapter, we set out to study the role of a near-wavelength focal spot on proton acceleration in a transparency-enhanced, TNSA-RPA hybrid acceleration scheme. It is therefore imperative that the findings relevant to the scaling of proton energies with

intensity, driven by a changing focal spot size, are briefly reviewed.

Early studies of the scaling of proton parameters with laser intensity, in the TNSA regime, demonstrate that the scalings vary depending on the particular laser parameter used to alter the intensity (i.e. laser energy, pulse duration or focal spot size) [83, 151]. These studies were however conducted for fixed focal spot size, and so it was highlighted that additional research would be required to isolate the spot size effects from the intensity scaling [151]. The effect of focusing geometry on the scalings of maximum proton energy and flux with intensity were subsequently investigated in Brenner *et al.* [152], wherein the scaling with intensity, driven by focal spot size and laser energy, were examined separately. A different scaling was observed depending on whether the focal spot or the laser energy was used to vary the intensity, with higher maximum proton energies and laser-to-proton conversion efficiencies measured for the larger focal spot case. This was attributed to the larger focal spot resulting in a larger proton emission area at the rear surface of the target, thus boosting the measured proton flux. Similar results were reported in Green *et al.* [153] and Passoni *et al.* [154]. These findings were explained in a subsequent study reported in Coury *et al.* [155], where the maximum proton energies were again measured to be higher when a larger focal spot was employed, compared with a relatively smaller spot (spot sizes in the range $4 < \phi_L < 40$ μm). This was attributed to spot size driven changes to the injection of fast electrons within the target, in turn resulting in alterations to the electron distribution in the sheath formed at the target rear. Similar results pertaining to the influence of focal spot size and electron injection were shown in Schreiber *et al.* [82]. As a consequence of these studies, the importance of the laser focal spot, beyond simply a means of varying the intensity, not just on the accelerated protons, but also on the fast electron population within the target, was highlighted. This emphasises the importance of considering the influence of focal spot size effects, not just in the scope of the TNSA mechanism, but more broadly within laser-solid interactions.

All of the above investigations were performed using relatively large focal spots, of the order of tens of microns, to a minimum of ~ 5 μm, as the spot

size was scaled by defocusing the smallest spot deliverable by the particular OAP i.e. by introducing a spatial offset between the target and the focal plane of the laser. In this chapter, a tight focusing scheme, yielding near-wavelength sized focal spots, is of primary interest. Studies employing tight-focusing schemes are very limited, although this is increasing rapidly as small F-number focusing optics become more widely used due to their capacity to significantly enhance the peak laser intensity. Research employing tight focusing schemes is still however heavily focused on the TNSA mechanism, with relatively little investigating the effects on RPA or transparency enhanced schemes.

Studies of TNSA extending to high intensities (i.e. $> 10^{21}$ Wcm^{-2}) have shown that the scaling of maximum achievable proton energies may slow as a function of intensity, relative to the conventional scaling of $I_L^{1/2}$ (see Chapter 2.7.1). In an experimental and numerical study reported in Nakatsutsumi *et al.* [156], where the scaling of proton energy with intensity is investigated (the highest intensities are achieved through F/1 focusing), it is suggested that a fundamental limit on the maximum achievable energies of protons accelerated via TNSA may exist for high intensity interactions. This is attributed to self-generated magnetic fields which build up at the rear surface of the target and act to limit sheath-driven acceleration processes by magnetising the sheath electrons and thus deflecting protons away from the acceleration region. A similar slowing in the scaling of proton energy with peak intensity is observed in the experimental study presented in Ref. [128], although magnetic fields are not invoked in the explanation. In this work, a spot size induced change in the injection cone of the fast electron population, similar to that discussed in Coury *et al.* [155], is discussed, with this change influencing the spatial profile of the accelerating sheath field at the target rear. An additional explanation for such behaviour is discussed in this thesis, in Chapter 5, where an electron temperature scaling of the form reported in Haines *et al.* [48] is found to fit the slower scaling of maximum proton energies with intensity when applied to the energy scaling reported in Ref. [80]. Finally, a recent study reported in Dover *et al.* [35], using a short pulse laser system ($\tau_L \sim 40$ fs), agreed with the concept of this scaling resulting from a slower

electron temperature scaling, but suggested that the source of this slowing could be a spatial restriction to the heating of fast electrons due to the combination of high laser intensity and small focal spot size. This is discussed in more detail in Chapter 5. If intensities were to be pushed beyond the limits currently achievable, different physics would begin to have more of an important influence on ion acceleration via the TNSA mechanism, for example the generation of synchrotron radiation [157] and radiation reaction [158], which would alter the absorption of laser energy, and the partitioning of that energy, within the target.

In terms of the RPA mechanism, an experimental study employing an F/1 OAP, reported in Dollar *et al.* [91], showed that RPA is de-optimised when employing an extremely tight focusing geometry. Rapid deformation of the target surface results in enhanced heating of the plasma electrons, even when using circularly polarised laser pulses, due to the alteration in absorption dynamics. This acts to boost the generation of sheath fields, as required by TNSA, but at the expense of reducing the drive efficiency of the laser pulse required for RPA to effectively accelerate protons to high kinetic energies.

We have reviewed the prior work investigating the influence of 1) focal spot size in general and 2) extremely tight focusing schemes, on laser driven ion acceleration in the TNSA and RPA regimes. There have been, however, no studies of this effect in the transparency-enhanced, TNSA-RPA hybrid scheme reported in Higginson *et al.* [26]. This motivates the further investigation of this regime through the employment of a tight focusing scheme, as it has shown great promise for efficiently generating protons with energies of ~ 100 MeV.

4.3 Experimental method

The experimental investigation presented in this chapter uses the Vulcan Petawatt laser, described in Chapter 3.3, located at the Rutherford Appleton laboratory, U.K. The specific laser parameters and diagnostics employed are reviewed here before proceeding to discuss the experimental measurements and analysis.

Pulses of p-polarised light of central wavelength 1054 nm were delivered with

pulse durations of $\tau_L = (0.9 \pm 0.1)$ ps and on-target energies of $E_L = (220 \pm 50)$ J. A F/3.1 OAP was used to focus the light to a nominal spot size of $\phi_L = (4.5 \pm 0.9)$ μm (FWHM), with a PPM placed in the focusing beam to improve the temporal intensity contrast of the pulse (see chapter 3.11), as illustrated in Fig. 4.1 (a). The fraction of the laser energy contained within this FWHM region, henceforth referred to as the fractional encircled energy, f_{EE}, was measured by imaging the focal spot at low laser power using a CCD camera and microscope objective (thus avoiding laser damage), and was measured as $f_{EE} = (37 \pm 3)\,\%$. The encircled energy measured at low power was corrected to account for any wavefront aberrations measured on the corresponding full power shot using the same plasma mirror, as diagnosed by a wavefront sensor [113] (see chapter 3.4). An example focal spot, measured at low power, showing the spatial size and the encircled energy, is presented in Fig. 4.2 (a). These pulse parameters result in nominal on-target intensities of $I_L = (3 \pm 2) \times 10^{20}$ Wcm^{-2}. The measured temporal intensity contrast ratio of the delivered pulses was 10^{-10} at 500 ps and 10^{-5} at 10 ps prior to the peak of the pulse. This includes the enhancement due to the use of a single plasma mirror, which enhances the contrast ratio by approximately two orders of magnitude. As both plasma mirror forms employed were manufactured from the same material and had the same anti-reflection coating, the contrast enhancement is the same in both cases. These conditions are very similar to those in prior work from our group, reported in Higginson *et al.* [26], which is used throughout this chapter as the benchmark for the F/3.1 focusing configuration.

A second configuration, in which the PPM was replaced by an ellipsoidal FPM (see Chapter 3.4.2 for details), was employed to achieve F/1 focusing [126, 127], as shown in Fig. 4.1 (b). This optic re-images the F/3.1 focal spot with a demagnification of up to $\times 3$, resulting in focal spot sizes of $\phi_L = (1.6 \pm 0.2)$ μm FWHM, resulting in nominal intensities of $I_L = (1.5 \pm 0.8) \times 10^{21}$ Wcm^{-2}. Despite both plasma mirror geometries having the same plasma reflectivity, the nominal intensity is less than the theoretical maximum enhancement factor of $\times 9$. This is due to a reduction in focal spot encircled energy when employing the FPM, with the fractional encircled energy measured to be $f_{EE} = (27 \pm 4)\,\%$, represent-

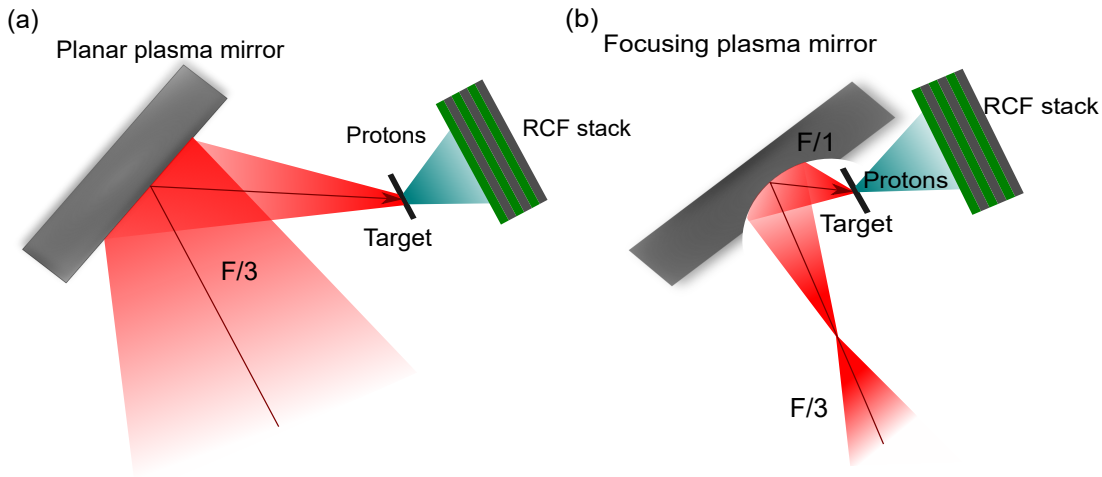

Figure 4.1: Illustration of the two focusing configurations employed in the experimental studies presented in this chapter, using a planar plasma mirror (F/3) (a) and a focusing plasma mirror (F/1) (b).

ing a reduction of factor ~ 0.27 when compared with the PPM configuration. This reduction in encircled energy when employing the FPM arises due to the increased sensitivity to small shot-to-shot variations in laser pointing and focal position, as detailed in Chapter 3.4.2 and explored in the works by Wilson *et al.* [126, 127], which have a greatly increased impact relative to the conventional F/3.1 OAP focusing method. Furthermore, as the focal spot size approaches the diffraction limit, wavefront aberrations which had less of an effect on the F/3.1 focusing will become more dominant. Both of these effects will change the energy balance between the central FWHM of the focal spot and the surrounding, lower-intensity wings, resulting in a reduction in the encircled energy. The first of these effects is specific to the focusing plasma mirror approach. The effect of wavefront aberrations as the diffraction limit is approached is, however, applicable to all tight focusing schemes, and so the effect of encircled energy reduction must be considered regardless of the focusing methodology.

Plastic foil targets were employed with a range of thicknesses, between $\ell = 60$ nm and $\ell = 1.5$ μm, and were irradiated at $(27 \pm 3)^\circ$ with respect to the target normal, as in Higginson *et al.* [26]. The targets were positioned using a magnifying microscope objective imaging system, with an alignment reference laser of the same central wavelength as the Vulcan main beam. This target

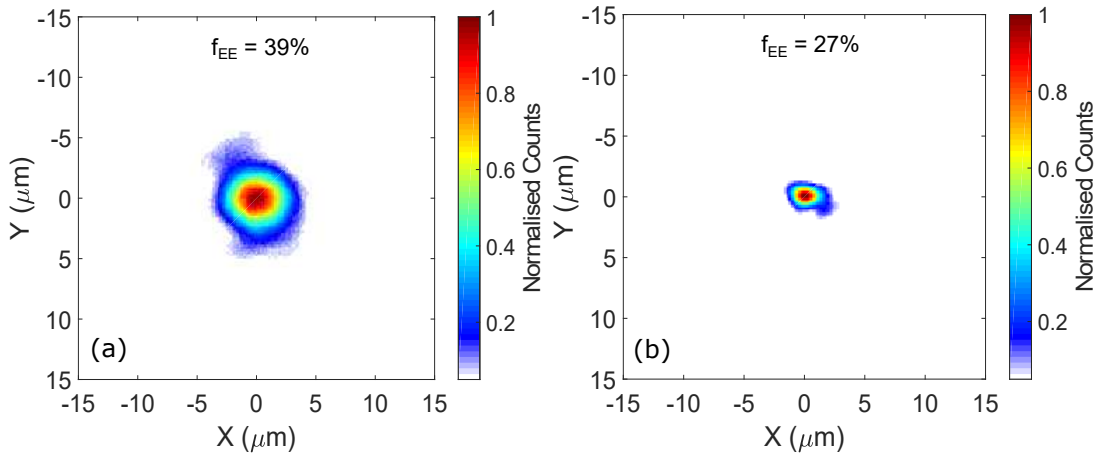

Figure 4.2: Example focal spot spatial intensity distributions for the PPM (F/3) (a) and FPM (F/1) (b) focusing configurations, measured using the Vulcan laser, operating in a low power, CW mode. The measured fractional encircled energy is given for each case.

placement system has a calibrated accuracy of 1.6 μm due to the depth of focus of the objective, which is well within the Rayleigh range of both focusing geometries ($\sim$ 5 μm for the F/1 configuration), and results in an uncertainty in the peak on-target intensity of $\pm$10%. The spatial and spectral dose distributions of the accelerated proton beam were measured using stacked RCF (see Chapter 3.5.1 and Nürnberg *et al.* [159]), interspersed with Mylar, iron and copper filters. The stack was positioned 45 mm from the rear surface of the target and orientated such that protons accelerated along both the laser and target normal axes were measured. The spectrum of the light back-reflected from the target along the laser propagation axis, comprising both reflected laser light and generated harmonics, was also measured to enable determination of the plasma holeboring velocity v_{hb}, using the approach outlined in Chapter 3.5.2.

4.4 Experimental Results and Analysis

This section summarises the experimental measurements made using the FPM (near-wavelength sized focal spots), and makes comparison with the measurements reported in Higginson *et al.* [26], using a more conventional PPM focusing scheme (larger focal spot). Throughout this section, scans in target thickness are discussed, ensuring only data with comparable peak nominal intensities are com-

pared within each dataset (i.e. F/3 and F/1). Discussion will focus on notable variations between the PPM and FPM configurations in three proton beam parameters, namely the maximum proton energy, the proton energy spectra and the laser-to-proton energy conversion efficiency. Additionally, changes in the holeboring velocity of the target critical surface are explored.

4.4.1 Maximum proton energy scaling with target thickness

As discussed in the introduction, section 4.1, laser-driven proton sources have the potential to fulfil a range of applications, but require enhanced maximum kinetic energies before doing so. Proton energy scaling relations for both the TNSA and RPA acceleration mechanisms predict an increase in maximum proton energy with increasing laser intensity [80, 87]. It is therefore not unreasonable to think that a hybrid TNSA-RPA mechanism, which has already been shown to yield proton energies of $\sim$ 100 MeV [26], may generate even higher proton energies if the laser intensity were to be increased. As explored in Chapter 3.4.2, one approach for achieving such an intensity enhancement is through the employment of a tight focusing scheme, reducing the focal spot size. The consequences of such an approach have not previously been studied for a transparency-enhanced, TNSA-RPA hybrid acceleration scheme, and given the current potential for such a scheme to yield record proton energies, it would seem appropriate that this be explored in some depth.

Before proceeding to discuss the maximum proton energies achieved by employing the F/1 experimental configuration, we must first consider the maximum proton energies measured using the conventional PPM setup. These are presented in blue in Fig. 4.3. It can be seen that the proton energies increase rapidly with increasing target thickness, ℓ, up to a peak value of $\epsilon_{max} = 94 - 101$ MeV for a thickness of $\ell = 90$ nm. The uncertainty on this measurement results from the energy resolution of the RCF stack employed. Strong proton signal was observed on the RCF layer corresponding to 94 MeV protons, with no measurable signal

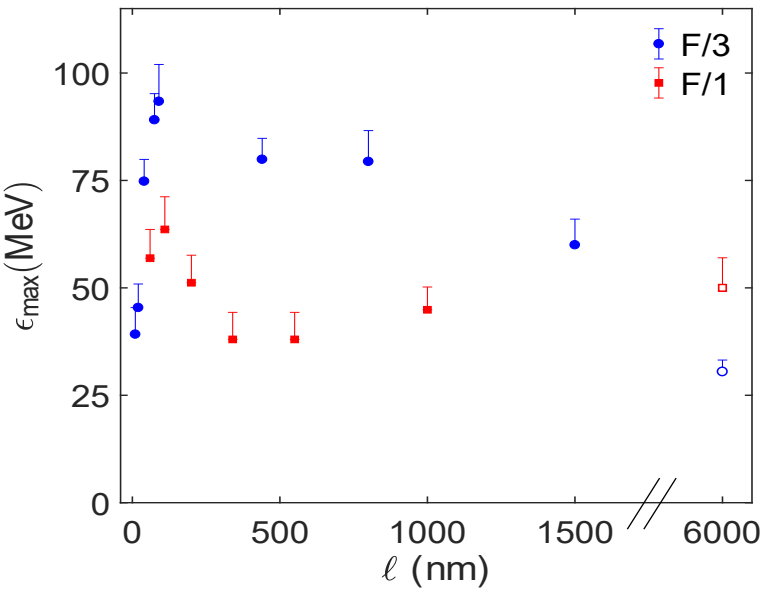

Figure 4.3: Maximum proton energy as a function of target thickness for the F/3 and F/1 focusing configurations, shown in blue and red respectively. Hollow points represent 6 μm thick Al targets, used as a benchmark in a regime where the target remains opaque for the full duration of the interaction. Each data point represents a single interaction.

on the 101 MeV layer, thus defining the possible range of maximum proton energies. After this peak, the proton energies decrease slowly with increasing target thickness. The key factor dictating the target thickness for which this peak occurs is the transparency time, i.e. the time during the pulse at which the target undergoes RSIT [26]. If this occurs too early, as is the case for target thicknesses less than 90 nm, then the RPA phase of the acceleration cannot take place and the target expansion becomes significant. If transparency occurs too late in the interaction, as for the thicker targets, then the enhancement to the maximum proton energy, driven by the volumetric heating of the target or the formation of an electron jet, is negligible in magnitude.

The maximum proton energies measured using the F/1 configuration are shown in red in Fig. 4.3. Before a thickness scan investigating the hybrid acceleration mechanism was undertaken, multiple test shots using 6 μm thick aluminium foils were conducted for both the F/3 and F/1 configurations as a benchmark, with one example of the measured maximum proton energies in each case shown by the hollow data-points. In this thick target case, where proton acceleration will proceed via the TNSA mechanism, the F/1 case yields enhanced proton en-

ergies ($\epsilon_{max} \sim 50$ MeV) relative to the F/3 case ($\epsilon_{max} \sim 30$ MeV). This would be expected from the proton energy scaling relations with intensity reported in Mora [80], and is in agreement with previous experimental studies of proton acceleration in the TNSA regime employing tight focusing schemes such as the FPM [126, 127, 128]. The agreement with previous experimental measurements and predicted scaling relations in the TNSA regime gives additional confidence that the FPM optics are behaving as expected, in particular that the intensity enhancement due to the tighter focusing is indeed being achieved.

When we move to lower target thicknesses ($\ell \leq 1$ μm), into the range where proton acceleration will proceed via the hybrid mechanism, potentially aided by the onset of transparency, the proton energies measured using the FPM setup are universally lower than those observed when a lower intensity, looser focus is employed. It can be seen that for lower target thicknesses, the proton energy increases to a peak occurring at the same target thickness (i.e. $\ell = 90$ nm) as the PPM case, but now with a lower measured maximum energy of $\epsilon_{max} = 64 - 72$ MeV. This represents a decrease in maximum proton energy of $31 \pm 6\%$. The uncertainty in this measurement again results from the spectral resolution of the RCF stack design employed. For target thicknesses greater than this peak location, the proton energies drop off before beginning to rise again for thicknesses of $\ell > 500$ nm. Target thicknesses greater than 500 nm will likely not undergo transparency, or will undergo transparency very late in the pulse, and so a transition to a TNSA dominated acceleration scheme is likely to occur. It is therefore clear that the underpinning physical process driving the decrease in proton energy in the FPM case, or alternatively boosting the proton energies in the PPM case, is reliant on the target undergoing RSIT at a point sufficiently early in the interaction (near the peak of the pulse).

4.4.2 Proton energy spectra and laser-to-proton conversion efficiency

Given that the maximum proton energies discussed in the previous section show clear distinctions between the F/3 and F/1 focusing schemes, it is important that the spectral properties of the proton beam in each case are investigated more thoroughly. The first step in this process is to examine the proton energy spectra, as understanding the energy distribution of the accelerated protons, as opposed to simply the maximum recorded energy, is often useful in understanding the underpinning interaction physics. Measurement of the energy spectra is also essential if the laser-to-proton energy conversion efficiency is to be determined (as discussed in the next section), which is a key parameter for many of the envisioned applications of laser-driven proton sources, as discussed in the introduction (see section 4.1).

Example proton energy spectra, sampled between 3.9 MeV and the maximum measured proton energy, for a range of target thicknesses, are shown for the two focusing configurations in Fig. 4.4. The F/3 spectra are shown with the solid lines, and the F/1 spectra are shown with the dashed lines. The vertical error-bars in the presented data are defined by the uncertainty in the detected proton dose N_p based on the RCF dose calibration (as briefly discussed in Chapter 3.5.1). The number of protons produced at the lowest energy (i.e. 3.9 MeV) is approximately equal in all cases with a value of $N_p \sim 2 \times 10^{12}$ protons per MeV per steradian, regardless of focusing geometry or target thickness. This continues to be true, i.e. the number of protons is approximately the same regardless of focusing geometry or target thickness, up to proton energies of $\epsilon_p \sim 30$ MeV. Beyond this energy however, we see the spectra diverge, with the F/1 spectra not only showing lower maximum energies, but also lower proton numbers when compared with a F/3 case of similar target thickness.

The effect of the lower proton numbers in the higher energy region of the spectra, combined with the lower maximum energy of the spectra, is clearly seen when considering the laser-to-proton energy conversion efficiency, which as a parame-

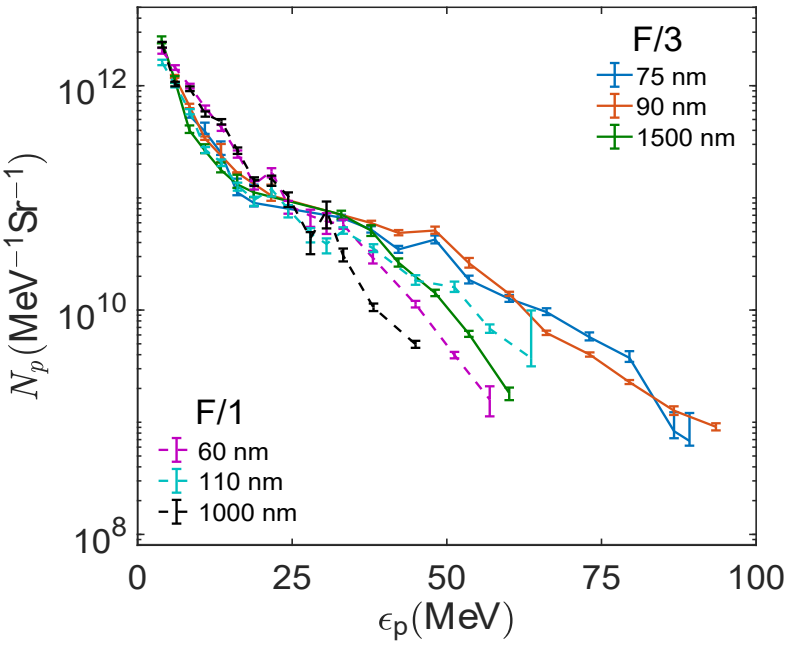

Figure 4.4: Proton energy spectra, i.e. number of protons per MeV per unit solid angle as a function of proton energy, for a range of target thicknesses for both F/3 and F/1 focusing schemes, shown by the solid and dashed lines, respectively.

ter is often just as important as the maximum proton energies when considering potential applications of laser-driven ion sources. The conversion efficiency, η_p, for both focusing cases, is shown in Fig. 4.5, with the F/3 data displayed in blue and the F/1 in red. The conversion efficiency is determined by summing across the full proton energy spectra, and normalising to the incident total laser energy on target, as discussed in Chapter 3.5.1, with the error-bars originating from the uncertainties in the proton numbers of the energy spectra. The energy on target was used as opposed to the encircled energy for two main reasons. Firstly, this enabled direct comparison of the F/1 data with F/3 results published in Higginson *et al.* [26]. Secondly, in a manuscript currently accepted but not yet published by Wilson *et al.* [160], the contribution of the laser energy not contained within the FWHM of the focal spot to proton numbers, and thus laser-to-proton energy conversion efficiency, is shown. This is of particular importance in the F/1 focusing case, where the higher peak intensity results in relativistically intense laser light outwith the FWHM of the focal spot. This is shown, in the TNSA regime, to result in a boosted conversion efficiency. It is therefore necessary to consider

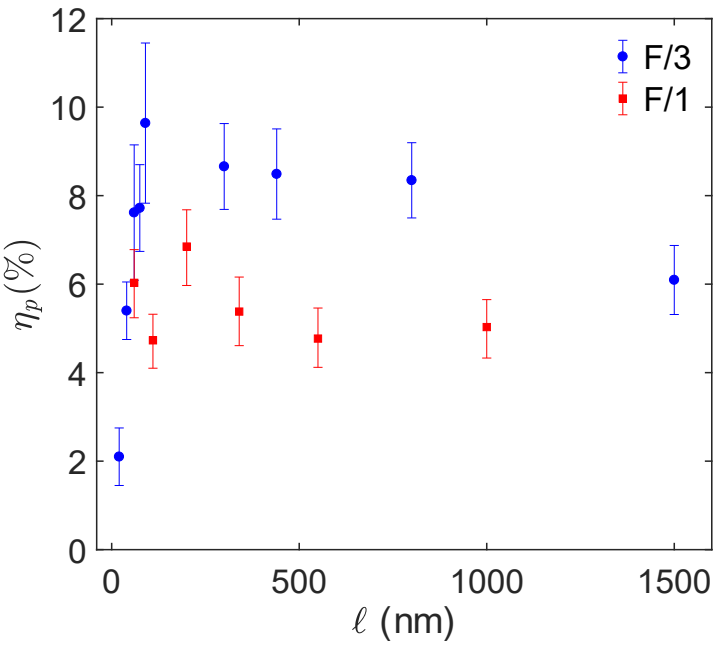

Figure 4.5: Laser-to-proton energy conversion efficiency as a function of target thickness, for both F/3 and F/1 focusing configurations, shown in blue and red respectively.

all laser energy incident on the target in order to gain accurate insight into the interaction dynamics for these high intensities.

For F/3 focusing, we see a similar trend to the maximum proton energy data, i.e. a rapid increase in η_p with increasing target thickness up to a peak value of $\sim 10\%$, occurring for a target thickness of $\ell = 90$ nm, before slowly decreasing as the thickness is further increased. Again, similar to the maximum proton energies, we see the F/1 configuration yielding lower conversion efficiencies across the range of target thicknesses where a hybrid, RSIT supported ion acceleration mechanism dominates, but tending to converge/cross-over with the F/3 data for thicker targets, where TNSA is the dominant mechanism. When comparing the measured conversion efficiency values for target thicknesses around the peak in the F/3 data, we see a reduction factor of $40 \pm 10\%$ when employing F/1 focusing. The largest relative difference in conversion efficiency occurs for $\ell \sim 90$ nm, with the difference decreasing for thicknesses greater or less than this. This would indicate that, similar to the conclusion drawn from the maximum proton energy data, the onset of transparency is the key to the physics underpinning the changes in laser-to-proton energy conversion efficiency.

4.4.3 Holeboring velocity

Given the significantly different proton beam properties observed in the previous sections, in terms of maximum energy, spectral shape, and laser-to-proton energy conversion efficiency, it is clear that the underpinning physics of the interaction, as the target undergoes transparency, has changed when switching from the F/3 to F/1 focusing geometries. In order to further investigate the plasma dynamics, the spectrum of light backscattered up the laser chain was measured (including both reflected laser light and generated harmonics), using the setup discussed in chapter 3.5.2. This allows for determination of the peak recession velocity of the plasma critical surface (holeboring velocity v_{hb}, see Chapter 2.7.2) by measuring the maximum red-shift in the wavelength of the second harmonic light [161]. This light is generated by the critical surface moving under the influence of the radiation pressure of the incident laser light [162].

The measured holeboring velocity, normalised to the speed of light in vacuum, c, is presented in Fig. 4.6, with the F/3 data again shown in blue and the F/1 data shown in red. The wavelength shift used to determine the peak holeboring velocity was the difference between the nominal location of the 2ω signal (i.e. $\lambda_{2\omega} = 527$ nm) and the maximum wavelength for which the measured signal remained distinguishable above the background level. The uncertainties in the presented data reflect the margin of error in determining this peak wavelength. In the F/3 focusing case, the holeboring velocity peaks at $0.09c$ for a target thickness of $\ell = 90$ nm, the same thickness as the peaks in both maximum proton energy and laser-to-proton energy conversion efficiency. Below this thickness, the holeboring velocity falls off rapidly, as would be expected, due to the target undergoing RSIT early in the interaction, prior to the arrival of the peak of the laser pulse [26]. For F/1 focusing, as with the proton measurements reported previously, the holeboring velocity is once again lower across the full range of target thicknesses, with the possible exception of $\ell = 60$ nm, where due to the steep gradient, it could be argued that the value of v_{hb} measured in the F/1 case is similar to that expected from the F/3 focusing configuration. As the holeboring

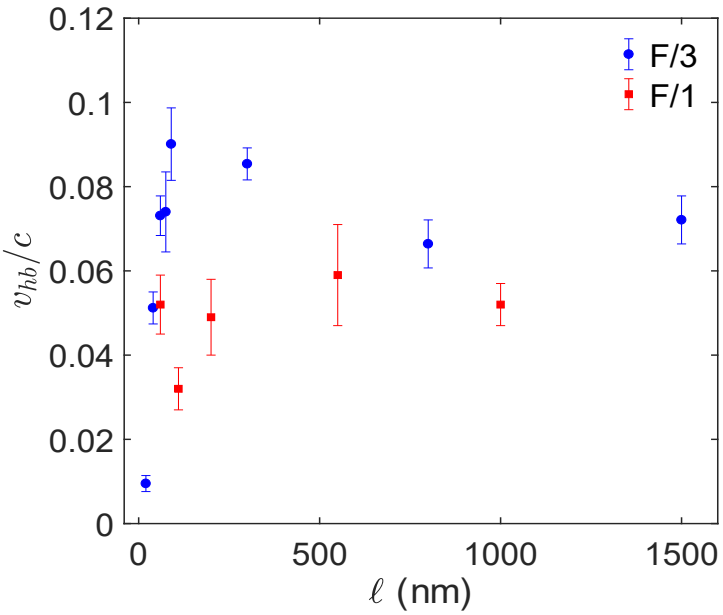

Figure 4.6: Holeboring velocity, normalised to the speed of light in vacuum, c, as a function of target thickness, for both F/3 and F/1 focusing configurations, shown in blue and red respectively.

velocity scales with laser intensity [28, 90], this result potentially points to a higher laser intensity being achieved in the F/3 case compared with the F/1, in spite of the nominally larger focal spot size and comparable laser energy and pulse duration. Furthermore, as the F/1 configuration yields higher maximum proton energies when employing a 6 μm Al target, as would be expected from proton energy scalings in the TNSA regime [80], it is clear that any such intensity enhancement of the F/3 case, or diminishment of the F/1 case, must not only occur during the interaction, but also be subject to the onset of transparency.

4.5 PIC simulation results

In order to provide an explanation of the seemingly counter-intuitive proton beam properties, along with the holeboring velocity, the fundamental underlying physics of the interaction must be investigated. As a comprehensive investigation of this kind is not possible experimentally, we turn to numerical simulation, enabling the finer details of the interaction physics to be modelled. The fully relativistic PIC code EPOCH was used [136], with both the two and three dimensional (2D

and 3D) versions being employed. More details regarding the operation of PIC codes, along with some discussion of the key considerations and limitations, are included in Chapter 3.6.

Before proceeding to discuss the results of the PIC simulations performed, the key simulation parameters are presented. In the 2D simulation cases (which constitute the majority of the results presented in this section), the simulation box was defined to be 130 μm $\times$ 70 μm in size, consisting of 26000×5760 simulation cells. The number of particles per cell varies with target thickness, with 1733 particles per cell used in the 75 nm simulations primarily used throughout this chapter. The lowest particles per cell value used was for the $\ell = 1$ μm thick target simulation, which was run with 130 particles per cell. The simulation boundaries were set as free space and the targets were initialised as a uniform mixture of C^{6+} and H^{+} ions, representative of the plastic foils employed experimentally. The initial electron density was set to $420n_c$, where n_c is the critical density for the fundamental laser frequency, and the temperature of this electron population was initialised as 10 keV. The laser pulse was defined as having a Gaussian spatial and temporal profile, and was focused to the front surface of the target at an angle of 30°, in order to closely match the experimental conditions. Two pulse durations were used, $\tau_L = 400$ fs representing the conditions of the experimental data reported in the previous section ($\lambda_L = 1$ μm in this longer pulse case), and $\tau_L = 25$ fs, representing a typical pulse duration achievable using a short pulse, Ti:Sapphire laser system ($\lambda_L = 800$ nm in this short pulse case), as is discussed in section 4.5.3. The 400 fs case is shorter than the experiment ($\sim$ 900 fs), but this is justified to counteract the exaggerated ion expansion observed in 2D PIC simulations as a result of the reduced degrees of freedom [26]. Furthermore, it is vital to address the intensity scaling with focal spot size in the 2D simulations. Due to the 2D nature of the simulation, having only one transverse dimension, laser intensity scales linearly with focal spot size in this case, i.e. as the focal spot size is increased, a fixed energy is spread over a line of changing length, as opposed to a spot of changing area. In separate parameter scans, the target thickness was varied between $\ell = 20$ nm-1 μm and the focal spot size was varied

in the range $\phi_L = 1.2 - 10$ μm, for otherwise fixed parameters. The simulations were run with the same parameters as those used in Higginson *et al.* [26], which showed good agreement with experimentally measured trends, indicating that the no numerical considerations, such as resolution, alter the results in a significant way.

Many of the simulation parameters for the 3D simulations were similar to the 2D case, with a few notable exceptions, due to the increased computational requirements. The simulation box size now becomes 20 μm $\times$ 10 μm $\times$ 10 μm, with $1000 \times 720 \times 720$ simulation cells. The simulations were run with 6 particles per cell, limited by the computational expense of such large, 3D simulations. The targets in the 3D case had an equivalent areal density to a 2D 50 nm thick target, pre-expanded to a Gaussian profile with a FWHM of 0.5 μm along the laser axis. This target setup was used for all focusing conditions in order to make the simulations computationally feasible by reducing the required spatial resolution. This is a justified assumption as the finite temporal intensity contrast of the laser pulse employed experimentally will, even with the use of a plasma mirror, cause the target to undergo significant expansion early in the interaction [99, 146]. In terms of pulse duration, the 3D simulations were limited to the short pulse, $\tau_l = 25$ fs case, again due to computational restrictions, although this pulse duration is relevant to current and next-generation laser systems. With fixed energy, the short pulse simulations in both 2D and 3D yielded peak nominal intensities of 2.5×10^{22} Wcm^{-2}, representative of the capabilities of upcoming, next-generation laser facilities such as ELI [163].

4.5.1 Focal spot size dependence of the onset and effect of transparency-induced self-focusing

Using 2D PIC simulations, with the parameters discussed above, the interaction of a laser pulse with an ultra-thin foil target was investigated for the two focusing geometries employed experimentally, in order to better understand the underpinning physics which result in the counter-intuitive proton and plasma parameters

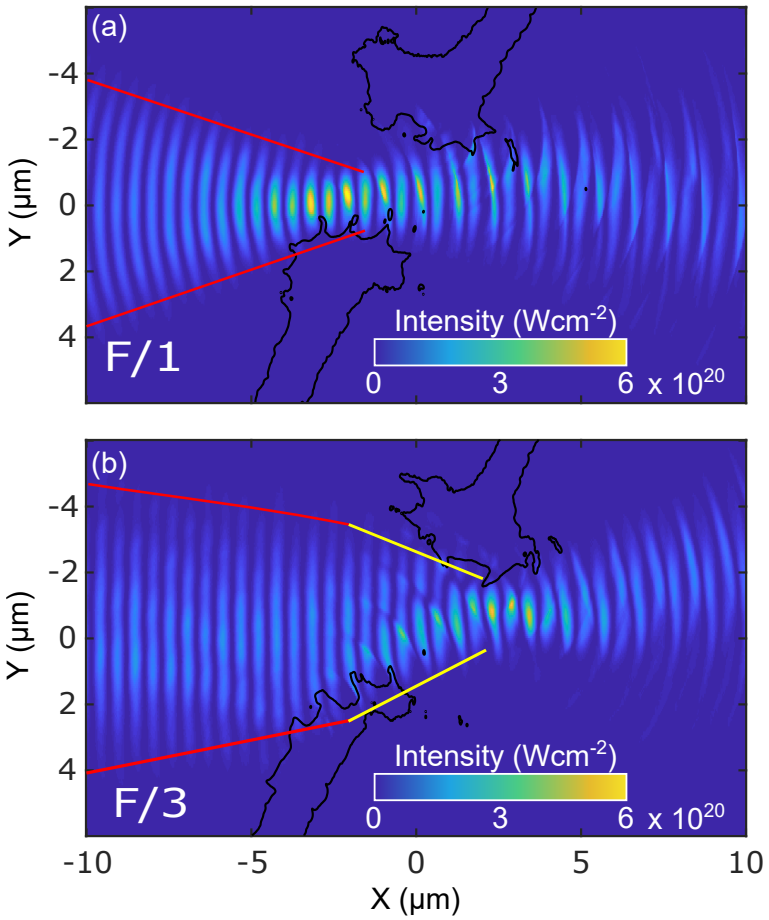

Figure 4.7: 2D maps of the spatial intensity profile of the laser pulse as it propagates through a $\ell = 75$ nm target undergoing RSIT, for incident F/1 and F/3 focusing geometries in (a) and (b), respectively. The initial target position is indicated by the white dashed line. The red lines highlight the nominal focusing cone of the incident laser pulse, with the yellow lines in the F/3 case highlighting the self-focusing cone as it propagates through the target. Both cases are shown at $t = 0$, i.e. when the peak of the pulse is incident on the initial target front surface. The black lines show the electron density at $n_e = \gamma n_c$.

measured.

2D intensity maps of the laser pulse, at a fixed time (once the target has undergone RSIT), as it transmits through a relativistically transparent CH target of thickness $\ell = 75$ nm, are shown for the F/1 and F/3 focusing configurations in Figs. 4.7 (a) and 4.7 (b) respectively. The initial target position is indicated with the white dashed line and the nominal focusing cone is shown in red. In the F/1 focusing scenario, the laser pulse focuses to near the front surface of the target to a spot size of $\phi_L = 1.5$ μm, before becoming distorted by the expanding plasma. As the laser light is transmitted through the target following the onset of transparency, the light is purely divergent, having already been focused to

near the diffraction limit of ~ 1.3 μm. As the nominal focal spot is already near wavelength in size, there is minimal scope for any additional, plasma-induced, focusing. This therefore results in the peak intensity achieved during the interaction being approximately equal to the calculated nominal intensity. In the F/3 focusing case, we similarly see the pulse focus towards the front surface of the target, forming a focal spot of $\phi_L = 5$ μm, before again becoming distorted by the expanding plasma. As the pulse propagates through the transparent target however, the pulse undergoes additional, plasma-induced self-focusing, with the final focal spot size, and instantaneous intensity, similar to the F/1 case. This self-focusing region is highlighted in yellow in Fig. 4.7 (b).

It is clear from these two cases that the onset of self-focusing, and thus its effect on laser-solid interactions in the transparency regime, has a strong dependence on the incident focal spot size, which will be explored further in this section. It is also interesting to note that the effect of self-focusing changes the spatial location of the peak instantaneous intensity when comparing the F/1 and F/3 focusing configurations. For F/1 focusing, the peak intensity occurs at the nominal focal position of the laser pulse, i.e. the front surface of the target. Conversely, in the F/3 case, the highest intensity is achieved at the rear of the target, following the onset of transparency. This has an additional effect on the acceleration of protons, beyond simply increasing the intensity, by perhaps enhancing the impact of transparency-induced effects such as boosting the energy of the electrons forming the jet for example, which would map onto the accelerated proton population.

The effect of transparency-induced self-focusing on the peak, instantaneous laser intensity was verified by comparing the peak intensities achieved when propagating laser pulses of varying focal geometries (F-number) and thus nominal focal spot sizes (at focus) in vacuum (Fig. 4.8 (a)) and through the transparent plasma produced by an expanding $\ell = 75$ nm CH foil target (Fig. 4.8 (b)). In Fig. 4.8 (a), we see the pulses have a Gaussian profile, centred around $t = 0$, where $t = 0$ is defined as the time at which the peak of the laser pulse interacts with the target (or the corresponding spatial location in the vacuum case). The intensity increases linearly as the focal spot size is reduced from $\phi_L = 10$ μm to $\phi_L = 1.5$

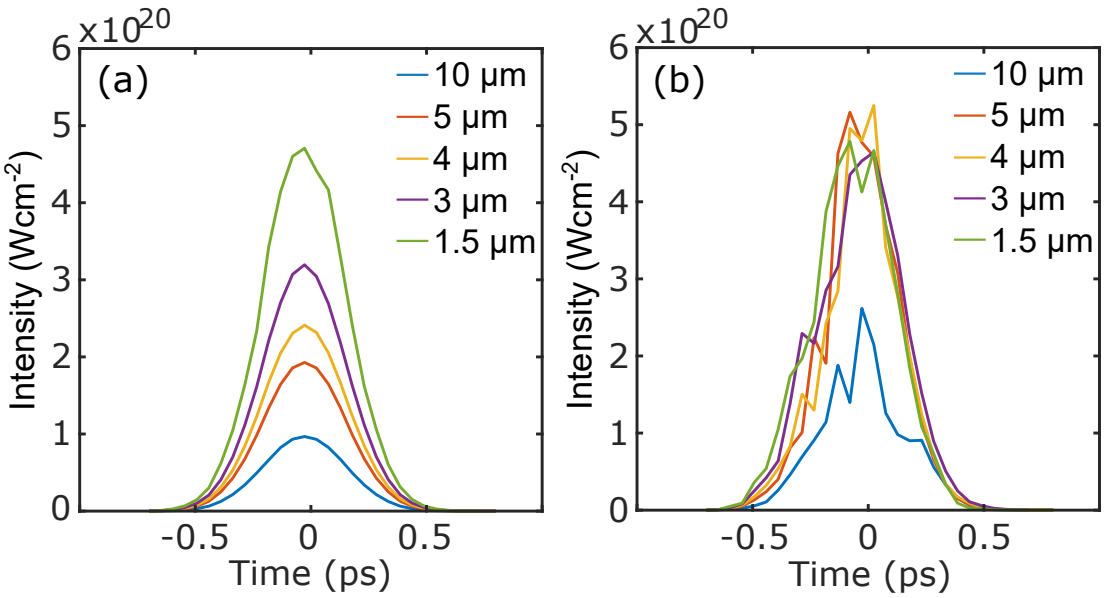

Figure 4.8: (a) 2D PIC simulated temporal profile of the peak focused 2D intensity of a laser pulse propagating in vacuum, for a range of focal spot sizes. (b) Same as (a), but for the interaction of the laser with a $\ell = 75$ nm CH foil target, expanded to the point of relativistic transparency. The time at which the peak of the laser pulse interacts with the target is defined as $t = 0$.

μm, as would be expected, with the linear scaling resulting from the 2D nature of the simulations as previously discussed. In Fig. 4.8 (b), the laser temporal intensity profiles have been significantly altered as a result of their transmission through the relativistically-transparent target foil. With the exception of the $\phi_L = 10$ μm case, a similar peak intensity is achieved for all focal spot sizes investigated, as a result of the laser pulse self-focusing to yield a near wavelength sized focal spot as it propagates through the transparent target. The reason for the $\phi_L = 10$ μm case not reaching a similar intensity is two-fold. Firstly, as the focal spot size is larger, the self-focusing length within the target is simply too short for the pulse to focus to near the laser wavelength, i.e. a larger initial spot size will require a greater propagation length. Secondly, the larger focal spot size results in a reduced nominal intensity (i.e. prior to self-focusing). This will delay the onset of transparency, thus minimising the effect of self-focusing on the intensity, as the target will undergo RSIT late in the pulse, some time after the peak. In spite of this, some small increase in instantaneous intensity is observed in the $\phi_L = 10$ μm case. This points to the existence of a limit to the focal spot size, under this specific target condition, below which self-focusing is capable of

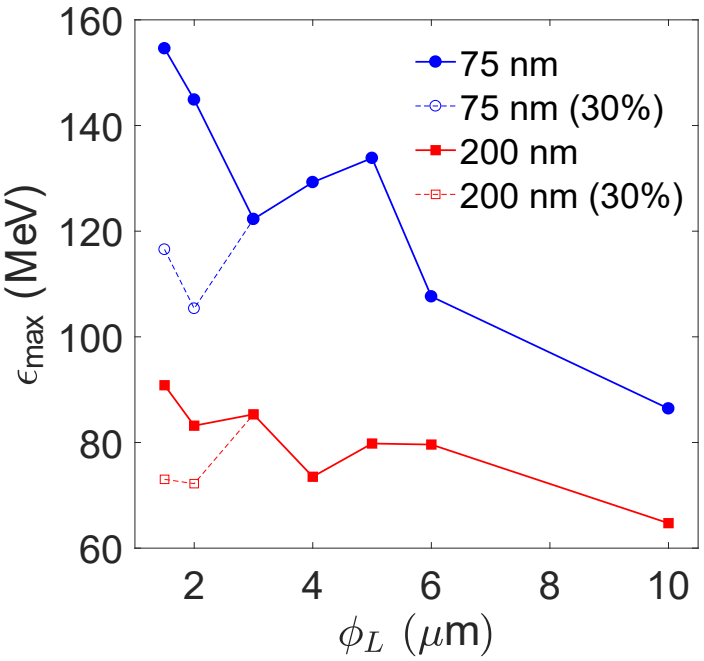

Figure 4.9: Maximum proton energy scaling from 2D PIC simulations with focal spot size, for two target thicknesses; $\ell = 75$ nm and $\ell = 200$ nm; shown in blue and red respectively. Hollow data points represent where a 30% reduction in encircled energy has been applied, in order to represent the experimentally measured values.

focusing the pulses to a near wavelength sized spot size as the target undergoes RSIT, thus driving the pulses to enhanced, comparable laser intensities. It is important to note that this applies to varying focal spot sizes at focus. If the spot size is changed by relocating the target or defocusing the pulse such that the laser is out of focus, the curvature of the wavefront at this point (converging or diverging depending on which side of focus the target is located), will likely significantly affect the outcome. Some degree of intensity enhancement may still be achieved but the peak intensity achieved will likely not be comparable across the different focal spot sizes due to the differing wavefront curvatures in each case.

It has been shown that, due to the effects of self-focusing, the instantaneous intensity may be enhanced relative to the calculated nominal intensity, allowing for comparable intensities to be achieved for a range of focal spot sizes. Such changes in the intensity would be expected to have some impact on the energies of the accelerated protons, and so this will now be explored for a range of focal

spot sizes, and for two target thicknesses, $\ell = 75$ nm and $\ell = 200$ nm. This is presented in Fig. 4.9, with the $\ell = 75$ nm case shown in blue and the $\ell = 200$ nm case shown in red. The hollow points, connected by dashed lines, represent, for the smallest spot cases ($\phi_L < 3$ μm), a factor reduction in encircled energy of 30%. This reduction in encircled energy is intended to represent the $\sim 30\%$ reduction measured experimentally when switching from F/3 to F/1 focusing due to the combination of on-shot variations in the laser pointing resulting in unoptimised FPM alignment and small uncompensated wavefront aberrations which will have minimal effect on a larger focal spot but have a significant effect as the diffraction limit is approached. The sensitivity to such wavefront aberrations and optic alignment/optimisation is a potential issue for any tight-focusing scheme, and so should be considered here in order to gain a more complete understanding of how self-focusing may affect interactions in both the idealised case, and when realistic pulse conditions are considered. In the $\ell = 200$ nm case in Fig. 4.9, any effects of self-focusing are minimal, as the target will undergo transparency late in the interaction. This can be seen by the largely smooth, but slow, increase in proton energies as the spot size is reduced.

In contrast, for $\ell = 75$ nm, where the target will undergo transparency near the peak of the pulse, the influence of self-focusing strongly affects the maximum proton energy achieved for focal spot sizes in the range $3 < \phi_L < 6$ μm. The enhancement in proton energy observed for these spot sizes is beyond the scope of the general trend of increasing proton energy with decreasing spot size. The range of focal spot sizes resulting in boosted proton energies corresponds with the range for which self-focusing is seen to play a key role in enhancing the instantaneous intensity from Fig. 4.8 (b). This indicates that self-focusing boosted intensity is the driver for this localised peak in maximum proton energies, as focal spots smaller than this range cannot undergo significant further focusing as they are already close to the laser wavelength, and focal spots larger than the range will not see significant intensity enhancement for the reasons discussed earlier.

It is important to note that, in the idealised case, where the encircled energy is the same for all focal spot sizes, the tight focus (and therefore highest nominal

intensity) case still yields the highest proton energies, although the self-focusing driven peak reduces the margin by which this is true. However, when the previously discussed reduction in encircled energy is factored in for the smallest focal spot sizes, we see that the peak at $\phi_L = 5$ μm becomes the highest proton energy achievable. This agrees with the experimentally measured proton energies for similar target thicknesses, presented in Fig. 4.3, in which the F/3 data, corresponding to a focal spot size of $\phi_L \sim 5$ μm, does indeed yield higher proton energies than the F/1 focusing configuration. An optimum in ion acceleration efficiency from thin foil targets for a similar focal spot size ($\phi_L = 5$ μm) had been observed in a previous study [142]. The underpinning mechanism investigated in that study is however different to that explored here. Furthermore, the physical reason for the optimum is different in that case. In Liu *et al.* [142], less efficient proton acceleration using larger focal spots results from lower intensities, thus reducing the accelerating field, but if the focal spot is too small, the accelerated proton numbers drop, thus reducing the efficiency, despite the higher proton energies achieved. In the study presented in this thesis however, it is the intensity-driven transparency-time (as seen in the next section), and the ability of the plasma to self-focus the laser light to near the laser wavelength, which determines the peak intensity and thus by extension the maximum proton energies.

4.5.2 Role of transparency time on the onset and influence of self-focusing

We have, so far, seen that self-focusing in transparent ultra-thin targets displays a strong dependence on the incident focal spot size, and can lead to an enhancement in instantaneous laser intensity, and consequently the maximum proton energies for the focal spot sizes which are subject to the greatest degree of self-focusing. It has also become evident however, that the transparency time, i.e. the time at which the target undergoes RSIT, also plays a key role in determining the influence of self-focusing in laser-solid interactions. The transparency time, for a fixed

focal spot size, and thus nominal laser intensity, may be tuned through variation of the target thickness, as undertaken experimentally. An opportunity therefore exists to simultaneously investigate the effect of transparency time on the self-focusing behaviour and to directly compare the results of the 2D simulations with the experimentally measured data.

The link between the target thickness and the transparency time, as measured using 2D PIC simulations, is shown in Fig. 4.10, for two focal spot sizes of $\phi_{F/3}$ and $\phi_{F/1}$, displayed in blue and red respectively. These focal spot sizes are representative of the F/3 and F/1 focusing geometries employed experimentally. The transparency time on the y-axis is given in picoseconds, relative to the peak of the pulse, defined as $t = 0$ (illustrated by the black dashed line). A negative transparency time is therefore representative of the target undergoing transparency prior to the arrival of the peak of the main pulse. The F/3 focusing case undergoes transparency at the peak of the pulse for a target thickness of $\ell \sim 95$ nm, while for F/1 focusing, this occurs for a thickness of $\ell = 120$ nm. Furthermore, across the full range of target thicknesses explored, the F/1 focusing case undergoes transparency earlier in the pulse than for F/3 focusing, due to the higher nominal intensity prior to the onset of RSIT. The exception to this is the $\ell = 40$ nm case, although this apparent equality in transparency time is likely due to the limited temporal resolution of the simulations. Finally, it is worth noting that for thicknesses of $\ell > 200$ nm, the target becomes opaque to the incident laser pulse.

In the previous subsection, it was shown that the peak laser intensity may be enhanced due to self-focusing for spots sizes in the approximate range $3 < \phi_L < 6$ μm. The F/3 focusing geometry employed experimentally falls within this range, with a focal spot size of $\phi_{F/3} \sim 5$ μm. It would therefore be expected that a significant enhancement to the instantaneous intensity would be observed in this case. Conversely, the F/1 focusing configuration falls outside this range, with a focal spot size of $\phi_{F/1} \sim 1.5$ μm. As such, minimal intensity enhancement would be expected in this case. The peak instantaneous intensity achieved by each focusing configuration, for the range of target thicknesses investigated experimentally, is

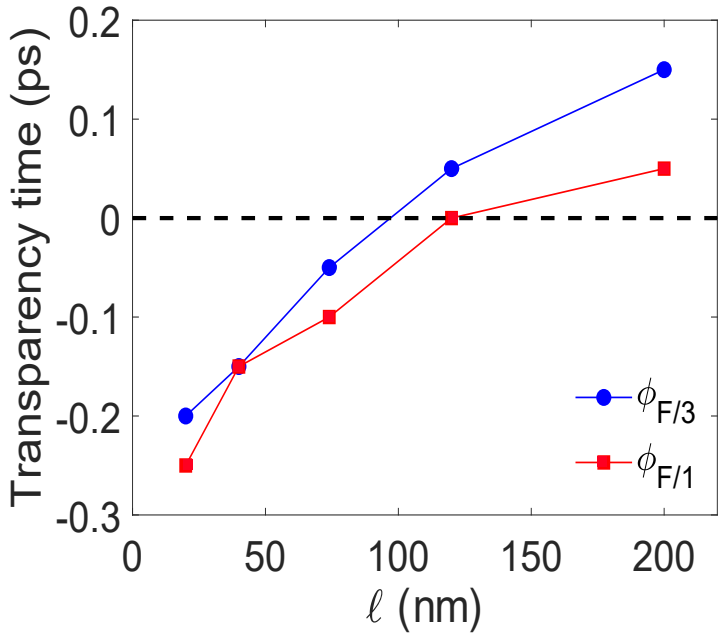

Figure 4.10: Transparency time, defined relative to the peak of the pulse, as a function of target thickness, ℓ, for F/3 and F/1 focusing conditions, shown in blue and red respectively. The black dashed line at $t = 0$ illustrates transparency occurring at the peak of the pulse.

presented in Fig. 4.11, with the F/3 shown in blue and the F/1 shown in red. The dotted line represents the nominal intensity of each focusing configuration, and the dashed line represents the maximum intensity limit, as imposed by the diffraction limit. It is important to note that the encircled energy of the F/1 case has been reduced by a factor 30% relative to F/3 focusing, in order to match the experimental conditions, although the peak nominal intensity remains higher than that of the F/3 focusing scheme.

In the F/1 case, the peak instantaneous intensity achieved is flat across the full range of target thicknesses explored, regardless of whether transparency occurs or not, and the magnitude of the intensity enhancement is minimal. This is due to the nominal focal spot already being close in size to the laser wavelength, and so the degree of transparency, or the time at which it occurs, can have little impact on the focal spot size, and thus by extension the peak intensity. In the F/3 focusing case, for target thicknesses of $\ell > 500$ nm, minimal intensity enhancement is observed ($\sim 10\%$ increase), due to the target remaining opaque for the duration of the interaction. The laser pulse is therefore unable to propagate through

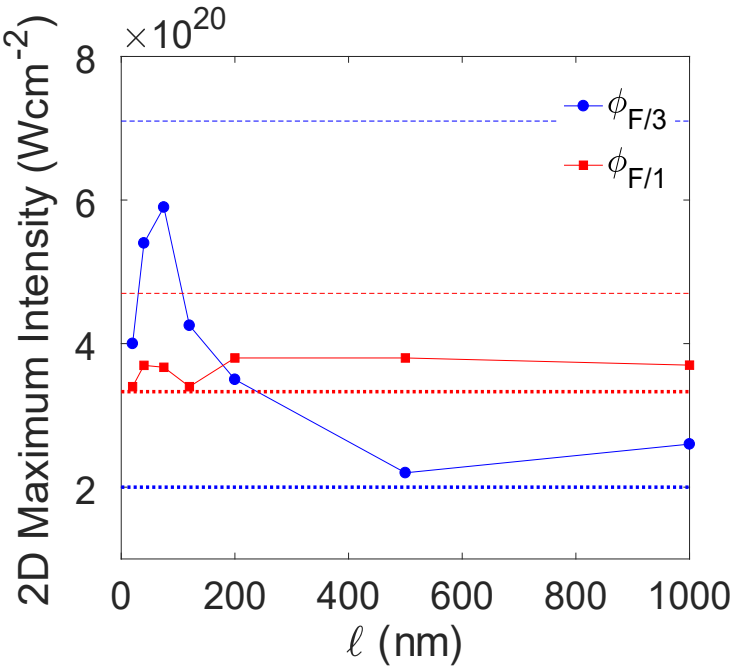

Figure 4.11: Maximum intensity achieved in 2D PIC simulations as a function of target thickness for the F/3 and F/1 focusing configurations, shown in blue and red respectively. The dotted lines represent the peak nominal intensity, and the dashed lines represent the maximum intensity possible if the pulse were focused to the diffraction limit.

the target, thus preventing transparency-induced self-focusing from taking place. Conversely, for thinner targets, RSIT will occur during the interaction, allowing for the laser to be transmitted and thus enabling self-focusing to take place. This is evidenced by the substantial intensity enhancements achieved for such target thicknesses, with the peak (approaching the laser wavelength) occurring for $\ell = 100$ nm, for which transparency occurs near the peak of the pulse. It is important to note that this is the same target thickness for which the highest proton energies are measured experimentally. Target thicknesses above or below this thickness do still exhibit a significant boost in intensity, but this is de-optimised by the onset of transparency occurring too late or early in the interaction respectively. It can be seen that for target thicknesses of $\ell < 200$ nm, F/3 focusing achieves higher peak instantaneous intensities than the F/1 case, in spite of the lower nominal intensity.

In order to more thoroughly compare the results from the PIC simulations with those measured experimentally, we now explore the scaling of maximum proton energy with target thickness, for the two fixed focal spot size, and therefore

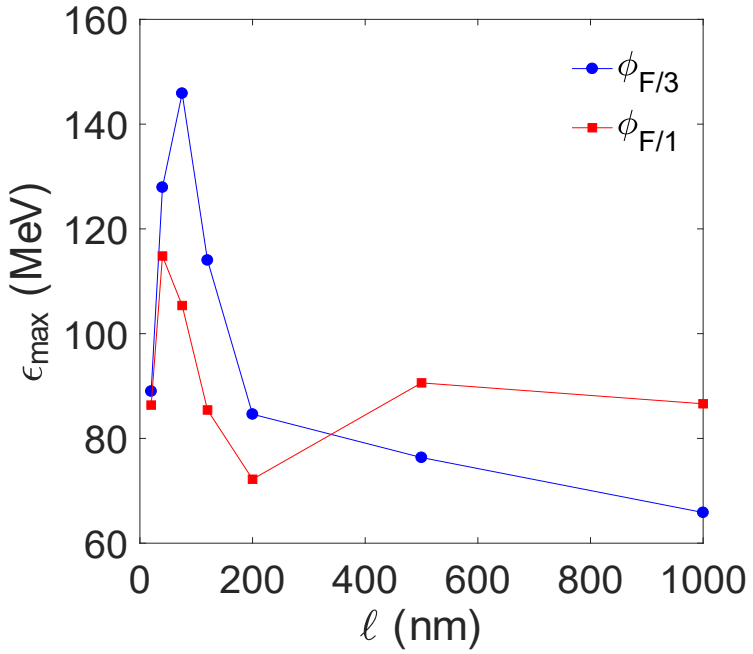

Figure 4.12: Maximum proton energy from 2D PIC simulations as a function of target thickness for the two focusing cases, F/3 and F/1, shown in blue and red respectively.

nominal intensity, cases. Once again, the encircled energy in the F/1 case has been reduced by the usual factor of 30%. This is presented in Fig. 4.12, with the F/3 and F/1 cases shown in blue and red respectively. It can be seen that for targets of approximate thickness $\ell < 350$ nm, the F/3 focusing case yields higher proton energies than the F/1 case, despite the lower nominal intensity, with a peak occurring for a thickness of $\ell = 100$ nm. This peak occurs for the same target thickness as the peak instantaneous intensity due to self-focusing, as shown in Fig. 4.11. Furthermore, the F/3 case yielding higher energies, and peaking at around $\ell = 100$ nm, is in good agreement with the proton energies measured experimentally (see Fig. 4.3). From the PIC simulation results however, we see that the F/1 case becomes favourable for thicknesses of $\ell > 350$ nm, as at this point, the target remains opaque to the incident laser pulse for the majority of the interaction. In the experimental data, shown in Fig. 4.3, a crossover of this kind is observed to occur, but for target thicknesses in excess of $\ell = 1.5$ μm. This is likely due to the influence of the laser temporal intensity contrast on the experimental interaction. The rising edge profile of the pulse in the simulation will not exactly match the experiment, affecting the range of target thicknesses

for which some degree of transparency will occur. This will allow self-focusing, and the associated intensity enhancement, to occur for thicker targets, which will have a knock-on impact on the maximum energy of the accelerated protons.

4.5.3 Influence of transparency-induced self-focusing in the ultra-high intensity, short pulse regime

The results discussed so far relate to the role transparency-induced self-focusing plays in laser-solid interactions employing existing, picosecond pulse duration laser systems. Currently, next generation, multi-petawatt laser facilities are coming online, enabling intensities of $> 10^{22}$ Wcm^{-2} to be achieved. In order to achieve the highest intensities, a combination of extreme tight-focusing and short pulse durations (i.e. tens of fs) is envisaged. It is therefore important to investigate the presence of transparency-induced self-focusing when employing such laser conditions and the influence this may have on the interaction of such pulses with thin-foil targets.

The peak instantaneous intensity achieved from the interaction of an ultra-high intensity, short pulse laser (τ_L = 25 fs) with an expanding, ℓ = 100 nm CH foil is presented in Fig. 4.13, and is compared with the results for a longer pulse (τ_L = 400 fs) case (displayed in blue) for a similar range of focal spot sizes. Due to the shorter pulse duration, it was feasible to carry out this study in both 2D and 3D, shown in red and green respectively, thus enabling the role of any dimensional effects to be identified. In order to enable direct comparison between the 2D and 3D results, the intensities of the 2D simulations are scaled by the square of the enhancement over the nominal intensity, to account for the slower scaling of intensity with focal spot size in 2D as discussed previously. The solid lines, with data points, represent the simulated peak instantaneous intensity, thus including self-focusing effects, whilst the dashed line represents the nominal intensities (i.e. no target). In the τ_L = 400 fs case, intensity enhancement resulting from transparency-induced self-focusing occurs for all focal spot sizes, with the exception of the smallest spot case (ϕ_L = 1.5 μm), for the reasons

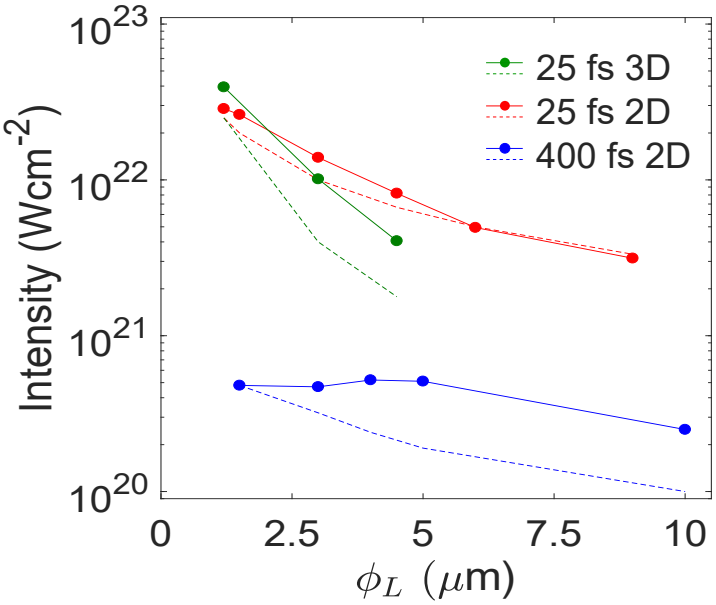

Figure 4.13: Peak intensity as a function of focal spot size for $\tau_L = 400$ fs (blue) and $\tau_L = 25$ fs (red) from 2D PIC simulations. 3D PIC simulation results for the $\tau_L = 25$ fs case shown in green for comparison. Dashed lines represent the nominal peak intensity (without a target), with solid lines representing the peak achieved intensity during the interaction.

already discussed. Importantly, the highest peak intensity is achieved not for the smallest spot case as would previously have been expected, but for the $\phi_L = 4$ μm case, where the peak intensity due to self-focusing is increased by a factor of > 2.

In the short pulse case however, in 2D, minimal intensity enhancement, and therefore by extension, self-focusing, is observed for any focal spot size, with a maximum intensity enhancement factor measured of ~ 1.4 . In the 3D case, some intensity enhancement is observed for all focal spot sizes. There is clearly a dimensional effect in that the intensity falls off more steeply in the 3D case than in the comparable 2D case. However, it is important to note that the trend is similar in both cases, and that crucially, in spite of the intensity enhancement, the tightest nominal focus remains the highest peak intensity, as the intensity boost is approximately fixed across the range of focal spots. Therefore, whilst the specific value of the intensity may be different than expected, the scaling will be as expected, contrary to the long pulse case. This indicates that self-focusing does not play a significant role in such short pulse interactions as the plasma does

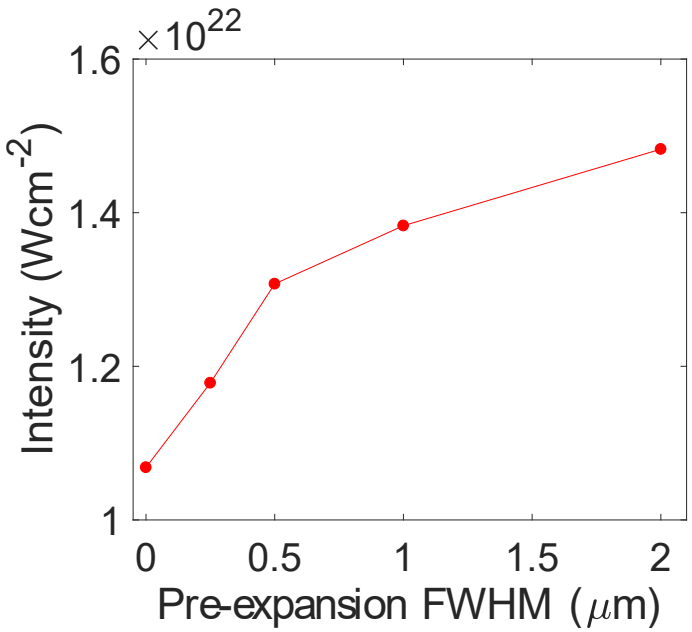

Figure 4.14: Peak intensity achieved from 2D PIC simulations as a function of target expansion profile FWHM, for a $\tau_L = 25$ fs pulse interacting with a expanded $\ell = 100$ nm CH foil target. The pulse was focused to a nominal spot size of $\phi_{F/3} = 5$ μm.

not expand to same degree over the course of the interaction due to the shorter pulse duration. This does however point to the possibility of inducing self-focusing by pre-expanding the target using a controlled pre-pulse, thus enabling a boosted intensity enhancement for the larger focal spot sizes.

The possibility of effectively 'switching on' self-focusing by deliberately inducing pre-expansion of the target is explored in Fig. 4.14. In this figure, the peak instantaneous intensity achieved, using the short pulse laser parameters, is displayed for a range of target pre-expansion profiles. All targets have been expanded from an initial 100 nm CH foil, in the form of a Gaussian spatial profile, with the stated values of FWHM. The 0 μm expansion case represents an initially unexpanded target, as used in the previous simulation studies, with the exception of the 3D cases, which were pre-expanded as previously discussed. It can be seen that as the FWHM of the pre-expansion profile is increased, the peak instantaneous intensity also increases, indicating the ability for the pulse to self-focus within the target. The scaling of this increase slows with increasing expansion FWHM. This is likely due to the target approaching an expansion profile where it is not sufficiently dense by the time of the arrival of the main pulse to impact the

laser pulse in a meaningful way, as the plasma will be effectively 'snow-ploughed' by the intense pulse. It is therefore likely that an optimal expansion profile exists, perhaps in the range of $2-3$ μm, for which the intensity is maximised, prior to over-expansion of the target. Identification of the exact expansion FWHM of this optimum is beyond the scope of the simulations performed, but the existence of such an optimum may be inferred from the data shown. Beyond the scope of deliberately pre-expanding the target to induce self-focusing, this result demonstrates that, for these pulse and target parameters, pre-expansion of the target due to poor temporal intensity contrast may inadvertently induce self-focusing, and thus somewhat boost the peak achievable intensities. It is therefore a possibility with future laser systems to further increase the intensity frontier by exploiting self-focusing of the laser pulse, by tuning the temporal intensity contrast or by delivering controlled pre-pulses to optimise the pre-expansion profile of the target.

4.6 Conclusions

In this chapter, the influence of employing an extremely tightly focused laser pulse on the characteristic properties of laser accelerated protons in a transparency-enhanced TNSA-RPA hybrid acceleration scheme was explored experimentally and numerically. Near-wavelength sized focal spots were achieved through the use of FPMs, to deliver a F/1 focusing geometry and nominal intensities of $> 10^{21}$ Wcm^{-2}, with the results compared with the data measured using a conventional F/3 OAP focusing configuration.

In contrast to what would be expected using existing scalings, the maximum proton energies achieved using the F/1 focusing scheme were reduced when compared with F/3 focusing by a factor of $\sim$ 30%. Investigation of the proton energy spectra show that, in addition to the reduced maximum energy, the proton numbers for energies $>$ 30 MeV are reduced when employing the tight focusing scheme. The above factors combine to result in a factor reduction in laser-to-proton conversion efficiency of $\sim$ 40%. In addition to the measured pro-

ton parameters, the recession velocity of the target critical surface was determined to be lower for F/1 focusing. These results suggest that the nominal laser intensities are not representative of the the actual peak intensities achieved during the interaction, when the target undergoes RSIT.

In order to further investigate the physics underpinning this behaviour, PIC simulations were carried out in 2D. It was shown that in the F/3 case, the laser pulse undergoes significant self-focusing as the pulse is transmitted through the target following the onset of RSIT. This does not occur in the smaller F-number focusing case, as the nominal focal spot is already near wavelength in size. The self-focusing effect is shown to result in enhanced instantaneous intensities and a subsequent boost to the maximum proton energies for nominal focal spot sizes in the range of $3 < \phi_L < 6$ μm.

Self-focusing in density gradients formed on the front surface of thick foil targets has been shown previously to influence the properties of the accelerated TNSA protons [44, 45], but this is the first case where the influence of self-focusing through a relativistically transparent, ultra-thin foil target has been explored. In addition to the role of focal spot size, the effect of transparency time on the self-focusing, as controlled by the target thickness, was explored. It was found that the maximum intensities were achieved when transparency occurred near the peak of the pulse. Under realistic conditions, and for suitable target thicknesses and thus transparency times, the F/3 focusing case was shown to achieve higher peak instantaneous intensities than the F/1 case. The result of this was a boost in proton energies, enabling the F/3 focusing configuration to generate higher proton energies, in good agreement with the experimentally measured data.

Finally, the influence of this transparency-induced self-focusing, for conditions approximating next generation laser facilities, for example ELI [163], was explored. It was found that self-focusing has a minimal impact on laser-solid interactions in this regime as the short pulse duration ($\tau_L = 25$ fs) prevents sufficient plasma expansion to occur over the duration of the interaction, with the smallest nominal spot size always yielding the highest peak instantaneous intensities. It is shown that some degree of self-focusing, and thus intensity enhancement, may

however be induced in such a case by pre-expanding the target via the use of a controlled pre-pulse for example. This could provide a potential pathway to further advancing the intensity frontier achieved using such laser systems.

This study highlights the importance of considering not just the enhanced intensity when employing a tight focusing scheme, but also the geometrical impact such a focusing scheme may have. The vital role of transparency-induced self-focusing in the acceleration of protons via a transparency-enhanced TNSA-RPA hybrid scheme has been demonstrated, influencing several key proton beam parameters such as maximum energy and laser-to-proton conversion efficiency. Furthermore, the sensitivity of this self-focusing mechanism to incident focal spot size, transparency time and target expansion profile has also been explored. The implications of this new understanding of laser-solid interactions in the transparency regime will help guide future efforts to optimise and control proton acceleration using the hybrid scheme using both current and next generation laser systems.

Chapter 5

Temperature of fast electrons at intensities beyond 10^{21} Wcm^{-2}

5.1 Introduction

The interaction of a high intensity laser pulse with a thick (tens of microns), solid density target results in rapid ionisation of the target and subsequent heating of plasma electrons to relativistic energies ($E_f > m_e c^2$), driving multi mega-amp currents into the target [23, 30, 60], as introduced in Chapter 2.6.2. This current of fast electrons is the source of many particle and radiation generating mechanisms, such energetic ions accelerated via the TNSA mechanism [71, 73] and bremsstrahlung emission of energetic x-rays [164, 165]. Protons accelerated via the TNSA mechanism, as discussed in detail in Chapter 2.7.1, are already in use for proton imaging purposes [130, 166] and for the heating of warm/hot dense matter states [167], with future applications such as proton oncology being proposed [139]. X-rays of the form generated in laser-solid interactions via bremsstrahlung radiation are also regularly used for radiographic purposes [164, 168] and as a diagnostic of plasma conditions [61, 169]. Furthermore, the fast electrons themselves may be used as an energy transfer mechanism in the fast ignition approach to inertial confinement fusion (ICF), acting to couple energy from the 'ignition' laser pulse to a pre-compressed deuterium-tritium fuel capsule [13, 170]. As such, it is vital that the physics underpinning the generation, transport and properties

of these fast electrons is well understood; a challenging task given that the fast electron current cannot be directly measured at present due to its existence within the solid density target foil. The properties of the fast electron population must therefore be inferred from secondary measurements, such as the energy spectra of the accelerated protons or from the yield and spectrum of the emitted x-rays [60, 155].

Extensive studies exploring the properties of the fast electron population have already been carried out, investigating a variety of properties such as beam divergence [171] and the influence of self-induced magnetic fields [171, 172]. In the study presented in this chapter, the particular property of interest is the temperature of the fast electron spectrum i.e. the average energy of the population of fast electrons. The scaling of the temperature of fast electrons with laser irradiance has been subject to substantial prior investigation, which will be explored in detail in section 5.2. These past studies have however been limited by existing laser technology, which has placed an upper limit on the achievable laser intensity at an approximate maximum of 10^{21} Wcm^{-2}. With new facilities already online achieving laser intensities of $> 10^{23}$ Wcm^{-2} [85], and with further such facilities being commissioned within the next few years, such as ELI and Apollon [163, 173], it is therefore not only timely, but important that the scaling of electron temperature to higher intensities is explored.

The focusing plasma mirror setup, as outlined in Chapter 3.4.2, enables the experimental exploration of laser-plasma interactions at higher intensities (up to $I_L = 5 \times 10^{21}$ Wcm^{-2}) than previously possible using current generation laser systems. In this chapter, the influence of peak laser intensity, driven by variation of the focal spot size, on the temperature of the fast electron population within tens of micron thick targets is explored. The FPM provides a means of enhancing laser intensity by almost an order of magnitude using current laser systems [126, 127, 128], thus enabling experimental investigation of fast electron temperature into a regime previously unreachable. Whilst this does not reach the intensities predicted for next-generation laser systems, the intensity is sufficient to effectively bridge the gap between existing and upcoming laser systems. This allows for

existing scaling laws to be probed empirically beyond the range in which they have already been tested, which may highlight areas in which current theoretical models will prove inaccurate/incomplete.

5.2 Review of electron temperature scaling with laser intensity

Several experimental and theoretical studies have been carried out investigating the scaling of the temperature of the fast electrons with peak intensity [28, 35, 48, 60]. Due to limitations on laser technology, theoretical models have only been tested experimentally up to intensities of mid 10^{20} Wcm^{-2}, and only one previous study has examined the effect of near-wavelength scale focal spots. In this section, the findings of these studies are briefly summarised, including the outlining of predicted electron temperature scaling laws and when they are applicable, which are utilised extensively throughout the remainder of the chapter.

Early research into the scaling of the temperature of fast electrons with intensity for relativistically intense, normally incident, laser pulses, carried out using PIC simulations, showed that the electron temperature increased with increasing pulse irradiance ($I\lambda^2$) [28]. The simulations undertaken in Wilks *et al.* [28] show that substantial absorption of laser energy (between 26% and 50% depending on the degree of plasma surface deformation for p-polarised light and a sharp density gradient) into an overdense plasma results in heated electrons with a temperature on the order of the ponderomotive potential, for laser intensities on the order of 10^{19} Wcm^{-2}. This temperature scaling was shown to take the form

$$k_B T_e = m_e c^2 \left[\left(1 + \frac{a_0^2}{2} \right)^{1/2} - 1 \right], \tag{5.1}$$

This study formed the basis of almost every future study of laser solid interactions where the fast electron population is relevant, with the scaling law given in Eqn. 5.1 being widely used throughout the field. This temperature scaling law is applicable to the fast electrons which are directly heated by the laser. The bulk

electrons within the target will have a significantly lower temperature. There are however some obvious limitations to this formulation. Firstly, this is an analytical and numerical study, and therefore requires empirical verification. Secondly, the peak laser intensity investigated here is lower by several orders of magnitude when compared with the typical intensities now routinely achievable at current generation laser systems ($10^{18} - 10^{19}$ Wcm^{-2} compared with $10^{20} - 10^{22}$ Wcm^{-2}). Finally, this model assumes that the electron experiences the peak electric field over a full laser cycle, thus maximising the energy transfer between the laser pulse and the plasma electrons. This is likely a fair assumption for relatively low intensities and in cases where the laser propagates through a long scale-length of underdense plasma. For higher intensities and high laser temporal intensity contrast, this assumption may no longer hold. This is due to the increasing influence of the ponderomotive force and radiation pressure on the interaction as the intensity is increased, which act to drive electrons out of the area of influence of the laser pulse, thus limiting the energy transfer between the laser and the electrons. Furthermore, for steep density gradients, the laser can no longer deposit significant energy in the pre-plasma, and absorption within the overdense plasma is restricted by the collisionless skin depth.

The first of these limitations was addressed in the following years in a series of experimental studies employing picosecond laser pulses incident on solid density targets, with laser intensities of up to $\sim 10^{19}$ Wcm^{-2}. One of the most widely cited studies will be discussed here, presented in Beg *et al.* [60], employing a p-polarised laser pulse incident on target at an angle of 30° and focused using an F/4.2 OAP. Measurements of x-ray bremsstrahlung radiation and K_α emission were used to determine a new, empirically derived scaling law

$$k_B T_e \propto a_0^{2/3} \tag{5.2}$$

This is significantly slower than that predicted by Eqn. 5.1. Later studies have shown that this scaling, shown in Eqn. 5.2, extends to higher intensities (up to $\sim 10^{20}$ Wcm^{-2}) [61]. It is therefore clear that this empirical data provides a

good description of the scaling of electron temperature across a range of intensities, including those commonly used in current laser-solid experiments. This empirical scaling law cannot however provide an explanation as to the physics driving this weaker scaling, with respect to that found through modelling in Eqn. 5.1. Evidently, coupling of energy between the laser and the plasma electrons is being restricted in some manner, but the underpinning physics of this remained unknown.

An explanation of the physics underpinning this slower scaling was presented in Haines *et al.* [48], a theoretical study of energy and momentum conservation within the collisionless skin-depth of the plasma. A scaling law was derived to describe the temperature of fast electrons, which was found to be in good agreement with the empirical scaling law presented in Beg *et al.* [60] and experimental results reported in Chen *et al.* [61]. The scaling law can be expressed in two forms, as shown below, one using physical parameters and the other expressed in terms of the normalised vector potential

$$k_B T_e = m_e c^2 \left\{ \left[1 + \frac{2}{m_e c} \left(\frac{m_e I}{n_c c} \right)^{1/2} \right]^{1/2} - 1 \right\}, \tag{5.3}$$

$$k_B T_e = m_e c^2 \left[\left(1 + 2^{1/2} a_0 \right)^{1/2} - 1 \right], \tag{5.4}$$

The physical reasoning underpinning the slower scaling of electron temperature relative to the ponderomotive scaling (Eqn. 5.1) is due to the relativistic motion of plasma electrons in the oscillating laser field. In the case of an overdense plasma, and for large amplitude electromagnetic fields, the relativistically corrected collisionless skin-depth is significantly smaller than the laser wavelength (for an intensity of 10^{20} Wcm^{-2}, and employing the equation for relativistically corrected skin-depth given in Haines *et al.* [48], $\ell_s \sim 22$ nm compared with $\lambda_L \sim 1$ μm). As a result, a relativistic electron will traverse a distance greater than the skin-depth before seeing even a quarter of a wavelength of the laser pulse. This is demonstrated in Fig. 5.1, where the collisionless skin-depth, ℓ_s,

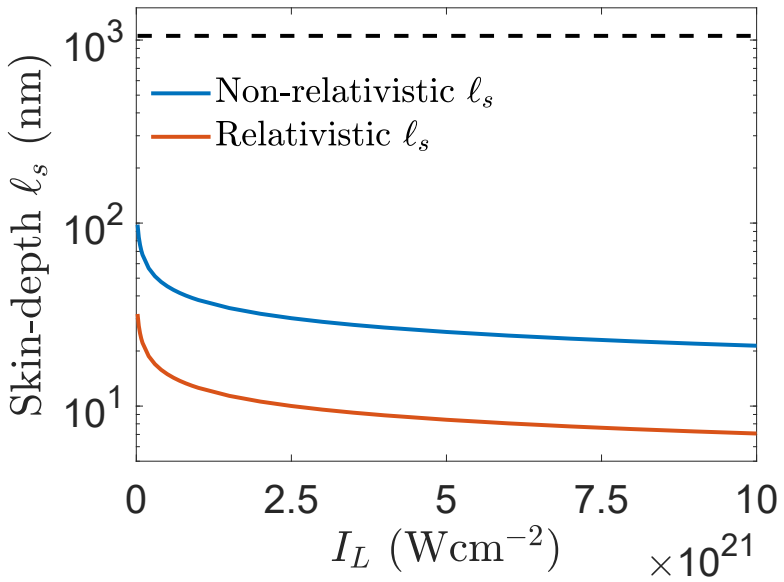

Figure 5.1: Scaling of the plasma collisionless skin-depth ℓ_s as a function of laser intensity, using both non-relativistic and relativistic models, shown in blue and orange respectively. The laser wavelength, λ_L, is shown by the black dashed line, for comparison.

has been calculated using both the non-relativistic and relativistic [48] formulae

$$\ell_s = \frac{c}{\sqrt{\omega_{p,e}^2 - \omega^2}} \tag{5.5}$$

$$\ell_s \approx \frac{c}{\omega_{p,e}} \left(\frac{\omega}{\omega_{p,e}} \right)^{2/3} a_0^{1/3} \tag{5.6}$$

It can be seen that even at the lowest intensities examined ($\sim 10^{19}$ Wcm^{-2}), the skin-depth is greater than an order of magnitude less than the laser wavelength. This has the effect of limiting the energy transferred from the laser to the plasma electrons, and so the full ponderomotive potential cannot be reached (see Chapter 2.3.2), in turn resulting in lower fast electron temperatures. For example, at an intensity of 2×10^{21} Wcm^{-2}, the ponderomotive scaling would predict an electron temperature of ~ 20 MeV. In comparison, for the same intensity, the ℓ_s-limited model predicts a temperature of ~ 3.4 MeV.

Recently, an experimental study of electron temperature scaling was conducted for peak laser intensities of up to mid 10^{21} Wcm^{-2}, achieved through the use of a short pulse ($\tau_L \sim 40$ fs) laser focused to a spot size of $\phi_L \sim 1.5$ μm

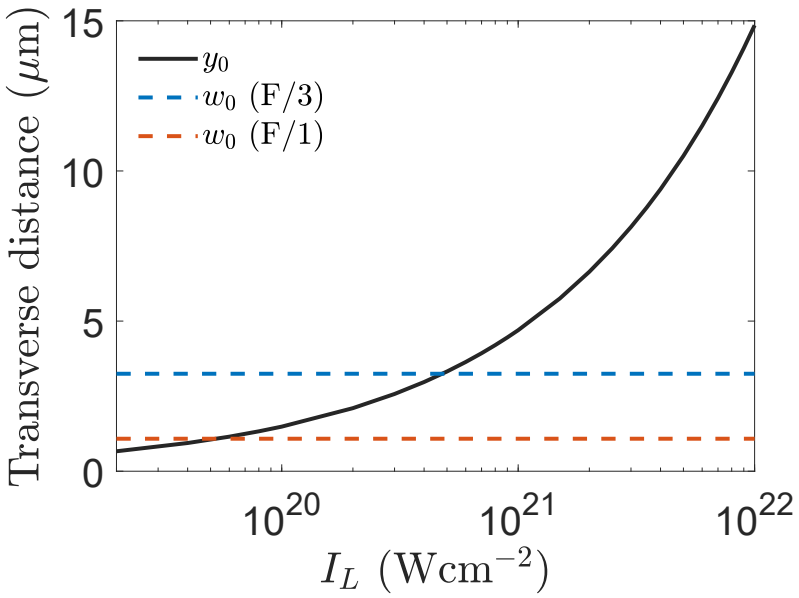

Figure 5.2: Scaling of maximum transverse distance travelled by a relativistic electron, y_0, with laser intensity, shown in black. Dashed blue and orange lines represent the mode waist, w_0, of the two focusing conditions employed in this chapter, F/3 and F/1, respectively, for comparison.

(FWHM) with energy on target of $E_L \sim 10$ J [35]. In this study, it was shown that for tight focusing conditions, and under the specific conditions of this investigation, the focal spot size can act to limit the energy coupling from the laser to the plasma electrons. The mechanism for this is similar to that outlined in Haines *et al.* [48], with the limiting factor being the transverse size of the focal spot, as opposed to the longitudinal collisionless skin-depth. Once the electron has exceeded the bounds of the focal spot, energy coupling is greatly reduced, thus preventing the ponderomotive potential from being achieved. When written in terms of transverse momentum p_y, the ponderomotive scaling is given by

$$k_B T_e = m_e c^2 \left\{ \left[1 + \left(\frac{p_y}{m_e c} \right)^2 \right]^{1/2} - 1 \right\}. \tag{5.7}$$

In the case where the focal spot size is smaller than the transverse extent of the electron motion for a given laser intensity, the transverse acceleration of the electron is assumed to cease at a point $y = w_0$, where w_0 is the $1/e$ radius of the focal spot (see Chapter 3.1.2). In this case, the final momentum of the electron

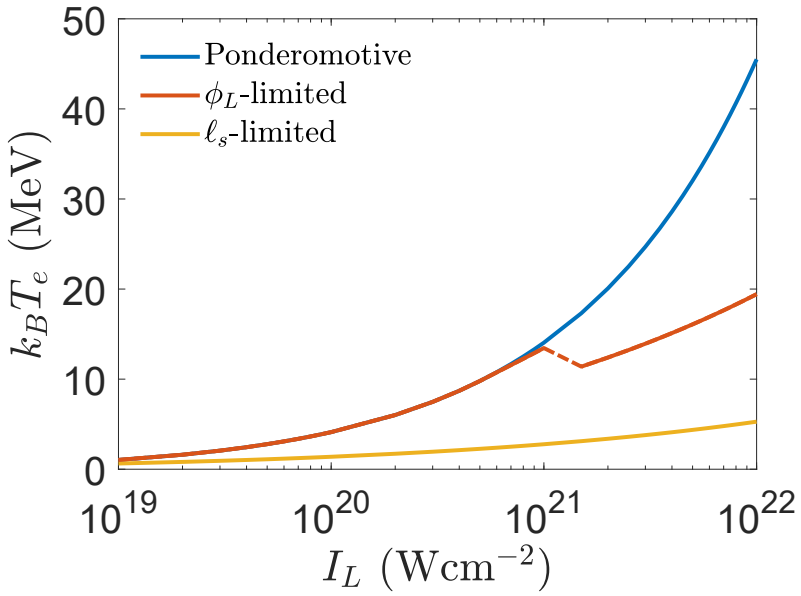

Figure 5.3: Scaling of the temperature of fast electrons with laser intensity I_L, according to the three primary temperature models employed in this investigation. The ponderomotive scaling is that set forward in Wilks *et al.* [28], the spot size limited scaling is set out in Dover *et al.* [35] and the skin depth limited case outlined in Haines *et al.* [48]. The dashed portion of the orange line represents a discontinuity where the focal spot size has been changed, in order to match the parameters of the experiment reported in this chapter.

is limited, expressed mathematically as

$$p_y = a_0 m_e c \left[1 - \left(1 - \frac{w_0}{y_0}\right)^2\right]^{1/2}, \tag{5.8}$$

where y_0 is the maximum transverse acceleration distance of the electron, given by $y_0 = a_0\lambda_L/2\pi$. If the focal spot size is larger than y_0, the ponderomotive scaling is recovered, as there is no restriction imposed on the heating of the plasma electrons. In the case where the focal spot size is smaller than y_0, the electron temperature scaling with intensity slows, deviating from the ponderomotive potential. The scaling of y_0 with laser intensity is presented in Fig. 5.2. It can be seen that greater intensities result in a larger transverse acceleration distance, thus requiring a larger focal spot size in order to prevent the heating of the electrons from being restricted. The dashed lines represent typical beam waist sizes for the focusing conditions employed in this chapter. For F/3 focusing, intensities of greater than $\sim 4.5 \times 10^{20}$ Wcm^{-2} will result in the electrons exceeding

the bounds of the focal spot. This required intensity is greatly reduced however when an F/1 focusing scheme is employed, with an intensity of $\sim 5\times10^{19}$ Wcm^{-2} being sufficient for the electrons to transversely escape the focal spot.

The temperature scalings reviewed in this section are presented graphically as a function of the laser intensity in Fig. 5.3. It can be seen that at the lowest values of I_L, corresponding to intensities of $\sim 3\times10^{20}$ Wcm^{-2}, the models all predict similar electron temperatures, with the skin depth limited case being slightly smaller than the ponderomotive or spot size limited cases. When extended to higher intensities however ($> 10^{21}$ Wcm^{-2}), in the range achievable by employing F/1 focusing, these models diverge significantly, with both the spot size and skin depth limited models predicting severely limited electron temperatures, although still increasing with intensity. If correct, this would have a significant impact a wide range of aspects in the field laser-plasma interactions, including ion acceleration and x-ray production via bremsstrahlung radiation and so demands thorough investigation.

5.3 Experimental method

The experimental investigation presented in this chapter was carried out primarily in an experimental campaign performed using the Vulcan petawatt laser, as described in Chapter 3.3. The proton measurements, presented in section 5.7, where made on a separate experimental campaign, but using the same laser system with nominally identical laser parameters.

The Vulcan Petawatt laser produces pulses of horizontally polarised light of central wavelength 1054 nm. Pulse durations of (900 ± 300) fs and pulse energies of (230 ± 30) J (on-target) were measured. The laser pulse was focused initially using a F/3.1 OAP to a nominal focal spot size of $\phi_L = (4.5\pm1.0)$ μm (FWHM), measured using a low power, CW laser mode prior to the delivery of each high power pulse. Two plasma mirror configurations were employed, making use of plasma optics of planar and ellipsoidal geometries (see Chapters 3.11 and 3.4.2), positioned in the focusing beam to enhance the laser temporal intensity contrast.

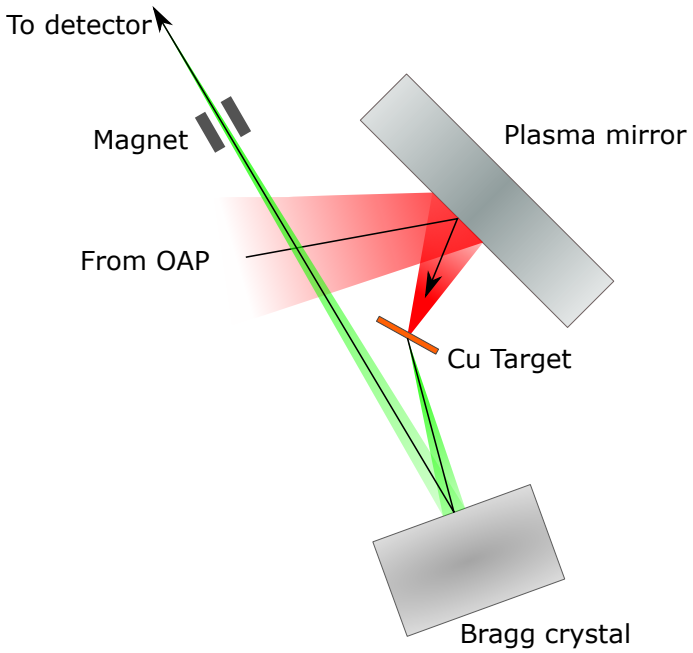

Figure 5.4: Sketch illustrating the in-chamber setup of the primary interaction and diagnostic experimental configuration employing a PPM. This setup is identical in the FPM case, only with the plasma optic type switched, retaining the target position.

In the PPM case, the $\phi_L = 4.5$ μm focal was maintained (along with the F/3.1 focusing geometry), with fractional encircled energy of $f_{EE} \sim 40\%$. The FPM setup was used to form a smaller focal spot of size $\phi_L = (1.7 \pm 0.2)$ μm FWHM and fractional encircled energy $f_{EE} \sim 30\%$. The smaller focal spot size corresponds to a focusing geometry of approximately F/1. The peak calculated laser intensity when employing the PPM setup is $(5.0 \pm 2.0) \times 10^{20}$ Wcm^{-2}, increasing to $(3.5 \pm 1.5) \times 10^{21}$ Wcm^{-2} for the FPM setup [126, 127]. In both cases, the plasma mirror reflectivity and temporal intensity contrast enhancement are similar. The intensity contrast ratio in both plasma mirror configurations was 10^{-12} at 500 ps and 10^{-7} at 10 ps prior to the arrival of the peak of the pulse.

In both focusing cases, pulses were incident normal to the target front surface, with two target types being investigated. K_α measurements were made using 25 μm thick copper targets, and maximum proton energy measurements employed 6 μm thick aluminium foils. The transverse dimensions of the copper targets were varied in the range 1×1 mm to 4×4 mm, for the purposes of a secondary objective that is not reported here. Variation of the transverse target dimensions was found to have no effect on the yield of copper K_α photons for the target and

laser parameters used. The primary diagnostic of fast electron temperature was the measurement of x-ray K_α emission from the copper atoms of the target.

As discussed in Chapter 3.5.3, K_α photons are emitted with a characteristic energy (8.05 keV in the case of copper) into the full 4π solid angle. Copper K_α emission from the target rear was imaged using a spherically-bent Quartz Bragg crystal with a radius of curvature of $R_{curv} = 380$ mm, reflectivity of 6×10^{-4} and atomic spacing of $2d = 3$Å, imaging the x-rays onto Fujifilm BAS-TR image plate (see Chapter 3.5.4). The viewing angle at the target rear was $\sim 50°$ from target normal, with a viewing distance of 210 mm and an image distance of 2 m. This geometry results in an image magnification at the IP of approximately $\times 9$. A simple sketch of the in-chamber setup used is shown in Fig. 5.4 for the PPM configuration (in the FPM case, the setup is identical, but with the plasma mirror switched). A 1 T magnet was placed before the detector in order to sweep away any charged particles which may act as a significant source of background signal. The IP was double-stacked and wrapped in a single layer of 13 μm thick aluminium, to ensure the measured signal corresponded with 8 keV copper K_α photons. The measured signal of the scanned IP was converted to PSL using Eqn. 3.14 from Chapter 3.5.4, and this was subsequently converted into photon number using the calibration reported in Curcio *et al.* [133].

To support this measurement of the temperature of fast electrons made via the yield of copper K_α photons, measurements of maximum proton energy, accelerated via the TNSA mechanism (see Chapter 2.7.1), were made, and similarly compared with predictions made using the Mora model [80] (see Chapter 2.7.1). This allowed for the fast electron temperature to be verified using an independent method to the K_α x-ray yield. The spatial and spectral properties of the proton beam were measured using a stack of HDV-2 and EBT-3 dosimetry film (RCF) (see Chapter 3.5.1 for further details), interspersed with iron and mylar filters of varying thickness. The RCF stack was positioned 4.5 cm from the rear surface of the 6 μm aluminium target, centred on target normal, such that the full proton beam was captured.

5.4 Analytical K_α model

The temperature of fast electrons may be inferred through the influence it has on the yield of copper K_α photons emitted during an interaction. In order to relate the measured yield of copper K_α photons to the temperature of the fast electrons, an analytical model was developed, which is employed throughout this investigation. This model calculates the photon yield for a given distribution of electron kinetic energies, for a given input electron temperature model and target conditions.

5.4.1 Modelling K_α photon yield

Firstly, it is important to consider the properties of the input electron population, as this will have a significant impact on the resulting yield of copper K_α photons. This electron population is injected at the front surface of the target, with some escaping at the target rear whilst the remaining population refluxes within the target until all energy is lost. This refluxing is achieved in the model by having the electrons reflect at the front and rear surfaces of the target. The fraction of the electrons which will reflux, as opposed to escape at the target surfaces, is determined based on a simple model of sheath strength, as outlined in section 5.4.2. The initial fast electron spectrum $f(E_0)$ is assumed to take the form of a 3D Maxwellian distribution

$$f(E_0) = 2\left(\frac{E_0}{\pi (k_B T_e)^3}\right)^{1/2} \exp\left(-\frac{E_0}{k_B T_e}\right) \tag{5.9}$$

In this equation, the temperature of the spectrum $k_B T_e$ can be altered depending on which of the temperature models, outlined in section 5.2, is desired. In the model calculations, the electron spectrum is divided into energy bins of width 0.05 MeV and a central energy of E_0. As the electrons propagate through the target, they lose energy via a combination of collisional and radiative loses, which are calculated using the ESTAR stopping tables for electrons in solid density copper [174].

As the electrons travel through the target, they will produce K_α photons via the process outlined in Chapter 3.5.3. In order to calculate this, the cross-sections for K_α photon production are integrated over discrete distances of 0.1 μm within the target. The total K_α photon yield, N_K, is calculated using a similar approach as that used in Myatt *et al.* and Quinn *et al.* [131, 175], given by

$$N_k = \eta_R N_{fast} \omega_k n_{Cu} \int_0^\infty f\left(E_0\right) dE_0 \int_0^{s(E_0)} \sigma_k \left[E\left(E_0, s\right)\right] ds. \tag{5.10}$$

In this equation, the parameter η_R is the fraction of electrons which reflux, given simply by $\eta_R = N_{reflux}/N_{fast}$, which will be discussed in more detail in section 5.4.2. N_{fast} is the total number of fast electrons, which is calculated as

$$N_{fast} = \frac{\eta_{L\rightarrow e} E_L}{k_B T_e}, \tag{5.11}$$

assuming a laser-to-electron energy conversion efficiency of $\eta_{L\rightarrow e} = 30\%$. The atomic density of copper is $n_{Cu} = 8 \times 10^{22}$ cm^{-3} and the fluorescence yield $\omega_k = 0.44$ is the fraction of K-shell ionisation processes resulting in K_α photon emission. The relativistically correct K-shell ionisation cross-section in copper, σ_k, is calculated using the method outlined in Quarles [176], given by

$$\sigma_k = 828 \times 10^{-16} \left(\frac{R}{UI^2}\right) \ln U, \tag{5.12}$$

given in units of cm^2 eV^2. Here, I is the ionisation potential, taking a value of 8.979 keV, U is the ratio of the kinetic energy of the incident electron E to the ionisation potential I and R is the relativistic correction factor given by

$$R = \left(\frac{2+I}{2+E}\right)\left(\frac{1+E}{1+I}\right)^2 \left(\frac{\left(I+E\right)\left(2+E\right)\left(1+I\right)^2}{E\left(2+E\right)\left(1+I\right)^2 + I\left(2+I\right)}\right)^{3/2}, \tag{5.13}$$

where E and I are in rest-mass units. Finally, the absorption of 8.05 keV K_α photons in the bulk solid density copper target following their emission is calculated as

$$N_{trans} = N_k \exp\left(-\frac{\mu L_{Cu}}{2}\right), \tag{5.14}$$

where $\mu = 463$ cm^{-1} is the attenuation coefficient of 8.05 keV photons in cold, solid copper and L_{Cu} is the thickness of the copper target (i.e. 25 μm for the targets under investigation here).

5.4.2 Modelling electron refluxing

As briefly mentioned previously, it is vital that electron refluxing (or recirculation) within the target is considered within the K_α yield model. Refluxing of fast electrons was first shown numerically to be of great importance in high intensity laser-solid interactions in the investigations presented in Sentoku *et al.* [75], where it was observed that the refluxing of plasma electrons would increase the effective electron density, which in turn results in boosted proton energies. Since then, experimental studies have been carried out investigating this behaviour, confirming that it plays a key role in laser interactions with relatively thin target foils [131] and that refluxing electrons have a significant contribution to the production of K_α photons [132], both of relevance to the work carried out here. The presence of refluxing within the targets employed in this work is made clear when the raw images of the emitted K_α photons are considered, as shown in Fig. 5.5. In this case, the target transverse dimensions are being increased from 1×1 mm to 4×4 mm, in steps of 1 mm. As mentioned in section 5.3, the variation in target transverse size was undertaken for a secondary objective beyond the scope of this work. It can clearly be seen that in addition to the bright central spot, the entire target is illuminated by the emission of K_α photons, resulting from a large population of recirculating electrons. This is confirmed by the variation in brightness of this source with target transverse size. In the larger targets, the refluxing electrons will transversely spread over the duration of the interaction, resulting in a lower density, and thus dimmer source of K_α photons. In contrast, electrons recirculating within the smaller targets will reach the edges, and be reflected back into the target, resulting in an increased density and corresponding photon signal [78].

The refluxing of fast electrons within the analytical model developed is based around the reflection of electrons at the front and rear surfaces of the target. In

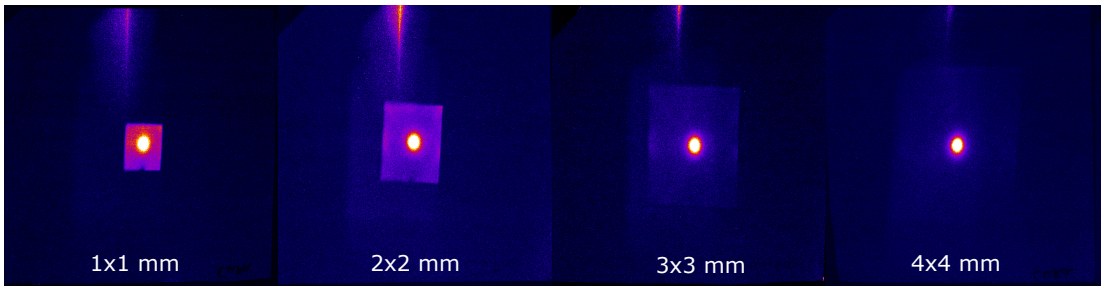

Figure 5.5: Raw image of the measured copper K_α photon signal for target transverse sizes ranging from 1×1 mm to 4×4 mm. The visible illumination of the entire target foil results from the refluxing of fast electrons within the target [78].

order to determine which electrons have sufficient energy to escape the target and which will remain trapped, the 'escape' kinetic energy must be determined, requiring estimation of the strength of the sheath electric field at the target rear surface. This calculation follows the form presented in [177], but will be outlined here as it forms a key part of the analytical model. To begin, the fast electron density at the target rear surface must be determined. In order to calculate this, the divergence of the fast electron beam must be understood. Assuming ballistic transport of the electrons with a fixed divergence angle θ_{Div}, and a target of thickness L, the radius of the electron bunch, B, at the target rear can be written as

$$B = w_0 + L \cdot \tan\theta_{Div}, \tag{5.15}$$

where w_0 is the radius of the laser focal spot. From this, the resulting electron density of the bunch can be estimated as

$$n_e = \frac{N_{fast}}{c\tau_L \pi B^2}, \tag{5.16}$$

where N_{fast} is the total number of fast electrons, given by Eqn. 5.11, c is the speed of light in vacuum, τ_L is the laser pulse duration and B is the radius of the electron bunch at the target rear, as defined in Eqn. 5.15. This electron density can then be used to calculate the Debye length for the hot electrons, determined by

$$\lambda_D = \left(\frac{\epsilon_0 k_B T_e}{e^2 n_e}\right)^{1/2}, \tag{5.17}$$

where $k_B T_e$ is the temperature of the electron population and n_e is the bunch density as given in Eqn. 5.16. The strength of the sheath electric field may now, finally, be determined as a function of the electron temperature and the Debye length, expressed mathematically as

$$E_s = \frac{k_B T_e}{e\lambda_D}, \tag{5.18}$$

where the parameters take their previously defined meanings. This peak field strength, for typical experimental parameters, is calculated to be of the order of TV m^{-1}. It is important to note here that the temporal evolution of the sheath field is not included in this model, with the field assumed to take a peak value for the duration of the interaction. This field strength may now be converted into the 'escape' kinetic energy, which is convenient for comparing with the energies of the fast electrons in order to determine if an electron of a given energy will escape the field at the rear surface or remain trapped. This 'escape' energy can be expressed as

$$K_{esc} = eE_s d_s, \tag{5.19}$$

where d_s is the longitudinal extent of the sheath field at the target rear, estimated to take a value of $d_s \sim 10$ μm [177]. The escape energy is plotted as the dashed vertical lines alongside electron energy spectra representative of the F/3 and F/1 focusing geometries in Fig. 5.6 (a). It can be seen that for the higher intensity (and therefore temperature) F/1 case, the escape energy increases compared with the F/3 case. This is offset however by the increase in electron numbers at higher kinetic energies, thus resulting in an overall decrease in the refluxing fraction.

The validity of this refluxing model can be tested using two methods. Firstly, comparison of the escape energy with the peak values predicted in a previous study presented in Link *et al.* [178], using a more complex capacitor model, show similar values. Whilst the simple model used here does not include the temporally evolving dynamics included in the capacitor model, agreement of the peak field values predicted is encouraging. It is however obvious at this point to ask if the temporal evolution has a significant effect on the refluxing fraction.

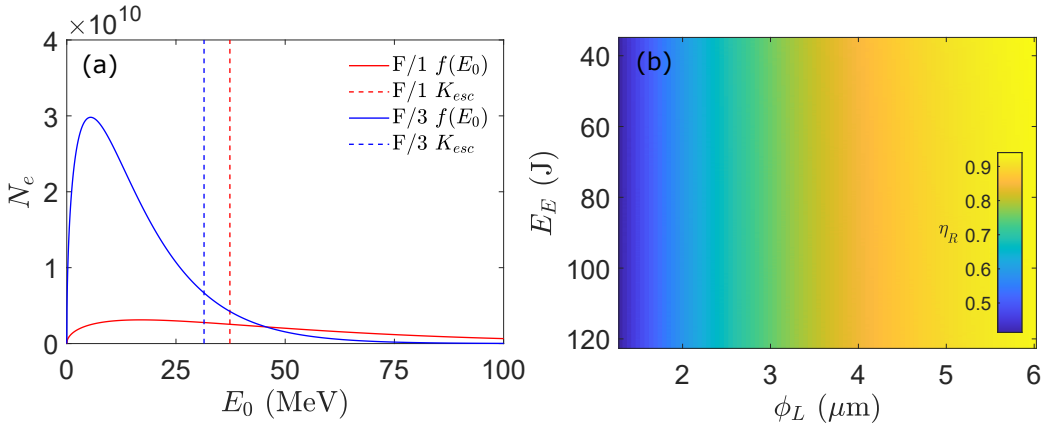

Figure 5.6: (a) Representative electron energy spectra $f(E_0)$ of the F/3 and F/1 cases, shown in blue and red solid lines respectively, assuming a ponderomotive temperature scaling. The escape kinetic energy K_{esc} is shown in dashed lines for each case. (b) 2D parameter space of electron refluxing fraction η_R with E_E and ϕ_L. The ponderomotive temperature scaling is used for this example case.

A similar capacitor model was presented in Myatt *et al.* [175], and refluxing fractions for a range of intensities were plotted, where the electron temperature was assumed to scale according to the ponderomotive scaling shown in Eqn. 5.1. A 2D parameter space is presented in Fig. 5.6 (b), showing the variation of refluxing fraction with laser energy and focal spot size, where the intensity range is similar to that used in Myatt *et al.* [175], also using the ponderomotive temperature scaling. The refluxing fractions predicted in the model developed here agree with those reported in Myatt *et al.* [175] across the range of comparable intensities explored, indicating that the fixed field approximation has a minimal impact on the resulting refluxing fraction. For example, at an intensity of $\sim 2\times10^{20}$ Wcm^{-2}, corresponding to the nominal intensity achieved for the reported central pulse values in section 5.3 ($E_E = 92$ J and $\phi_L = 4.5$ μm), the calculated refluxing fraction is $\sim$ 87%. From Myatt *et al.* [175], assuming a capacitor (and thus target) radius of 1 mm (same transverse dimension as experimentally employed targets), the predicted refluxing fraction using the temporally evolving capacitor model is $\sim$ 90%.

One further assumption which must be considered is that electrons may only escape from the target rear during their first pass. Should they be trapped and recirculated at this time, they will remain so for the remainder of the interaction.

This assumption is justified based on the evolution of the sheath field strength at the target rear, and the loss of kinetic energy by the fast electrons as they propagate through the target. Firstly, the sheath field strength is fixed throughout the interaction in the model. This is an assumption made to simplify the model. In reality the field will evolve temporally throughout the course of the interaction, but for the timescales of interest (a few picoseconds [83]), the field will only increase in strength until it saturates at the peak of pulse, whereupon it will remain approximately fixed for the remainder of the interaction [178]. As such, if the electron is not energetic enough to escape the field on the first pass, it is highly unlikely to do so on any subsequent passes of the target. This concept is further reinforced by considering the energetics of the refluxing electrons. As discussed in section 5.4.1, the electrons will lose energy as they propagate through the target, through a combination of collisional and radiative processes. As such, the energy of an electron on the second pass of the target will be less than on the first, thus preventing escape. It is, in principle, possible for the refluxing electrons to re-gain energy from the laser pulse as they re-interact with the laser at the front surface of the target, as pointed out in Gray *et al.* [76], but only if they return within the bounds of the focal spot of the laser and temporally during the pulse. A brief estimation of electron divergence shows that this is unlikely to occur for the laser and target parameters employed in this study. If we take a 'test' electron, originating from the centre of the laser focal spot, and calculate its path through the target using Eqn. 5.15, assuming ballistic transport and a divergence angle of $\theta_{Div} = 25°$ [177], we find that it will return to the front surface a distance of ~ 23 μm from its point of origin. Given the largest focal spots employed in this investigation have a spot radius of ~ 3.5 μm, it is clear that the vast majority of refluxing electrons will return well outside the FWHM of the laser focal spot, and thus re-gain minimal energy.

It is vital that the refluxing of electrons within the target is properly accounted for, as it is these electrons which will primarily contribute to the yield of K_α photons. From Fig. 5.6, it is clear that across the parameter space investigated, large variations in refluxing fraction may occur. Without due cognisance of this

behaviour, accurate estimation of the K_α photon yield, and thus by extension the temperature of the fast electrons, is rendered impossible.

5.5 Experimental results and analysis

5.5.1 K_α photon yield

This section presents the findings relating to the production of copper K_α photons in the interaction of the laser pulse with 25 μm thick copper targets. The raw measurements are reported, and the process of adapting these into a more usable form will be discussed. Finally, these experimental results will be compared with the results of the analytical model outlined previously, using the temperature models explored in section 5.2. Measurements made using the larger focal spot (and F-number) case will be referred to as F/3, whilst the second case, employing smaller focal spots will be referred to as F/1, both relating to the focusing F-number used in each case.

To begin, it is necessary to determine the experimentally measured yield of copper K_α photons. Raw example images of this have already been shown in Fig. 5.5. From such images, the signal in PSL may be extracted using the method outlined in Chapter 3.5.4, which is converted into number of photons using the calibration reported in Curcio *et al.* [133]. This measured photon yield is then corrected for the transmission through the mylar and aluminium filters (located in front of the Bragg crystal and before the detector respectively), and for the reflectivity of the Bragg crystal. Finally, the measured signal is scaled to account for the solid angle covered by the detector, to give the final measure of K_α photons emitted per steradian solid angle. This final yield is presented, as a function of peak laser intensity, in Fig. 5.7. In this figure, the F/3 data, shown by the blue circles, represents a focal spot size in the region of $4-5$ μm, and the F/1 data, shown by the orange squares, represents focal spot sizes of approximately $1.4-1.8$ μm. It is important to note that all three laser parameters (focal spot size, laser energy and pulse duration) are varying subtly across these two datasets. The y-

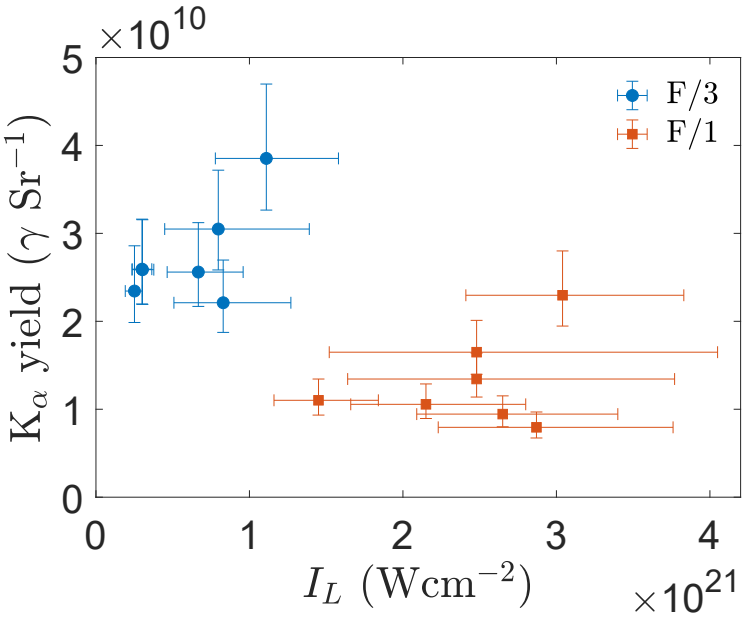

Figure 5.7: Yield of copper K_α photons (in photons per steradian) plotted as a function of peak laser intensity I_L. The F/3 case is shown by the blue circles, and F/1 focusing is shown by the orange squares.

axis error-bars are determined from the uncertainty in the conversion from PSL to photon signal, and the x-axis error-bars are a cumulation of the uncertainties in the measurement of the laser parameters contributing to the calculation of the peak laser intensity. It can be seen that two general trends exist within this data. Firstly, as one moves from F/3 to F/1 focusing, there is a drop in the yield of K_α photons. Secondly, within each dataset (i.e. both F/3 and F/1), there is a general increase in photon yield with increasing intensity, although this is less clear in the F/1 dataset. The combination of these two trends results in the apparent scatter of the data. As such, it is important that the origin of these trends is understood, and some appropriate correction is applied to isolate the spot size related behaviour.

To better understand the physics underpinning these trends, a 2D parameter space was generated, consisting of E_E and ϕ_L . The experimentally measured photon yield in this parameter, normalised to the maximum value measured for convenience, is shown in Fig. 5.8 (a). From this plot a potential issue, which may result in the two competing trends, becomes clear, namely that both the laser focal spot size and encircled energy are varying simultaneously. Further

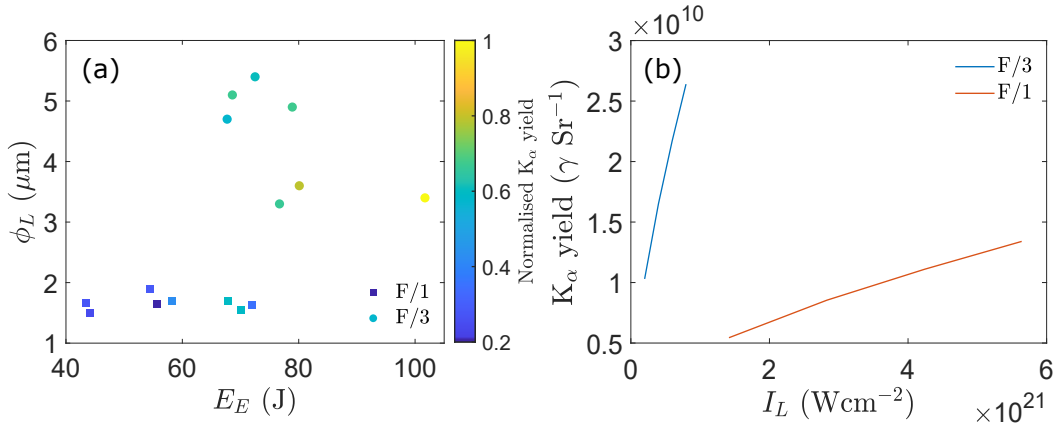

Figure 5.8: (a) Experimental 2D parameter space showing the yield of copper K_α photons, normalised to the maximum measured value, as a function of laser focal spot size ϕ_L and encircled energy E_E. F/3 focusing is shown by the circular data points, with F/1 being shown by the squares. (b) Modelled scaling of K_α photon yield as a function of laser intensity for two fixed focal spot size cases, corresponding to F/3 and F/1 focusing configurations, shown in blue and orange respectively. Within each focusing dataset, the intensity is increased via the laser energy.

investigation was however required to confirm that this scatter in laser parameters does in fact result in the observed data trends.

The developed analytical model was employed in order to further investigate this. Two configurations were modelled, with identical pulse durations and focal spot sizes representative of the F/3 and F/1 focusing geometries. A range of energies were investigated in each case, with the results presented in Fig. 5.8 (b). It can be seen that almost the exact behaviour observed in the experimentally measured photon yield is recovered, with the F/1 case resulting in a generally reduced photon yield compared with the F/3 data, and an increasing trend shown within each respective dataset. The two parameters have a differing influence on the yield of K_α photons due to their role in determining the properties of the fast electron population. Both E_E and ϕ_L directly influence the intensity of the laser pulse, and thus by extension the temperature of the fast electron population. The encircled energy however additionally directly influences the number of fast electrons generated (see Eqn. 5.11). When the intensity is increased via the focal spot size, for fixed total energy, the number of electrons generated is reduced, due to the higher average energies. This temperature increase would also occur for increasing E_E, however the effect of this on the electron numbers is mitigated

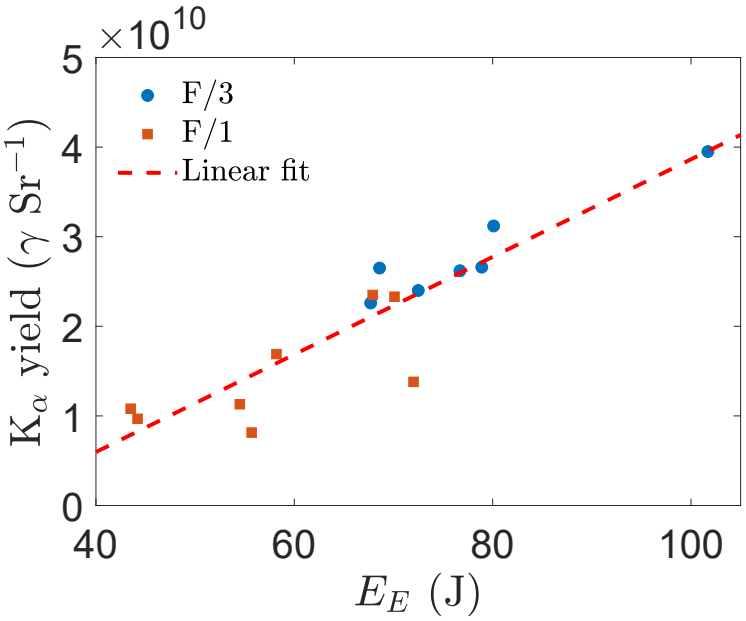

Figure 5.9: Scaling of K_α photon yield with encircled energy E_E. Experimental data for F/3 and F/1 focusing shown by the blue circles and orange squares respectively, with a linear fit to this data shown with the red dashed line.

by the simultaneous energy increase. As a result, increasing intensity via energy results in a higher number of fast electrons than would be obtained for a similar intensity increase driven by focal spot size. The larger electron population subsequently enables a larger yield of K_α photons to be produced. It is therefore clear that the effects of varying intensity via E_E and ϕ_L must be considered separately.

In order to achieve this, the measured yield of K_α photons was plotted as a function of the encircled energy E_E, displayed in Fig. 5.9. The photon yield is shown to scale linearly with E_E for this range of parameters. The form of the linear fit is given by;

$$N_k = 5.4 \times 10^8 E_E - 1.6 \times 10^{10} \tag{5.20}$$

where the R^2 value of the fit is $R^2 = 0.82$. It is clear from the intercept value that as the laser energy approaches zero, this fit breaks down, as the energy is insufficient to generate a significant fast electron population, and thus x-ray yield, but for the range of laser energies explored in this thesis, the fit holds well. It is important to pause at this point to fully consider the implications of this scaling.

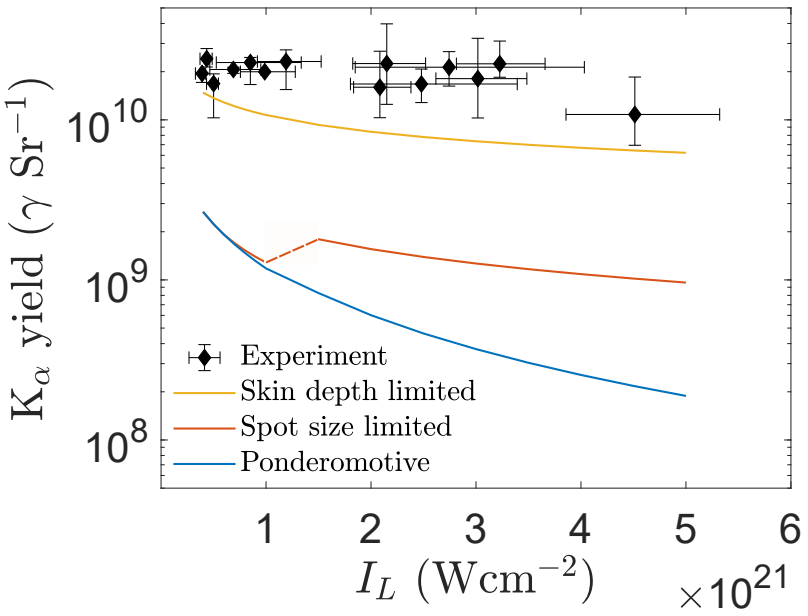

Figure 5.10: K_α photon yield, for both F-numbers employed, following the encircled energy correction process, shown in black. Analytical model results for K_α photon yield, employing ponderomotive, spot size limited and skin-depth limited temperature models are shown in blue, orange and yellow respectively. The dashed portion of the spot size limited case represents a discontinuity where the spot size is changed from $\phi_L = 4$ μm to $\phi_L = 1.5$ μm, in accordance with the experimental parameters.

Given that a linear scaling accurately represents the experimentally measured data, whilst still including the effects of focal spot size, it is clear that the scaling with intensity, driven by the encircled energy, is the dominant factor. This is not surprising due to the differing influence of these parameters on the number of electrons generated, as discussed previously. This once again emphasises that laser intensity must not be considered as an all encompassing parameter, and that the influence of each contributing parameter must be examined separately. Within the range of parameters investigated, the focal spot size has a minimal influence on the yield of K_α photons and so both F/3 and F/1 focusing cases will be considered together from this point forward.

It is clear that the main driver for enhanced K_α photon yields is the encircled energy. However, multi-petawatt laser systems being commissioned currently are adopting short pulse, tight focusing configurations as the means of attaining ultra-high intensities ($> 10^{23}$ Wcm^{-2}), with similar, or reduced, laser energies when compared with the Vulcan PW system. As such, it is important that

the scaling of K_α photon yield, and thus electron temperature, with intensity, independent of laser energy, is investigated. To this end, the linear fit to the measured data, shown graphically by the dashed red line in Fig. 5.9 and expressed mathematically in Eqn. 5.20, was used to take account of the encircled energy scaling and normalise out for it, thus leaving only the scaling with focal spot size. This was achieved by taking the average encircled energy across the full dataset, and scaling each yield value according to the difference in encircled energy between the average and the measured value, using the scaling presented in Eqn. 5.20. The results of this correction process are shown in Fig. 5.10. It is seen that the experimentally measured yield of K_α photons is now unchanging in the intensity range 5×10^{20} to 4×10^{21} Wcm^{-2} (for both F-numbers employed), and drops slightly in the range 4×10^{21} to 5×10^{21} Wcm^{-2} by a factor of ≤ 2.

Comparison of the photon yield measured experimentally with that predicted by the analytical model show a higher yield than calculated using any of the temperature models outlined in section 5.2. Furthermore, the scaling of this yield with intensity is much slower than would be predicted by employing any of the existing temperature models. This can be quantified by performing a power law fit of the form $N_k = aI_L^b$ to the experimental and model data, and comparing the exponent. The experimentally measured photon yield scales with intensity to the power of $b = -0.1 \pm 0.1$. In comparison, the analytical model, when using the ponderomotive temperature model, predicts an exponent value of $b = -0.9 \pm 0.1$, and when employing the ℓ_s-limited temperature model, an exponent value of $b = -0.35 \pm 0.01$. A fit to the spot size limited model is not possible due to the discontinuity resulting from the changing focal spot size. Of the three electron temperature models tested, it is therefore shown that the skin-depth limited case, as set out in Haines *et al.* [48], is the closest in terms of both absolute yield and scaling with intensity, but even this model substantially differs from the experimental measurements of both quantities. This may be the result of some new physics, which is acting to restrict the heating of the plasma electrons to a greater degree than is predicted in Haines *et al.* [48], thus reducing the temperature of the electron population. Some mechanisms

by which this may occur are explored in the following sections. Alternatively, the electron population contributing to the generation of K_α photons may have a multi-temperature energy spectrum, with the lower temperature components essentially lower the average of the full population. Whichever is the case, it is clear that, at these intensities ($> 10^{20}$ Wcm^{-2}), the ponderomotive scaling of electron temperature radically over-predicts the electron temperature, resulting in significantly reduced predicted yields of copper K_α photons when compared with those measured experimentally. This is an important result, as the ponderomotive scaling is still often used as the 'go to' temperature scaling for electron heating at intensities of around 10^{20} Wcm^{-2} and beyond.

Furthermore, the modification to the ponderomotive scaling, proposed in Dover *et al.* [35], to account for the influence of near wavelength focal spots, does not place a strict enough limit on the electron temperature to account for the K_α photon yield measured in this particular case. This result can be rationalised by considering the relative magnitudes of the focal spot size and the plasma skin-depth. From the relativistic model for collisionless skin depth, discussed in section 5.2, the plasma skin-depth is of the order of tens of nanometres for the intensities investigated here. In comparison, the focal spot radii used both in this study, and in that presented in Dover *et al.* [35], are of the order 700-800 nm. As such, it would be expected that the skin-depth would be the limiting factor in the heating of the plasma electrons. Of course, this refers to heating at the boundary between the under and overdense plasma, heating of plasma electrons within the scale length of underdense plasma will also take place, with the temperature of this population likely following the scaling predicted in Dover *et al.* [35].

Thus far we have explored the electron temperature indirectly through observation of its influence on the yield of K_α photons, as predicted by the analytical model. It is however important that we now directly investigate the scaling of this temperature with laser intensity, by converting from photon yield. In order to achieve this, the electron temperature measured experimentally must be estimated, and compared with the temperatures predicted by the models outlined

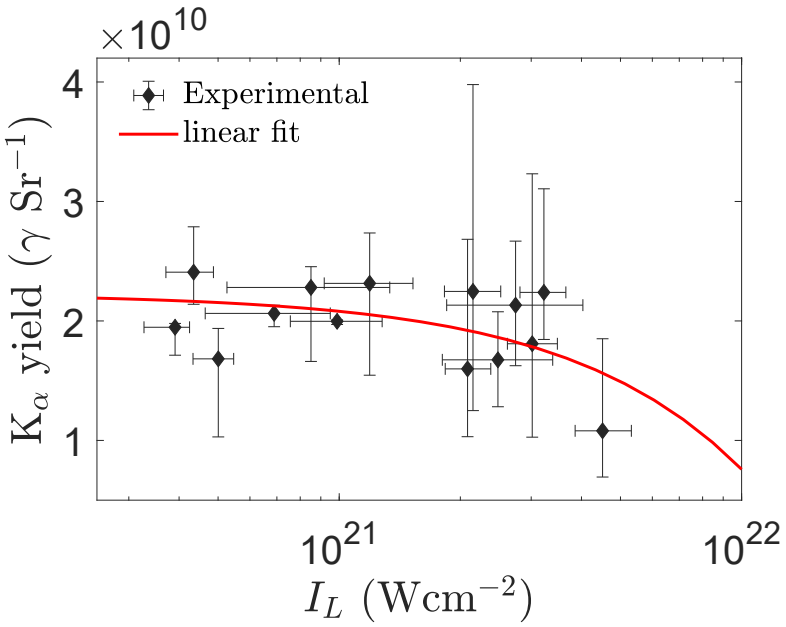

Figure 5.11: Experimentally measured yield of copper K_α photons, shown in black, as a function of laser intensity (shown with a logarithmic x-axis), with a linear fit to this data shown by the solid red line.

previously (see section 5.2). A linear fit to the experimentally measured yield of K_α photons is presented in Fig. 5.11, where a logarithmic scale is used on the x-axis, and is described mathematically by the formula;

$$N_k = -1.5 \times 10^{12} I_L + 2.2 \times 10^{10} \tag{5.21}$$

Due to the scatter in the experimentally measured K_α photon yield, the R^2 value of this fit is $R^2 = 0.27$. This indicates a fairly poor fit, however it remains useful as a means of quantifying the general trend of K_α photon yield with intensity. As with the previous fit, the intercept is not zero, as would be expected physically, but this is purely the result of the fit being limited in the range of its applicability. When the intensity drops below the range considered here, the interaction physics will be substantially altered (for example, below $\sim 10^{18}$ Wcm^{-2}, the electrons will be non-relativistic), and the fit will no longer be valid. As such, this fit may only be applied over the range of intensities considered here. The input electron temperature used in the analytical model may then be tuned until the output yield matches this fit line. The temperatures resulting from this fitting

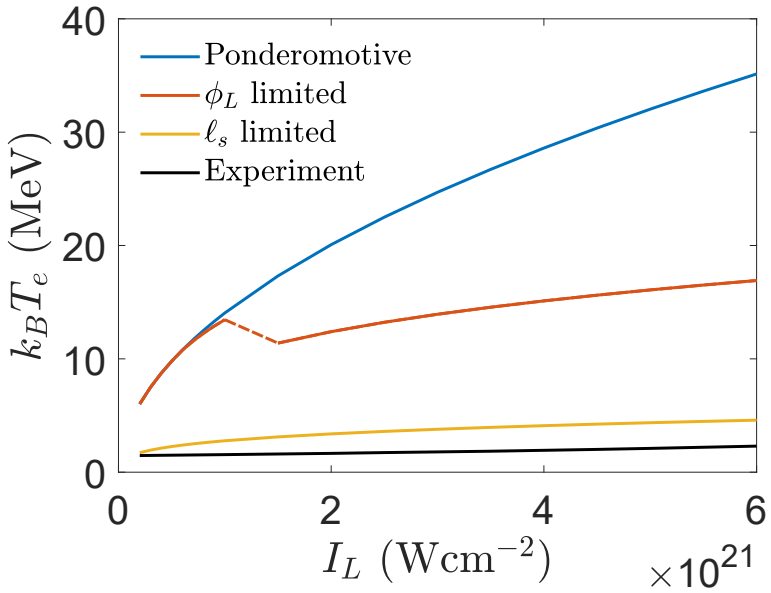

Figure 5.12: Extrapolated fast electron temperature scaling based on experimental fit as a function of laser intensity, shown by the black solid line. Ponderomotive, spot size limited and skin-depth limited temperature models are shown in blue, orange and yellow respectively. The dashed portion of the spot size limited case represents a discontinuity where the spot size is changed from $\phi_L = 4$ μm to $\phi_L = 1.5$ μm, in accordance with the experimental parameters.

process are presented in Fig. 5.12, and are compared with the temperatures predicted by existing scaling laws. It is clear that the ponderomotive and ϕ_L-limited temperature models predict significantly higher electron temperatures across the full range of intensities investigated than is inferred experimentally. If we take an example case for an intensity of 5×10^{21} Wcm^{-2}, we see the ponderomotive and ϕ_L-limited models predict electron temperatures of $k_BT_e = 32.0$ and $k_BT_e = 16.1$ MeV respectively. This is significantly higher than the experimentally inferred value of $k_BT_e = 2.1$ MeV for this intensity. Furthermore, the scaling of electron temperature with intensity measured experimentally is significantly slower than that predicted by the models. This can be most clearly seen when considering the exponent of an applied power law fit to the experimental and model data, again of the form of $y = ax^b$. The ponderomotive temperature scaling yields an exponent of $b = 0.51 \pm 0.01$, compared with the experimentally inferred value of $b = 0.1 \pm 0.3$. A fit cannot be obtained to the ϕ_L-limited case due to the discontinuity, but visually it is clear that this temperature model scales more quickly with intensity than the experimentally measured case.

The skin-depth limited model comes significantly closer to the experimentally inferred temperatures, as would be expected given the previously discussed measurements of K_α photon yield. It can be seen that, for the lowest intensity investigated ($I_L = 2 \times 10^{20}$ Wcm^{-2}), the experimental temperature is similar to that predicted by the ℓ_s-limited model set out in Haines *et al.* [48], $k_B T_e = 1.72$ MeV compared with $k_B T_e = 1.47$ MeV. Such a small difference in temperature is likely below the threshold set by the inherent sensitivity of any detector or diagnostic approach employed. This explains why, for similar laser intensities, previous experimental studies of electron temperature have been shown to be in agreement with the ℓ_s-limited model [61]. As the intensity is increased however, the extrapolated temperature scaling on the experimental fit scales more slowly, resulting in lower temperatures being observed than would be predicted using this model. If we again take an example case for an intensity of $I_L = 5 \times 10^{21}$ Wcm^{-2}, the ℓ_s-limited model predicts an electron temperature of $k_B T_e = 4.4$ MeV, compared with the experimentally inferred value of $k_B T_e = 2.1$ MeV, an increase of almost a factor ~ 2. The scaling of electron temperature predicted by this model may also be compared with the scaling of the experimentally determined fit. The ℓ_s-limited temperature model yields an exponent value of $b = 0.29 \pm 0.01$. Whilst the ℓ_s-limited electron temperature model scales more slowly than the ponderomotive model, and thus is a better representation of the true temperature scaling, it still scales quicker than the scaling of the model fit to the experimental data, which yields an exponent value of $b = 0.1 \pm 0.3$.

It is however clear, from the data presented in Fig. 5.11 and the associated fit, that substantial uncertainties are associated with the experimentally measured copper K_α photon yields, and thus by extension, the inferred fast electron temperatures. The uncertainty on the gradient of the measured linear fit was determined using two independent methods, with the method providing the largest source of uncertainty used in Fig. 5.13, where the shaded region, bounded by the black dashed lines, represents the uncertainty in the extrapolated temperature scaling based on the experimental fit. From this plot, it is apparent that, despite the large uncertainties on the inferred temperature of the fast electrons,

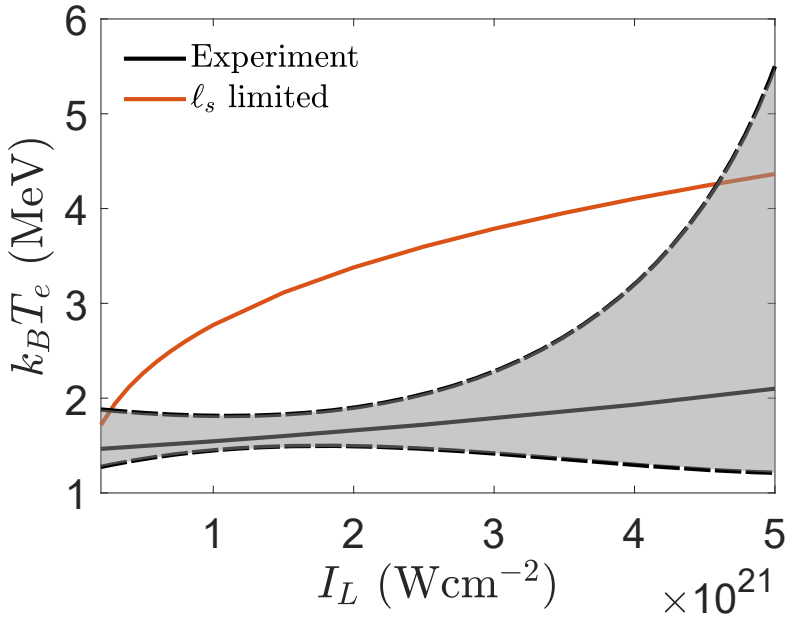

Figure 5.13: Uncertainty in the experimentally determined temperature scaling based on the linear fit shown by black dashed lines, with the temperature itself shown by the black solid line. The skin-depth limited model temperature is shown in orange for comparison.

the skin-depth limited model predicts temperatures greater than the experimentally observed values for almost the full range of intensities explored. This clearly demonstrates that the best predicted scaling of electron temperature falls outside the bounds measured experimentally, indicating that revision/modification of the existing model is required to explain the experimental data.

From the results presented in Figs. 5.10 and 5.12, it is clear that the electron temperature scaling presented in Haines *et al.* [48] is the closest temperature scaling to that exhibited by the experimental measurements, but still fails to capture the exact scaling of the electron temperature. This would suggest that even if the skin depth is partly responsible for the slower temperature scaling, some significant revisions must be made in terms of the interaction physics. It is therefore important that we consider potential additional physics, which may account for the alteration in electron temperature within this intensity range.

5.6 Intensity dependent modifications to the skin-depth limited temperature scaling

In this section, possible modifications to the skin-depth limited model of electron temperature are investigated using analytical and numerical approaches. We will consider two possible cases, each providing an alternative description of the physics resulting in the reduction in electron temperature. In the parameterised version of the skin-depth limited temperature model given in Eqn. 5.3, it can be seen that the temperature depends on the peak laser intensity and the plasma critical density. With regards to the density, it is assumed that the density within the skin-depth is equal to the critical density. Scenarios are explored here where relativistic effects or radiation pressure driven compression result in densities higher than critical within the skin-depth.

5.6.1 Relativistically corrected critical density

The first scenario relies on a well understood aspect of relativistic laser-solid interactions. Assuming the laser pulse is incident normal to the target, as is the case in the experimental measurements, the density at which it will reflect is given by the critical density n_c (see Chapter 2.4.4). In the case where the laser pulse is relativistically intense, the critical density is modified by relativistic effects, expressed as $n_h = \gamma n_c$, where γ is the peak relativistic correction factor such that;

$$k_B T_e = m_e c^2 \left\{ \left[1 + \frac{2}{m_e c} \left(\frac{m_e I}{n_h c} \right)^{1/2} \right]^{1/2} - 1 \right\}. \tag{5.22}$$

In the weakly relativistic case, this correction factor is very small and thus the temperature predicted by Eqn. 5.3 will be correct, within the bounds set by the uncertainties on any experimental measurements. As the laser intensity is increased however, into the intensity range investigated here, this correction becomes significant in magnitude (for $I_L = 10^{20}$ Wcm^{-2}, $\gamma \sim 6.3$ and for $I_L = 10^{21}$ Wcm^{-2}, $\gamma \sim 19.8$), resulting in the plasma density within the skin-depth region

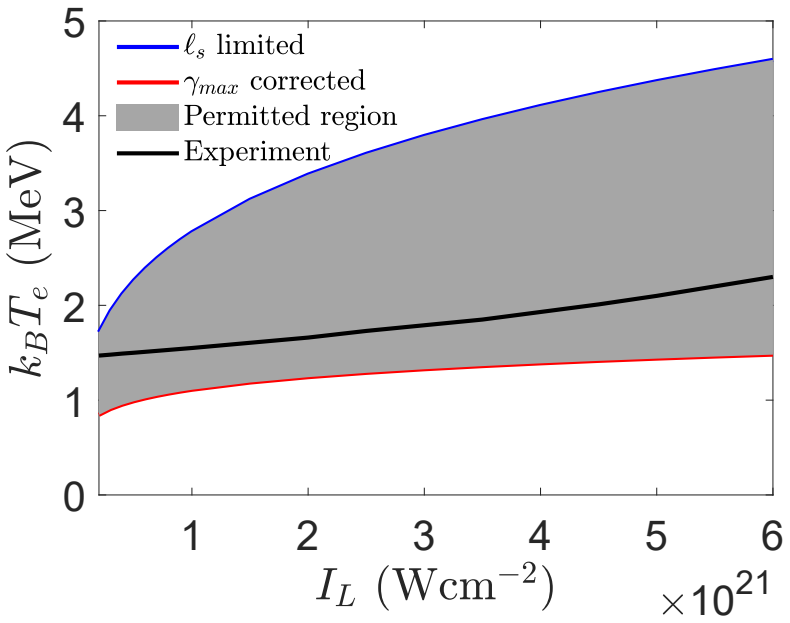

Figure 5.14: Extrapolated electron temperature determined from the fit to the experimental data, Eqn. 5.21, shown in black. The grey shaded area represents the range of electron temperatures predicted based on a γ correction to the critical density, with the $\gamma = 1$ case shown in blue and the γ_{max} case shown in red.

being increased by a similar factor. Such an increase in n_h, scaling with intensity, will result in a lower than expected electron temperature (see Eqn. 5.22), and a slower scaling with intensity, as observed experimentally.

The effect of this gamma correction on the electron temperature is shown in Fig. 5.14. The extrapolated temperature scaling from the experimental data is shown in black, with the unmodified skin-depth limited model plotted as the solid blue line. The unmodified model corresponds to the case where $\gamma = 1$, thus having no impact on the electron temperature. The lower solid line in Fig. 5.14, displayed in red, corresponds to the greatest possible density achievable solely due to the γ correction, assuming all electrons are accelerated to their maximum velocity, corresponding to $\gamma_{max} = (1 + a_0^2/2)^{1/2}$, for linear polarisation. Due to the limiting effect of the plasma skin-depth, preventing the plasma electrons from experiencing a full cycle of the laser pulse, most electrons will achieve a peak γ significantly less than this maximum possible value. Furthermore, individual electrons will experience a different field magnitude due to their relative phase to the laser pulse. This will result in a range of peak γ values, and since this is

equivalent to temperature, it is impossible to definitively state the exact resulting temperature of the electron population. We can, however, define the range of temperatures possible for a given intensity, shown by the shaded area of Fig. 5.14, which is bounded by the limits imposed by the $\gamma = 1$ and γ_{max} curves. We find that the experimentally inferred values of electron temperature fall within the bounds predicted by using the modified skin-depth limited model, indicating that this approach can provide an explanation of the physics underpinning the generation of fast electrons in laser-solid interactions.

5.6.2 Laser pressure driven density compression

In the second possible scenario, we explore the concept that as the laser intensity is increased, the growing radiation pressure results in the plasma at the front surface being compressed [179] (see Chapter 2.7.2), thus increasing the electron density within the skin-depth region. Additionally, any underdense plasma forming the density ramp at the target front surface may be swept up and driven into the skin-depth region, further increasing the density. Such an increase in density would lead to a lowering of the electron temperature, as observed experimentally. The possibility of such a density compression effect at the target front surface was investigated analytically using the model outlined in section 5.4 and numerically using the PIC code EPOCH [136].

Firstly, the analytical model is used to determine the magnitude of the density driven compression required to correct the electron temperature such that it now fits the experimentally measured photon yield. As such, we introduce a correction factor ψ to the critical density in Eqn. 5.3, given by;

$$k_B T_e = m_e c^2 \left\{ \left[1 + \frac{2}{m_e c} \left(\frac{m_e I}{\psi n_c c} \right)^{1/2} \right]^{1/2} - 1 \right\}. \tag{5.23}$$

By setting ψ as a free parameter and fitting the resulting electron temperature to the experimentally estimated values, the required density compression can be determined. This is shown, normalised to the density compression factor of the

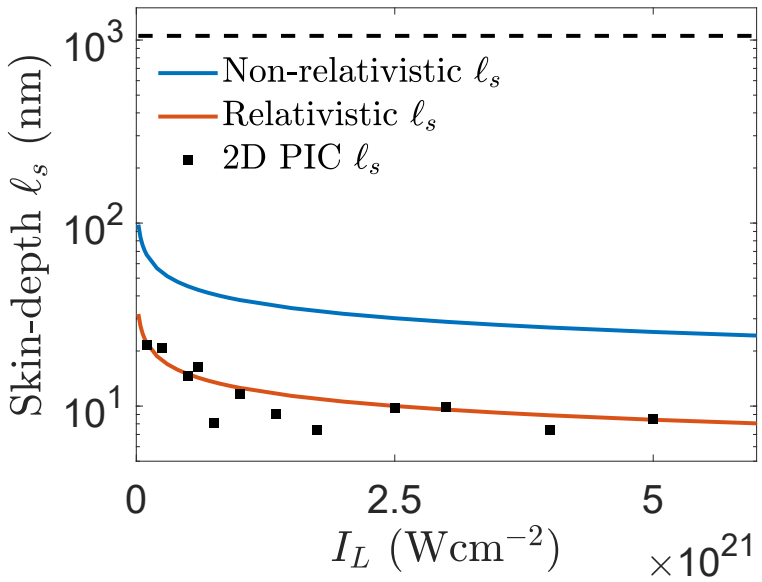

Figure 5.15: Comparison of analytically calculated skin-depth, for both the non-relativistic and relativistic cases (blue and orange respectively), with the skin-depth measured from 2D PIC simulations, shown by the black squares. The black dashed line represents the laser wavelength.

lowest intensity explored experimentally ($\sim 3 \times 10^{20}$ Wcm^{-2}), in Fig. 5.16, represented by the solid blue line. From this it is evident that the density compression factor at the highest intensities explored is approximately $\times 3.5$ higher than at the lowest intensity. A density compression of this magnitude is only postulated however, as that factor is required to make the model predictions match experiment.

In order to investigate whether such a compression at the target front surface can realistically occur in a laser-plasma interaction of this nature, and that the compression results in electron temperatures similar to those measured experimentally, a series of 2D PIC simulations were used. The PIC simulations were performed using the 2D version of EPOCH [136]. The simulation box was set to have dimensions of 15×20 μm, corresponding to 7500×5120 simulation cells. Only the front 5 μm of the target is simulated to reduce computational expense. This is an appropriate choice as we are only interested in the dynamics of the plasma in the region near the front surface. The boundaries were set to free space, with the exception of the z_{max} boundary (where z is the laser propagation axis), which was defined as a heat bath, enabling particles to re-enter the simulation

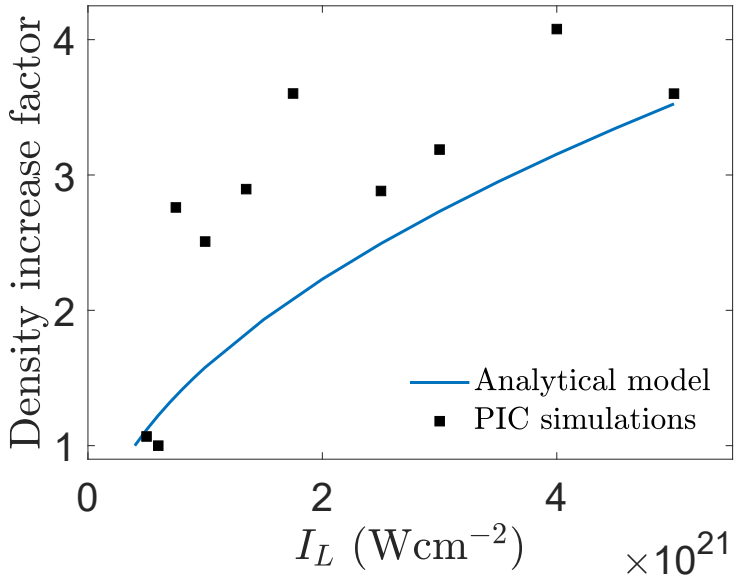

Figure 5.16: Electron density compression factor, normalised to the density of the lowest intensity case, as a function of peak laser intensity. The solid blue line represents the density compression obtained from the analytical model, required to fit to the experimentally measured electron temperatures. The black squares are the density compression factors observed from 2D PIC simulations.

box. This is designed to represent the ability for particles to enter from the unsimulated remainder of the target. The targets were initialised with a population of Al^{11+} ions, with an initial temperature of 10 eV. Aluminium ions were used as opposed to copper as these have been extensively benchmarked in previous simulations. Furthermore, the lower electron density resulting from the use of Al ions reduces the computational expense of the simulations. PIC simulations are generally unable to provide exact results, primarily being used to show trends and general behaviour, and using Al ions will likely have a minimal effect on the trends. An electron density of $777n_c$ was defined, with an initial electron temperature of 1 keV. This electron temperature was chosen to prevent numerical heating of the plasma due to an unresolved Debye length at early times if the initial temperature was set too low. Higher starting temperatures would result in expansion of the plasma prior to the arrival of the laser pulse. The simulations were run with the highest practical spatial resolution, limited by the available computational resource.

The laser pulse was normally incident to the target and was initialised with the

polarisation vector orthogonal to the plane of the simulation. This polarisation state was chosen following test simulations using polarisation states both in the plane of the simulation, and orthogonal to it. In the simulations where the polarisation was in the plane of the simulation, electron heating was exaggerated by the generation of dense bunches of electrons, which are stripped from the edges of the heavily curved target front surface, in a similar mechanism to that outlined in Duff *et al.* [146]. These bunches are then directly accelerated by the laser, resulting in energy gains otherwise infeasible due to conventional heating mechanisms. Due to the 2D nature of the simulations, this process is exaggerated, as the electrons are confined purely within the polarisation plane, and so are stripped and accelerated with enhanced efficiency. To counter this effect, we employ a polarisation state orthogonal to the plane of the simulation, as the electrons will no longer be stripped from the edges of the deformed front surface, resulting in a more realistic electron heating process. Furthermore, the laser being normally incident on the target minimises the differences in absorption between the two polarisation cases, ensuring that the simulations performed are the best representation of the realistic interaction physics we can achieve. By using a polarisation state out of the plane of the simulation however, we induce the opposite behaviour to that which we are trying to prevent, in that electron heating will be artificially suppressed in this case. This must be considered when comparing the 2D PIC temperatures with those inferred experimentally.

As the physics underpinning this model of electron temperature is dependent on the plasma skin-depth, this is the region of the simulated plasma in which the density is of interest. The density beyond the skin-depth is likely to have a minimal influence on the heating of electrons, as the laser is unable to penetrate this deeply into the plasma. Before exploring the density within the skin-depth, it is useful to discuss the magnitude of the skin-depth. If the skin-depth measured using the 2D PIC simulations were to be different to that of the analytical model, this could provide an explanation of the differences in temperature scaling. The simulated skin-depths, for laser intensities of $10^{20} < I_L < 5 \times 10^{21}$ Wcm^{-2}, are shown in Fig. 5.15 by the black squares, and are compared with the theoretically

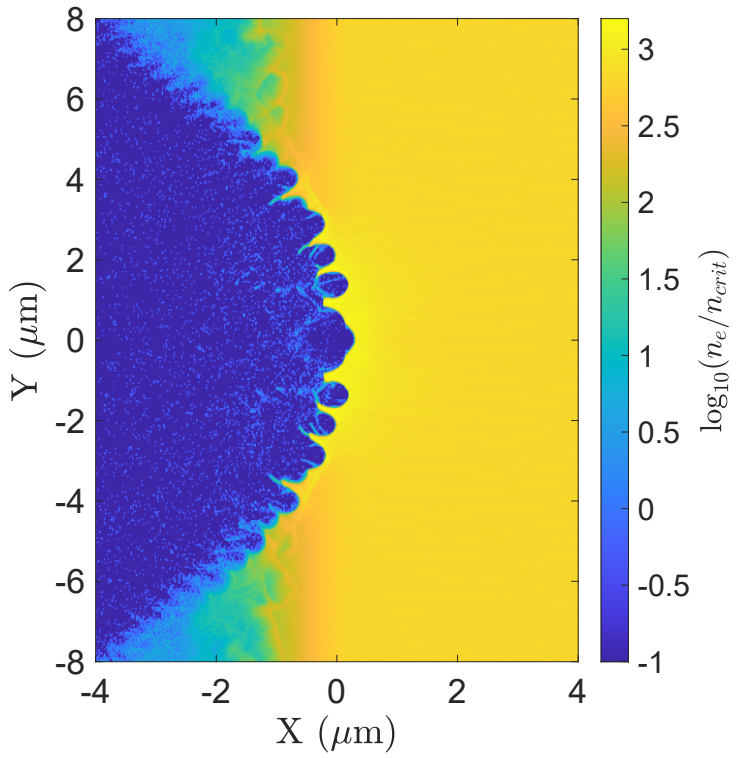

Figure 5.17: 2D map of electron density, normalised to the critical density, presented using a logarithmic colour scale. The polarisation of the incident laser pulse was orthogonal to the plane of the simulation and the intensity was $I_L = 10^{21}$ Wcm^{-2}. This density snapshot was taken at $t = 0$, i.e. when the peak of the pulse interacts with the target.

predicted values. The simulated skin-depth values are in good agreement with those predicted by the relativistically-corrected model. This indicates that the skin-depth itself is not the driver for any measured temperature changes, which must therefore be dependent on the properties of the plasma within that region.

The plasma density within the skin-depth was determined for a range of laser intensities, matching those of the experimental investigation, from a sub-sample along the central axis of the simulation box, corresponding to the centre of the incident laser focal spot. The density compression factor is shown in Fig. 5.16 by the black points, once again normalised to the density compression factor of the lowest intensity case. The normalised density compression factor is used as compression is exaggerated in 2D PIC simulations, and so the absolute magnitude of the compression would not be expected to agree between experiment and simulation in this case. Whilst the absolute value of the density compression may not be determined, the rate of scaling inferred from experiment, via the analytical

model, may be compared with the 2D PIC simulations. It can be seen that the scaling of the density compression observed in the 2D PIC simulations is similar to the value taken by the free parameter ψ in the analytical model when fitted to the experimental data. The rate of scaling determined from the PIC simulations varies slightly from that predicted by the model, with the simulated plasma compressing more quickly at lower intensities before slowing down at the higher end of the investigated intensity range. If, as performed previously, a power law fit is applied to the PIC density scaling, the density correction factor is found to scale with I_L to the power $b = 0.4 \pm 0.2$. The large uncertainty however is a result of the scatter in the data obtained from the PIC approach, and when the power law fit is applied, the exponent of the analytical model, $b = 0.49 \pm 0.01$, lies within the bounds of the uncertainties on the PIC exponent. This scatter results from the formation of large-scale, instability driven modulation structures on the plasma front surface, as shown for an intensity of 10^{21} Wcm^{-2} in Fig. 5.17. These structures are likely Raleigh-Taylor-like instabilities [96], which occur when a light fluid, in this case the laser pulse, pushes into a heavier fluid, the plasma. Depending on the position of these modulations relative to the sub-sampled region, a small but significant variation in density is induced. Such structures have been observed previously in PIC simulations employing *s*-polarised laser pulses, for example in Wilks *et al.* [28], and have been attributed to perturbations in the critical surface resulting from electron motion in the preceding underdense plasma.

We have thus far shown that a density compression similar to that expected from the experimental data (via the analytical model), can indeed occur during such interactions. We must however still explore if such a density compression will result in a reduction in electron temperatures as expected from the experimental/analytical results. From examination of the spectral properties of the electrons within the sub-sampled region, we find that the electron spectrum has a complex, multi-temperature shape, depending on the energy region examined. It is assumed that the energy region of the fast electron spectrum which contributes primarily to the production of K_α photons is the $1 < E_0 < 10$ MeV energy range.

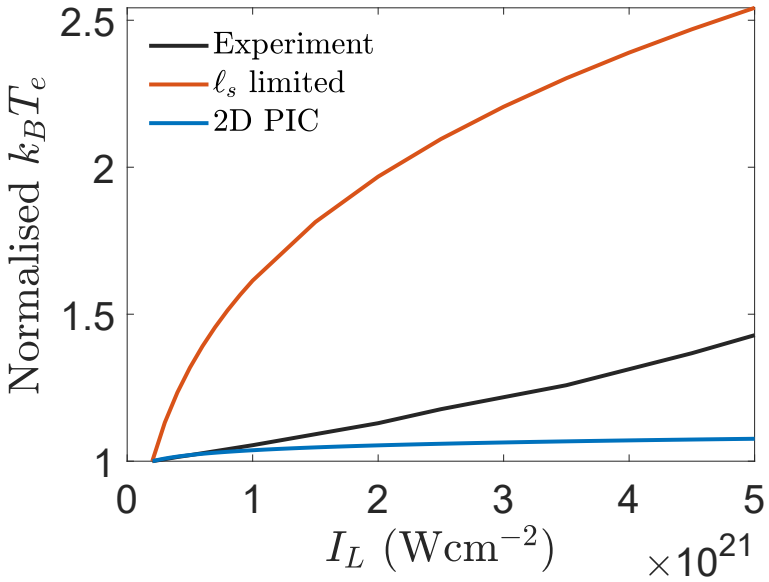

Figure 5.18: Comparison of fast electron temperature scaling with laser intensity. All temperatures are normalised to the lowest intensity case of each dataset. The extrapolated temperature scaling based on the experimental fit is shown in black, with the skin depth limited model shown in orange and the 2D PIC results in blue.

Electrons with energy $E_0 < 1$ MeV are assumed to form the population of 'bulk' electrons, and thus will not form part of the fast electron current. Even within this limited energy window of $1 < E_0 < 10$ MeV however, multiple temperatures may be defined, i.e. different temperature fits match the data better in different parts of the spectrum. It is impossible to determine exactly which of these temperatures is dominant, in all likelihood, the effect of all these temperatures will combine in some way when considering the yield of K_α photons. Furthermore, due to the 2D nature of the simulations, the exact magnitude of the temperature of fast electrons is unlikely to exactly match the experimentally determined values. As such, we instead examine the scaling of the fast electron temperature with intensity, and in order to account for the multiple temperatures, we take the average scaling of the temperatures over the range $1 < E_0 < 10$ MeV. This is feasible as the scaling of fast electron temperature is similar across this range of energies, in spite of differences in the magnitude of the temperature. The scaling of this temperature is presented in Fig. 5.18, and is compared with the experimentally inferred temperatures, and those predicted by the skin-depth limited model. In this figure, the temperature of fast electrons in each case has been nor-

malised to the temperature of the lowest intensity case, in order to enable easy comparison of the rate of scaling. It is apparent that the scaling observed from the PIC simulations is significantly slower than the skin-depth limited model, being more representative of the flatter scaling observed experimentally. The scaling of the temperature with intensity from the PIC simulations is remarkably flat, with the temperature increasing minimally for an intensity increase of greater than an order of magnitude. This is however not entirely unexpected due to the combination of the laser polarisation acting out of the plane of the simulation and the exaggerated compression in 2D mentioned previously, which will both act to artificially suppress the heating of electrons in the PIC simulations.

5.7 Experimental results and analysis - Maximum proton energy scaling in the TNSA regime

In the previous section, the scaling of electron temperature, as inferred from measurements of K_α photon yields, was discussed. The electron temperature scaling determined was found to be significantly different from that predicted by the commonly used ponderomotive scaling, and more in line with a skin-depth limited approach, which we find can be improved by considering relativistic corrections or radiation pressure induced compression, acting to increase the density within the skin-depth layer. In order to provide further evidence of the generated electron temperatures, a second, independent approach to determine the electron temperature is required to verify the findings.

To achieve this, the maximum kinetic energy of protons accelerated via the TNSA mechanism from the interaction of a high intensity laser pulse (using F/3 and F/1 configurations) with 6 μm thick aluminium targets was measured using RCF spectroscopy (see Chapter 3.5.1), with the results shown by the black diamonds in Fig. 5.19. A power law fit of the form $\epsilon_p = aI_L^b$ was applied to the data, shown by the solid red line, showing that the maximum proton energy scales with peak laser intensity to the power $b = 0.22 \pm 0.06$. In order to relate the measured maximum proton energies to the electron temperature, the model set out in Mora

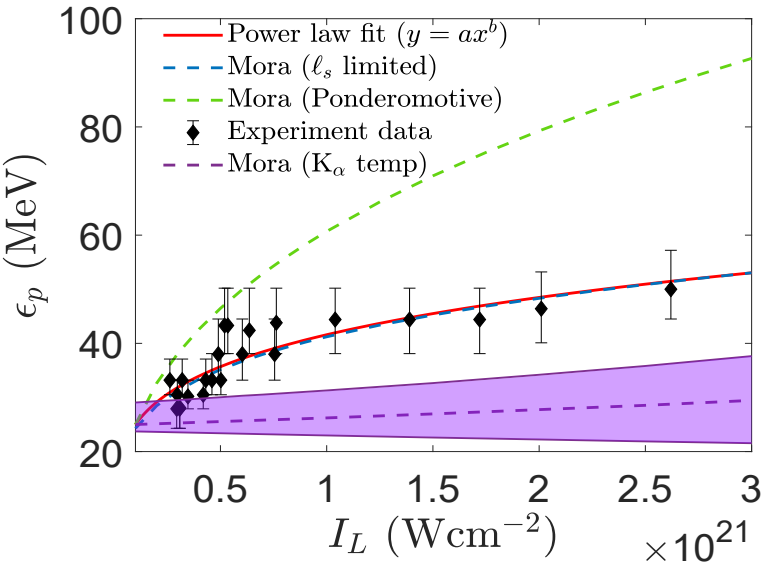

Figure 5.19: Experimentally measured proton energies shown in black, with a power law fit to this data of the form $\epsilon_p = aI_L^b$ shown by the solid red line. The predictions of the Mora model, employing electron temperatures given by the ponderomotive and ℓ_s limited models, are shown in green and blue respectively. The electron temperature inferred from the K_α measurements are shown in purple, with the shaded area representing the uncertainties.

[80] was used (as discussed in Chapter 2.7.1), where the maximum proton energy may be calculated using;

$$\epsilon_p = 2q_i k_B T_e \left\{ \ln \left[\tau + \left(\tau^2 + 1 \right)^{1/2} \right] \right\}^2, \tag{5.24}$$

where q_i is the ion charge, $k_B T_e$ is the electron temperature and τ is the acceleration time, given by $\tau = 0.55\omega_{p,i}\tau_L$ [83]. The ion plasma frequency is given by $\omega_{p,i} = \left[n_i \left(q_i e \right)^2 / \epsilon_0 m_i \right]^{1/2}$, where $n_i = n_e / q_i$ is the plasma ion density.

The predictions made using this model, employing the electron temperature scalings given in Eqns. 5.1 (ponderomotive) and 5.4 (ℓ_s-limited), are shown in Fig. 5.19 by the green and blue crossed data-points respectively. It can be seen that the experimentally measured scaling of proton energies with laser intensity is consistent with the skin-depth limited electron temperature case. This can seen quantitatively by performing a power fit to the proton energies calculated by the Mora model, of the form used in Fig. 5.19, and comparing the exponent to the experimentally measured value of $b = 0.22 \pm 0.06$. The exponent predicted when using the ℓ_s limited temperature model is given by $b = 0.23 \pm 0.01$, in good

agreement with the experimentally measured value. The proton energy scaling predicted using the ponderomotive model is faster, over-estimating the proton energies by an increasing margin as the laser intensity is increased. This can be seen more clearly by again considering the magnitude of the exponent, which in this case takes the value of $b = 0.38 \pm 0.01$. This is significantly larger than the experimentally measured value, resulting in a more rapid scaling with laser intensity.

When the electron temperatures inferred from the measured copper K_α yield are inserted into the same model for proton acceleration however, it can be seen that the calculated proton energies, shown in purple in Fig. 5.19, differ significantly from the experimentally measured values. The proton energies predicted using the K_α inferred electron temperatures are lower than those observed experimentally, and lie outside the bounds of the uncertainties on the experimental measurement. Furthermore, the scaling of the proton energies with increasing intensity is slower than the experimentally observed scaling. This would indicate that the population of electrons probed by the K_α diagnostic is, at least in part, different from the population contributing to ion acceleration via the TNSA mechanism. This would support the previously posited idea that the electron energy spectrum is best described by multiple temperatures, evidence for which was also observed in the 2D PIC simulations in section 5.6.2. The higher energy electrons, which are the primary driver behind the maximum proton energy measurements, are best described by the skin-depth temperature model set out in Haines *et al.* [48]. Both this population and a lower energy population, described by a different temperature scaling, contribute to the K_α derived temperature scaling.

In spite of the discrepancy between the K_α-derived and proton inferred electron temperature scalings, it is clear that, in this fixed pulse energy case, the scaling of maximum proton energy, generated through the TNSA mechanism, with peak laser intensity, may not be as rapid as previously thought, resulting in greatly reduced maximum proton energies when compared with what would be expected when using the ponderomotive electron temperature model. For example, at a peak laser intensity of 3×10^{21} Wcm^{-2}, the maximum proton energy

is reduced by a factor of ~ 2, when comparing the ponderomotive model with the experimental/ℓ_s-limited scaling. This will likely have significant implications for such studies employing the ultra-high intensity laser systems currently being commissioned, especially when coupled with the reduced acceleration time of short-pulse laser systems. Of course, for intensities beyond 10^{22} Wcm^{-2}, other factors come into play, particularly the influence of radiation reaction [158, 180], which will likely impact the dynamics of laser-solid interactions in a significant manner. At this time however, the influence of such physics is not accessible experimentally for laser-solid interactions, due to insufficiently high laser intensities. In order to fully understand the impact of this new physics on ion acceleration however, it is vital that the underpinning physics in the current regime is well understood as a benchmark.

5.8 Temperature dependent electron refluxing

In previous sections, we have seen that the electron temperature is greatly reduced compared with the ponderomotive scaling under the interaction conditions reported here, and that it scales significantly more slowly with increasing peak laser intensity. This will naturally alter the distribution of the generated electron spectrum, and will therefore change the fraction of the electron population refluxing within the target. Given that the refluxing of electrons is a significant contributor to the production of K_α photons [132], and is an important factor in the general dynamics of a laser plasma interaction [75, 131], it is useful to explore the effect of the measured temperature change on this process.

Two sample modelled electron spectra, representative of the F/3 and F/1 configurations (representing intensities of 2×10^{20} and 2×10^{21} Wcm^{-2} respectively), are shown in Fig. 5.20 (a). From comparison of these spectra with those presented in Fig. 5.6 (a), it can be seen that the escape energy remains the same, regardless of the change in electron temperature. The spectrum however is shifted in both cases, with higher electron numbers at lower kinetic energies. The result of this spectral shift is that the number of electrons with sufficient energy

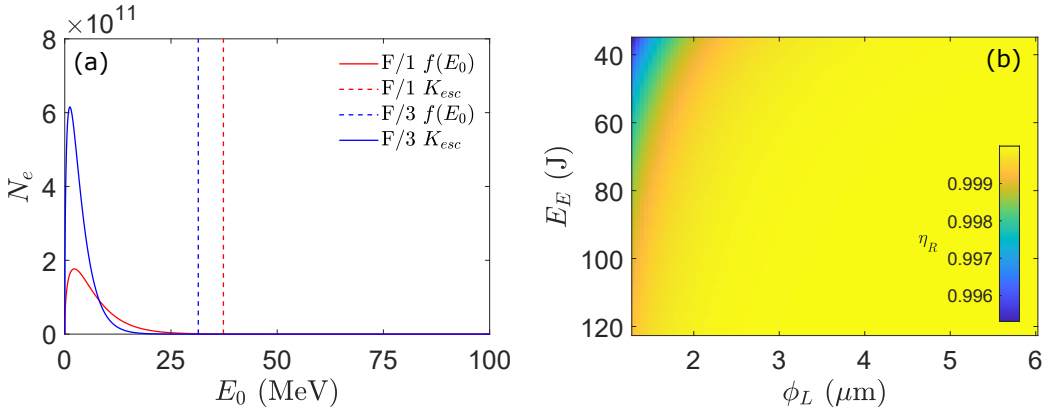

Figure 5.20: (a) Representative electron energy spectra $f(E_0)$ of the F/3 and F/1 cases, shown in blue and red solid lines respectively, assuming a skin-depth limited temperature scaling. The escape kinetic energy K_{esc} is shown in dashed lines for each case. (b) 2D parameter space of electron refluxing fraction η_R with E_E and ϕ_L. The skin-depth limited temperature scaling is again used.

to escape the electrostatic potential established at the target rear is significantly reduced. Furthermore, the reduction in fast electron temperature is such that variations in intensity and laser energy within the range investigated experimentally result in negligible changes in refluxing fraction, as shown in Fig 5.20 (b). This refluxing fraction is significantly higher than if the ponderomotive scaling was used, as in Fig. 5.6 (b). Using the ponderomotive scaling, only approximately $40 - 45\%$ of the electrons will reflux at intensities of 3×10^{21} Wcm^{-2}, with the remainder escaping the target. When the ℓ_s limited electron temperature scaling is assumed however, this fraction increases to $> 99\%$. As such, the vast majority of electrons will remain trapped in the target, resulting in an increased yield of photons through K_α or bremsstrahlung emission processes.

5.9 Conclusions

In this chapter, the scaling of fast electron temperature with laser intensities extending beyond 10^{21} Wcm^{-2} is explored experimentally, analytically and numerically. The intensity enhancement was obtained through the use of a tightly focused laser pulse, achieved by employing a F/1 focusing plasma mirror, with F/3 focusing employed to achieve a lower intensity in the range $10^{20} < I_L < 10^{21}$ Wcm^{-2} for comparison. The electron temperature within the target was deter-

mined using two independent methods. The primary method was the measurement of the emission of K_α photons, which enabled the electron temperature to be inferred via a developed analytical model of K_α photon yield. The secondary method was the measurement of the maximum kinetic energy of accelerated protons via the TNSA mechanism, which provides information about the temperature of the electrons via the Mora model [80]. Results from both diagnostics show a lower electron temperature than would be predicted by the highly cited ponderomotive model presented in Wilks *et al.* [28], with a slower scaling with laser intensity. Electron temperatures and scalings derived from the proton maximum energy are more consistent with the skin-depth limited model set out in Haines *et al.* [48], with the K_α derived data suggesting even lower and more slowly varying temperatures. Possible alterations to the skin-depth limited electron temperature model, based on relativistic corrections to the electron critical density or an intensity driven density compression effect within the skin-depth region are explored, with both found to provide a potential explanation of the lower temperatures / slower scaling. Alternatively, a multi-temperature electron energy spectrum, with each temperature region contributing differently to the production of K_α x-rays and high energy protons, may also result in the apparent discrepancy between the two diagnostics. Ultimately, the exact nature of the internal fast electron temperatures, and the physics underpinning this, remains unclear. Additional future work, including further experimental campaigns using a wider array of diagnostics, will be required to fully understand this important but complex aspect of laser-solid interactions. Finally, the effect of the measured temperature reduction on electron refluxing within the target has been explored, showing a greatly increased fraction of the fast electron population remaining trapped within the target.

This lower temperature scaling may have a substantial impact on the laser-plasma science that will be performed at future, multi-petawatt facilities. Given the difference in pulse durations (i.e. many hundreds of femtoseconds in this study, compared with a few tens of femtoseconds), further investigation is required to determine the extent to which this effect is significant for such pulse durations,

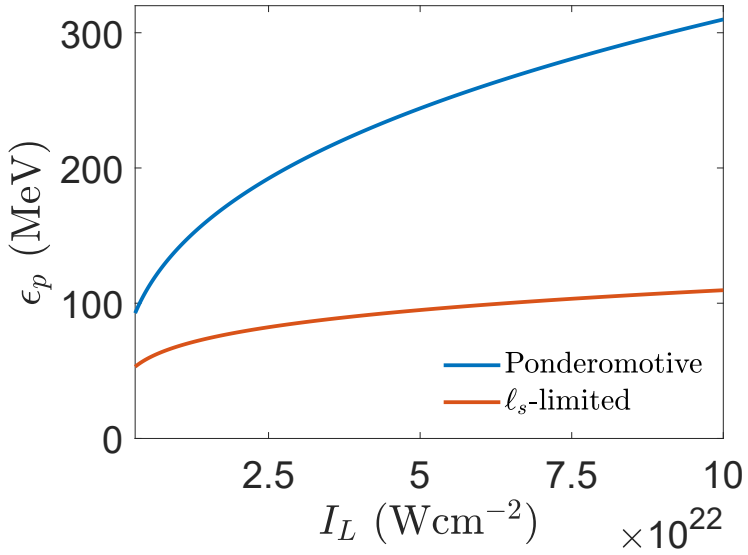

Figure 5.21: Maximum proton energy produced via the TNSA mechanism as a function of peak laser intensity, as calculated by the Mora model, for intensities of up to 10^{23} Wcm^{-2}. The ponderomotive and skin depth limited temperature model cases are shown in blue and orange respectively.

but evidence from other studies employing such short pulse systems, for example Dover *et al.* [35], suggest that some form of temperature limitation may still occur. In particular, laser-plasma processes driven by the heating of plasma electrons, such as the acceleration of protons via the TNSA mechanism [71, 73], or the generation of x-rays via bremsstrahlung radiation [61, 164], will likely scale much more slowly with increasing intensity than would have been previously anticipated. This may result in less significant gains, even when increasing the laser intensity by several orders of magnitude, as a result of the reduced heating effects. This is explored briefly in Fig. 5.21, where the maximum proton energy calculated by the Mora model, for proton acceleration in the TNSA regime, is presented for electron temperatures scaling with the ponderomotive and ℓ_s-limited models. It is shown that, for a peak laser intensity of 10^{23} Wcm^{-2}, the maximum proton energy is reduced by a factor of ~ 3 when the ℓ_s-limited temperature model is employed, compared with the ponderomotive case, when considering acceleration solely due to the TNSA mechanism.

In some circumstances, the limitation to the heating of the plasma electrons may prove beneficial however. For example, electron heating is detrimental to

RPA ion acceleration schemes [86] (see Chapter 2.7.2). Circular polarisation is often used in these scenarios as a means of suppressing the heating of the plasma electrons [57, 88]. The lower magnitude and slower scaling of electron temperature observed here may result in enhanced ion energies via this method when compared with current predictions.

Chapter 6

Conclusions & future work

The objective of the work presented in this thesis was to experimentally investigate the undepinning physics of laser-solid interactions at intensities beyond 10^{21} Wcm^{-2}. These intensities have been achieved through the use of ellipsoidal, focusing plasma mirrors [126, 127], enabling a near-wavelength focal spot to be generated. Over several experimental campaigns, involving a wide range of diagnostic techniques, and supported by numerical and analytical studies, a new understanding of laser-solid interactions in this higher intensity regime has been developed. Specifically, the role of higher laser intensity and a near-wavelength focal spot on proton acceleration in the relativistic self-induced transparency regime, and on electron heating for micron-thick targets was explored. The key findings and conclusions of each of these studies are summarised in this final chapter, with potential future research directions also discussed.

6.1 Laser self-focusing in relativistically transparent, ultra-thin targets

The investigation presented in Chapter 4 builds upon the previous work related to the generation and influence of near-wavelength focal spots presented in Refs. [126, 127, 128] and the acceleration of protons via a transparency-enhanced, hybrid acceleration scheme [26]. In chapter 4, the influence of focal spot size on the acceleration of protons via the mechanism outlined in [26] was explored.

Through comparison of the measured proton beam properties for the F/1 focusing scenario, namely maximum energy and laser-to-proton conversion efficiency, with an F/3 focusing geometry, significant differences in the proton beam properties are observed, with both the maximum energy and laser-to-proton conversion efficiency reduced in the F/1 focusing case. Furthermore, measurement of the recession velocity of the plasma critical surface in the region of the focal spot shows a reduction in velocity when comparing the F/1 and F/3 focusing regimes. The combination of the proton and holeboring velocity results is explained by the larger focal spot undergoing self-focusing as the laser propagates through the target following the onset of RSIT, as shown by 2D PIC simulations. This results in the F/3 focusing case achieving higher peak intensities than the F/1 case, despite the nominally lower initial intensity of F/3 focusing. It is shown that the degree of self-focusing, and thus by extension the intensity enhancement, is dependent on both the incident focal spot size and the thickness of the target foil. Further PIC simulations show that, when self-focusing occurs, the maximum proton energies are in good agreement with those measured experimentally, indicating that transparency-induced self-focusing plays an important role in the acceleration of protons in the transparency regime. These findings highlight the key role played by the laser focal spot for laser-driven proton acceleration in the relativistic self-induced transparency regime. In particular, it is shown that for less than perfect wavefront conditions (such as wavefront curvature), resulting in a reduction in focal spot quality and encircled energy, a larger focal spot size can result in higher peak intensities and maximum proton energies.

As many upcoming laser facilities are considering the use of tight focusing schemes as a route to higher intensities, the effect of self-focusing must be considered. Employing a tight focusing geometry introduces inherent practical challenges, including debris damage to the focusing optic due to the short focal length and sensitivity to wavefront aberrations. This work shows that these challenges may be overcome for picosecond pulse duration systems through the use of larger focal spot, achieving the intensity enhancement instead through focusing within the generated plasma itself.

In future, additional experimental and numerical studies of this mechanism are required to address several outstanding points. Firstly, direct experimental confirmation of self-focusing would be beneficial. This might be achieved through collection and re-imaging of the laser focal spot as it breaks through the transparent target, thus enabling direct measurement of the spot size at the rear surface of the target. Alternatively, the far field of the laser pulse may be imaged following transmission through the target, and the size of this compared for the F/3 and F/1 cases. A second useful point of investigation would be to explore the influence of different means of producing the varying focal spot sizes discussed in chapter 4, specifically the difference between varying the focal spot size at focus compared to defocusing the pulse. The precise details of the contribution of self-focusing to the overall transparency-enhanced hybrid acceleration scheme also remain to be resolve. The spatial location of the peak intensity (i.e. front or rear target surface) would appear to be of vital importance. F/3 focusing, which generates the highest peak intensity following transparency (therefore at the rear of the target), yields higher proton energies than F/1 focusing, where the peak intensity is at the front surface. This points to a potential avenue to further our understanding of the hybrid acceleration mechanism as a whole, by probing the differences in front/rear surface dynamics and how this impacts the proton acceleration mechanism. Finally, additional experimental and numerical investigation regarding the stability of this mechanism is required. The sensitivity to laser conditions remains largely unknown, although the 3D PIC simulations presented in Chapter 4 would suggest that for a 25 fs pulse, the effect of self-focusing is minimal. An obvious question is therefore, what is the minimum pulse duration required for self-focusing to take place, and what changes in the interaction to prevent this?

6.2 Measurement of fast electron temperature for intensities beyond 10^{21} Wcm^{-2}

Chapter 5 reports on an investigation of the scaling of fast electron temperature to intensities of up to $\sim 5 \times 10^{21}$ Wcm^{-2}, again achieved through the use of FPMs to obtain near-wavelength sized focal spots. Laser intensities of up to 10^{21} Wcm^2 where generated using a conventional, F/3 focusing scheme. The fast electron temperature is primarily determined through the measurement of copper K_α emission from 25 μm thick copper foil targets. The yield of K_α photons enable determination of the fast electron temperature through the use of the analytical model outlined in chapter 5. Additionally, measurements of maximum proton energy from 6 μm thick Aluminium targets is used as a secondary, independent measure of fast electron temperature, through the use of the acceleration model set out in Mora [80].

Unlike the results presented in chapter 4, the focal spot size is found to have a negligible impact on the magnitude and scaling of fast electron temperatures, for the explored range of laser and target parameters, with the laser encircled energy being the primary driving factor. When the influence of the laser energy is normalised out, the resulting scaling with intensity is very slowly increasing. This magnitude and scaling is compared with those predicted by existing fast electron temperature models [28, 35, 48], and is found to be in best agreement with the skin-depth limited model outlined in Haines *et al.* [48], with the more frequently used ponderomotive model [28] predicting temperatures that greatly exceed those measured across the full range of intensities explored. However, despite being the best fit, the skin-depth limited model still over-predicts the magnitude and scaling of the fast electron temperature. Modifications to this model are proposed based on a hypothetical increased density within the skin-depth region. Two mechanisms by which this may occur are set out, namely the relativistic correction to the critical density and a radiation pressure induced compression of the skin-depth layer, similar to that outlined in Iwata *et al.* [179]. Both mechanisms

are found to result in a reduction in fast electron temperature and slowing of the scaling with intensity, comparable with that determined experimentally. Alternatively, a multi-temperature electron energy spectrum may also explain the results, with the K_α diagnostic effectively measuring the average temperature of multiple electron populations. This explanation is supported by the observation that the skin-depth limited electron temperature model is found to accurately describe the scaling of maximum proton energies in the TNSA regime.

This result is significant as it shows a limitation to electron heating at high intensities, when the energy of the incident laser pulse is fixed. Furthermore, when the intensity exceeds $\sim 10^{21}$ Wcm^{-2}, the ponderomotive scaling is no longer able to fully capture the physics of the interaction, thus resulting in inflated temperature predictions. This is of relevance to future laser systems, as most, if not all, plan to employ tight-focusing, short pulse schemes to achieve higher intensities, with minimal increase in pulse energy. Many processes of use for applications, such as TNSA and bremsstrahlung, rely heavily on efficient heating of the plasma electrons at the target front surface. If this process is inhibited by the shortened skin-depth, increasing the laser intensity may not result in significant gains in ion energy or x-ray yield. On the other hand, mechanisms such as RPA require heating to be suppressed, and so may be more efficient than previously expected due to the skin-depth induced limiting of electron heating.

The primary question to be answered in further development of this work, is to ascertain the exact nature of the fast electron scaling with intensity, and to pin down the physics underlying this. In chapter 5, two underpinning mechanisms are proposed, supported by numerical and analytical studies, but neither can be directly or conclusively shown to be the cause of the slower scaling of fast electron temperatures. An in-depth investigation is required, involving a combination of new theoretical studies of the heating of electrons for short skin-depth plasmas and further experimental investigation, in order to fully understand the underpinning physics. It is also necessary to determine if a multi-temperature energy spectrum of the internal electron population is the cause of the apparently reduced fast electron temperatures. This may be tested experimentally in

future experiments by using a suite of x-ray diagnostics, each sensitive to different specific ranges of x-ray energies. This would enable regions of the spectrum to be probed separately, as opposed to the K_α measurement made here, which is sensitive to a broad range of electron energies.

6.3 Closing remarks

The work presented in this thesis provides new understanding of the physics of laser-solid interactions beyond 10^{21} Wcm^{-2}, through the use of near-wavelength focal spots. This is a regime which has only recently become accessible, and much of the physics is still not well understood. What is clear however, from the work presented in this thesis, is that future laser systems may perform differently from what would be predicted using existing models. These models were established when peak laser intensities were weakly relativistic, and are thus becoming increasingly obsolete as we transition into a more strongly relativistic regime. As laser facilities capable of generating intensities of up to 10^{23} Wcm^{-2} are currently coming online for operation [85], it is essential that an understanding of the fundamental physics of laser-solid interactions in this regime is quickly established, and the implications for experimental design and long-term research directions are carefully considered. As mentioned previously, due to the intensities achievable by these 'next-generation' laser facilities, QED effects such as radiation reaction will become important [158, 180], which may radically alter the interaction physics. If anything, this however makes having a good understanding of the underpinning physics of laser-solid interactions in the current regime even more important, as this will be required to act as a benchmark for future experimental measurements.

Bibliography

[1] T. H. Maiman. Stimulated optical radiation in ruby. *Nature*, 187(4736):493–494, 1960.

[2] D. Strickland and G. Mourou. Compression of amplified chirped optical pulses. *Optics Communications*, 55(6):447–449, 1985.

[3] A. Macchi, M. Borghesi, *et al.* Ion acceleration by superintense laser-plasma interaction. *Reviews of Modern Physics*, 85(2):751–793, 2013.

[4] H. Daido, M. Nishiuchi, *et al.* Review of laser-driven ion sources and their applications. *Reports on Progress in Physics*, 75(5):056401, 2012.

[5] J. Colgan, J. Abdallah Jr, *et al.* Exotic dense-matter states pumped by a relativistic laser plasma in the radiation-dominated regime. *Physical review letters*, 110(12):125001, 2013.

[6] P. A. Norreys, M. Santala, *et al.* Observation of a highly directional γ-ray beam from ultrashort, ultraintense laser pulse interactions with solids. *Physics of Plasmas*, 6(5):2150–2156, 1999.

[7] B. Dromey, M. Zepf, *et al.* High harmonic generation in the relativistic limit. *Nature physics*, 2(7):456–459, 2006.

[8] B. Dromey, S. Kar, *et al.* Bright multi-kev harmonic generation from relativistically oscillating plasma surfaces. *Physical Review Letters*, 99(8):085001, 2007.

[9] N. Booth, A. Robinson, *et al.* Laboratory measurements of resistivity in

warm dense plasmas relevant to the microphysics of brown dwarfs. *Nature communications*, 6(1):1–5, 2015.

[10] G. Sarri, K. Poder, *et al.* Generation of neutral and high-density electron–positron pair plasmas in the laboratory. *Nature communications*, 6(1):1–8, 2015.

[11] S. Bulanov, T. Esirkepov, *et al.* Oncological hadrontherapy with laser ion accelerators. *Physics Letters A*, 299(2):240–247, 2002.

[12] J. Cole, J. Wood, *et al.* Laser-wakefield accelerators as hard x-ray sources for 3d medical imaging of human bone. *Scientific reports*, 5(1):1–7, 2015.

[13] M. Tabak, J. Hammer, *et al.* Ignition and high gain with ultrapowerful lasers*. *Physics of Plasmas*, 1(5):1626–1634, 1994.

[14] E. Esarey, C. Schroeder, *et al.* Physics of laser-driven plasma-based electron accelerators. *Reviews of modern physics*, 81(3):1229, 2009.

[15] T. White, J. Vorberger, *et al.* Observation of inhibited electron-ion coupling in strongly heated graphite. *Scientific reports*, 2(1):1–5, 2012.

[16] W. Barth, K. Aulenbacher, *et al.* First heavy ion beam tests with a superconducting multigap ch cavity. *Physical Review Accelerators and Beams*, 21(2):020102, 2018.

[17] T. E. Cowan, J. Fuchs, *et al.* Ultralow emittance, multi-mev proton beams from a laser virtual-cathode plasma accelerator. *Physical Review Letters*, 92(20):204801, 2004.

[18] R. Kidder. Application of lasers to the production of high-temperature and high-pressure plasma. *Nuclear Fusion*, 8(1):3, 1968.

[19] J. Nuckolls, L. Wood, *et al.* Laser compression of matter to super-high densities: Thermonuclear (CTR) applications. *Nature*, 239(5368):139–142, 1972.

[20] E. Campbell, T. Sangster, *et al.* Direct-drive laser fusion: status, plans and future. *Philosophical Transactions of the Royal Society A*, 379(2189):20200011, 2021.

[21] J. Sanz. Self-consistent analytical model of the rayleigh-taylor instability in inertial confinement fusion. *Physical Review Letters*, 73(20):2700–2703, 1994.

[22] M. Roth, T. E. Cowan, *et al.* Fast ignition by intense laser-accelerated proton beams. *Physical Review Letters*, 86(3):436–439, 2001.

[23] A. R. Bell, J. R. Davies, *et al.* Fast-electron transport in high-intensity short-pulse laser-solid experiments. *Plasma Physics and Controlled Fusion*, 39(5):653, 1997.

[24] K. Quinn, L. Romagnani, *et al.* Weibel-induced filamentation during an ultrafast laser-driven plasma expansion. *Physical Review Letters*, 108(13):135001, 2012.

[25] R. R. Wilson. Radiological use of fast protons. *Radiology*, 47(5):487–491, 1946.

[26] A. Higginson, R. Gray, *et al.* Near-100 mev protons via a laser-driven transparency-enhanced hybrid acceleration scheme. *Nature communications*, 9(1):1–9, 2018.

[27] D. Doria, K. F. Kakolee, *et al.* Biological effectiveness on live cells of laser driven protons at dose rates exceeding 10^9 Gy/s. *AIP Advances*, 2(1):011209, 2012.

[28] S. C. Wilks, W. L. Kruer, *et al.* Absorption of ultra-intense laser pulses. *Physical Review Letters*, 69(9):1383–1386, 1992.

[29] W. L. Kruer. The Physics Of Laser Plasma Interactions. *Westview Press*, 2003.

[30] P. Gibbon. Short Pulse Laser Interactions with Matter: An Introduction. *Imperial College Press*, 2005.

[31] G. D. Gillen, K. Gillen, *et al.* Light propagation in linear optical media. CRC Press, 2017.

[32] A. Macchi. A superintense laser-plasma interaction theory primer. *Springer Science & Business Media*, 2013.

[33] D. Bauer, P. Mulser, *et al.* Relativistic ponderomotive force, uphill acceleration, and transition to chaos. *Physical review letters*, 75(25):4622, 1995.

[34] E. Startsev and C. McKinstrie. Multiple scale derivation of the relativistic ponderomotive force. *Physical Review E*, 55(6):7527, 1997.

[35] N. Dover, M. Nishiuchi, *et al.* Effect of small focus on electron heating and proton acceleration in ultrarelativistic laser-solid interactions. *Physical review letters*, 124(8):084802, 2020.

[36] C. I. Moore, J. P. Knauer, *et al.* Observation of the transition from thomson to compton scattering in multiphoton interactions with low-energy electrons. *Physical Review Letters*, 74(13):2439–2442, 1995.

[37] M. Göppert-Mayer. Über elementarakte mit zwei quantensprüngen. *Annalen der Physik*, 401(3):273–294, 1931.

[38] G. Voronov and N. B. Delone. Ionization of the xenon atom by the electric field of ruby laser emission. *JETP Letters*, 1(2):66–68, 1965.

[39] P. Agostini, G. Barjot, *et al.* Multiphoton ionization of hydrogen and rare gases. *IEEE Journal of Quantum Electronics*, 4(10):667–669, 1968.

[40] Y. Gontier and M. Trahin. Energetic electron generation by multiphoton absorption. *Journal of Physics B: Atomic and Molecular Physics*, 13(22):4383, 1980.

[41] L. Keldysh. Ionization in the field of a strong electromagnetic wave. *Soviet Physics JETP*, 20(5):1307–1314, 1965.

[42] V. Tikhonchuk. Interaction of a beam of fast electrons with solids. *Physics of Plasmas*, 9(4):1416–1421, 2002.

[43] M. Hegelich, S. Karsch, *et al.* MeV ion jets from short-pulse-laser interaction with thin foils. *Physical Review Letters*, 89(8):085002, 2002.

[44] R. J. Gray, D. C. Carroll, *et al.* Laser pulse propagation and enhanced energy coupling to fast electrons in dense plasma gradients. *New Journal of Physics*, 16(11):113075, 2014.

[45] P. McKenna, D. Carroll, *et al.* Effects of front surface plasma expansion on proton acceleration in ultraintense laser irradiation of foil targets. *Laser and Particle Beams*, 26(4):591–596, 2008.

[46] L. A. Gizzi, E. Boella, *et al.* Enahnced laser-driven proton acceleration via improved fast electron heating in a controlled pre-plasma. *Scientific Reports*, 11(1), July 2021.

[47] D. Rusby, R. Gray, *et al.* Escaping electrons from intense laser-solid interactions as a function of laser spot size. In *EPJ Web of Conferences*, volume 167, page 02001. EDP Sciences, 2018.

[48] M. Haines, M. Wei, *et al.* Hot-electron temperature and laser-light absorption in fast ignition. *Physical Review Letters*, 102(4):045008, 2009.

[49] G. A. Mourou, T. Tajima, *et al.* Optics in the relativistic regime. *Reviews of modern physics*, 78(2):309, 2006.

[50] J. D. Lawson. Laser and accelerators. *IEE Transactions on Nuclear Science*, 26(3):4217–4219, 1979.

[51] P. M. Woodward. A method of calculating the field over a plane aperture required to produce a given polar diagram. *Journal of the Institution of Electrical Engineers - Part IIIA: Radiolocation*, 93(10):1554–1558, 1946.

[52] D. W. Forslund, J. M. Kindel, *et al.* Theory of hot-electron spectra at high laser intensity. *Physical Review Letters*, 39(5):284–288, 1977.

[53] N. G. Denisov. On a singularity of the field of an electromagnetic wave propagated in an inhomogeneous plasma. *Soviet Physics JETP-USSR*, 4(4):544–553, 1957.

[54] J. P. Freidberg, R. W. Mitchell, *et al.* Resonant absorption of laser light by plasma targets. *Physical Review Letters*, 28(13):795–799, 1972.

[55] F. Brunel. Not-so-resonant, resonant absorption. *Physical Review Letters*, 59(52):52–55, 1987.

[56] W. L. Kruer and K. Estabrook. J×B heating by very intense laser light. *The Physics of Fluids*, 28(1):430–432, 1985.

[57] A. P. L. Robinson, M. Zepf, *et al.* Radiation pressure acceleration of thin foils with circularly polarized laser pulses. *New Journal of Physics*, 10(1):013021, 2008.

[58] B. Bezzerides, S. J. Gitomer, *et al.* Randomness, Maxwellian distributions, and resonance absorption. *Physical Review Letters*, 44(10):651–654, 1980.

[59] F. Jüttner. Das maxwellsche gesetz der geschwindigkeitsverteilung in der relativtheorie. *Annalen der Physik*, 339(5):856–882, 1911.

[60] F. N. Beg, A. R. Bell, *et al.* A study of picosecond laser-solid interactions up to 10^{19} Wcm^{-2}. *Physics of Plasmas*, 4(2):447–457, 1997.

[61] C. Chen, J. King, *et al.* A bremsstrahlung spectrometer using k-edge and differential filters with image plate dosimeters. *Review of Scientific Instruments*, 79(10):10E305, 2008.

[62] H. Alfvén. On the motion of cosmic rays in interstellar space. *Physical Review*, 55(5):425–429, 1939.

[63] J. R. Davies. Alfvén limit in fast ignition. *Physical Review E*, 69(6 Pt 2):065402, 2004.

[64] E. S. Weibel. Spontaneously growing transverse waves in a plasma due to an anisotropic velocity distribution. *Physical Review Letters*, 2(3):83, 1959.

[65] M. N. Quinn. Investigations of Fast Electron Transport in Intense Laser-Solid Interactions. PhD thesis, *University of Strathclyde*, 2011.

[66] P. McKenna, A. P. L. Robinson, *et al.* Effect of lattice structure on energetic electron transport in solids irradiated by ultraintense laser pulses. *Physical Review Letters*, 106(18):185004, 2011.

[67] S. Kar, D. Adams, *et al.* Magnetic collimation of petawatt driven fast electron beam for prospective fast ignition studies. *Journal of Physics: Conference Series*, 244(2):022041, 2010.

[68] J. S. Green, V. M. Ovchinnikov, *et al.* Effect of laser intensity on fast-electron-beam divergence in solid-density plasmas. *Physical Review Letters*, 100(1):015003, 2008.

[69] K. Akli, M. Storm, *et al.* Time dependence of fast electron beam divergence in ultraintense laser-plasma interactions. *Physical Review E*, 86(2):026404, 2012.

[70] H. Padda, M. King, *et al.* Intra-pulse transition between ion acceleration mechanisms in intense laser-foil interactions. *Physics of Plasmas*, 23(6):063116, 2016.

[71] R. A. Snavely, M. H. Key, *et al.* Intense high-energy proton beams from petawatt-laser irradiation of solids. *Physical Review Letters*, 85(14):2945–2948, 2000.

[72] S. P. Hatchett, C. G. Brown, *et al.* Electron, photon, and ion beams from the relativistic interaction of petawatt laser pulses with solid targets. *Physics of Plasmas*, 7(5):2076–2082, 2000.

[73] E. Clark, K. Krushelnick, *et al.* Measurements of energetic proton transport through magnetized plasma from intense laser interactions with solids. *Physical Review Letters*, 84(4):670–673, 2000.

[74] S. C. Wilks, A. B. Langdon, *et al.* Energetic proton generation in ultra-intense laser-solid interactions. *Physics of Plasmas*, 8(2):542–549, 2001.

[75] Y. Sentoku, T. E. Cowan, *et al.* High energy proton acceleration in interaction of short laser pulse with dense plasma target. *Physics of Plasmas*, 10(5):2009–2015, 2003.

[76] R. Gray, R. Wilson, *et al.* Enhanced laser-energy coupling to dense plasmas driven by recirculating electron currents. *New Journal of Physics*, 20(3):033021, 2018.

[77] A. J. Mackinnon, Y. Sentoku, *et al.* Enhancement of proton acceleration by hot-electron recirculation in thin foils irradiated by ultraintense laser pulses. *Physical Review Letters*, 88(21):215006, 2002.

[78] O. Tresca, D. C. Carroll, *et al.* Controlling the properties of ultraintense laser-proton sources using transverse refluxing of hot electrons in shaped mass-limited targets. *Plasma Physics and Controlled Fusion*, 53(10):105008, 2011.

[79] P. McKenna, D. C. Carroll, *et al.* Lateral electron transport in high-intensity laser-irradiated foils diagnosed by ion emission. *Physical Review Letters*, 98(14):145001, 2007.

[80] P. Mora. Plasma expansion into a vacuum. *Physical Review Letters*, 90(18):185002, 2003.

[81] P. Mora. Thin-foil expansion into a vacuum. *Physical Review E*, 72(5):056401, 2005.

[82] J. Schreiber, F. Bell, *et al.* Analytical model for ion acceleration by high-intensity laser pulses. *Physical Review Letters*, 97(4):045005, 2006.

[83] J. Fuchs, P. Antici, *et al.* Laser-driven proton scaling laws and new paths towards energy increase. *Nature Physics*, 2(1):48–54, 2006.

[84] A. Macchi, S. Veghini, *et al.* "Light sail" acceleration reexamined. *Physical Review Letters*, 103(8):085003, 2009.

[85] J. W. Yoon, Y. G. Kim, *et al.* Realization of laser intensity over 10^{23} wcm^{-2}. *Optica*, 8(5):630–635, 2021.

[86] T. Esirkepov, M. Borghesi, *et al.* Highly efficient relativistic-ion generation in the laser-piston regime. *Physical Review Letters*, 92(17):175003, 2004.

[87] T. Esirkepov, M. Yamagiwa, *et al.* Laser ion-acceleration scaling laws seen in multiparametric particle-in-cell simulations. *Physical Review Letters*, 96(10):105001, 2006.

[88] C. Scullion, D. Doria, *et al.* Polarization dependence of bulk ion acceleration from ultrathin foils irradiated by high-intensity ultrashort laser pulses. *Physical review letters*, 119(5):054801, 2017.

[89] J. Denavit. Absorption of high-intensity subpicosecond lasers on solid density targets. *Physical Review Letters*, 69(21):3052–3055, 1992.

[90] A. P. L. Robinson, P. Gibbon, *et al.* Relativistically correct hole-boring and ion acceleration by circularly polarized laser pulses. *Plasma Physics and Controlled Fusion*, 51(2):024004, 2009.

[91] F. Dollar, C. Zulick, *et al.* Finite spot effects on radiation pressure acceleration from intense high-contrast laser interactions with thin targets. *Physical Review Letters*, 108(17):175005, 2012.

[92] B. Qiao, M. Zepf, *et al.* Stable gev ion-beam acceleration from thin foils by circularly polarized laser pulses. *Physical review letters*, 102(14):145002, 2009.

[93] O. Klimo, J. Psikal, *et al.* Monoenergetic ion beams from ultrathin foils irradiated by ultrahigh-contrast circularly polarized laser pulses. *Physical Review Accelerators and Beams*, 11(3):031301, 2008.

[94] T. P. Yu, A. Pukhov, *et al.* Stable laser-driven proton beam acceleration from a two-ion-species ultrathin foil. *Physical Review Letters*, 105(6):065002, 2010.

[95] S. Kar, K. F. Kakolee, *et al.* Ion acceleration in multispecies targets driven by intense laser radiation pressure. *Physical Review Letters*, 109(18):185006, 2012.

[96] G. I. Taylor. The instability of liquid surfaces when accelerated in a direction perpendicular to their planes. i. *Proceedings of the Royal Society of London. Series A. Mathematical and Physical Sciences*, 201(1065):192–196, 1950.

[97] C. Palmer, J. Schreiber, *et al.* Rayleigh-taylor instability of an ultrathin foil accelerated by the radiation pressure of an intense laser. *Physical Review Letters*, 108(22):225002, 2012.

[98] B. Hegelich, I. Pomerantz, *et al.* Laser-driven ion acceleration from relativistically transparent nanotargets. *New Journal of Physics*, 15(8):085015, 2013.

[99] S. Williamson, R. Gray, *et al.* Energy absorption and coupling to electrons in the transition from surface-to volume-dominant intense laser–plasma interaction regimes. *New Journal of Physics*, 22(5):053044, 2020.

[100] L. Yin, B. Albright, *et al.* Gev laser ion acceleration from ultrathin targets: The laser break-out afterburner. *Laser and Particle Beams*, 24(2):291–298, 2006.

[101] L. Yin, B. Albright, *et al.* Monoenergetic and gev ion acceleration from the laser breakout afterburner using ultrathin targets. *Physics of plasmas*, 14(5):056706, 2007.

[102] B. Albright, L. Yin, *et al.* Relativistic buneman instability in the laser breakout afterburner. *Physics of Plasmas*, 14(9):094502, 2007.

[103] X. Yan, T. Tajima, *et al.* Theory of laser ion acceleration from a foil target of nanometer thickness. *Applied Physics B*, 98(4):711–721, 2010.

[104] H. Zhuo, Z. Chen, *et al.* Quasimonoenergetic proton bunch generation by dual-peaked electrostatic-field acceleration in foils irradiated by an intense linearly polarized laser. *Physical review letters*, 105(6):065003, 2010.

[105] B. Qiao, S. Kar, *et al.* Dominance of radiation pressure in ion acceleration with linearly polarized pulses at intensities of 10 21 w cm- 2. *Physical review letters*, 108(11):115002, 2012.

[106] H. W. Powell, M. King, *et al.* Proton acceleration enhanced by a plasma jet in expanding foils undergoing relativistic transparency. *New Journal of Physics*, 17(10):103033, 2015.

[107] C. Hooker, Y. Tang, *et al.* Improving coherent contrast of petawatt laser pulses. *Optics Express*, 19(3):2193–2203, 2011.

[108] G. G. Scott, V. Bagnoud, *et al.* Optimization of plasma mirror reflectivity and optical quality using double laser pulses. *New Journal of Physics*, 17(3):033027, 2015.

[109] F. von Zernike. Beugungstheorie des schneidenver-fahrens und seiner verbesserten form, der phasenkontrastmethode. *Physica*, 1(7-12):689–704, 1934.

[110] J. C. Wyant and K. Creath. Basic Wavefront Aberration Theory For Optical Metrology. *Applied Optics and Optical Engineering*, 1992.

[111] M. D. Perry, D. Pennington, *et al.* Petawatt laser pulses. *Optics Letters*, 24(3):160–162, 1999.

[112] C. N. Danson, C. Haefner, *et al.* Petawatt and exawatt class lasers worldwide. *High Power Laser Science and Engineering*, 7(54), 2019.

[113] I. Musgrave, M. Galimberti, *et al.* Review of laser diagnostics at the vulcan laser facility. *High Power Laser Science and Engineering*, 3:e26, 2015.

[114] G. Cheriaux, B. Walker, *et al.* Aberration-free stretcher design for ultrashort-pulse amplification. *Optics Letters*, 21(6):414–416, 1996.

[115] W. Shaikh, I. Musgrave, *et al.* A high contrast dual OPCPA pre-amplifier system using both picosecond and nanosecond pump pulses for the vulcan petawatt facility. In *Lasers, Sources and Related Photonic Devices. Optical Society of America*, 2010.

[116] C. Ziener, P. S. Foster, *et al.* Specular reflectivity of plasma mirrors as a function of intensity, pulse duration, and angle of incidence. *Journal of Applied Physics*, 93(1):768–770, 2003.

[117] G. Doumy, F. Quéré, *et al.* Complete characterization of a plasma mirror for the production of high-contrast ultraintense laser pulses. *Physical Review E*, 69(2):026402, 2004.

[118] P. Monot, G. Doumy, *et al.* High-order harmonic generation by nonlinear reflection of an intense high-contrast laser pulse on a plasma. *Optics Letters*, 29(8):893–895, 2004.

[119] B. Dromey, S. Kar, *et al.* The plasma mirror- a subpicosecond optical switch for ultrahigh power lasers. *Review of Scientific Instruments*, 75(3):645–649, 2004.

[120] D. Neely, P. Foster, *et al.* Enhanced proton beams from ultrathin targets driven by high contrast laser pulses. *Applied Physics Letters*, 89(2):021502, 2006.

[121] H. C. Kapteyn, A. Szoke, *et al.* Prepulse energy suppression for high-energy ultrashort pulses using self-induced plasma shuttering. *Optics Letters*, 16(7):490–492, 1991.

[122] T. Wittmann, J. P. Geindre, *et al.* Towards ultrahigh-contrast ultraintense laser pulses- complete characterization of a double plasma-mirror pulse cleaner. *Review of Scientific Instruments*, 77(8):083109, 2006.

[123] Y. Nomura, L. Veisz, *et al.* Time-resolved reflectivity measurements on a plasma mirror with few-cycle laser pulses. *New Journal of Physics*, 9(1):9, 2007.

[124] A. Kon, M. Nakatsutsumi, *et al.* Geometrical optimization of an ellipsoidal plasma mirror toward tight focusing of ultra-intense laser pulse. *Journal of Physics: Conference Series*, 244(3):032008, 2010.

[125] M. Nakatsutsumi, A. Kon, *et al.* Fast focusing of short-pulse lasers by innovative plasma optics toward extreme intensity. *Optics Letters*, 35(13):2314–2316, 2010.

[126] R. Wilson, M. King, *et al.* Ellipsoidal plasma mirror focusing of high power laser pulses to ultra-high intensities. *Physics of Plasmas*, 23(3):033106, 2016.

[127] R. Wilson, M. King, *et al.* Development of focusing plasma mirrors for ultraintense laser-driven particle and radiation sources. *Quantum Beam Science*, 2(1), 2018.

[128] R. Wilson. On the role of focal spot size in ultra-intense laser-solid interaction physics. PhD thesis, *University of Strathclyde*, 2018.

[129] http://www.srim.org.

[130] M. Borghesi, D. H. Campbell, *et al.* Electric field detection in laser-plasma interaction experiments via the proton imaging technique. *Physics of Plasmas*, 9(5):2214–2220, 2002.

[131] M. N. Quinn, X. H. Yuan, *et al.* Refluxing of fast electrons in solid targets irradiated by intense, picosecond laser pulses. *Plasma Physics and Controlled Fusion*, 53(2):025007, 2011.

[132] P. Neumayer, B. Aurand, *et al.* The role of hot electron refluxing in laser-generated k-alpha sources. *Physics of plasmas*, 17(10):103103, 2010.

[133] A. Curcio, P. Andreoli, *et al.* Imaging plates calibration to x-rays. *Journal of Instrumentation*, 11(05):C05011–C05011, may 2016.

[134] A. A. Vlasov. On vibration properties of electron gas. *Journal of Experimental and Theoretical Physics*, 8(3):291, 1938.

[135] C. Birdsall and A. Langdon. Plasma Physics via Computer Simulation. *Institute of Physics*, 2004.

[136] T. Arber, K. Bennett, *et al.* Contemporary particle-in-cell approach to laser-plasma modelling. *Plasma Physics and Controlled Fusion*, 57(11):113001, 2015.

[137] K. Yee. Numerical solution of initial boundary value problems involving maxwell's equations in isotropic media. *IEEE Transactions on antennas and propagation*, 14(3):302–307, 1966.

[138] R. Hockney. Measurements of collision and heating times in a two-dimensional thermal computer plasma. *Journal of Computational Physics*, 8(1):19–44, 1971.

[139] S. Kawata, T. Izumiyama, *et al.* Laser ion acceleration toward future ion beam cancer therapy- numerical simulation study. *Laser Therapy*, 22(2):103–114, 2013.

[140] F. Wagner, O. Deppert, *et al.* Maximum proton energy above 85 mev from the relativistic interaction of laser pulses with micrometer thick ch 2 targets. *Physical review letters*, 116(20):205002, 2016.

[141] I. J. Kim, K. H. Pae, *et al.* Radiation pressure acceleration of protons to 93 mev with circularly polarized petawatt laser pulses. *Physics of Plasmas*, 23(7):070701, 2016.

[142] T.-C. Liu, X. Shao, *et al.* Spot size dependence of laser accelerated protons in thin multi-ion foils. *Physics of Plasmas*, 21(6):063102, 2014.

[143] V. A. Vshivkov, N. M. Naumova, *et al.* Nonlinear electrodynamics of the interaction of ultra-intense laser pulses with a thin foil. *Physics of Plasmas*, 5(7):2727–2741, 1998.

[144] S. Williamson, R. Wilson, *et al.* Self-referencing spectral interferometric probing of the onset time of relativistic transparency in intense laser-foil interactions. *Physical Review Applied*, 14(3):034018, 2020.

[145] B. Gonzalez-Izquierdo, R. J. Gray, *et al.* Optically controlled dense current structures driven by relativistic plasma aperture-induced diffraction. *Nature Physics*, 12(5):505–512, 2016.

[146] M. Duff, R. Wilson, *et al.* High order mode structure of intense light fields generated via a laser-driven relativistic plasma aperture. *Scientific reports*, 10(1):1–10, 2020.

[147] B. Gonzalez-Izquierdo, M. King, *et al.* Towards optical polarization control of laser-driven proton acceleration in foils undergoing relativistic transparency. *Nature Communications*, 7:12891, 9 2016.

[148] S. Palaniyappan, C. Huang, *et al.* Efficient quasi-monoenergetic ion beams from laser-driven relativistic plasmas. *Nature communications*, 6(1):1–12, 2015.

[149] M. King, R. Gray, *et al.* Energy exchange via multi-species streaming in laser-driven ion acceleration. *Plasma Physics and Controlled Fusion*, 59(1):014003, 2016.

[150] T. Frazer, R. Wilson, *et al.* Enhanced laser intensity and ion acceleration due to self-focusing in relativistically transparent ultrathin targets. *Physical Review Research*, 2(4):042015, 2020.

[151] L. Robson, P. T. Simpson, *et al.* Scaling of proton acceleration driven by petawatt-laser-plasma interactions. *Nature Physics*, 3(1):58–62, 2007.

[152] C. Brenner, J. Green, *et al.* Dependence of laser accelerated protons on laser energy following the interaction of defocused, intense laser pulses with ultra-thin targets. *Laser and Particle Beams*, 29(3):345–351, 2011.

[153] J. S. Green, D. C. Carroll, *et al.* Enhanced proton flux in the MeV range by defocused laser irradiation. *New Journal of Physics*, 12(8):085012, 2010.

[154] M. Passoni, L. Bertagna, *et al.* Target normal sheath acceleration: theory, comparison with experiments and future perspectives. *New Journal of Physics*, 12(4):045012, 2010.

[155] M. Coury, D. C. Carroll, *et al.* Influence of laser irradiated spot size on energetic electron injection and proton acceleration in foil targets. *Applied Physics Letters*, 100(7):074105, 2012.

[156] M. Nakatsutsumi, Y. Sentoku, *et al.* Self-generated surface magnetic fields inhibit laser-driven sheath acceleration of high-energy protons. *Nature communications*, 9(1):1–9, 2018.

[157] C. S. Brady, C. Ridgers, *et al.* Laser absorption in relativistically underdense plasmas by synchrotron radiation. *Physical review letters*, 109(24):245006, 2012.

[158] M. J. Duff, R. Capdessus, *et al.* Modelling the effects of the radiation reaction force on the interaction of thin foils with ultra-intense laser fields. *Plasma Physics and Controlled Fusion*, 60(6):064006, 2018.

[159] F. Nürnberg, M. Schollmeier, *et al.* Radiochromic film imaging spectroscopy of laser-accelerated proton beams. *Review of Scientific Instruments*, 80(3):033301, 2009.

[160] R. Wilson, M. King, *et al.* Influence of spatial-intensity contrast in ultraintense laser-plasma interactions. *Scientific Reports*, 2022.

[161] M. Zepf, M. Castro-Colin, *et al.* Measurements of the hole boring velocity from doppler shifted harmonic emission from solid targets. *Physics of Plasmas*, 3(9):3242–3244, 1996.

[162] B. Gonzalez-Izquierdo, R. Capdessus, *et al.* Radiation pressure-driven plasma surface dynamics in ultra-intense laser pulse interactions with ultrathin foils. *Applied Sciences*, 8(3):336, 2018.

[163] G. Mourou and T. Tajima. The extreme light infrastructure: optics next horizon. *Optics and Photonics News*, 22(7):47–51, 2011.

[164] M. Perry, J. Sefcik, *et al.* Hard x-ray production from high intensity laser solid interactions. *Review of scientific instruments*, 70(1):265–269, 1999.

[165] C. M. Brenner, S. R. Mirfayzi, *et al.* Laser-driven x-ray and neutron source development for industrial applications of plasma accelerators. *Plasma Physics and Controlled Fusion*, 58(1):014039, 2016.

[166] A. J. Mackinnon, P. K. Patel, *et al.* Proton radiography of a laser-driven implosion. *Physical Review Letters*, 97(4):045001, 2006.

[167] D. A. MacLellan, D. C. Carroll, *et al.* Tunable mega-ampere electron current propagation in solids by dynamic control of lattice melt. *Physical Review Letters*, 113(18):185001, 2014.

[168] R. Edwards, M. Sinclair, *et al.* Characterization of a gamma-ray source based on a laser-plasma accelerator with applications to radiography. *Applied Physics Letters*, 80(12):2129–2131, 2002.

[169] A. L. Meadowcroft and R. D. Edwards. High-energy bremsstrahlung diagnostics to characterize hot-electron production in short-pulse laser-plasma experiments. *IEEE Transactions on Plasma Science*, 40(8):1992–2001, 2012.

[170] R. Kodama, H. Shiraga, *et al.* Nuclear fusion: Fast heating scalable to laser fusion ignition. *Nature*, 418(6901):933–934, 2002.

[171] R. Scott, C. Beaucourt, *et al.* Controlling fast-electron-beam divergence using two laser pulses. *Physical review letters*, 109(1):015001, 2012.

[172] M. Wei, A. Solodov, *et al.* Study of relativistic electron beam production and transport in high-intensity laser interaction with a wire target by integrated lsp modeling. *Physics of Plasmas*, 15(8):083101, 2008.

[173] D. Papadopoulos, J. Zou, *et al.* The apollon 10 pw laser: experimental and theoretical investigation of the temporal characteristics. *High Power Laser Science and Engineering*, 4, 2016.

[174] http://physics.nist.gov/physrefdata/star/text/estar.html.

[175] J. Myatt, W. Theobald, *et al.* High-intensity laser interactions with mass-limited solid targets and implications for fast-ignition experiments on OMEGA EP. *Physics of Plasmas*, 14(5):056301, 2007.

[176] C. Quarles. Semiempirical analysis of electron-induced k-shell ionization. *Physical Review A*, 13(3):1278, 1976.

[177] J. Schreiber. Ion acceleration driven by high-intensity laser pulses. PhD thesis, *Ludwig Maximilian University of Munich*, 2006.

[178] A. Link, R. R. Freeman, *et al.* Effects of target charging and ion emission on the energy spectrum of emitted electrons. *Physics of Plasmas*, 18(5):053107, 2011.

[179] N. Iwata, S. Kojima, *et al.* Plasma density limits for hole boring by intense laser pulses. *Nature communications*, 9(1):1–7, 2018.

[180] C. Ridgers, T. Blackburn, *et al.* Signatures of quantum effects on radiation reaction in laser–electron-beam collisions. *Journal of Plasma Physics*, 83(5), 2017.